Measurement and QCD Analysis of Jet Cross Sections in Deep-Inelastic Positron-Proton Collisions at $\sqrt{s} = 300$ GeV

Von der Fakultät für Mathematik, Informatik und Naturwissenschaften
der Rheinisch-Westfälischen Technischen Hochschule Aachen
zur Erlangung des akademischen Grades eines Doktors
der Naturwissenschaften genehmigte Dissertation

vorgelegt von

Diplom-Physiker
Markus Wobisch

aus Düsseldorf

Berichter: Universitätsprofessor Dr. G. Flügge
Universitätsprofessor Dr. Ch. Berger

Tag der mündlichen Prüfung: 4.2.2000

“Science is an intellectual dead end, you know?
It’s a lot of little guys in tweed suits cutting up frogs on foundation grants.”

Miles Monroe in: Woody Allen, The Sleeper, 1973

To Christel, Walter and Tobias

Contents

Introduction

According to our present understanding all phenomena are described by the interactions of elementary particles due to four fundamental forces: gravity and the electromagnetic, the weak and the strong interactions. The properties of gravity are described by the general theory of relativity. The electromagnetic, the weak and the strong interactions are described in the framework of the "Standard Model" of particle physics.

In this thesis we perform tests of Quantum Chromodynamics (QCD), the theory of the strong interaction, which describes the interactions of quarks and gluons due to their color charge. QCD does, however, not predict the absolute strength of the strong interaction, the "strong coupling constant" α_s. The value of α_s enters the theory as a parameter which has to be determined experimentally. Furthermore available calculational techniques do not allow to predict the momentum distributions of quarks and gluons inside a composite particle as the proton. These "quark and gluon density functions" have therefore also to be obtained from experiment.

The direct determination of α_s and the gluon and quark densities in the proton is the subject of the present work.

Deep-inelastic lepton-proton scattering experiments have played an important role in the understanding of the structure of the proton and in establishing QCD as the theory of the strong interaction [1]. Compared to earlier experiments with fixed proton targets the electron-proton collider HERA with its much larger lepton-proton center-of-mass energy allows to explore the proton structure at a significantly higher resolution.

The inclusive electron-proton cross section is directly sensitive to the quark densities in the proton, but allows only indirect conclusions on α_s and the gluon content. Observables which are *directly* sensitive to α_s and the gluon density in the proton are the multi-jet cross sections, i.e. the production rates of events in which the final state contains (besides the proton remnant) more than one collimated spray of hadrons, so called "jets".

Multi-jet cross sections in deep-inelastic scattering were measured for the first time by the E665 collaboration in a fixed target experiment [2]. The high center-of-mass energy at HERA produces more pronounced jet structures and provides a clean testing ground for QCD dynamics in analyses of the hadronic final state. In previous analyses at HERA the production rates of dijet events in deep-inelastic scattering at large momentum transfers Q^2 were used to determine the strong coupling constant α_s [3, 4, 5].

The aim of this thesis is to extend these analyses regarding both the experimental measurement and the scope of the QCD analysis. A large variety of jet observables is measured as a function of kinematic and jet specific quantities using different jet algorithms. The predictions of perturbative QCD are tested in inclusive jet, in dijet, in three-jet and in four-jet production. The internal structure of jets is studied in a dijet event sample.

In a QCD analysis of the inclusive jet and the dijet cross sections we determine α_s and study its "running" as a function of the transverse jet energy. The inclusion of H1 structure function data with their direct sensitivity to the quark densities provides the opportunity to perform a consistent direct determination of the gluon density simultaneously with the quark densities in the proton. Since both data sets are measured by one experiment the correlated experimental uncertainties can fully be taken into account. We perform the first simultaneous direct determination of α_s, the gluon and the quark densities in the proton.

The thesis is organized in three parts.

- The first part is devoted to the theoretical basis of the analysis.
  In chapter 1 we describe the theoretical framework in which α_s and the parton density functions are defined and discuss in what way different processes in positron-proton scattering are sensitive to these parameters. The concept of jet observables is introduced in chapter 2. We give the exact definitions of the jet algorithms and motivate the choice of the jet phase space used in the analysis. Properties of the theoretical predictions are studied in chapter 3 to identify those phase space regions and observables for which theoretical uncertainties are smallest.

- The second part contains all details of the experimental work.
  A brief description of the H1 detector is given in chapter 4 together with the experimental methods applied in the analysis. In chapter 5 we discuss the data selection and provide numerous control distributions which are the basis of the unfolding of the data as performed in chapter 6. All experimental results are presented in chapter 7 where they are compared to theoretical predictions.

- In part three we interpret the measurements in the framework of QCD.
  An outline of the QCD analysis and a description of the technical details of the fitting procedure is given in chapter 8. In chapter 9 we perform QCD fits in which we determine α_s and the gluon and quark densities in the proton.

Remarks:

Throughout this thesis we set $\hbar = c = 1$.

The results of this work fall in two categories: observables (e.g. jet cross sections) and theoretical parameters (e.g. the gluon density in the proton). Correspondingly we will carefully distinguish between the usage of the words "measurement" and "determination" (or "extraction").

Observables are *measurable* quantities which correspond to properties of phenomena in the physical world. Once they are (correctly) measured they constitute facts, which have to be described by any physical theory which claims to describe nature.

Theoretical parameters, on the other hand, are quantities which are defined (and have a meaning) only in a given theoretical framework. In this framework they are related to observables and can therefore be *determined* (or *extracted*) in a theoretical analysis of the observables. Once, however, the corresponding theory is disproven, the results of the parameters loose their relevance, whereas the observables measured are for eternity ...

Part I

Foundation: Theory of Jet Production in Deep-Inelastic Scattering

1

Basic Theoretical Concepts

In this chapter we give an overview of the general structure of cross sections in perturbative Quantum Chromodynamics (pQCD) and discuss the definitions of the strong coupling constant α_s and the parton density functions. We also introduce the kinematic variables and the structure functions needed to describe deep-inelastic scattering.

This chapter does not contain any new results. All information presented is taken from textbooks [6, 7, 8, 9, 10], lecture notes [11, 12] or other literature (as cited).

1.1 The Strong Coupling Constant α_s – Renormalization

Quantum Chromodynamics (QCD), the theory of the strong interaction, describes the interactions of quarks and gluons. Predictions for scattering processes are obtained by perturbative methods using the Feynman rules which can be derived from the Lagrangian density. Any cross section is then computed as a power series in the strong coupling constant $\alpha_s \equiv g_s^2/4\pi$ where g_s is the gauge coupling of QCD. The contributions from each order can be visualized by so-called Feynman diagrams, each of which is a combination of a number of fundamental vertices. In Fig. 1.1 the fundamental vertices of QCD are displayed. Quarks are represented by straight solid lines and gluons by helixes. Each vertex of Fig. 1.1 a) and b) in a Feynman diagram contributes one factor of $\sqrt{\alpha_s}$ and each vertex 1.1 c) a factor of α_s to the corresponding matrix element. The cross section of the process is then calculated as the absolute value squared of the sum of all contributing matrix elements, integrated over the available phase space.

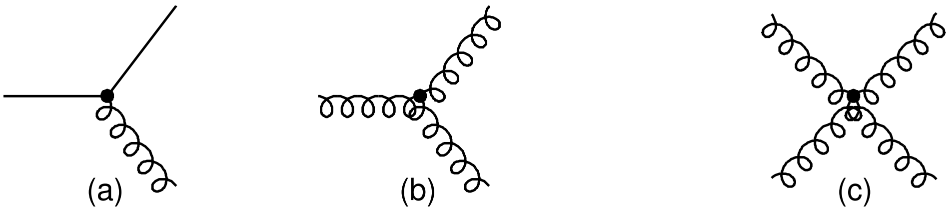

Figure 1.1: The fundamental vertices of QCD

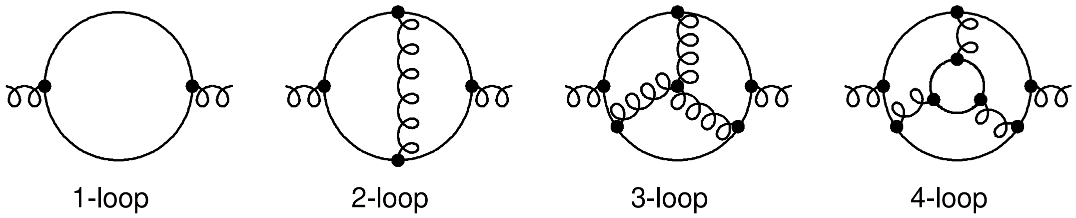

Figure 1.2: Loop corrections to the gluon propagator in QCD Feynman diagrams

Perturbative calculations in leading order (i.e. the lowest order in α_s contributing to the observable) contain only "tree-level" diagrams without internal loops. At higher orders in α_s any observable receives contributions from diagrams including loops as displayed in Fig. 1.2. The loop integrals in these graphs are performed over all (internal) loop momenta P. These integrals are divergent due to the contributions from $P \to \infty$. These so-called ultraviolet (UV) divergences can be made temporarily finite by some "regularization" procedure, e.g. by the introduction of an ultraviolet momentum cut-off or by dimensional regularization [13]. The regularized divergences are then removed by absorbing them into the definition of the coupling strength via a "renormalization procedure". This is done according to a specific (but arbitrary) prescription, which introduces a new dimensional scale μ_r (the "renormalization scale"). The "modified minimal-subtraction scheme" ($\overline{\text{MS}}$ scheme) [14] is widely used for this purpose and will also be employed in all calculations in this thesis.

The renormalization scale can be regarded as the momentum at which the subtractions which remove the UV divergences are performed. It follows that the renormalized coupling $\alpha_s(\mu_r)$ as well as the perturbative coefficients in the power series for the matrix elements depend on the choice made for μ_r. However, since μ_r is an arbitrary parameter, the value of any physical observable R (if calculated to all orders in α_s) has to be independent of μ_r. This is expressed mathematically by the "renormalization group equation"

$$\mu_r^2 \frac{\partial R}{\partial \mu_r^2} + \mu_r^2 \frac{\partial \alpha_s}{\partial \mu_r^2} \frac{\partial R}{\partial \alpha_s} = 0 . \tag{1.1}$$

From (1.1) follows a differential equation in which the μ_r dependence of $\alpha_s(\mu_r)$ is given by the β function of QCD which can be expanded as a power series in $\alpha_s(\mu_r)$

$$\frac{\partial a}{\partial \ln \mu^2} = \beta(a) = -\beta_0 a^2 - \beta_1 a^3 - \beta_2 a^4 - \beta_3 a^5 + \mathcal{O}(a^6) . \tag{1.2}$$

with $a(\mu_r) \equiv \alpha_s(\mu_r)/(4\pi)$. The coefficients β_0 [15] and β_1 [16] are universal (i.e. scheme independent). The results for β_2 [17] and β_3 [18] are available for the $\overline{\text{MS}}$ scheme. One finds

$$\begin{aligned}
\beta_0 &= 11 - \frac{2}{3} n_f , \\
\beta_1 &= 102 - \frac{38}{3} n_f ,
\end{aligned}$$

$$\begin{aligned}
\beta_2 &= \frac{2857}{2} - \frac{5033}{18} n_f + \frac{325}{54k} n_f^2 \, , \\
\beta_3 &= \left(\frac{149753}{6} + 3564 \, \zeta_3 \right) - \left(\frac{1078361}{162} + \frac{6508}{27} \, \zeta_3 \right) n_f \\
&+ \left(\frac{50065}{162} + \frac{6472}{81} \, \zeta_3 \right) n_f^2 + \frac{1093}{729} \, n_f^3 \, .
\end{aligned} \tag{1.3}$$

Here ζ is the Riemann zeta-function ($\zeta_3 = 1.202056903 \cdots$) and n_f is the number of active quark flavors[1]. To simplify the notation we define $b_N \equiv \beta_N / \beta_0$ $(N = 1, 2, 3)$. Integrating (1.2) leads to [19]

$$\begin{aligned}
\ln \frac{\mu^2}{\Lambda^2} &= \int \frac{\mathrm{d}a}{\beta(a)} \\
&= \frac{1}{\beta_0} \left[\frac{1}{a} + b_1 \ln a + (b_2 - b_1^2) a + \left(\frac{b_3}{2} - b_1 b_2 + \frac{b_1^3}{2} \right) a^2 \right] + \frac{b_1}{\beta_0} \ln \beta_0 \, .
\end{aligned} \tag{1.4}$$

The integration introduces a constant Λ, the so-called asymptotic scale parameter, which specifies the value of the renormalization scale μ_r at which $\alpha_s(\mu_r)$ diverges.

Using (1.4) one can determine the value of α_s at any scale μ_r if either Λ or, alternatively, the value of α_s at an arbitrary scale is known. The procedure of using the Λ parameter (which is typically of the order of 200 – 300 MeV) is nowadays disfavored since it is not uniquely defined beyond leading order [20] and its value depends on the number of active quark flavors. Instead it has become conventional to quote the value of α_s in the $\overline{\mathrm{MS}}$ scheme at the scale $\mu_r = M_Z = 91.187\,\mathrm{GeV}$ [21], the mass of the Z^0 boson which is very precisely measured ($\pm 0.007\,\mathrm{GeV}$). This value of the scale is safely in the perturbative region ($\alpha_s(M_Z) \ll 1$) and far away from the quark thresholds ($m_b \ll M_Z \ll m_t$).

To eliminate Λ and to obtain $\alpha_s(\mu_r)$ as a function of $\alpha_s(M_Z)$ one may set $\mu_r = M_Z$ in (1.4) and subtract this from (1.4) at an arbitrary scale μ_r. This yields

$$a(\mu_r) = \frac{a(M_Z)}{1 + a(M_Z) L} \, , \tag{1.5}$$

$$\begin{aligned}
\text{with} \qquad L &= \beta_0 \ln \frac{\mu_r^2}{M_Z^2} + b_1 \ln \frac{a(M_Z)}{a(\mu_r)} + (b_2 - b_1^2)(a(M_Z) - a(\mu_r)) \\
&+ \left(\frac{b_3}{2} - b_1 b_2 + \frac{b_1^3}{2} \right) (a^2(M_Z) - a^2(\mu_r)) \, .
\end{aligned}$$

For a given value of $\alpha_s(M_Z)$ the value of $\alpha_s(\mu_r)$ can now be evaluated using two different procedures. One can obtain an approximate solution (at N-loop accuracy) by iteratively solving (1.6) and discarding the terms of $\mathcal{O}(1/\ln^N(\mu_r^2/\Lambda^2))$. Alternatively one may solve (1.6) exactly using numerical methods. The latter method was used in a recent determination of the world average value of $\alpha_s(M_Z)$ [22] and will also be used in this thesis.

---

[1] In this thesis we always work in phase space regions where the process relevant energy scales are above the mass of the bottom quark ($m_b \simeq 4.5\,\mathrm{GeV}$) and below the mass of the top quark ($m_t \simeq 173\,\mathrm{GeV}$), and hence $n_f = 5$ is used in all cases.

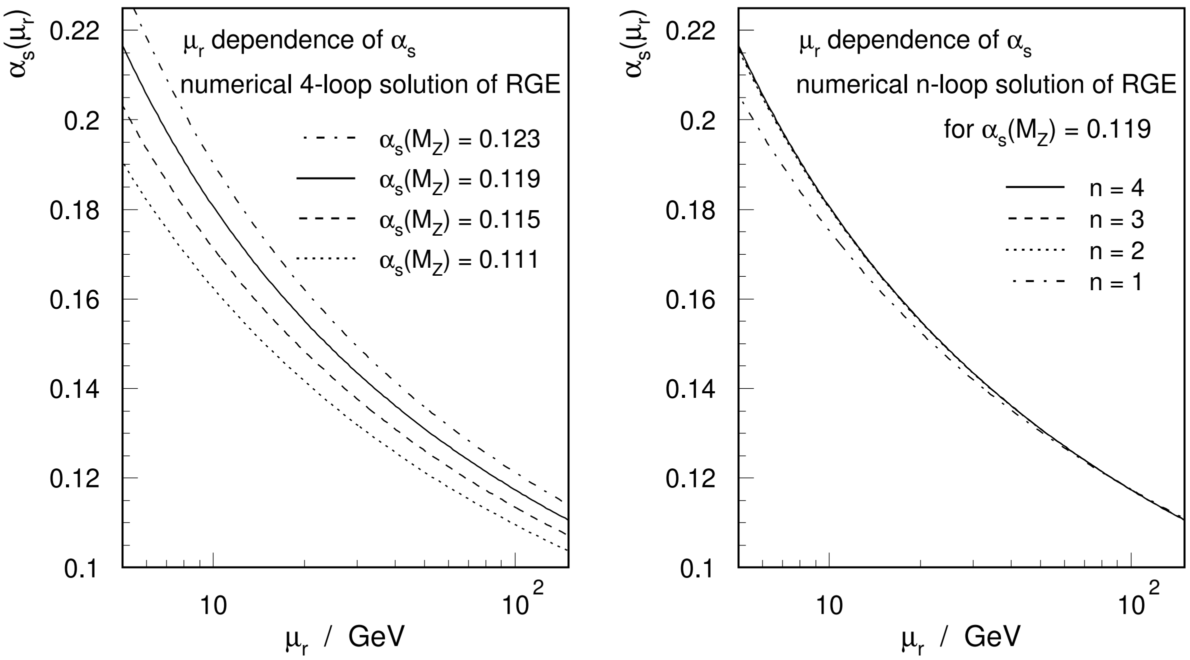

Figure 1.3: Solutions of the renormalization group equation ($\overline{\text{MS}}$ scheme, $n_f = 5$). On the left the running of $\alpha_s(\mu_r)$ is displayed for different values of $\alpha_s(M_Z)$ using the 4-loop formula. The right plot shows the running of $\alpha_s(\mu_r)$ in different approximations of the renormalization group equation.

Solution of the Renormalization Group Equation

The basic property of the solution (1.6) of the renormalization group equation manifests itself already at 1-loop accuracy (i.e. $b_1 = b_2 = b_3 = 0$). $\alpha_s(\mu_r)$ depends logarithmically on μ_r ("the running coupling") and approaches zero as μ_r becomes large. At large energies where $\alpha_s(\mu_r) \ll 1$ the quarks and gluons can therefore be considered as free particles whose interactions are calculable in perturbation theory as a power series in α_s. This is the "asymptotic freedom" of QCD.

In Fig. 1.3 we display the running of α_s in the range $5 < \mu_r < 130\,\text{GeV}$. The left plot shows the 4-loop solution for different values of $\alpha_s(M_Z)$. A 7% difference at $\mu_r = M_Z$ leads to an increased difference of 14% at $\mu_r = 5\,\text{GeV}$. On the right we compare the solutions of (1.6) in 1-, 2-, 3- and 4-loop accuracy. The 1-loop result deviates from the others, but the differences between the 2-, 3- and 4-loop solutions are too small to be visible in the plot. We therefore display the ratios of the different curves in Fig. 1.4. The left plot shows the ratio of the 2-, 3- and 4-loop curves to the 1-loop solution and the right plot the corresponding ratios to the 4-loop result. While the corrections to the 1-loop result are significant at small scales (5% at $\mu_r = 5\,\text{GeV}$) the higher order corrections to the 2-loop result are negligible (5 per mil at $\mu_r = 5\,\text{GeV}$).

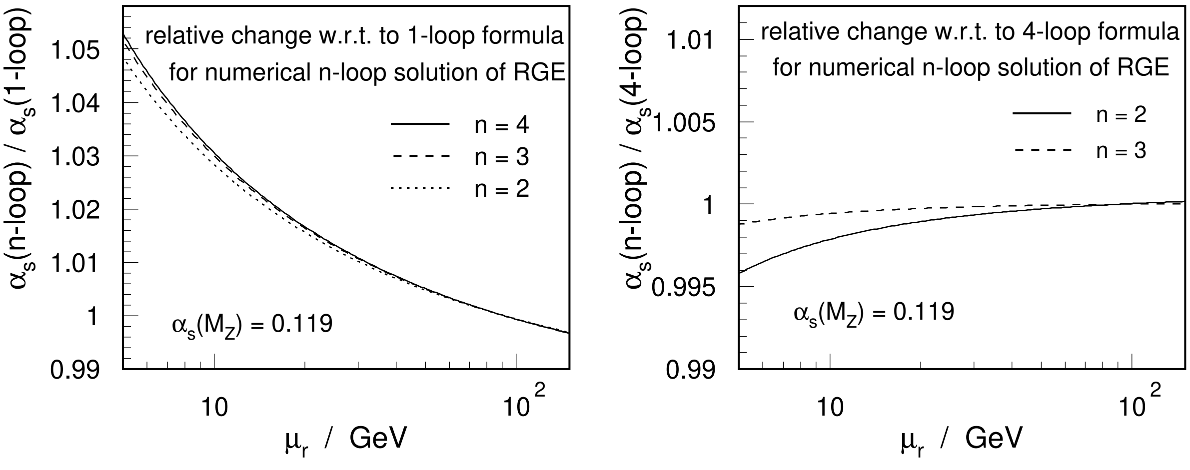

Figure 1.4: A comparison of the 1-, 2-, 3- and 4-loop solutions of the renormalization group equation for $\alpha_s(M_Z) = 0.119$. Shown are the ratios of the different results to the 1-loop result (left) and to the 4-loop result (right).

The Current World Average Value of $\alpha_s(M_Z)$

The value of $\alpha_s(M_Z)$ is a *universal* (i.e. process independent) parameter in QCD which has to be determined from experiment. The status of $\alpha_s(M_Z)$ determinations in different processes has been summarized by the Particle Data Group throughout the last decade (see Fig. 1.5). Recent reviews in [20, 23, 21, 22] have determined a world average value of

$$\begin{aligned} \alpha_s(M_Z)_{\text{world average}} &= 0.118 \pm 0.004 \qquad \text{W.J. Stirling (1997) [20]}\,, \\ &= 0.119 \pm 0.005 \qquad \text{S. Catani (1997) [23]}\,, \\ &= 0.119 \pm 0.002 \qquad \text{Particle Data Group (1998) [21]}\,, \\ &= \underline{\underline{0.119 \pm 0.004}} \qquad \text{S. Bethke (1998) [22]}\,. \end{aligned}$$

The central values and the estimated uncertainties are similar for all authors. Only the Particle Data Group obtains a significantly smaller uncertainty as a consequence of not taking into account the correlations between the theoretical uncertainties of the single values. The analysis by S. Bethke [22] contains the most recent experimental results and studies regarding the influence of the statistical methods used in the averaging procedure on the result. In this thesis we will therefore refer to this value and its uncertainty as the world average value.

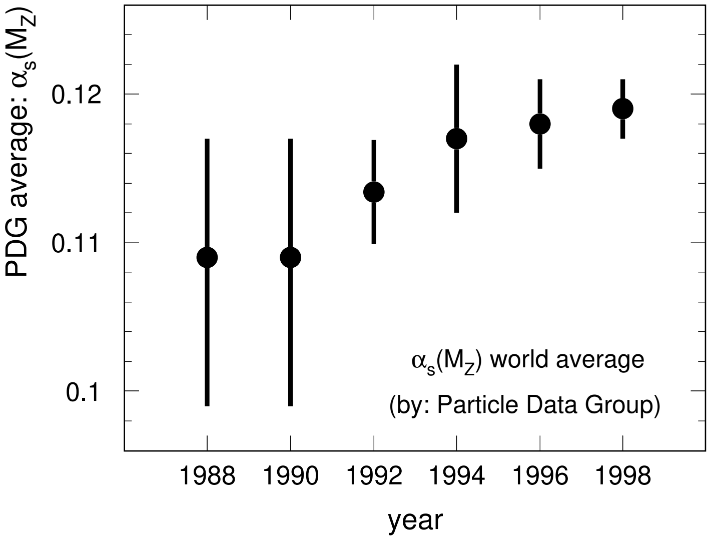

Figure 1.5: The development of the world average value of $\alpha_s(M_Z)$ over the last decade as determined by the Particle Data Group [21].

1.2 Parton Density Functions – Factorization

At short distances (corresponding to high energies) where $\alpha_s(\mu_r) \ll 1$, the interactions of single partons (i.e. quarks and gluons) can be calculated in perturbative QCD whereas at macroscopic distances partons appear only in bound states of colorless hadrons ("color confinement"). The interactions of partons in a hadron take place at long distances (i.e. low energies) where perturbation theory is no longer applicable. The momentum distributions of partons inside a hadron can therefore not be computed from first principles but have to be parameterized by so-called "parton density functions" $\tilde{f}_{a/h}(x)$ which give the probability density of finding a parton a inside the hadron h carrying a fraction x of the hadron's (longitudinal) momentum. Any cross section involving partons in the initial state is then given by the product of the partonic cross section and the parton density function, summed over all contributing partons and integrated over all values of x.

This procedure is called "factorization" of the perturbative (short-distance) and the non-perturbative (long-distance) process. The non-perturbative contributions are factorized into the parton density functions which have to be determined from experiment. The parton density functions specify a *universal* (i.e. process independent) property of the corresponding hadron. Once determined in a single process they can be used as input for perturbative calculations of any other process involving this hadron.

The scattering of a virtual photon $\gamma^\star$ and a quark q in the proton is described in lowest order by the diagram in Fig.1.6 a). The higher order corrections to this process include graphs as the one shown in Fig.1.6 b) with additional gluon emissions. The contributions from these diagrams have to be integrated over all transverse momenta $k_\perp$ of the gluons relative to the

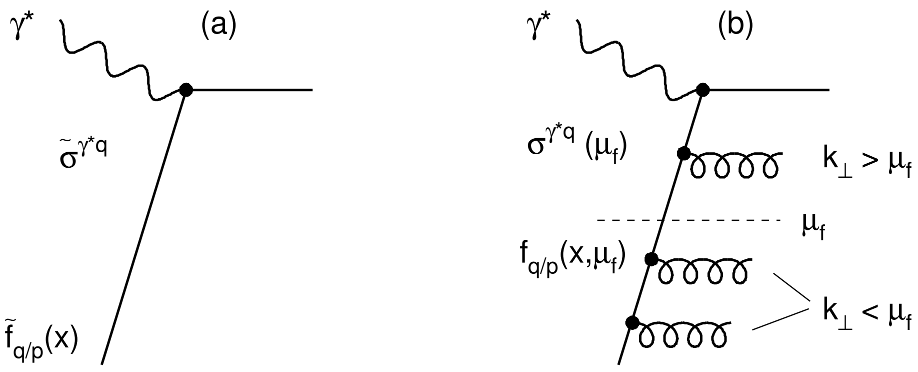

Figure 1.6: Feynman diagrams for the scattering of a virtual photon and a quark in lowest order (left) and in higher orders α_s (right). The redefinition of the quark density function absorbs all gluon emissions with relative transverse momenta $k_\perp < \mu_f$ into the quark density. This introduces a dependence on the chosen factorization scale μ_f in both, the quark density $f_{a/p}(x, \mu_f)$ and the partonic cross section $\sigma^{\gamma^\star q}(\mu_f)$ of the hard scattering process.

initial quark and become divergent at $k_\perp \to 0$, i.e. for collinear gluon emissions. These divergences are not cured by renormalization.

It is, however, possible to extract the collinear divergences mentioned from the perturbative coefficients to all orders in perturbation theory as universal factors which can be absorbed into a redefinition of the parton density functions according to a given prescription, called "factorization scheme". This procedure introduces a new scale μ_f (the factorization scale) corresponding to the transverse momentum $k_\perp$ below which parton emissions are included in the (redefined) parton density functions $f_{a/h}(x, \mu_f)$.

The parton density functions are now only defined within the given scheme and depend, just like the perturbative coefficients, on the choice of μ_f. A common factorization scheme which will also be used in this thesis is again the $\overline{\text{MS}}$ scheme. In analogy to the renormalization group equation (1.1) there is an equation expressing that any physical observable (when calculated to all orders in α_s) is independent of the choice of μ_f. This relation, known as the Dokshitzer-Gribov-Lipatov-Altarelli-Parisi (DGLAP) equation [24, 25], is a system of coupled differential equations describing the μ_f dependence of the parton density functions

$$\mu_f \frac{\partial}{\partial \mu_f} \begin{pmatrix} q_i(x, \mu_f) \\ g(x, \mu_f) \end{pmatrix} = \frac{\alpha_s}{2\pi} \sum_{q_j, \bar{q}_j} \int_x^1 \frac{\mathrm{d}\eta}{\eta} \begin{pmatrix} P_{q_i,q_j}\left(\frac{x}{\eta}, \alpha_s\right) & P_{q_i,g}\left(\frac{x}{\eta}, \alpha_s\right) \\ P_{g,q_j}\left(\frac{x}{\eta}, \alpha_s\right) & P_{g,g}\left(\frac{x}{\eta}, \alpha_s\right) \end{pmatrix} \begin{pmatrix} q_i(\eta, \mu_f) \\ g(\eta, \mu_f) \end{pmatrix}, \tag{1.6}$$

where g is the gluon density and q_i are the quark densities for flavor i. We have used the short-hand notation $\alpha_s \equiv \alpha_s(\mu)$. The DGLAP splitting functions (or "evolution kernels") $P_{ab}(z)$ are calculable as power series in α_s

$$P_{q_i q_j}(z, \alpha_s) \;=\; \delta_{ij} P^{(0)}_{qq}(z) + \frac{\alpha_s}{2\pi} P^{(1)}_{q_i q_j}(z) + \cdots,$$

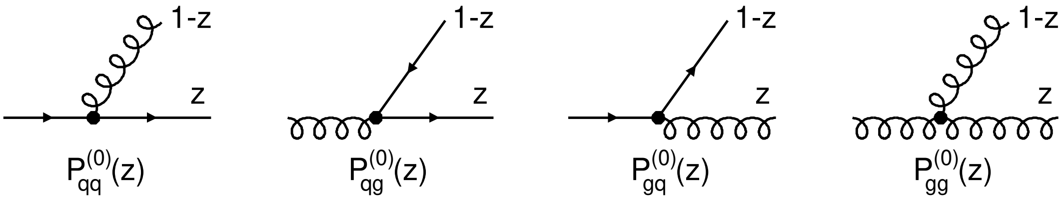

Figure 1.7: The Feynman diagrams of the leading-order splitting functions

$$
\begin{aligned}
P_{qg}(z,\alpha_s) &= P^{(0)}_{qg}(z) + \frac{\alpha_s}{2\pi} P^{(1)}_{qg}(z) + \cdots\,, \\
P_{gq}(z,\alpha_s) &= P^{(0)}_{gq}(z) + \frac{\alpha_s}{2\pi} P^{(1)}_{gq}(z) + \cdots\,, \\
P_{gg}(z,\alpha_s) &= P^{(0)}_{gg}(z) + \frac{\alpha_s}{2\pi} P^{(1)}_{gg}(z) + \cdots\,. \qquad (1.7)
\end{aligned}
$$

The diagrams corresponding to the leading order contributions $P^{(0)}_{ab}(z)$ are displayed in Fig. 1.7. These splitting functions can be interpreted as the probability densities of finding a parton a in a parton b with a longitudinal momentum fraction z of the parent parton and a transverse momentum much less than μ_f [25]. The perturbative expansion of the splitting functions has been calculated to next-to-leading order ($\mathcal{O}(\alpha_s)$) [26] (the analytical expressions are e.g. given in [10]). The DGLAP equations (1.6) are usually solved by direct numerical integration in x space [27] or analytically in moment space [28].

While the x dependence of the parton distributions is not predicted by perturbative QCD, the μ_f dependence is given by the DGLAP equations (1.6), in a similar way as the running of α_s is described by the renormalization group equation. However, the evolution of a single parton density function involves mixing with other parton flavors and therefore requires the full knowledge of *all* parton distributions over the *entire* range $0 \leq x \leq 1$.

The Parton Density Functions of the Proton

The best knowledge of the parton density functions of the proton is obtained in global fits to a large number of data sets which are separately sensitive to different parton flavors or to different linear combinations of parton flavors. In these fits the x dependence of the single parton distributions is parameterized by flexible functional forms (over the whole range $0 \leq x \leq 1$) at a "starting scale" $\mu_{f,0}$ (typically chosen in the range $1 \leq \mu_{f,0} \leq 2\,\text{GeV}$). These parton densities are evolved by the DGLAP equations to larger μ_f where they are used to compute the perturbative cross sections which are then compared to the data. The parameters of the functional forms are iteratively adjusted in a χ^2 minimization procedure to give an optimized description of all data sets.

The most recent results have been obtained in the fits by the CTEQ collaboration [29] and by the groups MRST [30] and GRV [31]. These results are available in the form of tables over the whole x and μ_f range along with computer code to perform the interpolations between

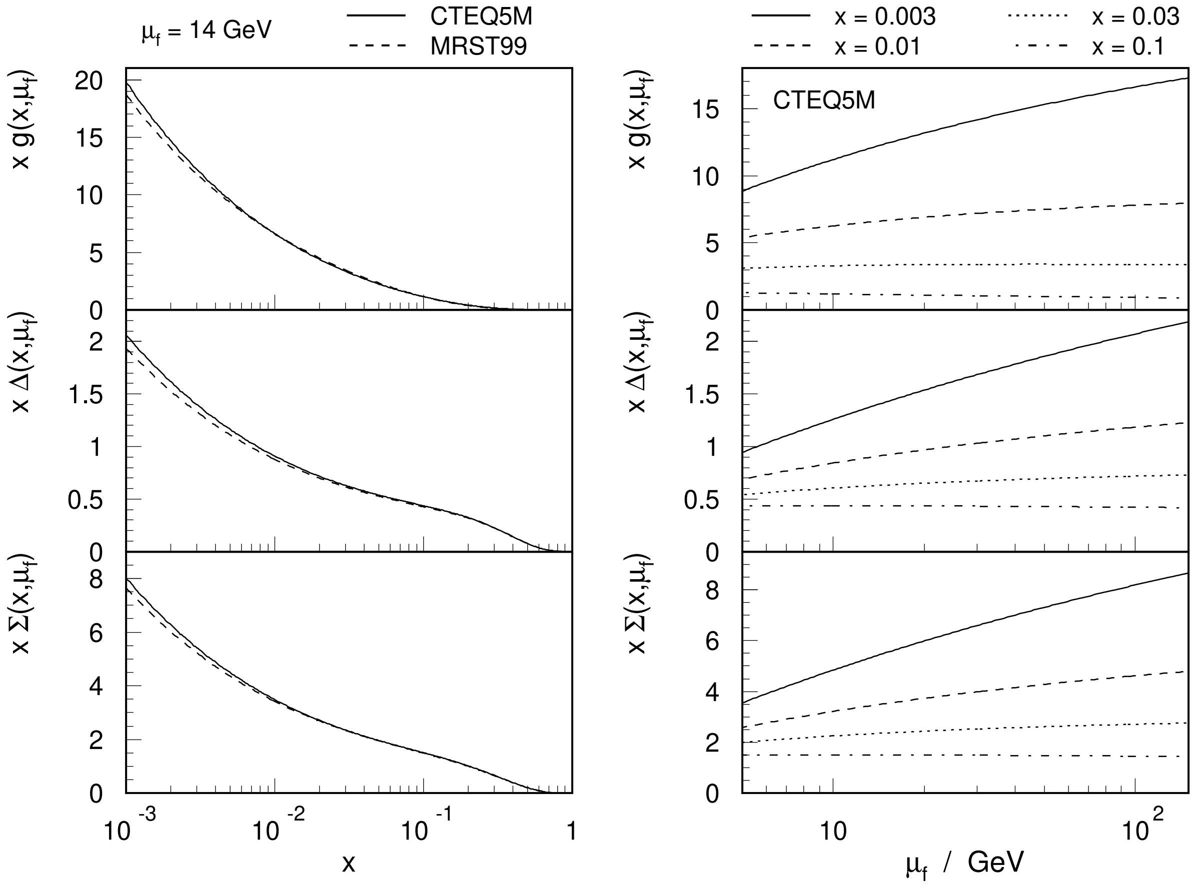

Figure 1.8: The x dependence (left) and the μ_f dependence (right) of parton density functions obtained in global fits.

the single values. The global fits give parameterizations of the world's best knowledge of the parton distributions. However, a determination of the uncertainties of these results, important to estimate the uncertainties of the theoretical predictions for other processes, is still missing.

In Fig. 1.8 parton distributions obtained from recent global fits are displayed. In addition to the gluon density $xg(x,\mu_f)$ we have plotted two linear combinations of the quark densities (a motivation for these choices will be given later in section 8.2.2) defined as

$$\begin{aligned} x\Sigma(x,\mu_f) &\equiv x\sum_a \left(q_a(x,\mu_f)+\bar{q}_a(x,\mu_f)\right), \\ x\Delta(x,\mu_f) &\equiv x\sum_a e_a^2(q_a(x,\mu_f)+\bar{q}_a(x,\mu_f)), \end{aligned}$$

where the sums run over all quark flavors a and e_a denotes the electrical charge of the quarks. Fig. 1.8 shows the x dependence of these parton distributions at fixed μ_f (left) and the μ_f dependence at four different x values (right).

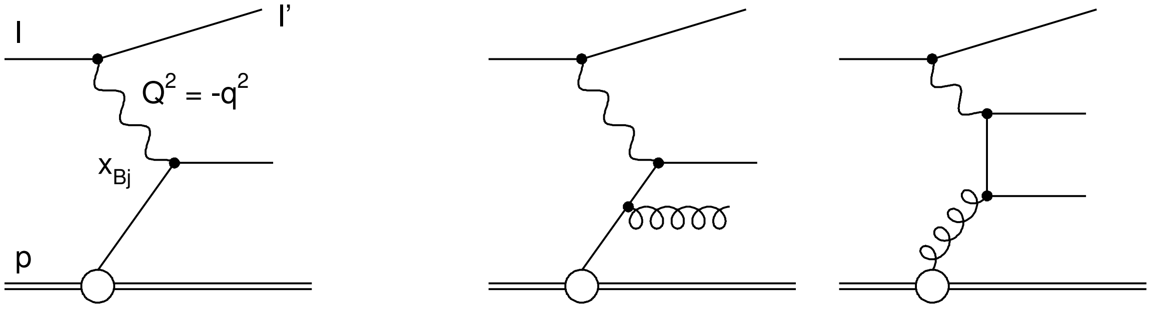

Figure 1.9: Diagrams of different processes in deep-inelastic lepton-proton scattering: The Born process (left), the QCD-Compton process (middle) and the boson-gluon fusion process (right).

1.3 Deep-Inelastic Lepton-Proton Scattering

The deep-inelastic scattering process of a charged lepton and a proton proceeds either via the exchange of a photon, Z^0 ("neutral current") or $W^{\pm}$ boson ("charged current"). In the following we discuss the neutral current reaction which is at lowest order described by the Feynman diagram shown in Fig. 1.9 (left) where l (l') denotes the four-momentum of the incoming (scattered) lepton and p the four-momentum of the proton. At a fixed center-of-mass energy $\sqrt{s} = \sqrt{(l+p)^2}$ the kinematics is completely given by two variables. Usually these are selected from the four-momentum transfer Q^2, the Bjorken scaling variable $x_{\rm Bj}$ and the inelasticity variable y defined as[2]

$$Q^2 \;=\; -q^2 \equiv -(l-l')^2\,, \qquad x_{\rm Bj} \;\equiv\; \frac{Q^2}{2\,p\cdot q}\,, \qquad y \;\equiv\; \frac{p\cdot q}{p\cdot l}\,. \tag{1.8}$$

The double differential cross section can be decomposed into a Born cross section and two factors which include the QED and the weak radiative corrections from higher orders

$$\frac{{\rm d}^2\sigma_{\rm NC}}{{\rm d}x_{\rm Bj}\,{\rm d}Q^2} \;=\; \left(\frac{{\rm d}^2\sigma_{\rm NC}}{{\rm d}x_{\rm Bj}\,{\rm d}Q^2}\right)_{\rm Born} \left(1+\delta_{\rm NC}^{\rm QED}(x_{\rm Bj},Q^2)\right)\,\left(1+\delta_{\rm NC}^{\rm weak}(x_{\rm Bj},Q^2)\right)\,. \tag{1.9}$$

The double differential Born cross section can be written as

$$\left(\frac{{\rm d}^2\sigma_{\rm NC}}{{\rm d}x_{\rm Bj}\,{\rm d}Q^2}\right)_{\rm Born} \;=\; \frac{2\pi\alpha^2}{x_{\rm Bj}\,Q^4}\,\phi_{\rm NC}(x_{\rm Bj},Q^2)\,, \tag{1.10}$$

where α is the electromagnetic coupling constant and $\phi_{\rm NC}$ is a linear combination of structure functions which are used to parameterize the structure of the proton

$$\phi_{\rm NC}(x_{\rm Bj},Q^2) \;=\; Y_+\tilde{F}_2(x_{\rm Bj},Q^2) \;-\; Y_-\,x_{\rm Bj}\tilde{F}_3(x_{\rm Bj},Q^2) \;-\; y^2\tilde{F}_L(x_{\rm Bj},Q^2)\,. \tag{1.11}$$

---

[2] In this thesis the Bjorken scaling variable $x_{\rm Bj}$ is always written with a subscript to distinguish it from the "proton momentum fraction" x which appears in the formulae for the parton density functions. While the Bjorken scaling variable is an *observable* event property, the variable x is (as described in section 1.2) only defined in a theoretical calculation within a given factorization scheme.

The helicity dependences of the electroweak interactions are contained in the functions $Y_\pm = 1 \pm (1-y)^2$. The structure function $\tilde{F}_2$ receives contributions from γ exchange, from γ/Z^0 interference and from Z^0 exchange while $\tilde{F}_3$ has only contributions from γ/Z^0 interference and Z^0 exchange. In the kinematic region $Q^2 \ll M_Z^2$ the latter contributions are, however, negligible and $\tilde{F}_2$ is reduced to the electromagnetic structure function F_2. Defining $R \equiv F_L/(F_2 - F_L)$ the neutral current cross section can be written as

$$\left(\frac{\mathrm{d}^2\sigma_{\mathrm{NC}}}{\mathrm{d}x_{\mathrm{Bj}}\,\mathrm{d}Q^2}\right)_{\mathrm{Born}} = \frac{2\pi\alpha^2}{x_{\mathrm{Bj}}\,Q^4}\left[2 - 2y + \frac{y^2}{1+R}\right] F_2(x_{\mathrm{Bj}}, Q^2)\,. \tag{1.12}$$

It is seen that the structure function $F_2(x_{\mathrm{Bj}}, Q^2)$ is not directly related to the observable cross section, but can only be extracted under an assumption for R. This initial assumption may lead to a bias in a further QCD analysis of the structure function data. To avoid this bias one can define a "reduced cross section" $\tilde{\sigma}_{\mathrm{NC}}(x_{\mathrm{Bj}}, Q^2)$ which is *directly* related to the measured cross section by

$$\tilde{\sigma}_{\mathrm{NC}}(x_{\mathrm{Bj}}, Q^2) \equiv \frac{1}{Y_+}\,\frac{Q^4\,x_{\mathrm{Bj}}}{2\pi\alpha^2}\left(\frac{\mathrm{d}^2\sigma_{\mathrm{NC}}}{\mathrm{d}x_{\mathrm{Bj}}\,\mathrm{d}Q^2}\right)\,. \tag{1.13}$$

In a QCD fit to the reduced cross section one can then determine the value of R and quote the corresponding value of $F_2(x_{\mathrm{Bj}}, Q^2)$. This method is used in recent measurements by the H1 collaboration [32].

The perturbative expansion for $\tilde{\sigma}_{\mathrm{NC}}(x_{\mathrm{Bj}}, Q^2)$ (and for $F_2(x_{\mathrm{Bj}}, Q^2)$) has been calculated to next-to-leading order [26]

$$\tilde{\sigma}_{\mathrm{NC}}(x_{\mathrm{Bj}}, Q^2) = \tilde{\sigma}_{\mathrm{NC}}(x_{\mathrm{Bj}}, Q^2)_{\mathrm{LO}} + \tilde{\sigma}_{\mathrm{NC}}(x_{\mathrm{Bj}}, Q^2)_{\mathrm{NLO}} + \mathcal{O}(\alpha_s^2)\,. \tag{1.14}$$

Differences between $\tilde{\sigma}_{\mathrm{NC}}(x_{\mathrm{Bj}}, Q^2)$ and $F_2(x_{\mathrm{Bj}}, Q^2)$ are due to higher order contributions while at leading order both are identical. They are related to the quark densities via

$$\tilde{\sigma}_{\mathrm{NC}}(x_{\mathrm{Bj}}, Q^2)_{\mathrm{LO}} = F_2(x_{\mathrm{Bj}}, Q^2)_{\mathrm{LO}} = x_{\mathrm{Bj}} \sum_a e_a^2 \left(q_a(x_{\mathrm{Bj}}, \mu_f^2) + \bar{q}_a(x_{\mathrm{Bj}}, \mu_f^2)\right)\,, \tag{1.15}$$

where the sum runs over all quark flavors a. For the choice $\mu_f^2 = Q^2$ one obtains in leading order the direct correspondence between the quark densities and the structure function and the reduced cross section. At next-to-leading order the reduced cross section and the structure function receive contributions from the middle and right diagram in Fig. 1.9. At this order also the gluon density starts to contribute to the cross section.

Recent H1 results [32, 33] of the structure function $F_2(x_{\mathrm{Bj}}, Q^2)$ are shown in Fig. 1.10 together with data from fixed target experiments. The H1 data alone cover a wide kinematic range of $1.5 < Q^2 < 30000\,\mathrm{GeV}^2$ and $8 \cdot 10^{-5} < x_{\mathrm{Bj}} < 0.65$. A next-to-leading order QCD fit to the combined data sets has been performed based on the DGLAP equations. The resulting parton distributions give a good description of the data over the whole kinematic range.

In the QCD analysis in part three of this thesis we will use the data from [32] as additional input for their sensitivity to the quark densities.

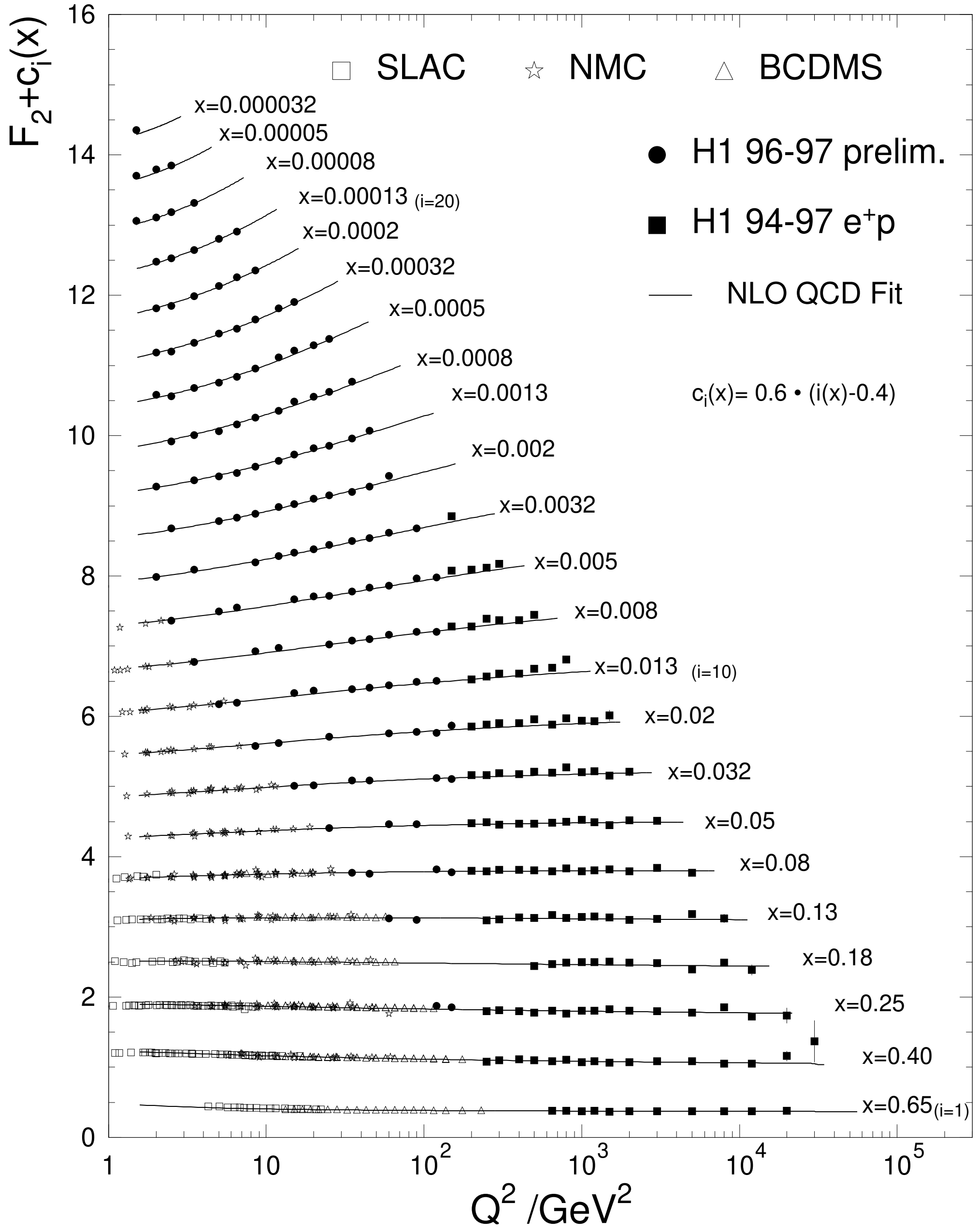

Figure 1.10: The proton structure function $F_2(x_{\mathrm{Bj}}, Q^2)$ obtained from recent measurements by the H1 collaboration along with measurements from fixed target experiments. The results from a next-to-leading order QCD fit to these data are compared to the measurements.

2

Jet Production in Deep-Inelastic Scattering

In this chapter we introduce the jet algorithms used in this analysis and give the exact definitions of all observables to be measured. We also give an overview of the theoretical models used in the QCD analysis and in the unfolding procedure of the data.

2.1 Jet Observables

In perturbative QCD cross sections for short distance processes are formulated in terms of interactions of partons (quarks and gluons), i.e. particles carrying non-zero color charge. Subsequent long distance processes, as showering and hadronization of the primary partons result in final states which consist of colorless hadrons. Due to the confinement of the color charge there can be no unique association of a collimated spray of final state hadrons (a "jet") with a single initial quark or gluon.

To be able to compare the partonic cross sections predicted by the theory with observables measured on the level of hadrons one deliberately chooses event properties which are only weakly effected by long distance processes and which have a close correspondence between partonic and hadronic final states, so-called "jet observables". The residual extent to which a jet observable is influenced by long distance processes depends on the exact definition. To be calculable order-by-order in perturbation theory, jet observables have to fulfill certain requirements.

2.1.1 General Requirements: Infrared and Collinear Safety

Cross sections in perturbative QCD become divergent for the emission of low energy particles[1] (infrared divergence) and whenever two massless partons become parallel (collinear

---

[1] "Particle" refers throughout this work either to an energy deposit in the detector, to a parton in a perturbative QCD calculation or to a hadron (i.e. to any particle produced in the hadronization process including soft photons and leptons from secondary hadron decays). The masses of particles are neglected. In deep-inelastic scattering the scattered lepton is excluded from the final state.

divergence). For inclusive cross sections these singularities are canceled by contributions from virtual corrections. For this cancellation to also take place in the jet cross section, it is necessary that the observable is infrared and collinear safe.

- **Infrared Safety**
  An observable is infrared safe if it is insensitive to the emission of low energy particles. This is the case if it has the same value for a n-parton configuration as for a corresponding $(n+1)$-parton configuration obtained by adding an additional parton with $E \rightarrow 0$ to the final state.

- **Collinear Safety**
  An observable is collinear safe if its value is not changed when replacing a pair of collinear particles by a single particle carrying the summed momentum.

While these requirements are absolutely necessary for an observable to be calculable in perturbation theory they also reduce the sensitivity to experimental limitations such as limited angular resolutions and trigger thresholds of calorimeter cells.

Examples of observables which are not collinear safe are the sum over all momenta squared of the final state particles or any variable which uses the properties of the most energetic particle in the event.

Observables which are not infrared safe are for instance the angle of the jet with the highest transverse energy in $\bar{p}p$ collisions or (for the reasons discussed below) in deep-inelastic scattering in the Breit frame. In leading order two jets are produced with identical transverse energies, such that the decision which of the jets end up with the highest transverse energy depends on the emission of arbitrary soft gluons.

2.1.2 Process Specific Requirements in Deep-Inelastic Scattering

In addition to the infrared and collinear safety of a jet observable further requirements are needed in processes that involve hadrons in the initial state. While in e^+e^- annihilation the total final state arises from the short distance interaction, this is not the case in processes with initial state hadrons, where a fraction of the final state particles is not related to the hard process but to soft interactions of the remaining partons in the incident hadrons (i.e. the hadron remnant).

In perturbative QCD the cross section diverges for particles produced collinear to the hadron direction. These initial state collinear singularities are not canceled by corresponding virtual corrections but are dealt with by the factorization of the singular contributions in a universal (i.e. process independent) way into the parton density functions of the hadron.

According to the factorization theorem of QCD [10] the universal factorizability of initial state divergences is guaranteed for inclusive cross sections. In order to be applicable for jet cross sections in hadron collisions and in deep-inelastic scattering the definition of the jet observable has to enable us to factorize the initial state collinear singularities into universal

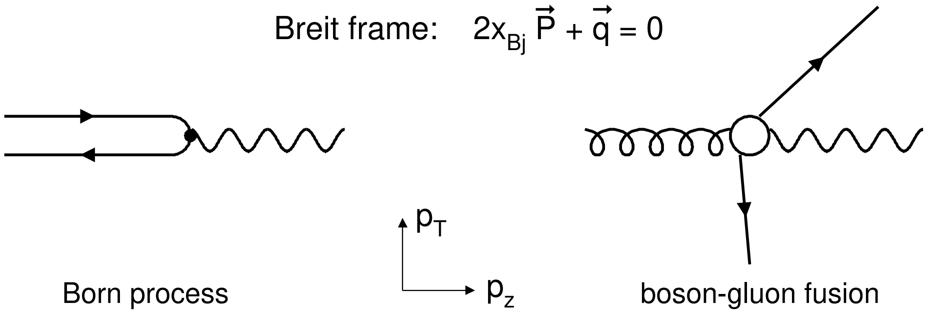

Figure 2.1: Deep-inelastic scattering in the Breit frame: in the Born process at $\mathcal{O}(\alpha_s^0)$ (left) and in boson-gluon fusion at $\mathcal{O}(\alpha_s)$ (right).

parton distributions [34, 35]. It has been discussed in [35] that in jet production in deep-inelastic scattering the factorization property is only given in a special family of reference frames, one of them being the "Breit frame".

2.1.3 The Breit Frame

The Breit frame is defined by $2x_{\rm Bj}\vec{P} + \vec{q} = 0$, where $\vec{p}$ and $\vec{q}$ are the momenta of the incoming proton and the exchanged virtual boson (photon/Z^0), respectively. The z-axis is chosen to be the direction of the incoming proton and the rotation in the x-y plane is performed such that the scattered lepton points in the positive x direction (i.e. $\phi_{e,\rm Breit} = 0°$). In the Breit frame the virtual photon (which is purely space-like with a four-momentum $q = \{0, 0, 0, -Q\}$) interacts head-on with a parton from the proton. In the Born process (Fig. 2.1, left) the incoming quark with longitudinal momentum $p_{z,\rm quark} = Q/2$ is back-scattered with momentum $p_{z,\rm quark} = -Q/2$. In processes of $\mathcal{O}(\alpha_s)$ (e.g. boson-gluon fusion in Fig. 2.1, right) two partons emerge with balanced transverse momenta[2]. In the special case when $x_p \equiv x_{\rm Bj}/x = 1/2$ the Breit frame coincides with the photon-gluon center-of-mass frame while in general both frames are related to each other by a longitudinal boost along the z axis. The transverse energies of particles and jets are therefore identical in both frames.

It follows from the definition of the Breit frame that the transverse energy of the hadronic final state does not have to balance the transverse energy of the scattered lepton (as this is the case in the laboratory frame), but directly reflects the hardness of the underlying QCD process. The Breit frame is hence very well suited to study QCD jets.

All jet observables measured in this thesis are defined in the Breit frame.

---

[2] By "transverse" we refer to the component perpendicular to the z-axis. The transverse energy is defined as $E_T \equiv E \sin\theta$ where θ is the polar angle. Throughout this work "transverse energy" will always refer to transverse energies in the Breit frame (unless stated otherwise).

2.2 Jet Algorithms

One sort of jet observables are the "jet shape variables" (or "event shapes") which are defined by linear sums over all momenta of the hadronic final particles. In deep-inelastic scattering the soft physics, related to the proton remnant, is usually separated by simply restricting the phase space of the analysis to the photon hemisphere of the Breit frame (i.e. including only momenta with $p_z < 0$) [36, 37, 38]. Each final state topology is assessed with a continuous number between zero and a maximum value (the latter is different for different variables) which reflects the amount of QCD radiation in an event.

A more detailed look into the properties of the hadronic final state can be obtained by using "jet algorithms" which decompose the topology of the final state into local regions of collimated energy flow, the so-called "jets". This procedure provides a flexible way to separate the proton remnant from the hadronic final state resulting from the hard process, based on the transverse momenta of particles relative to the proton direction. Properties of the jets, such as jet multiplicities, angular distributions and distributions of the invariant mass of the multi-jet system can then be used to study various aspects of the dynamics of the underlying short distance process.

There is, however, no unique procedure to define jets. Any jet cross section, as well as the properties of the jets will always depend on the exact definition. Different jet definitions are in different ways sensitive to low-energy particles and therefore differently affected by higher order corrections and by hadronization corrections. In this section we give a detailed description of the jet algorithms used in the present analysis and compare their basic features.

2.2.1 Classifications of Jet Definitions

A large variety of jet definitions has been proposed in the last decades (see e.g. [39] and references therein). The different jet definitions can be classified according to the following criteria.

Jet Clustering Algorithms and Other Definitions

"Jet clustering algorithms" define jets by successive recombinations of pairs of particles in an iterative procedure (the ARCLUS algorithm [40] iteratively recombines three particles into two). Other approaches are used in cone algorithms which define jets by maximizing the transverse energy flow through a cone of fixed size [41, 42] or by the DECO procedure [43] where the event is decomposed by a topological function which is calculated from all particles simultaneously.

It has been shown [44, 45] that cone jet definitions suffer from several ambiguities (related to the assignment of particles to jets) which introduce uncertainties when comparing the predictions of perturbative calculations to measured jet cross sections. We will therefore only use clustering algorithms which allow an unambiguous assignment of particles to jets.

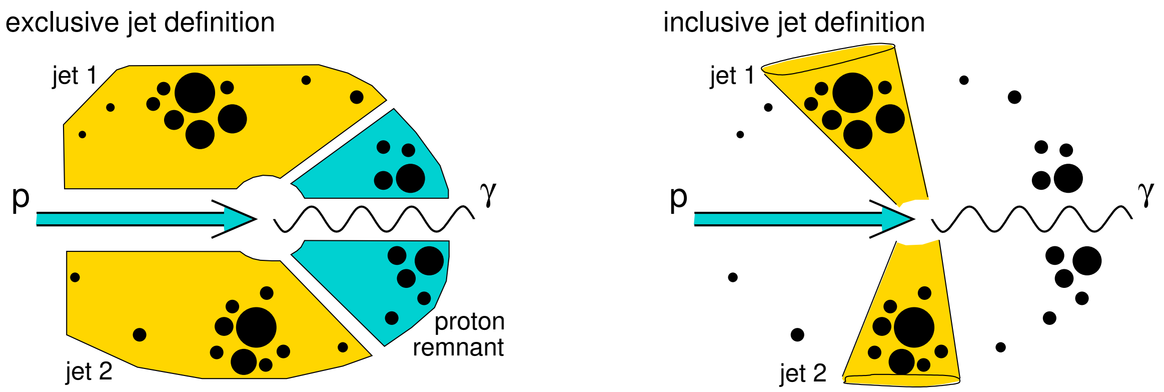

Figure 2.2: An example of how the final state particles in a deep-inelastic scattering event in the Breit frame are combined into jets by an exclusive jet definition (left) and by an inclusive jet definition (right).

The Order of the Clustering Steps

For jet clustering algorithms one has to specify the *order* in which particles are recombined into jets. The oldest clustering scheme, the JADE algorithm [46, 47] uses the invariant mass as the ordering variable. This introduces, however, a strong attractive kinematic correlation between soft particles leading to a non-intuitive assignment of particles to jets and producing many soft and wide-angle jets [48].

It has been proposed [49, 50, 51] that the relative transverse momenta $k_\perp$ or the angles between particles are better suited as ordering variables. In this analysis we will use both $k_\perp$ and angular ordered jet algorithms.

Inclusive and Exclusive Jet Definitions

The way in which the event is decomposed into jets and (depending on the process) the remnant(s) of the beam hadron(s) is very characteristic for the various jet definitions. In e^+e^- annihilation, where the entire final state emerges from the hard process, one typically uses *exclusive* jet definitions which cluster every final state particle into one of the hard jets. The final state consists of a specific number of hard jets and nothing else. In hadron collisions the final state contains also energy flow associated with the remnants of the beam hadrons. In typical jet definitions used in this process only a fraction of the final state particles is therefore included into the hard jets. The final state of an event contains some number of hard jets with specified properties plus any number of particles not included in jets. We will call these jet definitions “inclusive”.

The exclusive jet definitions can be extended to processes involving initial state hadrons by explicitly introducing beam remnant jets to which particles can be clustered [47, 50]. In Fig. 2.2 an example is shown of how the final state of a deep-inelastic scattering event in the

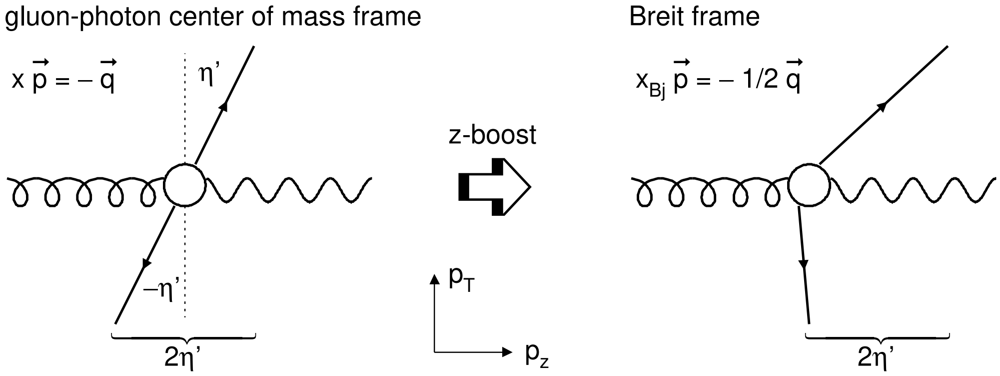

Figure 2.3: A photon-gluon fusion event in deep-inelastic scattering in the center-of-mass frame (left) and in the Breit frame (right). Both frames are related to each other by a longitudinal boost along the z direction. Since differences in the pseudorapidity are invariant under longitudinal boosts the pseudorapidity of the jets in the center of mass frame can be reconstructed from the difference of the pseudorapidities in the Breit frame.

Breit frame is decomposed by an exclusive (left) and by an inclusive jet definition (right)

$$\begin{array}{lrcl} \text{exclusive jet definition:} & e\,p & \rightarrow & e + n\,\text{hard jets} + \text{beam remnant}\,(+\,\text{nothing})\,, \\ \text{inclusive jet definition:} & e\,p & \rightarrow & e + n\,\text{hard jets} + \text{anything}\,. \end{array}$$

Symmetries and Variables Defining the Distance Measure

The choice of variables used to define the distance measure in the clustering procedure is influenced by the symmetries present in the reaction. In e^+e^- annihilation the laboratory frame (where the jet finding is usually performed) coincides with the center-of-mass frame of the hard process. Emphasizing the rotational invariance the distance measure is usually defined in terms of energies E, polar angles θ and azimuthal angles ϕ of particles.

The laboratory frame in $\bar{p}p$ collisions and the Breit frame in deep-inelastic scattering have the common property that the center-of-mass frame is typically boosted along the z direction (see Fig. 2.3). Therefore one prefers to use variables which are invariant under longitudinal boosts such as the transverse energy $E_T \equiv E \sin\theta$, the pseudorapidity[3] $\eta \equiv -\ln(\tan(\theta/2))$ and the azimuthal angle ϕ.

Recombination Schemes

Whenever a pair of particles is merged during the clustering procedure into one four-vector this is done according to a given “recombination scheme” which specifies how the new vector

---

[3] The pseudorapidity can also be defined by $\eta \equiv \frac{1}{2}\ln\frac{p+p_z}{p-p_z}$. For massless particles pseudorapidity differences are invariant under longitudinal boosts. For massive particles this is only the case for differences in the (true) rapidity defined by $y \equiv \frac{1}{2}\ln\frac{E+p_z}{E-p_z}$.

is calculated. Different schemes have been proposed in the literature [52, 50]. They differ by the properties of the four-vectors in the intermediate clustering steps and also in the properties of the final jets. In our analysis we will use recombination schemes which are formulated in the variables that are also used to evaluate the respective distance measure.

For the exclusive jet definitions (which perform the clustering based on energies and angles) we are using the "E-scheme" in which particles are merged by adding their four-vectors

$$E\text{-scheme:} \qquad \mathbf{p}' \; = \; \mathbf{p}_1 + \mathbf{p}_2 \, . \tag{2.1}$$

In this procedure the merged particles and the resulting jets are massive.

The inclusive jet definitions in our analysis are using a distance measure which, being based on transverse energies E_T and differences in the pseudorapidities $\Delta\eta$ and azimuthal angles $\Delta\phi$, is invariant under longitudinal boosts. To maintain this property during the whole clustering procedure the merged particles and the final jets have to be defined to be massless (otherwise we would have to use differences in the true rapidity Δy instead of $\Delta\eta$). We therefore use the E_T-recombination scheme in which the transverse energy of the combined four-vector is given by the (scalar) sum of the transverse particle energies. The direction of the (massless) four-vector is calculated from the E_T weighted averages of the particle variables η and ϕ

$$\begin{array}{llcl} E_T\text{-scheme:} \qquad & E'_T & = & E_{T,1} + E_{T,2} \, , \qquad\qquad\qquad\qquad\qquad\qquad (2.2) \\ & \eta' & = & \dfrac{E_{T,1}\,\eta_1 \; + \; E_{T,2}\,\eta_2}{E_{T,1} + E_{T,2}} \, , \qquad \phi' = \dfrac{E_{T,1}\,\phi_1 \; + \; E_{T,2}\,\phi_2}{E_{T,1} + E_{T,2}} \, . \end{array}$$

The resulting jets are massless.

2.2.2 Exclusive Jet Definitions

The exclusive $k_\perp$ Algorithm for DIS

The (exclusive) $k_\perp$ algorithm for DIS has been proposed in [50] as a modification of the Durham algorithm (invented for e^+e^- annihilation, see e.g. [49]) to account for the proton remnant. In this definition the proton remnant is implicitly considered as a particle of infinite momentum. Unlike in the definition of the modified JADE algorithm for DIS [47] it does, however, not appear explicitly in the clustering procedure as an additional particle. The clustering procedure is defined by a reference scale S and a resolution parameter y_{cut} which specify at which relative $k_\perp^2 = y_{\text{cut}} S^2$ the final jets are separated from each other and from the proton remnant. The relative $k_{\perp ij}^2$ between two particles i, j is here defined as

$$k_{\perp ij}^2 \equiv 2 \min(E_i^2, E_j^2) \, (1 - \cos\theta_{ij}) \, . \tag{2.3}$$

At small θ_{ij} the $k_{\perp ij}^2$ such defined is an approximation of the relative transverse momentum squared of the lower energetic particle with respect to the higher energetic one, but has the advantage of being monotone with θ_{ij}, while the relative transverse momentum becomes smaller again for $\theta_{ij} > 90^\circ$.

The clustering procedure starts with a list of all particles.

1. We compute the distance y_{ip} of every final state particle i to the proton remnant and the relative distance y_{ij} of every pair of particles i, j

$$y_{ip} = 2\,\frac{E_i^2}{S^2}\,(1-\cos\theta_{ip})\,, \qquad y_{ij} = 2\,\frac{\min(E_i^2, E_j^2)}{S^2}\,(1-\cos\theta_{ij})\,, \tag{2.4}$$

   where θ_{ip} is the angle between the i-th particle and the $+z$ direction and θ_{ij} is the angle between the particles i and j.

2. The smallest value of all $\{y_{ip}, y_{ij}\}$ is labeled $y_{\min}$.

   - If $y_{\min}$ belongs to the set $\{y_{ip}\}$ and $y_{\min} < y_{\mathrm{cut}}$ the particle i is considered to be part of the proton remnant and removed from the list of particles.
   - If $y_{\min}$ belongs to the set $\{y_{ij}\}$ and $y_{\min} < y_{\mathrm{cut}}$ the particles i and j are recombined in the E-scheme.

3. The procedure is repeated until $y_{\min} > y_{\mathrm{cut}}$. The remaining particles are the hard jets which are considered in the analysis.

The Angular Ordered Cambridge Algorithm

The Cambridge algorithm for e^+e^- annihilation has been proposed in [51] as a modification of the Durham algorithm in that now the clustering is performed in the order of smallest angles θ_{ij} between particles. We have extended this definition to consider the proton remnant in deep-inelastic scattering according to the prescription in the exclusive $k_\perp$ algorithm. A brief description has already been given in [53].

In the exclusive $k_\perp$ algorithm the variables y_{ij} and y_{ip} act both as ordering variables (step 1) and "test variables" which define the end of the clustering procedure (steps 2 and 3). In the Cambridge algorithm these functions are separated. While the y_{ij} and y_{ip} (as defined before) are still used as test variables, the ordering variables are chosen to be v_{ij} and v_{ip} which are defined in terms of angles only (see below).

The clustering procedure starts with a list of all particles and an empty list of jets.

1. We compute the distance v_{ip} of every final state particle i to the proton remnant as well as the relative distance v_{ij} of every pair of particles i, j

$$v_{ip} = 2\,(1-\cos\theta_{ip})\,, \qquad v_{ij} = 2\,(1-\cos\theta_{ij})\,. \tag{2.5}$$

2. The smallest value of all $\{v_{ip}, v_{ij}\}$ is labeled $v_{\min}$.

- If $v_{\rm min}$ belongs to the set $\{v_{ip}\}$ and the corresponding value y_{ip} (as defined in (2.4)) fulfills $y_{ip} < y_{\rm cut}$ the particle i is considered to be part of the proton remnant and removed from the list of particles.
- If $v_{\rm min}$ belongs to the set $\{v_{ij}\}$ and the corresponding value y_{ij} (as defined in (2.4)) fulfills $y_{ij} < y_{\rm cut}$ the particles i and j are recombined in the E-scheme.

3. If in any of the two cases above $y_{ij} > y_{\rm cut}$ or $y_{ip} > y_{\rm cut}$ the corresponding merge is not carried out but the lower energetic particle of i and j (or particle i if $v_{\rm min}$ was from the set $\{v_{ip}\}$) is put into the list of jets and removed from the list of particles. This step of singling out the lower energetic particle is called "soft freezing" [51].
4. This procedure is repeated until only a single particle is left which is then also included in the list of jets.

Both exclusive jet definitions require two parameters, the reference scale S and the resolution parameter $y_{\rm cut}$. When the clustering procedures are finished the hard jets are separated from each other and from the proton remnant by relative transverse momenta $k_\perp^2 \geq y_{\rm cut} S^2$. No further "hardness cuts" need to be applied.

2.2.3 Inclusive Jet Definitions

The inclusive $k_\perp$ Algorithm

The inclusive $k_\perp$ algorithm has been proposed in [54, 34]. The clustering procedure starts with a list of all particles and an empty list of jets.

1. For each particle i as well as for each pair of particles i, j the distances d_i and d_{ij} are calculated

$$d_i = E_{T,i}^2 \quad \text{and} \quad d_{ij} = \min(E_{T,i}^2, E_{T,j}^2)\,\frac{R_{ij}^2}{R_0^2} \quad \text{with} \quad R_{ij}^2 = (\Delta\eta_{ij})^2 + (\Delta\phi_{ij})^2\,, \tag{2.6}$$

   where R_0 is a parameter which is always set to $R_0 = 1$ in this analysis (as recommended in [54, 34]).

2. The smallest value of all d_i and d_{ij} is labeled $d_{\rm min}$.
3. If $d_{\rm min}$ belongs to the set $\{d_{ij}\}$, the particles i and j are merged into a new particle using the E_T recombination scheme.
4. If $d_{\rm min}$ belongs to the set $\{d_i\}$, the particle i is removed from the list of particles and added to the list of jets.
5. The procedure is finished when no particles are left (i.e. all particles are included in jets).

The last jets that entered the list are the ones with highest transverse energies. These jets are considered in the analysis.

The Angular Ordered Aachen Algorithm

The Aachen algorithm is a new jet definition, invented for the present work (a brief description has already been given in a previous publication [53]). In analogy to the modification from the exclusive $k_\perp$ algorithm to the Cambridge algorithm, we have modified the inclusive $k_\perp$ algorithm to obtain an inclusive algorithm with angular ordering.

The clustering procedure starts with a list of all particles.

1. Find the pair of particles i, j for which the distance d_{ij} is smallest
$$d_{ij} \;=\; \frac{R_{ij}^2}{R_0^2} \;=\; \frac{(\Delta\eta_{ij})^2 + (\Delta\phi_{ij})^2}{R_0^2}\,. \tag{2.7}$$
2. If $d_{ij} < 1$ the particles i and j are merged into a new particle using the E_T recombination scheme. As for the inclusive $k_\perp$ algorithm we set $R_0 = 1$.
3. The procedure is finished when all distances between pairs of particles are $d_{ij} > 1$. The remaining particles are sorted in the order of their transverse energies. The particles with the largest transverse energies are the jets which are considered in the analysis.

In inclusive jet and dijet production in the Breit frame this definition is identical to the inclusive $k_\perp$ algorithm for perturbative calculations at NLO.

While for the exclusive jet definitions the parameters S and $y_{\rm cut}$ define the resolution by which jets are resolved, the clustering procedure for both inclusive jet definitions is independent of an external resolution scale. In the inclusive jet definitions particles with $R_{ij} < R_0$ are subsequently merged, so that all final jets are separated by distances $R_{ij} > R_0$. It is still possible that particles inside a jet have a distance $R_{ij} > R_0$ to the jet axis and that particles with $R_{ij} < R_0$ are not part of the jet.

The inclusive jet definitions provide a list of many jets, from which, however, only those of highest E_T are of physical interest. To measure the n-jet cross section one would use the n jets of largest E_T. Additional hardness cuts can be applied for example on the transverse energies of the single jets or on properties of the n-jet system.

2.3 Jet Cross Sections in QCD

The predictions of perturbative QCD for jet production in deep-inelastic scattering have been calculated in various approximations. Phenomenological models have been constructed to simulate non-perturbative (hadronization) processes. Here we introduce the calculations and models used in this analysis.

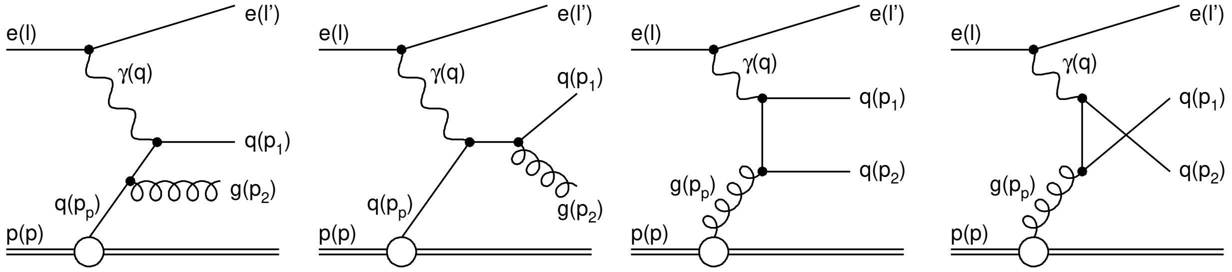

Figure 2.4: The leading order diagrams for jet production of high E_T (in the Breit frame) in deep-inelastic scattering.

2.3.1 Leading Order Matrix Elements

The main observables investigated in this analysis are the inclusive jet and the dijet cross sections in the Breit frame. The leading order contributions to these processes are represented by the diagrams displayed in Fig. 2.4. These diagrams which are of order $\mathcal{O}(\alpha_s)$ describe (from left to right) the QCD-Compton process with initial and final state gluon radiation and the boson-gluon fusion process. An important qualitative difference between the jet cross section and the inclusive cross section (i.e. the structure function) is that the former are *directly* (i.e. already at leading order) sensitive to the gluon density in the proton. In most phase space regions the jet cross section is dominated by boson-gluon fusion.

At leading order there is a one-to-one correspondence between partons and jets. The leading order jet cross section does therefore not depend on details of the jet definition (as the radius parameter R_0 for the inclusive jet definitions introduced in section 2.2.3). Furthermore the predictions are subject to the ambiguities in the choice of the renormalization and factorization scales. Hence we can not expect this calculation to make reliable quantitative predictions for jet cross sections. However, if the perturbative expansion is well behaved, we can expect the leading order calculation to predict the order of magnitude of a given cross section and the rough features of an observable.

In addition to the kinematic variables $x_{\rm Bj}$ and Q^2 as introduced in section 1.3 we need three further variables to describe the leading order jet cross section. These are usually chosen to be z, x_p and ϕ (see e.g. [55]). The variable ϕ denotes the angle between the plane given by the incoming and the scattered lepton and the plane given by the incoming parton and the jets in the photon-parton center-of-mass frame (see Fig. 2.5). The other variables are defined as

$$z \equiv \frac{p_p \cdot p_1}{p_p \cdot q} \quad (0 \leq z \leq 1)\,, \qquad\qquad x_p \equiv \frac{Q^2}{2p_p \cdot q} \quad (x_{\rm Bj} \leq x_p \leq 1)\,, \tag{2.8}$$

where the particle momenta are labeled according to Fig. 2.4. In these variables the singularity structure of the QCD-Compton and the boson-gluon fusion process is exhibited

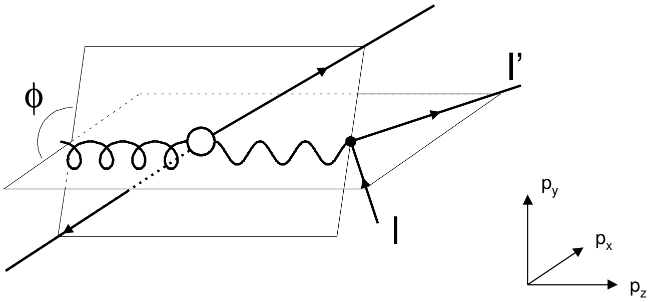

Figure 2.5: The variable ϕ denotes the angle between the plane given by the incoming and the scattered lepton and the plane given by the incoming parton and the jets in the photon-parton center-of-mass frame.

by [55]

$$
\begin{aligned}
\mathrm{d}\sigma_{\mathrm{jet}}^{\mathrm{QCDC}} &\propto \frac{4\left[(p_p q - p_1 p_2)^2 (p_p p_1)^2 + (p_p q)^4\right]}{2 p_p p_2 \, 2 p_1 p_2 (p_p q)^2} = \frac{1 + x_p^2 z^2}{(1-z)(1-x_p)}\,, \qquad (2.9)\\
\mathrm{d}\sigma_{\mathrm{jet}}^{\mathrm{BGF}} &\propto \frac{4\left[(p_p p_1)^2 + (p_p p_2)^2\right]\left[(p_p q - p_1 p_2)^2 + (p_1 p_2)^2\right]}{2 p_p p_1 \, 2 p_p p_2 (p_p q)^2} = \frac{\left[z^2 + (1-z)^2\right]\left[x_p^2 + (1-x_p)^2\right]}{z(1-z)}\,. \qquad (2.10)
\end{aligned}
$$

The matrix elements of both processes diverge for the following kinematic configurations

$$
\begin{array}{rcl}
\multicolumn{3}{c}{\underline{\text{QCD-Compton}}}\\
p_2 \text{ collinear to } p_p & \Rightarrow & z \to 1\;,\\
p_2 \text{ collinear to } p_1 & \Rightarrow & x_p \to 1\;,\\
p_2 \text{ soft} & \Rightarrow & z,\, x_p \to 1\,,
\end{array}
\qquad\qquad
\begin{array}{rcl}
\multicolumn{3}{c}{\underline{\text{boson-gluon fusion}}}\\
p_1 \text{ collinear to } p_p & \Rightarrow & z \to 0\;,\\
p_2 \text{ collinear to } p_p & \Rightarrow & z \to 1\;,\\
p_1 \text{ soft} & \Rightarrow & z \to 0\;,\\
p_2 \text{ soft} & \Rightarrow & z \to 1\;.
\end{array}
$$

Now we express the variables z and x_p in terms of the dijet variables E_T and η' and demonstrate to which regions of the jet phase space these configurations belong. While the variables E_T and η' are defined in the Breit frame they are both invariant under longitudinal boosts and therefore identical to the corresponding variables in the center-of-mass (CM) frame (see Fig. 2.3)

$$
\begin{aligned}
\eta' &\equiv \frac{1}{2}\left|\eta_{1,\,\mathrm{Breit}} - \eta_{2,\,\mathrm{Breit}}\right| = \frac{1}{2}\left|\eta_{1,\,\mathrm{CM}} - \eta_{2,\,\mathrm{CM}}\right| = \left|\eta_{1,\,\mathrm{CM}}\right| = \left|\eta_{2,\,\mathrm{CM}}\right|\,,\\
E_T &\equiv E_{T,\,\mathrm{jet,\,Breit}} = E_{T,\mathrm{jet,\,CM}}\,. \qquad (2.11)
\end{aligned}
$$

Using these variables we can disentangle the angular dependence (η') and the dependence on the hardness scale (E_T) of the matrix elements. We introduce the center-of-mass energy $\hat{s} \equiv (p_p + q)^2$ of the photon-parton system and obtain from (2.8)

$$
\frac{Q^2}{\hat{s}} = \frac{x_p}{1-x_p} \qquad \text{and} \qquad \frac{E_T^2}{\hat{s}} = z(1-z)\,. \qquad (2.12)
$$

Using the relation $\hat{s} = 4E_T^2 \cosh^2(\eta')$ it follows that

$$\frac{E_T^2}{Q^2} = \frac{1-x_p}{x_p}\, z(1-z)\,, \qquad 4\cosh^2(\eta') = \frac{1}{z(1-z)}\,. \tag{2.13}$$

Comparing (2.13) to (2.9) and (2.10) one sees that all divergences are either in the region of vanishing transverse jet energies $E_T \to 0$ or infinitely large pseudorapidities $\eta' \to \infty$. The requirement $E_T > E_{T,\mathrm{min}} > 0$ alone is sufficient to remove all divergences from both contributions. If we apply a hard cut on the transverse jet energy it is therefore not necessary to make further angular jet cuts. This allows to investigate the inclusive jet cross section at large E_T where only properties of single jets are measured, regardless of the properties of the other jet(s) in the event.

The momentum fraction x of the parton emerging from the parton density function of the proton is related to the center-of-mass energy by $x = x_{\mathrm{Bj}}(1 + \hat{s}/Q^2)$. A special property of the (simplified) leading-order picture in which the final state contains no further partons apart from the ones that are identified as jets, is that the center-of-mass energy of the partonic subprocess is identical with the invariant mass of the dijet system $\hat{s} = M_{jj}^2$. The fractional parton momentum x is therefore identical to the observable ξ which we define as $\xi \equiv x_{\mathrm{Bj}}(1 + M_{jj}^2/Q^2)$. In this approximation one can directly conclude from the dijet cross section measured differentially in ξ to the parton densities in the proton $f_{a/p}(x = \xi)$.

At higher orders in the perturbative expansion the final state may contain further partons which are not contained in the jets. In general the dijet mass can be lower than the center-of-mass energy such that the observable ξ gives only an approximate representation of the parton momentum fraction ($M_{jj}^2 \le \hat{s} \Rightarrow \xi \le x$). This reflects that (as described in section 1.2) the fractional parton momentum x is not an observable quantity. The value of x specifies only the (arbitrary) point within the theoretical calculation below which parton emissions are calculated via the (process specific) matrix elements and above which these are considered to be part of the proton's (universal) parton density functions.

Beyond the leading order approximation there is no longer any linear relation between the dijet cross section in a specific ξ range and the parton densities in the corresponding x range. Instead the variable ξ serves only as a lower bound of the integral over all momentum fractions x in the convolution of the matrix element and the parton density functions. The x-dependence of the parton density functions can only be extracted from the differential cross section through an unfolding procedure (as a fit).

2.3.2 Next-to-Leading Order Corrections

In the leading order approximation perturbative QCD can explain the appearance of specific event topologies. In order to make reliable quantitative predictions the perturbative calculations have to be performed (at least) in next-to-leading order (NLO). In inclusive jet and dijet production in DIS such calculations include diagrams as the ones shown in Fig. 2.6.

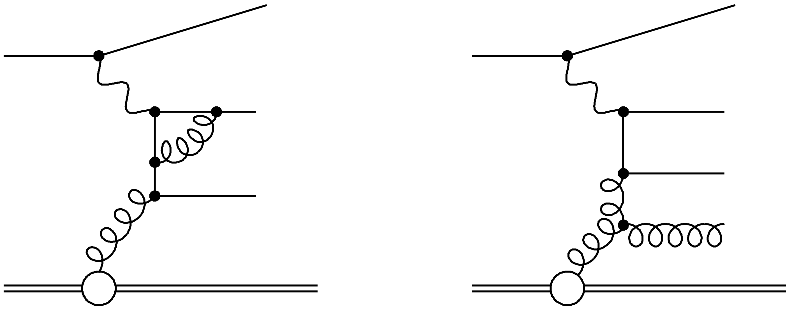

Figure 2.6: Contributions to the next-to-leading order corrections from virtual (left) and real diagrams (right) to the inclusive jet and the dijet cross section in the Breit frame. The diagram on the right contributes also to the leading order cross section in three-jet production.

Next-to-leading order calculations have two essential features. The real corrections (Fig. 2.6, right) are a first step in the modeling of the internal structure of jets, introducing a dependence of the jet cross section on the exact definition. The contributions from the virtual corrections (Fig. 2.6, left) have the effect of introducing a dependence of the perturbative coefficient functions on the renormalization scale which cancels part of the scale dependence of α_s. In the same way contributions from collinear initial state radiation introduce a dependence of the coefficients on the factorization scale which cancels part of the scale dependence of the parton distributions. The NLO corrections can substantially reduce the scale dependence and thereby allow reliable predictions for cross sections and a determination α_s and the parton density functions.

The realization of a NLO calculation for jet cross sections involves several complications related to the cancellation of the divergences from real and virtual contributions. Since the phase space integrals are too difficult to allow analytical calculations, numerical methods have to be used. However, before numerical methods are directly applicable the singular parts of the phase space have to be treated analytically. Two methods have been proposed for this purpose and four different computer programs are available for NLO calculations of jet cross sections in deep-inelastic scattering.

The Phase Space Slicing Method

The phase space slicing method [56] introduces a cut-off parameter (e.g. on the invariant mass of a two-parton system) below which soft and collinear radiation is considered to be unresolvable. In this phase space region soft and collinear approximations are applied. The contribution is integrated over analytically and added to the contributions from virtual corrections, yielding a finite result. The integration over the resolved region can safely be performed using Monte Carlo integration. In this approach it has to be checked that the cut-off parameter is chosen small enough for the soft and collinear approximations to be valid. Only in this case does the calculation become stable with respect to a variation of the cut-off. The two programs MEPJET [57] and JETVIP [58] are based on this technique.

The Subtraction Method

In the subtraction method [59] a local counterterm is computed which exactly matches the singular behavior of the real and of the virtual corrections. Adding and subtracting this term respectively from both singular parts yields finite results for both, allowing the Monte Carlo integration to be performed over the whole phase space. This approach is followed in the programs DISENT [60] and DISASTER++ [61].

We have performed a detailed comparison of the four programs in [62] with a statistical precision of better than 0.5%. All programs are in perfect agreement for leading order calculations. For NLO calculations the programs DISENT and DISASTER++ are also seen to be in good agreement with each other. The MEPJET program is typically 5% lower than the other programs. The JETVIP results are found to be unstable with respect to variations of the cut-off parameter and the program tends to underestimate statistical errors. Although a better agreement between the four programs is desirable, we take the agreement between DISENT and DISASTER++ (both using different subtraction terms) as an indication that these programs represent valid implementations of the NLO matrix elements.

In this analysis all NLO calculations are performed using the program DISENT (which is significantly faster than DISASTER++). The unique features of MEPJET are used to perform leading order calculations including quark mass effects in dijet production and to compute the three- and four-jet cross sections in leading order.

2.3.3 Parton Cascades

Perturbative fixed order calculations (beyond leading order) can give reliable quantitative predictions for observables for which multiple emission effects and non-perturbative contributions are small. They fail, however, to predict details of the structure of multi-particle final states as observed in the experiment. A complementary approach to describe these properties of the hadronic final state is used in "parton cascade models". Starting from the leading order matrix elements of a process subsequent parton emissions are calculated based on soft and collinear approximations. These parton cascade models are included in event generators together with models of the hadronization process.

Parton Showers

In the collinear limit the cross section for multiple emissions factorizes and can be described as a probabilistic series of parton splittings. The parton shower is divided into the time-like final state shower and the space-like initial state shower. The final state shower arises from the outgoing partons produced by fixed order, tree-level matrix elements. The initial state parton shower uses a backwards evolution [63], starting from the hard interaction and evolving downwards in scale back towards the incoming hadron, taking into account the parton density functions. Further emissions from the partons produced by initial-state radiation are then calculated using the final-state shower.

The implementation of the parton shower in the program HERWIG [64] uses evolution variables which naturally restrict the branching phase space to an angular ordered region, thus automatically including coherence effects. In the virtuality-ordered parton shower by LEPTO [65] these coherence effects are included by disallowing angular disordered emissions. In both programs HERWIG and LEPTO the parton shower is matched to to the $\mathcal{O}(\alpha_s)$ matrix elements.

Dipole Cascades

An alternative approximation of higher order emissions is the color dipole model (CDM) [66] which is implemented in the program ARIADNE [67]. In the CDM gluon emissions are described as radiations from the color dipole between pairs of partons. Since this procedure only produces further gluons the process $g \rightarrow q\bar{q}$ is added to the model. For deep-inelastic scattering the probability of the first emission is corrected to reproduce the matrix elements of $\mathcal{O}(\alpha_s)$ [68].

2.3.4 Hadronization Models

In the parton cascade models described above the higher order emissions are restricted to parton virtualities above a cut-off Q_0 which is typically chosen to be 1 GeV. At this point the perturbative evolution is stopped. The non-perturbative phase is described by a phenomenological hadronization model which performs the conversion of the final state partons into hadrons locally in phase space. Due to the universal cut-off of the parton cascade the hadronization procedure is independent of the hard process. The most successful hadronization models are the “cluster model” [69] (implemented in HERWIG) and the Lund “string fragmentation model” [70] (implemented in JETSET [71] and used by LEPTO and ARIADNE).

Cluster Fragmentation

In the first step of the cluster fragmentation model all outgoing gluons are split non-perturbatively into light (u and d) quark-antiquark pairs. Neighboring (color connected) $q\bar{q}$-pairs are then combined to form color-singlet “clusters” (see Fig. 2.7 (a)). Clusters which are too light to decay into two hadrons, are taken to represent the lightest single hadron of its flavor. Those clusters whose mass is above some limit are broken into sub-clusters, taking into account the available phase space and spin conservation. The resulting clusters are identified with hadrons according to their flavor content.

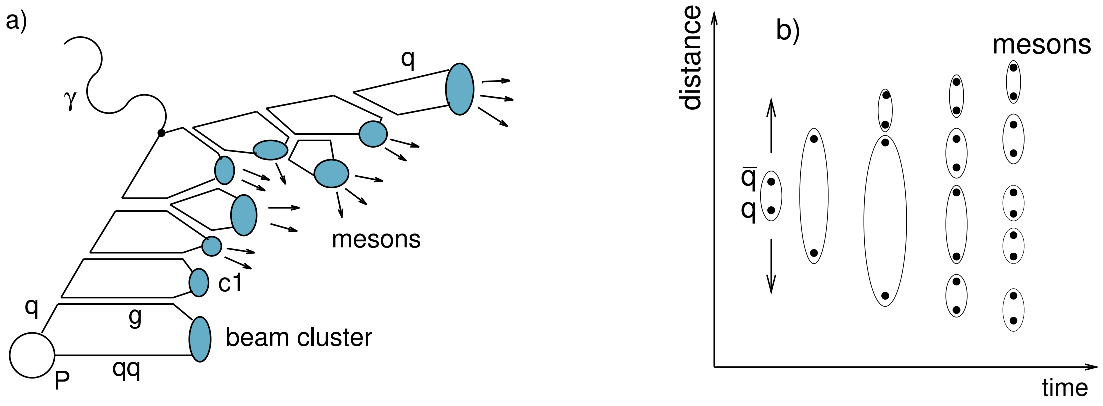

Figure 2.7: The hadronization of a partonic final state in the cluster model (left) and in the string fragmentation model (right).

String Fragmentation

The string model of fragmentation is based on the picture of a classical potential between two partons. The color field between a $q\bar{q}$-pair is visualized as a string and described by a Coulomb potential which turns into a linearly rising function towards larger distances r between partons, i.e. $V(r) \propto a/r + br$. At large separations r the energy stored in the string is proportional to r due to the linear term. In deep-inelastic scattering, strings are also assumed between the (anti-)quark and the proton remnant. Gluons cause kinks in the string with the four-momentum of the gluon. When the energy stored in the string is large enough, the string breaks up creating a new $q\bar{q}$-pair and forming new string pieces. The process is iterated until all the available energy is been used up. The resulting string fragments are combined into mesons and baryons (see Figure 2.7 (b)). The kinematics of the produced hadrons is given by the "Lund symmetric fragmentation function"

$$f(z) \propto \frac{(1-z)^a}{z} \, \exp\left(\frac{b\, m_\perp}{z}\right) , \tag{2.14}$$

where z is the longitudinal momentum fraction of a primary quark carried by the hadron. The transverse mass $m_\perp \equiv \sqrt{m^2 + p_\perp^2}$ is obtained from the mass m and the transverse momentum $p_\perp$ of the hadron (with respect to the original quark). In this model the $p_\perp$ distribution is assumed to be a Gaussian of width σ_q which enters (together with a and b) as a parameter.

2.3.5 Radiative QED Corrections

For a correct description of cross sections in deep-inelastic scattering it is important to take into account higher order QED corrections. Especially hard photon radiation may strongly influence the reconstruction of the event kinematics and (as in our case) the boost vector

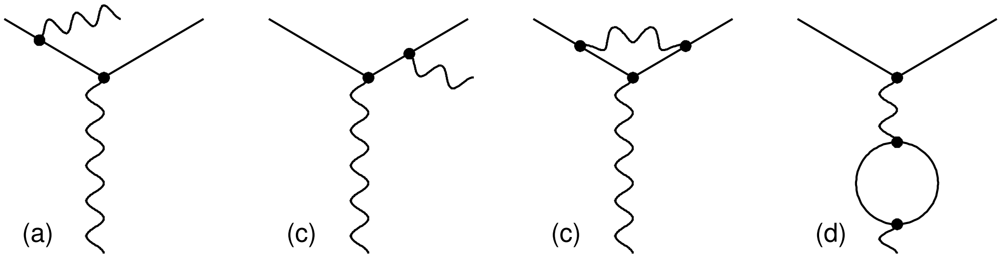

Figure 2.8: QED corrections at the leptonic vertex as included in the program DJANGO

to the Breit frame (as discussed in appendix A). Since the cross section for real photon emissions is proportional to the inverse mass squared of a particle, the largest corrections are those from the lepton line. The program DJANGO [72] is an interface of the program HERACLES [73] and the programs LEPTO and ARIADNE and provides a calculation of the diagrams shown in Fig. 2.8. These are the initial and the final state emissions of photons from the lepton, virtual corrections at the lepton vertex and loop-corrections to the photon propagator.

2.4 Definitions of the Jet Observables

In this section we give the exact definitions of the observables to be measured in this analysis and provide all information needed to perform the theoretical calculations for comparisons. All observables are measured in positron-proton collisions with beam energies of 27.5 GeV for the positrons, and 820 GeV for the protons. In all cases we measure *inclusive* jet cross sections (i.e. the n-jet cross section includes all events with n or more jets).

2.4.1 Multi-differential Jet Cross Sections

The kinematic range in which the jet cross sections are measured is solely defined by the kinematic variables y and Q^2.

$$0.2 < y < 0.6\,, \qquad 150 < Q^2 < 15\,000\,\mathrm{GeV}^2 \quad \text{or} \quad 10 < Q^2 < 70\,\mathrm{GeV}^2 \tag{2.15}$$

The two regions of Q^2 will be labeled "high Q^2" and "low Q^2", respectively. The gap in the Q^2 range is caused by the geometry of the H1 calorimeter which does not provide a uniform acceptance of the scattered positron over the whole range of y at intermediate Q^2 values. The lower limit on y has been chosen to exclude the kinematic region of large x-Bjorken where jets are predominantly produced in the forward direction (i.e. at the edge of the detector acceptance). The upper limit on y guarantees large energies of the scattered positron where trigger efficiencies are high (see section 5.1).

The jet finding is performed on the (massless) particles in the Breit frame (defined in section 2.1) using the inclusive and the exclusive jet algorithms introduced in section 2.2.

Any extrapolation of a jet cross section beyond the detector acceptance may introduce a bias towards the model used for the extrapolation. We therefore restrict the jet phase space to the angular range in which jets are well contained in the acceptance of the H1 detector. The four-vectors of the jets found in the Breit frame are boosted back to the laboratory frame where we apply the pseudorapidity cut

$$-1 < \eta_{\text{lab}} < 2.5\,. \tag{2.16}$$

As discussed in section 2.3.1 at order $\mathcal{O}(\alpha_s)$ jet production is described by three "jet variables" in addition to the two kinematic variables Q^2 and x_{Bj}. Integrating over the azimuthal angle ϕ between the jet and the lepton plane, two independent jet variables are left. These can be chosen e.g. as the "jet hardness scale" E_T and the angular variable η' (see section 2.3.1). However, different linear combinations of these (and the kinematic variables) are sensitive to different properties of the hard process.

In this analysis we measure the inclusive jet and the dijet cross sections. Since the theoretical predictions for both are calculated to next-to-leading order both can be used to determine α_s and the gluon density in the proton. The measurement of the properties of the dijet system provides more information than is provided by the single jet properties measured in the inclusive jet cross section. The dijet cross section therefore allows to perform more detailed tests of the theoretical predictions. For the same reason, however, the dijet cross section is also more sensitive to the limitations of fixed order predictions (as discussed below) whereas the predictions for the inclusive jet cross section are not effected.

The dijet cross section is thus better suited to *test* the theoretical predictions while the inclusive jet cross section is preferable to *determine the parameters* of the theory. The final aim is, however, to demonstrate consistency between the results obtained using both observables.

The Inclusive Jet Cross Section

To test the prediction of the renormalization group equation one wants to determine the value of the strong coupling constant at different values of the "process relevant hard scale" (which is then chosen to be the renormalization scale in the theoretical calculation). In jet production in deep-inelastic scattering two large scales are present. These are the four-momentum transfer at the lepton vertex Q^2 (which is only indirectly related to the hard QCD process) and the transverse jet energy in the Breit frame E_T (the physical scale at which e.g. hard gluon radiation from a quark is resolved). The conceptually simplest observable which is sensitive to both hard scales is the inclusive jet cross section measured double differentially as $\mathrm{d}^2\sigma_{\text{jet}}/(\mathrm{d}E_T\mathrm{d}Q^2)$ while integrating over all jet angles. In the inclusive jet cross section all jets are counted that pass the required cuts. A single event may therefore give multiple contributions to the distribution.

We measure the inclusive jet cross section using the inclusive jet algorithms only. Every jet found by the algorithms is included in the analysis if it passes the angular cut in (2.16). The results are presented for $E_T > 7\,\mathrm{GeV}$.

The Dijet Cross Section

The Breit frame (in which the jet algorithms are applied) is in general shifted with respect to the center-of-mass frame of the hard process by a longitudinal boost. The reconstruction of the properties of the hard process in the center-of-mass frame requires information of both jets which can only be obtained in the measurement of the dijet cross section. For a comprehensive test of the theoretical predictions we measure the dijet cross section as a function of the following (dijet-) variables

$$\begin{aligned} \overline{E}_T &\equiv \frac{1}{2}\left(E_{T,1}+E_{T,2}\right)\,, & M_{\mathrm{jj}} &\equiv \sqrt{(\mathbf{p}_1+\mathbf{p}_2)^2}\,, \\ \eta' &\equiv \frac{1}{2}\left|\eta_1-\eta_2\right|\,, & \xi &\equiv x_{\mathrm{Bj}}\left(1+\frac{M_{\mathrm{jj}}^2}{Q^2}\right)\,, \\ & & x_p &\equiv \frac{x_{\mathrm{Bj}}}{\xi}\,. \end{aligned}$$

where the index 1 (2) refers to the jet of highest (second highest) transverse energy in the event and $\mathbf{p}_i$ denotes the four-vector of the i-th jet. The $\overline{E}_T$ distribution is a similar observable as the E_T distribution of the inclusive jet cross section and will enable us to repeat the α_s analysis in a similar way. As discussed in section 2.3.1 the variable η' is (in the leading order approximation) identical to the jet pseudorapidity in the dijet center-of-mass frame and therefore allows to test the QCD prediction of the angular jet distribution. The invariant dijet mass M_{jj} reflects the center-of-mass energy of the QCD process. In the leading order picture the proton momentum fraction carried by the incoming parton is given by the variable ξ. The ξ distribution is directly sensitive to the x dependence of the parton density functions and therefore important in the determination of the gluon density in the proton. The last dijet variable is x_p, the partonic scaling variable (see (2.8)). Furthermore we measure the distributions of the kinematic variables Q^2, y and x_{Bj} and also the pseudorapidity distributions of the most forward and the most backward jet in the laboratory frame (where the angular cuts are applied) to test the overall description of the data by the theory.

Care has to be taken in the choice of the dijet selection cuts in order to minimize the influence of "infrared sensitive" phase space regions. These are the regions at the exclusive boundary of the phase space where, due the suppression of real emissions, the cancellation between soft and collinear singularities in fixed order calculations becomes incomplete and reliable results can only be obtained using resummed calculations [74]. These are however not (yet) available.

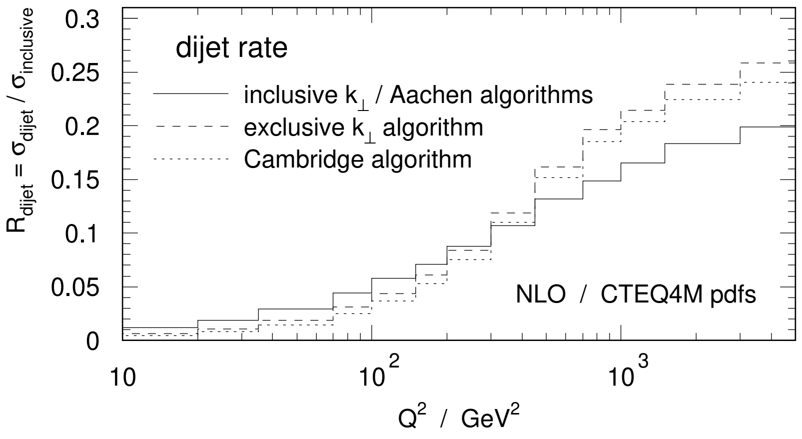

Figure 2.9: The next-to-leading order prediction of the dijet rate, defined as the ratio of the dijet cross section and the inclusive *ep* cross section in the same kinematic region. The dijet rate is shown for four different jet algorithms (from which two are identical at next-to-leading order).

Dijet selection cuts on the variable $k_\perp$ (as defined in (2.3)) avoid the infrared sensitive regions intrinsically. Therefore no further cuts are needed for the exclusive jet algorithms in addition to the intrinsic cuts which are applied due to the resolution parameter $y_{\rm cut}$ and the reference scale S^2 (as defined in section 2.2.2). These are chosen as

$$\text{exclusive jet algorithms:} \qquad S^2 = 100\,\text{GeV}^2 \quad \text{and} \quad y_{\rm cut} = 1\,. \tag{2.17}$$

If more than two jets are found we consider the two jets of highest transverse energy.

The inclusive jet definitions do not require any "hardness cuts" during the clustering procedure. Since these algorithms use the variable E_T for the clustering procedure it is a natural choice to use it also for the final dijet selection. While a simple cut $E_{T\,1,2} > E_{T\,\rm cut}$ is infrared sensitive (as discussed and demonstrated in [75, 76]) an additional (harder) cut on either the sum of the transverse jet energies, the E_T of the highest E_T jet or on the dijet mass can minimize the influence of the infrared sensitive phase space regions. Since both of the latter choices lead to significantly larger NLO corrections or larger hadronization corrections we decide to use the first scenario and apply the following cuts

$$\text{inclusive jet algorithms:} \qquad (E_{T,1} + E_{T,2}) > 17\,\text{GeV} \quad \text{and} \quad E_{T\,1,2} > 5\,\text{GeV}\,. \tag{2.18}$$

Using these selection cuts we compare in Fig. 2.9 the theoretical predictions of the dijet rate (i.e. the ratio of the dijet cross section and the inclusive *ep* cross section) for the different algorithms. One sees that due to the specific selection criteria the dijet rates have a slightly different Q^2 dependence. In the high Q^2 region the rates are, however, approximately of the same size for all algorithms, rising towards higher Q^2 up to 25%.

Three- and Four-Jet Cross Sections

The three- and four-jet cross sections are measured using the inclusive $k_\perp$ algorithm. In addition to the pseudorapidity cut in the laboratory frame (2.16) we require

$$\begin{array}{rlcl} \text{three-jet selection:} & E_{T\,1,2,3} > 5\,\text{GeV} & \text{and} & M_{3-\text{jet}} > 25\,\text{GeV} \\ \text{four-jet selection:} & E_{T\,1,2,3,4} > 5\,\text{GeV} & \text{and} & M_{4-\text{jet}} > 25\,\text{GeV} \end{array}$$

where $M_{3-\text{jet}}$ ($M_{4-\text{jet}}$) is the invariant mass of the three (four) jets with largest transverse energies.

2.4.2 Internal Jet Structure

In addition to the measurements of jet production rates it is also of interest to study the internal structure of jets. The internal jet structure is sensitive to QCD processes at smaller relative transverse momenta and also to the hadronization process. The phase space definition is given together with the results of the analysis in section 7.4. Here we introduce the definitions of the observables which are applied to the jets measured in an inclusive dijet event sample using the inclusive $k_\perp$ algorithm.

We investigate two observables which are sensitive to different aspects of jet broadening. The "jet shape" measures the radial distribution of the transverse jet energy and is effected by hard and by soft processes over the whole radial range. The multiplicities of subjets, resolved at a resolution scale which is a fraction of the jet's transverse energy are sensitive to more local structures of relative transverse momentum within a jet. Here the perturbative and the non-perturbative contributions are better separated. While at larger values of the resolution parameter perturbative contributions dominate, non-perturbative contributions become increasingly important towards smaller values.

Jet Shapes

The jet shape $\Psi(r/R_0)$ is defined as the fractional transverse jet energy contained in a subcone of radius r concentric with the jet axis (see Fig. 2.10), averaged over all considered jets in the event sample

$$\Psi(r/R_0) \equiv \frac{1}{N_{\text{jets}}} \sum_{\text{jets}} \frac{E_T(r/R_0)}{E_{T,\text{jet}}}\,, \tag{2.19}$$

where N_{jets} is the total number of these jets. As proposed in [44], only particles assigned by the jet algorithm to the jet are considered.

Often the denominator in the definition of Ψ is chosen to be the summed E_T of all particles within a radius R_0 to the jet axis. This means that $\Psi(r/R_0 = 1) = 1$. In our definition (2.19) of Ψ the denominator is given by the transverse energy of the jet. Since for the inclusive $k_\perp$ algorithm the particles assigned to a jet are not necessarily within a radius

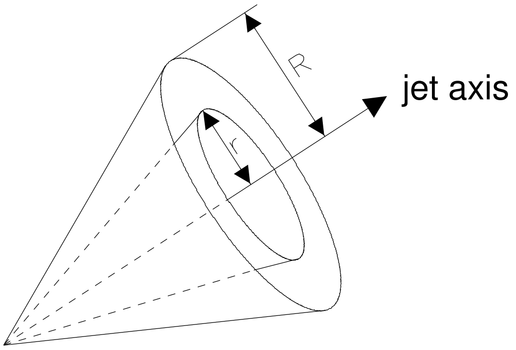

Figure 2.10: The jet shape $\Psi(r/R)$ is defined as the fractional transverse jet energy contained in a subcone of radius r concentric with the jet axis of a jet which is defined by the radius R.

of $r/R_0 < 1$ to the jet axis, $\Psi(r/R_0 = 1)$ is not constrained to have the value of one. With this choice of our observable we are also sensitive to the amount of transverse jet energy outside the radius R_0.

Subjet Multiplicities

For each jet in the sample the clustering procedure is repeated for all particles assigned to the jet. The clustering is stopped when the distances y_{ij} between all particles i, j are above some cut-off y_{cut}

$$y_{ij} = \frac{\min(E_{T,i}^2, E_{T,j}^2)}{E_{T,\text{jet}}^2} \frac{(\Delta\eta_{ij})^2 + (\Delta\phi_{ij})^2}{R_0^2} > y_{\text{cut}} \tag{2.20}$$

and the remaining particles are called “subjets”. The parameter y_{cut} defines the minimal relative transverse energy between subjets inside the jet and thus determines the extent to which the internal jet structure is resolved. From this definition it follows that for $y_{\text{cut}} > 0.25$ no subjet is resolved (therefore the number of subjets is one), while for $y_{\text{cut}} \to 0$ every particle in the jet is a subjet. The observable that is studied in this analysis is the average number of subjets for a given value of the resolution parameter, for values $y_{\text{cut}} \geq 10^{-3}$.

3

On the Feasibility of a QCD Analysis of Jet Production in DIS

Stringent tests of a theory and reliable determinations of its parameters can only be performed through comparisons or fits to observables for which the theory is predictive, i.e. for which approximations are expected to be valid and uncertainties are small. This chapter is devoted to the identification of such observables and to the estimation of the size of remaining theoretical uncertainties.

In the previous chapter we have described the jet algorithms and defined the phase space in which the jet analysis will be performed. Furthermore we have introduced the available theoretical models. In this chapter we use the predictions of these models to investigate the properties of the different jet definitions. In the first section we study the size of non-perturbative contributions to different jet observables and the uncertainties arising from the model and parameter dependence of the predictions. The topic of the second section are the predictions of perturbative next-to-leading order (NLO) calculations for jet cross sections. We investigate the size of the next-to-leading order corrections and the renormalization scale dependence for different choices of scales.

All predictions are obtained using the programs HERWIG5.9 [64], LEPTO6.5 [65] and ARIADNE4.08 [67]. The calculations are performed for the HERA running conditions of 1997 (820 GeV protons collided with 27.5 GeV positrons) using the CTEQ4L parameterization [77] of the parton distributions and the 1-loop formula for the running of α_s. The LEPTO predictions are obtained without the soft color interaction model.

The NLO calculations are performed in the $\overline{\text{MS}}$-scheme by the program DISENT [60] using CTEQ4M parton distributions and the 2-loop formula for the running of α_s. The renormalization scale is set to the transverse jet energy $\mu_r = E_T$, the factorization scale to the mean E_T of the jets $\mu_f = \sqrt{200}\,\text{GeV} \simeq \langle E_T \rangle$ (unless stated otherwise; see also the discussion in section 8.2).

The phase space definition and the jet selection criteria are as defined in section 2.4.

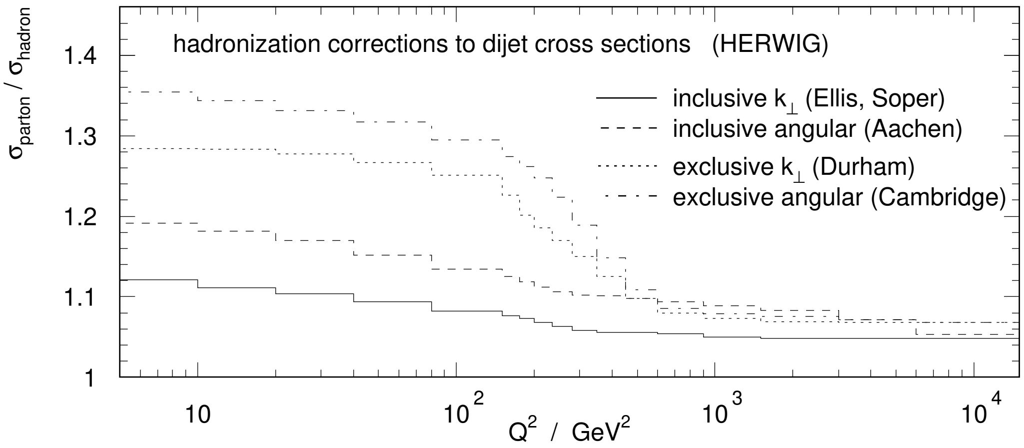

Figure 3.1: The hadronization corrections to the dijet cross section for different jet definitions as a function of Q^2 as predicted by the HERWIG cluster fragmentation model.

3.1 Hadronization Corrections to Jet Cross Sections

Before the prediction of a perturbative QCD calculation ("parton-level" cross section) can be compared to a measured "hadron-level" jet cross section, the size of non-perturbative contributions ("hadronization corrections") has to be estimated. There is, however, no unique way to separate perturbative and non-perturbative contributions in theoretical calculations. A consistent treatment requires a well defined matching of both contributions, e.g. by the introduction of an "infrared matching scale" [36]. Such approaches are not (yet) available for high E_T jet cross sections in deep-inelastic scattering and the only predictions are those of the phenomenological hadronization models described in section 2.3.4. These models are implemented in event generators that include leading order matrix elements and a perturbative parton cascade which is matched to the hadronization model. Based on these models, hadronization corrections are compared for the different jet definitions introduced in section 2.2.

3.1.1 The Size of Hadronization Corrections

We define the hadronization corrections to an observable $\mathcal{O}$ as the ratio of its value in a perturbative calculation ("parton-level": $\mathcal{O}_{\text{parton}}$) and its value in a calculation including both perturbative and non-perturbative contributions ("hadron-level": $\mathcal{O}_{\text{hadron}}$)

$$c_{\text{hadr.corr.}} = \mathcal{O}_{\text{parton}} \,/\, \mathcal{O}_{\text{hadron}} \,.$$

The HERWIG predictions of the hadronization corrections to the dijet cross section are shown in Fig. 3.1 as a function of Q^2 for the different jet definitions. While at $Q^2 \gtrsim 1000\,\text{GeV}^2$ all jet definitions have similar and reasonably small corrections (below 10%), large differences

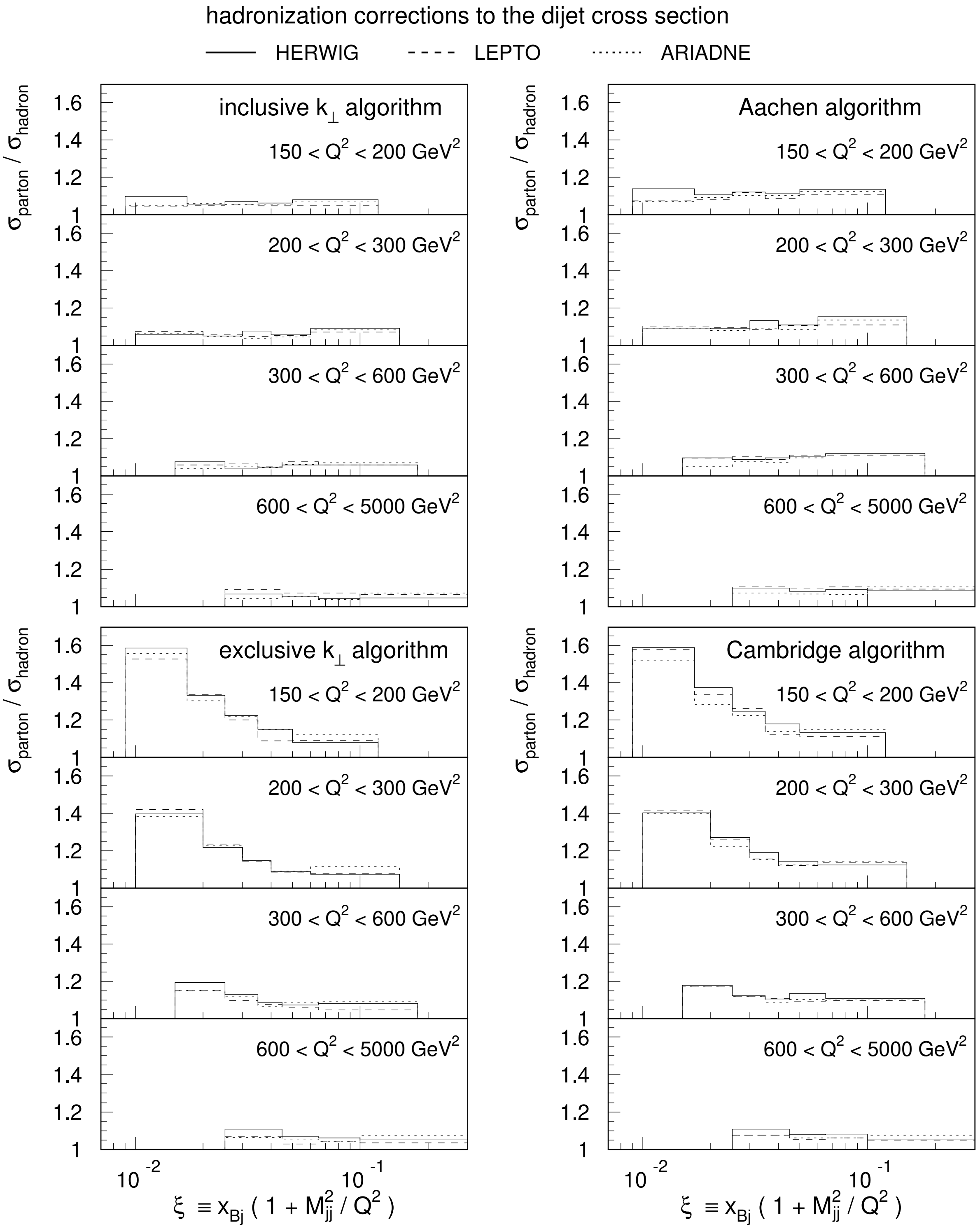

Figure 3.2: Hadronization corrections to the ξ distribution of the dijet cross section for different jet definitions.

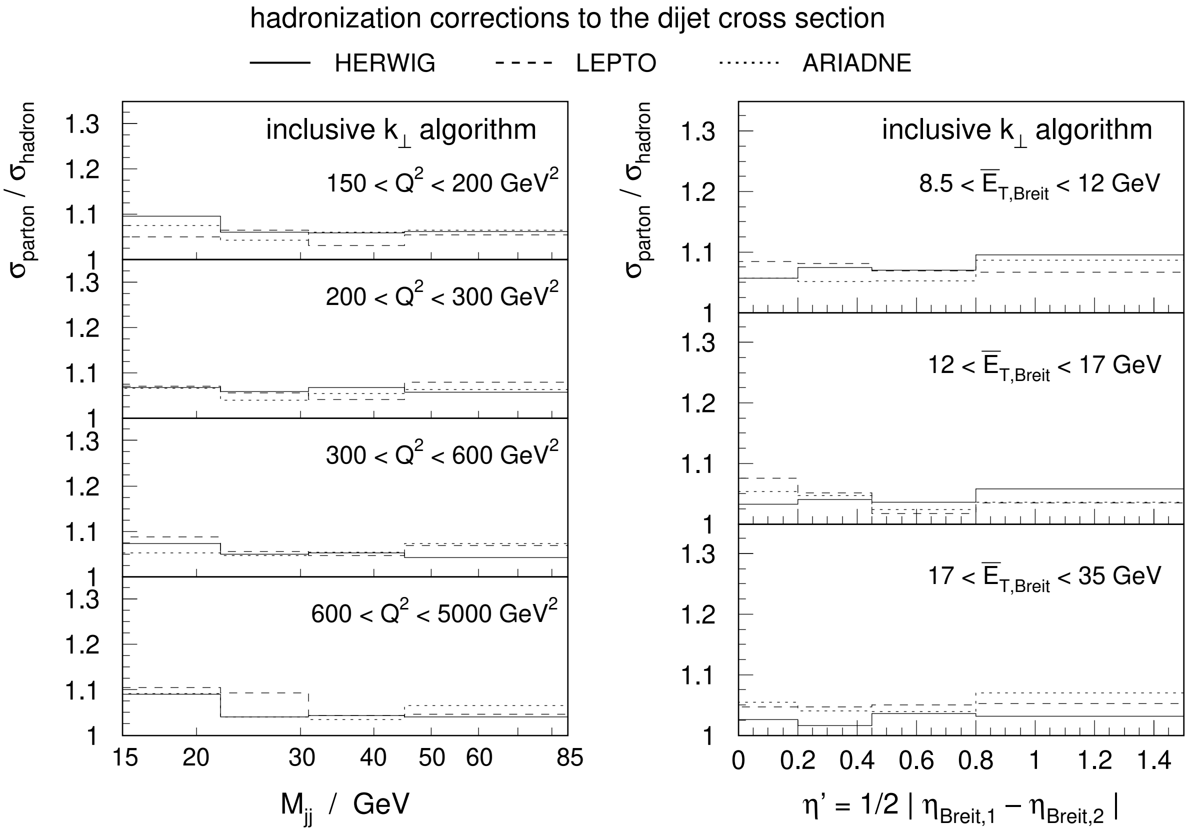

Figure 3.3: Hadronization corrections to the dijet cross section as defined by the inclusive $k_\perp$ algorithm for the dijet mass distribution (left) and the variable η' (right).

are seen at $Q^2 \lesssim 300\,\mathrm{GeV}^2$. In all cases the corrections are smaller for the inclusive jet definitions than for the exclusive definitions and smaller for the $k_\perp$ ordered than for the angular ordered algorithms. Only the inclusive $k_\perp$ algorithm shows a small Q^2 dependence and acceptably small corrections (below 10%) even down to $Q^2 = 10\,\mathrm{GeV}^2$. In Fig. 3.2 we display the hadronization corrections differentially in the variable ξ in different Q^2 regions for the four jet algorithms. For both inclusive algorithms the corrections are small and independent of ξ while a strong ξ dependence is observed for the exclusive algorithms. The predictions from the different models are in good agreement for all jet algorithms even in regions where the size of the correction is large. For the inclusive $k_\perp$ algorithm the model predictions agree better than 3%.

Having the smallest hadronization corrections, the inclusive $k_\perp$ algorithm seems to be the preferable choice for tests of perturbative QCD. We study the hadronization corrections of this algorithm also for other dijet distributions. In Fig. 3.3 the model predictions are shown for the distributions of the invariant dijet mass (left) and the variable η' (right) in different regions of Q^2 and $\overline{E}_T$, respectively. Also in these variables the hadronization corrections are flat and close to one, decreasing slightly towards higher $\overline{E}_T$.

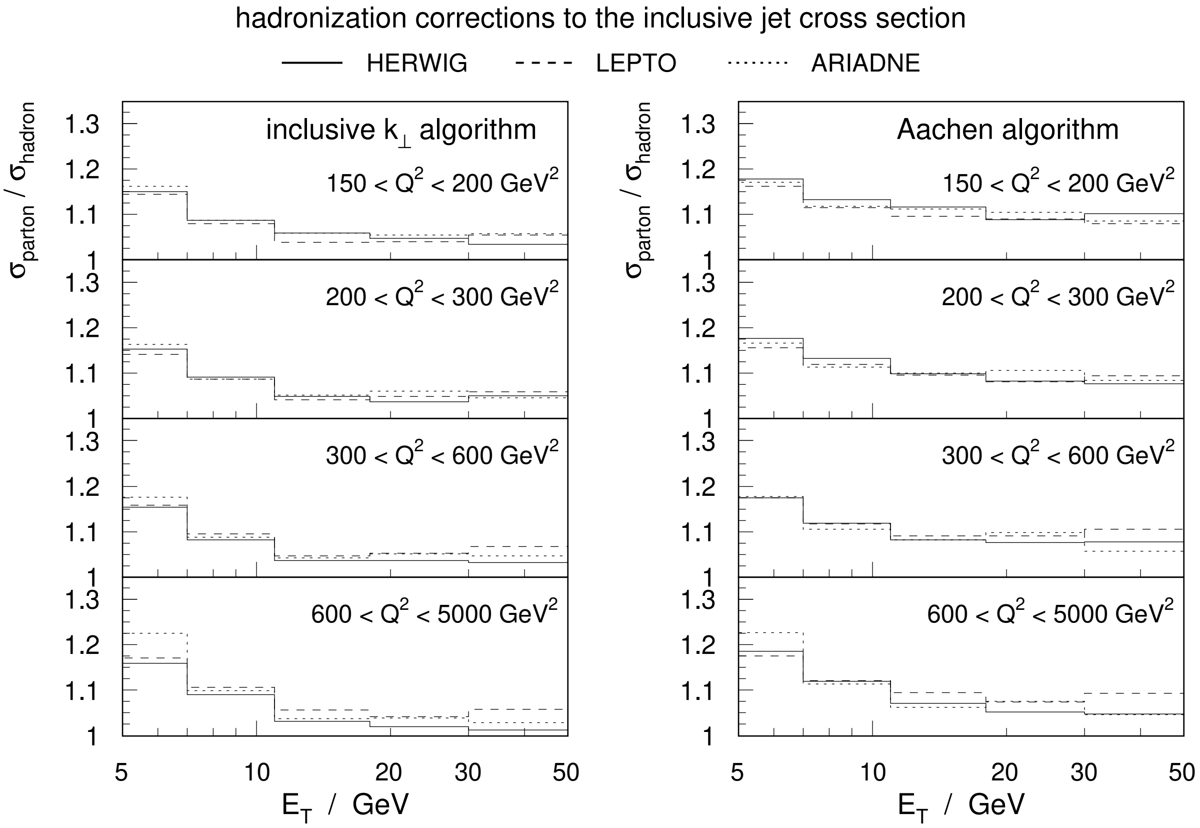

Figure 3.4: Hadronization corrections to the inclusive jet cross section for the inclusive $k_\perp$ algorithm (left) and the Aachen algorithm (right).

The corrections to the inclusive jet cross section are displayed in Fig. 3.4 as a function of the transverse jet energy E_T for the inclusive $k_\perp$ algorithm (left) and for the Aachen algorithm (right). At small transverse jet energies $5 < E_T < 7\,\mathrm{GeV}$ the hadronization corrections are 15–20%. At $E_T > 7\,\mathrm{GeV}$ (where the analysis is performed) the corrections for the inclusive $k_\perp$ algorithm are below 10%, decreasing slightly towards higher E_T. The corrections for the Aachen algorithm are 2–3% larger than those for the inclusive $k_\perp$ algorithm but show a similar E_T dependence.

3.1.2 Uncertainties in the Estimates of Hadronization Corrections

The predictions of the hadronization corrections may be different for different models and may also depend on the properties of the partonic final state that is fed into the hadronization model. In the discussion above we have already seen that the predictions for the jet observables under investigation are similar for the HERWIG cluster model and for the Lund string model. For the latter we have also shown that the predictions are independent of the partonic final state to which the hadronization is applied (the parton shower of LEPTO or the dipole cascade of ARIADNE).

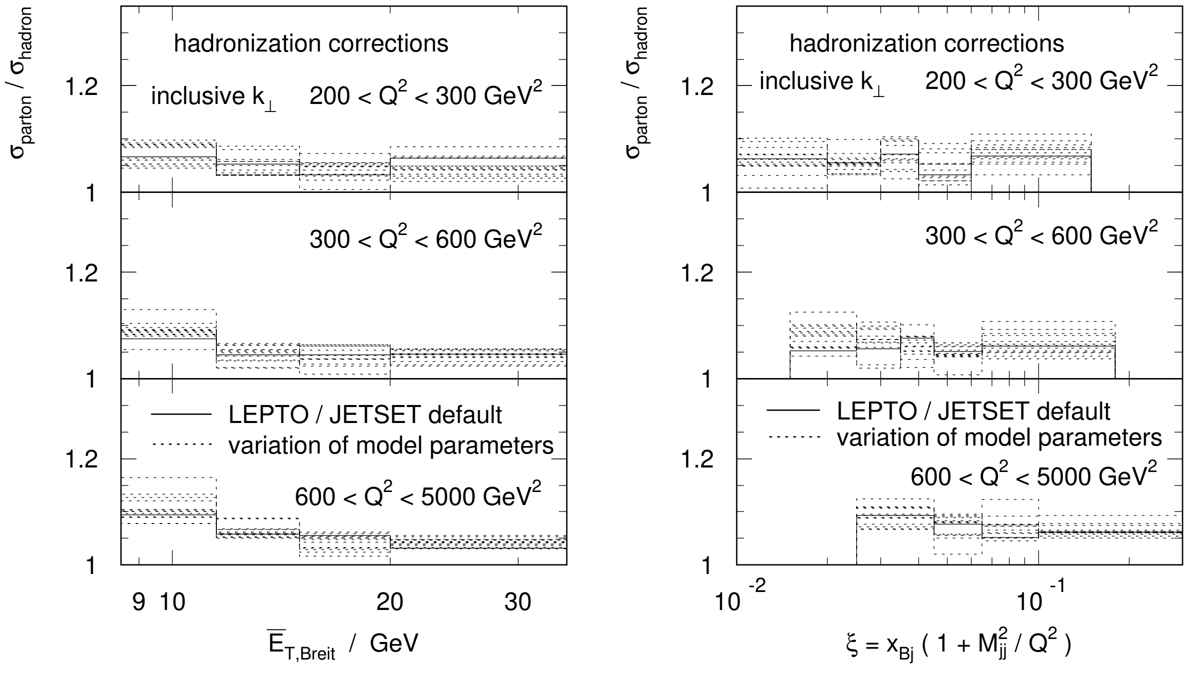

Figure 3.5: Hadronization corrections to the dijet cross section obtained using the inclusive $k_\perp$ algorithm. Displayed are the LEPTO/JETSET predictions for the $\overline{E}_T$ (left) and the ξ distribution (right) for different settings of the model parameters (dotted lines) and for the default settings (solid line).

LEPTO / JETSET model parameters	default	variation
Λ_{QCD} in initial state parton shower	0.25 GeV	0.25 – 0.4 GeV
Λ_{QCD} in final state parton shower	0.23 GeV	0.23 – 0.4 GeV
Q_0^{ISR} cutoff for initial state parton shower	1 GeV	0.7 – 2.0 GeV
Q_0^{FSR} cutoff for final state parton shower	1 GeV	0.5 – 4.0 GeV
width of Gaussian primordial k_t of partons in the proton	0.44 GeV	0.44– 0.7 GeV
width of Gaussian distribution in k_t when a non-trivial target remnant is split into a particle and a jet	0.35 GeV	0.35– 0.7 GeV
Gaussian width of p_t for primary hadrons	0.36 GeV	0.25 – 0.45 GeV
a parameter in the symm. Lund fragmentation function	0.3	0.1 – 1.0
b parameter in the symm. Lund fragmentation function	0.58	0.44 – 0.7

Table 3.1: Overview of the LEPTO and JETSET parameters and the ranges in which they are varied in the studies of the hadronization corrections.

The model predictions may, of course, depend on the settings of the parameters that define the perturbative parton cascade, as well as on parameters of the hadronization model. We investigate the sensitivity of the LEPTO/JETSET model predictions to variations of such parameters. The variations can be classified in two categories.

- Parameters defining the partonic final state, i.e. the evolution and the cut-off of the parton cascade
- Parameters defining the hadronization model

The full list of parameters and the ranges of their variations is given in table 3.1. Fig. 3.5 gives an overview of the effects of these variations for the dijet cross section as a function of $\overline{E}_T$ (left) and ξ (right). The default setting of LEPTO/JETSET is indicated by the solid line and all variations as dotted lines. The variations for the different parameter settings are throughout within a few percent, i.e. of the same size as the model dependence that we have observed before.

3.2 Properties of Jet Cross Sections in Perturbative QCD

3.2.1 Sensitivity to the Parton Distributions

One aim of the QCD analysis of the jet data is the determination of the gluon density in the proton as a function of the momentum fraction x. The dijet cross section is therefore measured as a function of the variable ξ which is in the leading order picture equal to the proton momentum fraction x carried by the parton. From the ξ distribution of the data (the results are shown in Fig. 7.8, left) one sees directly that the dijet cross section is sensitive to fractional parton momenta in the range $0.01 < x < 0.3$.

The inclusive jet cross section is measured in different regions of Q^2 as a function of the transverse jet energy E_T which is not directly related to the parton momentum fraction. In Fig. 3.6 we therefore display the x ranges which contribute to the inclusive jet cross section in the next-to-leading order calculation in the different Q^2 and E_T bins of the analysis (see Fig. 7.1). One sees that the accessible x range depends weakly on Q^2 and strongly on E_T. The inclusive jet cross section covers a similar x range as the dijet cross section.

The gluon induced fraction to the total jet cross section is also shown in Fig. 3.6. At moderate Q^2 ($150 < Q^2 < 200\,\mathrm{GeV}^2$) the inclusive jet cross section is dominated by gluon induced processes which account for 72% of the cross section at lower E_T ($7 < E_T < 11\,\mathrm{GeV}$) and 45% at high E_T ($30 < E_T < 50\,\mathrm{GeV}$). At higher Q^2 ($600 < Q^2 < 5000\,\mathrm{GeV}^2$) the latter value is reduced to $\approx 40\%$ and is almost independent of E_T.

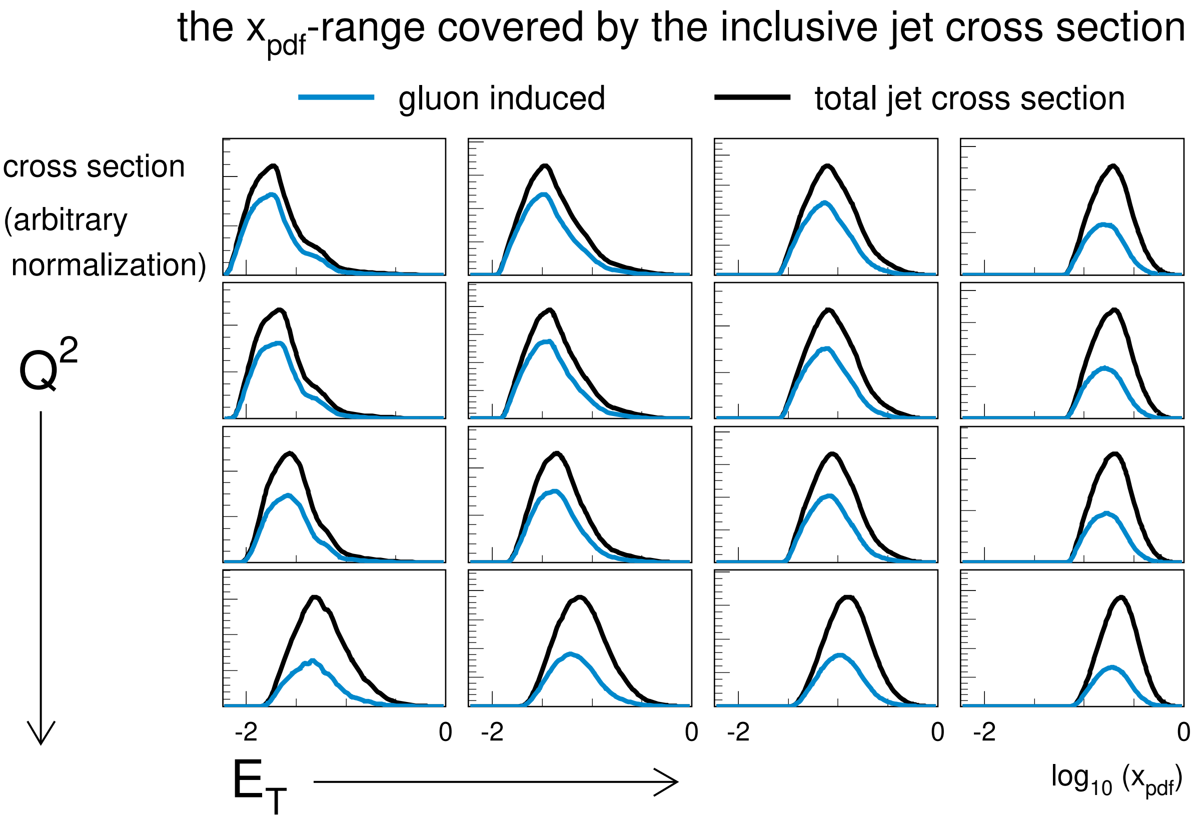

Figure 3.6: The next-to-leading order prediction for the inclusive jet cross section. Displayed is the total jet cross section (in arbitrary normalization) and the gluon induced contribution as a function of the proton momentum fraction x carried by the parton in the Q^2 and E_T bins of the analysis.

3.2.2 Z^0 Exchange and Quark Mass Effects

In the present work we use the next-to-leading order calculation as implemented in the program DISENT which includes neither contributions from Z^0 exchange nor the QCD matrix elements for massive quarks. To estimate the size of these effects we use the leading order calculation as implemented in the program MEPJET and calculate the dijet cross section for the inclusive $k_\perp$ algorithm with and without these effects.

In Fig. 3.7 we show the ratios of these calculations as a function of Q^2. The effects from Z^0 contributions (shown on the left hand side) reduce the dijet cross section at large Q^2. At $Q^2 < 2500\,\mathrm{GeV}^2$ these corrections are, however, below 2%. Integrated over the highest Q^2 bin chosen in our analysis ($600 < Q^2 < 5000\,\mathrm{GeV}^2$) the effect is already negligible.

The effects of quark masses in the leading order dijet cross section (shown on the right hand side) are 2.5% at $Q^2 = 10\,\mathrm{GeV}^2$ and are decreasing towards higher Q^2. At $Q^2 > 150\,\mathrm{GeV}^2$ the effect is below 1.5%. Massive NLO calculations are not available for jet cross sections, but given the small size of the effect we consider it safe to neglect this influence.

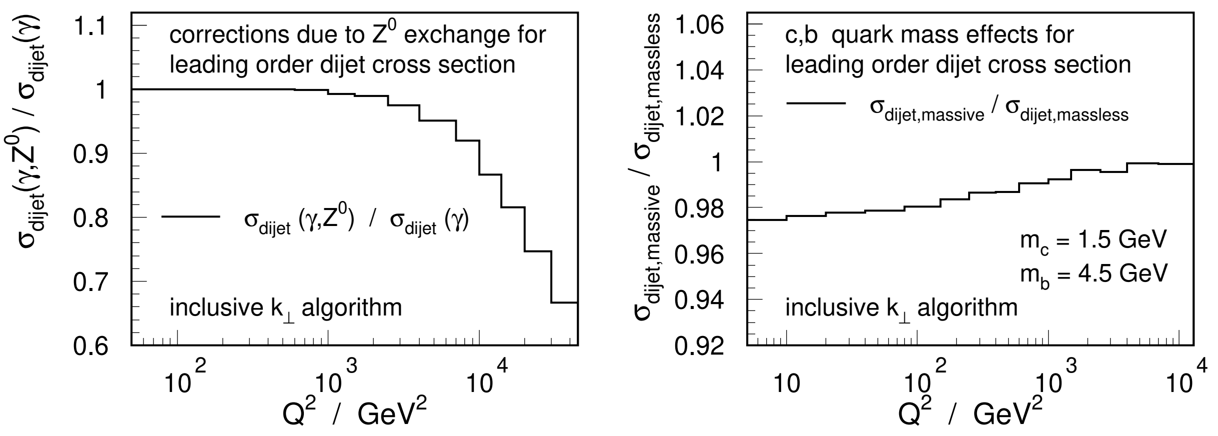

Figure 3.7: Contributions from Z^0 exchange and γ/Z^0 interference to the dijet cross section (left) and effects of quark masses (right) in the leading order calculation.

3.2.3 Next-to-Leading Order Corrections, Renormalization and Factorization Scale Dependence

The predictions of perturbative QCD are calculated as a power series in the strong coupling constant α_s. When calculated to all orders, the perturbative cross sections do not depend on the choice of the renormalization and factorization scales. The truncation of the perturbative expansion at a fixed order, however, introduces a dependence of the cross section on these scales. Since both contributions, the truncated fixed order calculation and the higher order corrections depend on the scales, a “good” choice of the scales can reduce the size of the higher order corrections.

For inclusive jet and dijet production in the Breit frame in deep-inelastic scattering only the coefficients of the leading and the next-to-leading order (i.e. $\mathcal{O}(\alpha_s)$ and $\mathcal{O}(\alpha_s^2)$) are known [78]. The determination of parameters of the theory, based on the next-to-leading order approximation, is only meaningful when the contributions from higher orders ($\mathcal{O}(\alpha_s^3)$) can be expected to be small. The size of these contributions depends on the choice of the renormalization and factorization scale in the calculation. To obtain an indication of the possible size of higher order corrections, we study the next-to-leading order (NLO) corrections and the renormalization and factorization scale dependence of the jet cross sections. Three different choices of the renormalization scale are used in these studies: $\mu_r^2 = E_T^2$, $\mu_r^2 = Q^2$ and $\mu_r^2 = E_T^2 + Q^2$. The factorization scale is set to the average transverse jet energy $\mu_f^2 = 200\,\mathrm{GeV}^2 \simeq \langle E_T^2 \rangle$ (see the discussion in section 8.2).

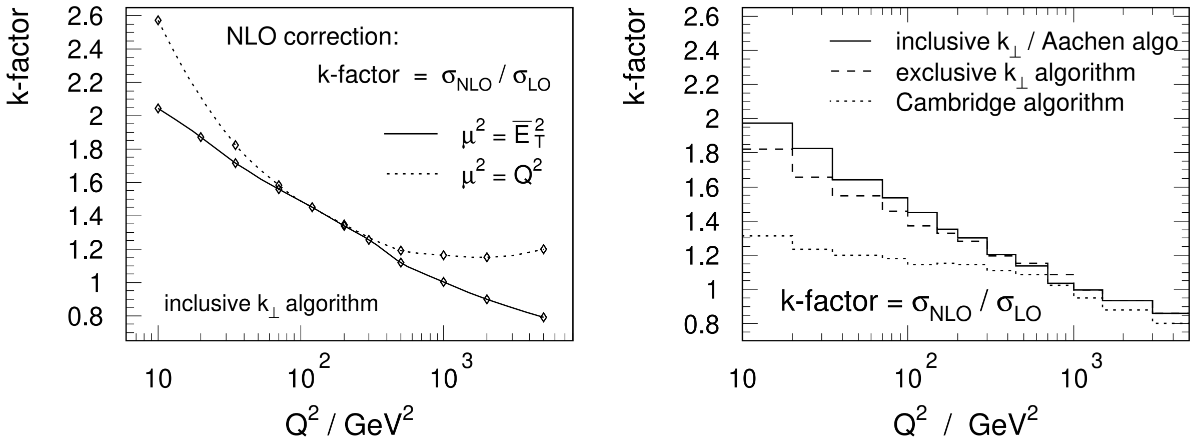

Figure 3.8: The next-to-leading order corrections to the dijet cross section as a function of Q^2 for the inclusive $k_\perp$ algorithm (left) using different renormalization scales μ_r^2 and for different jet algorithms (right) at $\mu_r^2 = \overline{E}_T^2$.

NLO Corrections

The contributions from higher orders have not yet been calculated. If we assume, however, that the perturbative expansion is well behaved, the contributions from higher orders should be small in those regions where the NLO corrections are small. We define the NLO correction (the "k-factor") as the ratio of the NLO cross section and the leading order (LO) cross section

$$k \;\equiv\; \frac{\sigma_{\rm NLO}}{\sigma_{\rm LO}} \;=\; \frac{\sigma(\mathcal{O}(\alpha_s)) + \sigma(\mathcal{O}(\alpha_s^2))}{\sigma(\mathcal{O}(\alpha_s))}\,. \tag{3.1}$$

This definition is, of course, only meaningful if the cross sections in the numerator and the denominator are calculated using the same parton density functions and the same α_s value.

The NLO corrections to the dijet cross section are shown in Fig. 3.8 as a function of Q^2. On the left hand side the k-factor for the inclusive $k_\perp$ algorithm is plotted for two choices of the renormalization scale, $\mu_r^2 = \overline{E}_T^2$ and $\mu_r^2 = Q^2$. For both choices the k-factor shows a strong Q^2 dependence and becomes large at small Q^2. The NLO corrections are smaller throughout for the scale $\mu_r^2 = \overline{E}_T^2$ than for $\mu_r^2 = Q^2$ (except at $Q^2 \simeq 150\,\text{GeV}^2$ where the corrections are equal since both scales are of the same size). The k-factors obtained for the different jet definitions are compared in Fig. 3.8 (right) for $\mu_r^2 = \overline{E}_T^2$. For all jet definitions we observe a similar Q^2 dependence. At $Q^2 = 10\,\text{GeV}^2$ the k-factors are extremely large, except for the Cambridge algorithm where a reasonably small value is found ($k < 1.3$).

In Fig. 3.9 we display the NLO corrections to the inclusive jet cross section in different bins of E_T and Q^2 (the bins are identical to those in the subsequent analysis). The k-factor is plotted as a function of the scale factor x_μ defined as the ratio of μ_r^2 to the nominal value $\mu_{r,0}^2$. As in the case of the dijet cross section we observe a decrease of the k-factors towards larger Q^2 for all choices of $\mu_{r,0}^2$. In most bins the k-factor is closest to one for $\mu_r^2 = E_T^2$,

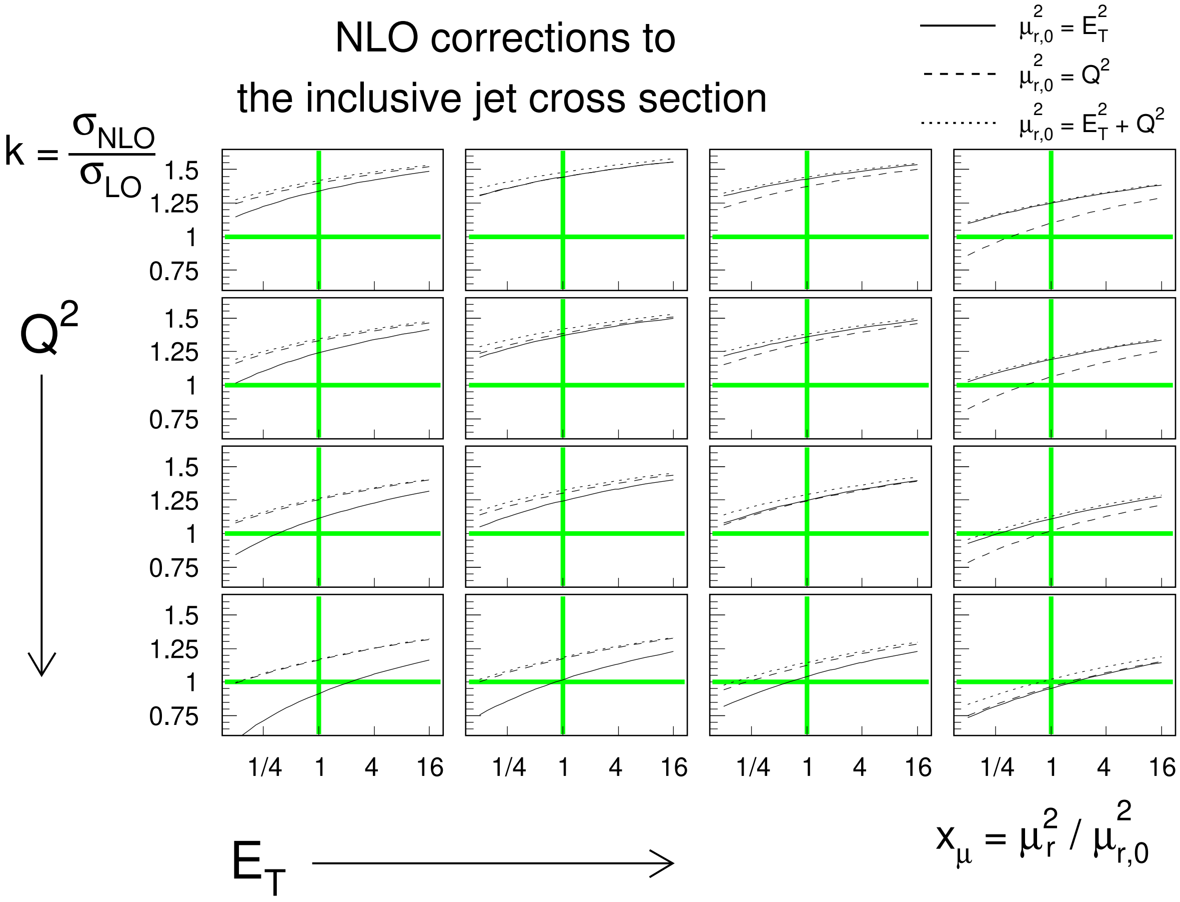

Figure 3.9: The k-factor for the inclusive jet cross section in bins of E_T (horizontal) and Q^2 (vertical) for three different choices of the renormalization scale: $\mu_r^2 = E_T^2$, $\mu_r^2 = Q^2$ and $\mu_r^2 = E_T^2 + Q^2$, as a function of the scale factor x_μ.

except in the region where E_T is large and Q^2 is small. The scale $\mu_r^2 = E_T^2 + Q^2$ gives always larger NLO corrections than $\mu_r^2 = E_T^2$.

Renormalization and Factorization Scale Dependence

The scale dependence of the cross section in the fixed order calculation is of the same order in α_s as the uncalculated higher order contributions [11] and can therefore be used to estimate the size of these contributions. The range within which the scale dependence is tested is, however, a matter of taste and convention. It is customary to vary the scales μ^2 by a factor x_μ ranging from 0.25 to 4 and quote the resulting change in the cross section as the corresponding uncertainty. Although the resulting number has no precise meaning, this convention allows at least a qualitative comparison of the corresponding uncertainties between different processes.

In the following we investigate the renormalization scale dependence of the jet cross

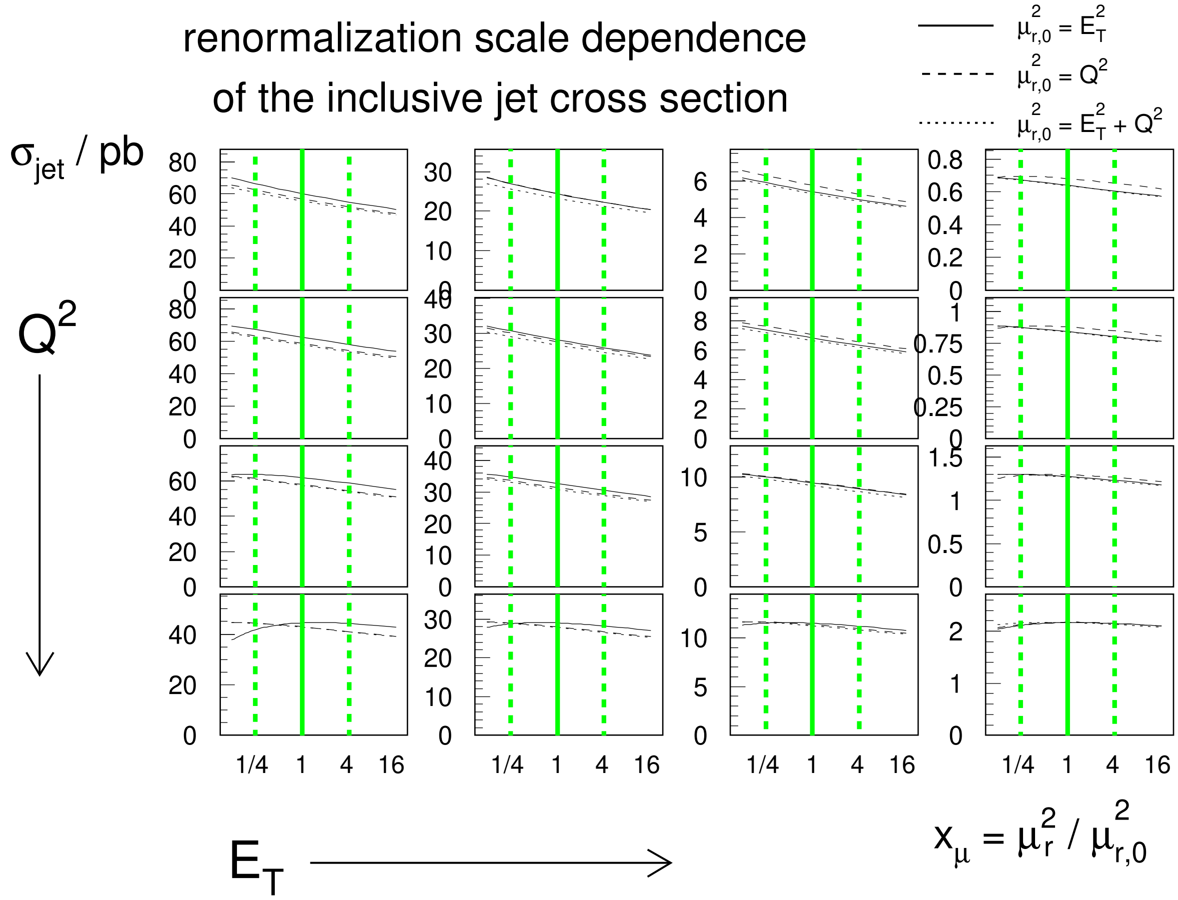

Figure 3.10: The renormalization scale dependence of the inclusive jet cross section in bins of E_T (horizontal) and Q^2 (vertical) for three different choices of the nominal renormalization scale: $\mu_r^2 = E_T^2$, $\mu_r^2 = Q^2$ and $\mu_r^2 = E_T^2 + Q^2$. Shown is the change of the cross section under variations of μ_r^2 by a factor x_μ around the central value $\mu_{r,0}^2$.

sections for different choices of the nominal scale. The renormalization scale dependence of the inclusive jet cross section is displayed in Fig. 3.10 in bins of E_T and Q^2 (as chosen in the analysis) for $\mu_r^2 = E_T^2$, $\mu_r^2 = Q^2$ and $\mu_r^2 = E_T^2 + Q^2$. We see that the renormalization scale dependence is directly related to the k-factor (c.f. Fig. 3.9). In those regions where the k-factors are large (especially at low Q^2) we also observe a large scale dependence. At large Q^2 the scale dependence is significantly reduced for all choices of $\mu_{r,0}^2$. For $\mu_r^2 = E_T^2$ the cross section becomes even flat within the range $0.25 < x_\mu < 4$ at high Q^2 (where the k-factors are close to one).

Similar studies have been performed for the dijet cross section using the inclusive $k_\perp$ algorithm. Fig. 3.11 shows the x_μ dependence at four different values of Q^2 for the leading order and the next-to-leading order calculation using $\mu_{r,0}^2 = \overline{E}_T^2$ and $\mu_{r,0}^2 = Q^2$. At $Q^2 > 500\,\mathrm{GeV}^2$ the scale dependence is significantly reduced at NLO compared to the LO calculation for both choices of $\mu_{r,0}^2$.

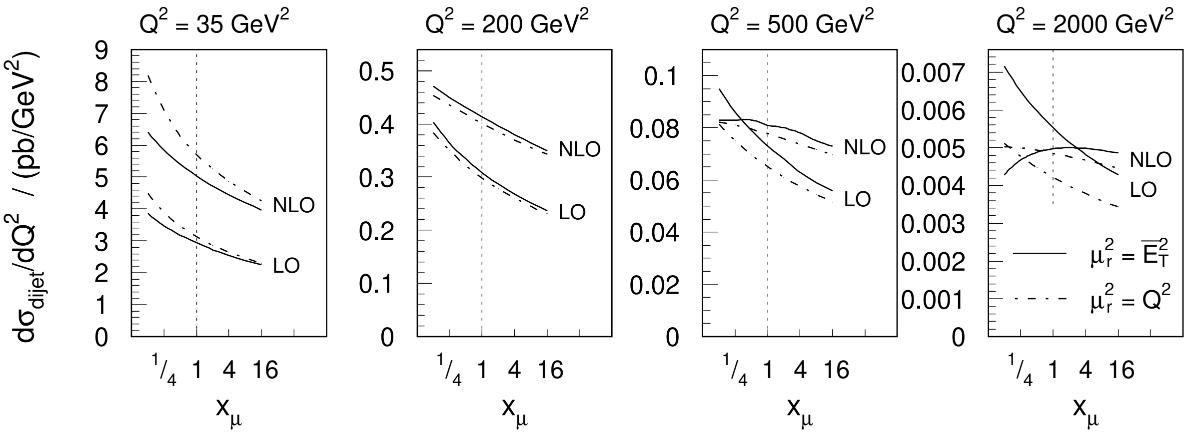

Figure 3.11: The renormalization scale dependence of the dijet cross section as defined by the inclusive $k_\perp$ algorithm. Shown is the change of the dijet cross section in leading order (lower lines) and in next-to-leading order (upper lines) under variations of the scale μ_r^2 by a factor of x_μ for $\mu_{r,0}^2 = \overline{E}_T^2$ (solid lines) and $\mu_{r,0}^2 = Q^2$ (dashed-dotted lines).

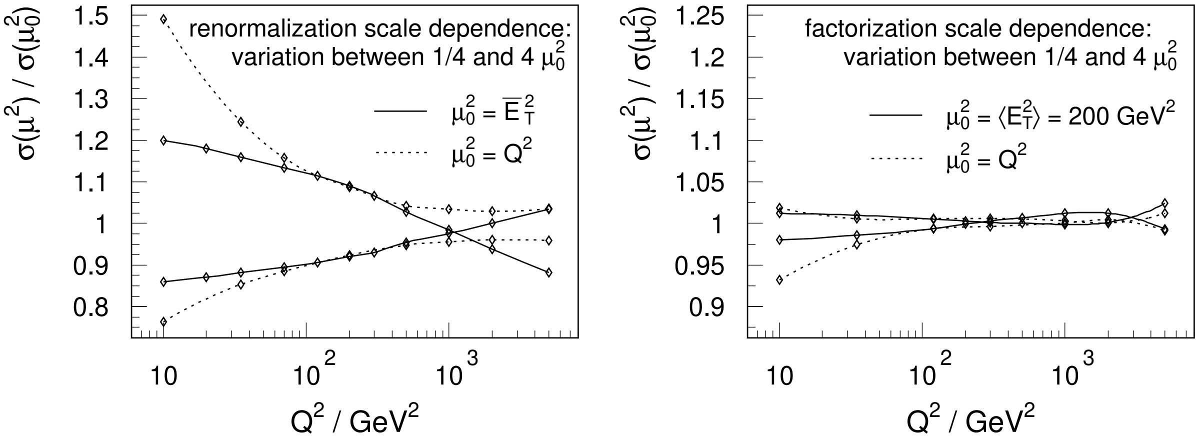

Figure 3.12: The renormalization (left) and factorization scale dependence (right) of the dijet cross section for the inclusive $k_\perp$ algorithm as a function of Q^2. Shown are the ratios of the cross sections obtained when varying the scales by a factor of 1/4 and 4 to the one obtained for the nominal scale.

At $Q^2 = 200\,\mathrm{GeV}^2$ it is already visible that the scale dependence of the NLO calculation becomes larger and at $Q^2 = 35\,\mathrm{GeV}^2$ (where the k-factor is almost two) the scale dependence of the NLO calculation is of the same size as that of the leading order calculation.

The relative change of the dijet cross section under variation of the scale μ_r^2 over the range $0.25 < x_\mu < 4$ is shown in Fig. 3.12 (left) as a function of Q^2. In this plot the reduced scale dependence for $\mu_{r,0}^2 = \overline{E}_T^2$ compared to $\mu_{r,0}^2 = Q^2$ is clearly seen. At $Q^2 > 150\,\mathrm{GeV}^2$ the scale dependence is below 10% and independent of $\mu_{r,0}^2$.

The factorization scale dependence of the dijet cross section is shown in the same representation in Fig. 3.12 (right) and can be seen to be significantly smaller (below 2% over the whole Q^2 range) than that of the renormalization scale.

3.3 Summary: Uncertainties in the QCD Predictions

The QCD predictions for the jet cross sections to be used in the QCD analysis of the jet data fall into perturbative and non-perturbative contributions. Both parts are affected by uncertainties which have been investigated in this chapter.

Uncertainties in the Hadronization Corrections

While the perturbative contributions are well defined this is not the case for the non-perturbative contributions. The application of predictions of phenomenological hadronization models which are matched to parton cascade models introduces two kinds of uncertainties. The first category consists of intrinsic uncertainties of the model predictions. These have been estimated by comparing the differences between different models and by variations of model parameters and are found to be of the order of a few percent. The second uncertainty concerns the ambiguity when applying the (unmatched) model predictions to next-to-leading order calculations. Investigations on this topic have been performed in a previous publication [53] based on comparisons of the final state topologies in parton cascade models and NLO calculations. It was found that although some properties (such as angular jet distributions) are very similar, other final state properties (such as the internal jet structure) are very much different.

In summary we draw the conclusion that the phenomenological models can be used to compare the size of the hadronization corrections for different observables. The application of these corrections to NLO calculations introduces uncertainties which can not be reliably estimated. Such a procedure should only be used when the estimated corrections are small, i.e. not much larger than 10%. As we have shown in this chapter this is the case for the inclusive jet definitions (inclusive $k_\perp$ and Aachen algorithm) if sufficiently hard cuts on the transverse jet energies are applied ($E_T > 7\,\mathrm{GeV}$). The inclusive jet algorithms shall therefore be used in this analysis to obtain the main results. The exclusive jet algorithms for which the hadronization corrections are very large (up to 60%) are only used to demonstrate the consistency of the procedure.

For the inclusive jet algorithms the uncertainties from the model and parameter dependence of the predictions are always below 3%. We take the uncertainty due to the matching of the parton level into account by increasing the quoted uncertainty in those kinematic regions where the corrections are large. In detail we define the uncertainty for each bin of the observables to be half of the size of the correction, but at least 3%.

For the hadronization corrections we use the averages of the model predictions by HERWIG, LEPTO and ARIADNE.

Uncertainties in the Perturbative Calculations

The perturbative QCD calculations in next-to-leading order depend on two purely technical parameters, namely the renormalization and the factorization scale.

We have shown that the factorization scale dependence is very small (below 2%). The choice of a fixed value of the factorization scale of $\mu_f^2 = 200\,\mathrm{GeV}^2 \simeq \langle E_T^2 \rangle$ for the QCD analysis is motivated later in section 8.2.

The renormalization scale dependence of the jet cross sections is seen to be directly related to the size of the next-to-leading order corrections. We have shown that the NLO corrections are sizable at $Q^2 \lesssim 100\,\mathrm{GeV}^2$ (the k-factor being larger than 1.5). We conclude that in this kinematic region the NLO calculation is only a poor approximation of perturbative QCD and not predictive since contributions from higher orders in α_s may be large. This means that jet data measured in this region can not be used for precise determinations of α_s and the gluon density in the proton.

In the region of large momentum transfers $Q^2 \gtrsim 150\,\mathrm{GeV}^2$ the renormalization scale dependence and the NLO corrections are reasonably small (the k-factors are below 1.4 and decreasing towards larger Q^2). In most phase space regions both effects are smaller for the scale $\mu_r^2 = E_T^2$ than for $\mu_r^2 = Q^2$. We therefore decide to use $\mu_r^2 = E_T^2$ to obtain the main results of this analysis. A further motivation for this choice is the fact that in jet production (in deep-inelastic scattering as in in other processes) the transverse jet energy E_T^2 is the *physical* scale at which hard QCD radiation is resolved.

The uncertainties of the NLO calculations from the renormalization and factorization scale dependence are defined as the relative change of the cross sections when the respective scale is varied by a factor x_μ in the range $0.25 < x_\mu < 4$.

Part II

Observation: Measurement of Jet Cross Sections in Deep-Inelastic Positron-Proton Collisions at $\sqrt{s} = 300\,\mathrm{GeV}$

4

Experimental Setup and Methods

The "Deutsches Elektronen-Synchrotron" (DESY) in Hamburg, Germany, started a series of high energy physics experiments in the year 1964 with the electron-synchrotron. In subsequent years the e^+e^- colliders DORIS and PETRA were added. The construction of the "Hadron-Electron Ring Accelerator" (HERA) started in 1984 and in 1991 HERA was put into operation. HERA is the first electron-proton collider in the world. The electron-proton center-of-mass energy of $\sqrt{s} \simeq 300\,\text{GeV}$ is by more than a factor of ten larger than those reached in previous electron-proton scattering experiments with fixed proton targets.

In this chapter we give a brief overview of the HERA collider and the layout of the H1 detector and we describe those detector components that are needed for the measurement of jet cross sections at large momentum transfers. We introduce different methods to reconstruct the event kinematics and give an outline of the experimental method of unfolding measured data distributions.

4.1 The Hadron-Electron Ring Accelerator

The HERA collider consists of two separate storage rings, placed in a subterranean ring tunnel of 6.3 km circumference. Electrons (or positrons) and protons are separately accelerated up to energies of 27.5 GeV and 820 GeV respectively, and brought to collision at the North Hall and the South Hall where the multi-purpose detectors of the H1 and the ZEUS experiments are located[1] (Fig. 4.1, left). These experiments have been taking data since 1992. The fixed target experiments HERMES and HERA-B are located in the West Hall and in the East Hall. Since 1995 the HERMES experiment measures collisions of the polarized positron beam with polarized gas targets (H_2, D, ^{3}He, ^{4}He) to study phenomena related to the spin of the target particles. The HERA-B experiment utilizes the proton beam by inserting tungsten wire targets into the beam halo, to search for decay modes of the B^0-$\bar{B}^0$ system, indicating a violation of the combined charge conjugation and parity (CP) conservation.

---

[1] The present analysis is based on the data taken between April 1994 and 1997 where HERA was operated with positron beams rather than electron beams because the former showed a much larger lifetime. In 1998 the protons were accelerated to 920 GeV and the positron beam was again replaced by an electron beam.

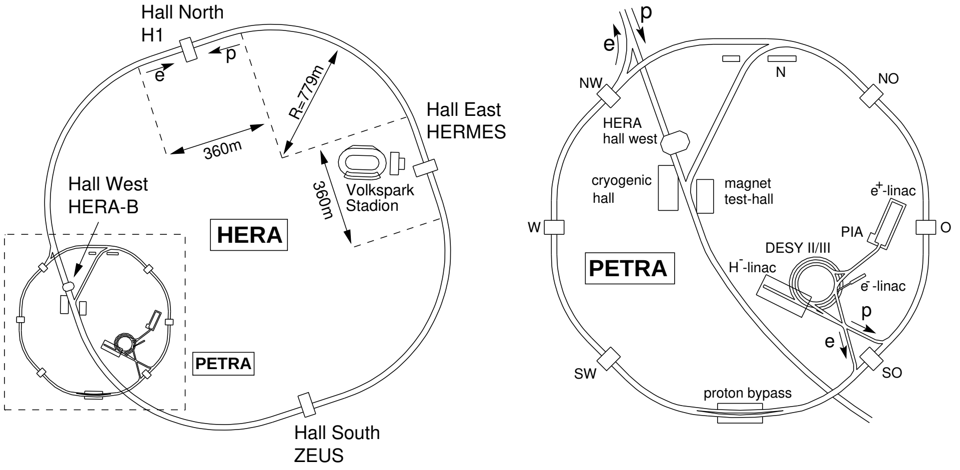

Figure 4.1: The electron-proton collider HERA (left), and the area of the DESY (right) including the preaccelerators LINAC I–III, DESY I–III and PETRA.

The protons are produced by passing H^- ions (accelerated to an energy of 50 MeV in LINAC III) through a stripper foil. The protons are collected in bunches and accelerated in DESY III (to 7.5 GeV) and in PETRA (to 40 GeV) before they are injected into HERA.

Positrons are provided by a 500 MeV linear accelerator, and are accelerated in DESY II (to 7 GeV), in PETRA (to 12 GeV) and are finally injected into HERA (Fig. 4.1, right). The positrons and protons are stored in typically 190 colliding bunches, with a length of ≈ 8 mm (110 mm) and typical currents of 30 mA (80 mA) for the positrons (protons). The bunch crossing interval is 96 ns, corresponding to a bunch crossing rate of 10.4 MHz. The lifetime of the positron (proton) beam is ≈ 10 (100) hours.

The HERA laboratory frame is defined by a right-handed coordinate system where the positive z-axis points along the proton beam direction. The x-axis and the y-axis point to the center of the HERA ring and upwards respectively. The nominal interaction point is taken as the origin. Polar angles θ are defined with respect to the positive z-direction and azimuthal angles ϕ are defined such that $\phi = 0$ points to the positive x-direction.

4.2 The H1 Detector

The final state particles from the positron-proton collisions are detected by the HERA detectors H1 and ZEUS. Both are designed as nearly hermetic multi-purpose detectors. An isometric view of the H1 detector is shown in Fig. 4.2. To account for the asymmetric beam energies of the colliding particles the forward region (i.e. the region towards the proton direction) is equipped with enhanced instrumentation. A detailed description of the H1 detector can be found in [79]. In the measurement of jet cross sections in deep-inelastic scattering,

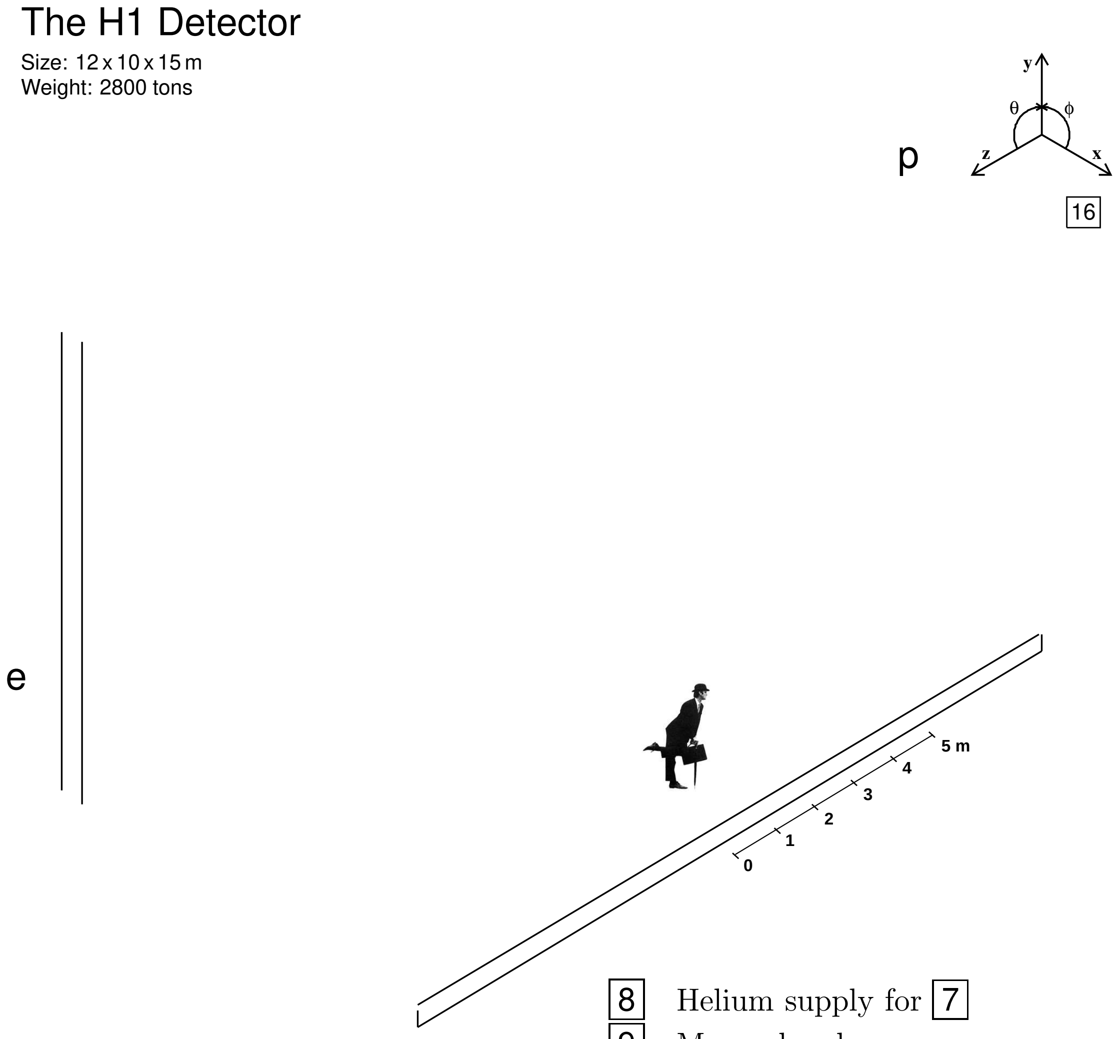

1	Beam pipe and beam magnets
2	Central track detectors
3	Forward track detectors
4	Electromagnetic LAr calorimeter
5	Hadronic LAr calorimeter
6	Superconducting coil (1.15 T)
7	Compensating magnet
8	Helium supply for 7
9	Muon chambers
10	Instrumented iron yoke
11	Forward muon toroid
12	SPACAL and Backward DC
13	PLUG calorimeter
14	Concrete shielding
15	Liquid argon cryostat
16	H1 coordinate system

Figure 4.2: An isometric view of the H1 detector

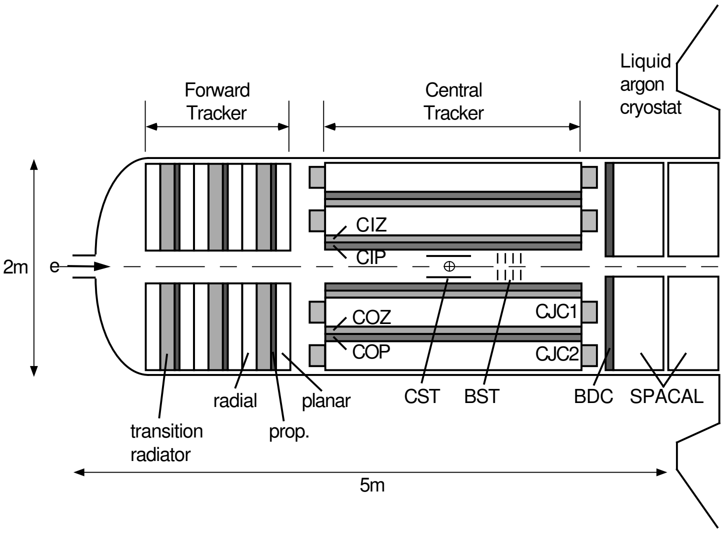

Figure 4.3: Side view of the tracking system in the H1 detector and the backward calorimeter (SPACAL)

the liquid argon (LAr) calorimeter, the backward calorimeter, the tracking chamber system and the luminosity detectors are of particular importance.

4.2.1 Tracking

The H1 tracking system includes three major components which cover polar angles in the range of $5° < \theta < 178°$ with full azimuthal coverage (Fig. 4.3). The central tracking chambers and the forward track detector are placed around the beam pipe between $z = -1.5$ and $z = 2\,\mathrm{m}$. The backward drift chamber (BDC) is located in front of the backward calorimeter. A superconducting solenoid, which surrounds both the tracking system and the LAr calorimeter, provides a uniform magnetic field of 1.15 T.

The Central Tracker

The central tracking device consists of six chambers in total which are housed in an aluminum tank. The main components are the two concentric drift chambers (CJC1, CJC2) with wires strung parallel to the beam axis. They cover the range of polar angles $15° < \theta < 165°$. The transverse momenta of charged particles are measured with a resolution of $\delta p_T/p_T < 0.01 \cdot p_T/\mathrm{GeV}$. Two polygonal drift chambers with wires strung perpendicular to the beam axis improve the determination of the z coordinate and complement the measurement of the track momenta. These are the central inner and central outer z-chambers (CIZ, COZ) which are placed at radii of 18 cm (CIZ) and 47 cm (COZ). They achieve a z resolution of typically $300\,\mu\mathrm{m}$. The central tracker is completed by two Multi-Wire Proportional Chambers: The central inner proportional chamber (CIP) and the central outer proportional chamber (COP)

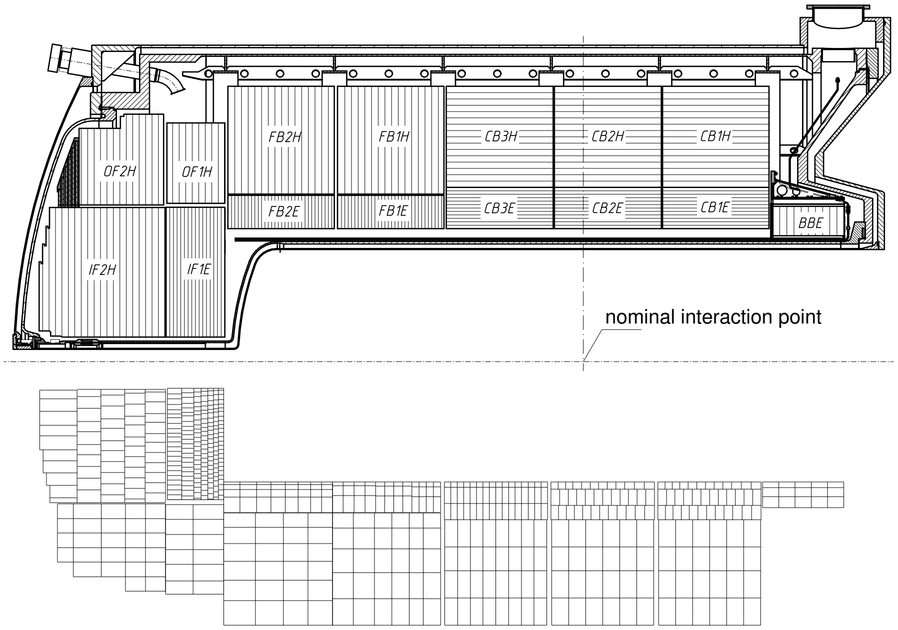

Figure 4.4: Side view of the H1 liquid argon calorimeter. The upper part shows the structure of the absorber plates, the lower part shows the cell structure.

which deliver a fast trigger signal with a time resolution better than the 96 ns separation time between consecutive HERA bunch crossings.

The central tracking chambers are used in this analysis to reconstruct the event vertex and to measure the polar angle of the scattered positron and the momenta of charged particles of the hadronic final state.

The Forward Tracker

The forward track detector which covers the polar angular range $5^\circ < \theta < 25^\circ$ is composed of a tracking chamber system made of three identical modules aligned along the z direction. Each module consists (in increasing z) of a planar drift chamber, a multi-wire proportional chamber, transition radiators, and a radial drift chamber. In the present analysis the forward track detector is used to determine the interaction vertex for events without tracks in the CJC.

4.2.2 Calorimetry

The H1 detector comprises four subdetectors, each with full azimuthal acceptance, designed to measure the energy of scattered particles: The liquid argon (LAr) calorimeter, the spaghetti calorimeter (SPACAL), the tail catcher and the plug calorimeters. The main

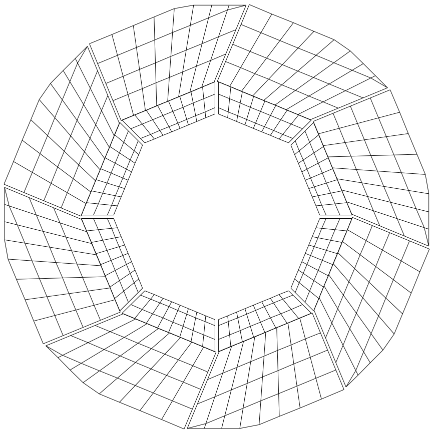

Figure 4.5: Radial view of the octant and cell structure of the CB1 ring of the H1 Liquid Argon calorimeter

component is the LAr calorimeter which covers the central and the forward region, while the backward region is covered by the SPACAL. The instrumented iron of the return yoke for the magnetic field (the tail catcher) is used for muon identification and to provide a rough calorimetric measurement of hadronic particles leaking out of the LAr calorimeter. In this analysis it is mainly used to reject muon induced background. The plug calorimeter (not used in this analysis) closes the gap in acceptance between the LAr calorimeter and the beam pipe in the forward direction.

The Liquid Argon Calorimeter

The finely segmented liquid argon (LAr) calorimeter [80] is situated inside the solenoid to reduce the amount of uninstrumented material particles have to traverse before they are absorbed in the calorimeter. It consists of an electromagnetic section and a hadronic section, both contained in a single liquid argon cryostat, and covers a polar angular range of $4° < \theta < 154°$. It is segmented along the beam axis in eight self supporting wheels. The wheels are constructed from eight identical stacks or octants (Figs. 4.4 and 4.5). The two forward wheels (IF1 and IF2 in Fig. 4.4) are assembled as two half rings in an effort to minimize uninstrumented regions due to cracks. Every wheel of the LAr calorimeter is divided into an inner electromagnetic section with lead absorber plates and an outer hadronic section with steel absorber plates (in both cases liquid argon is used as the active material). The most backward wheel, the BBE, has only an electromagnetic section. Both sections are highly segmented in the transverse and longitudinal directions with about 44 000 cells in total. The electromagnetic part has a depth between 20 and 30 radiation lengths. The total depth of the LAr calorimeter varies between 4.5 and 8 hadronic interaction lengths. The LAr calorimeter is non-compensating. The charge output for hadrons is about 30% smaller

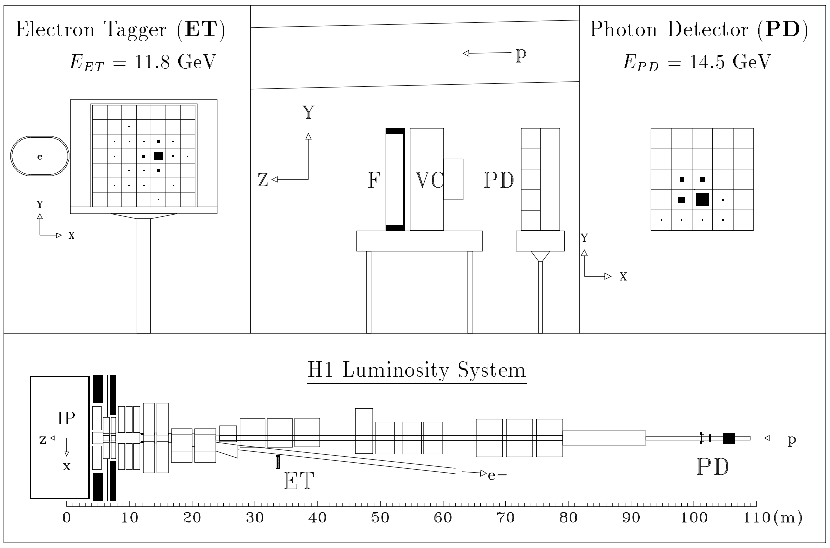

Figure 4.6: A Bethe-Heitler bremsstrahlung event measured in the H1 luminosity system

than for electrons of the same energy. A weighting technique is employed offline to correct for this effect.

The LAr calorimeter is used in this analysis to measure the scattered positron at large four-momentum transfers ($Q^2 \gtrsim 100\,\mathrm{GeV}^2$) and to measure the energy flow of the hadronic final state. The systematic uncertainty of the electromagnetic energy scale is between 0.7% and 3% (depending on the wheel). The uncertainty of the hadronic energy scale of the LAr calorimeter is 2% for the inclusive DIS measurement [32, 81]. For measurements of exclusive final states, however, the uncertainty is 4% (see the related discussion in section 5.5).

The SPACAL

The backward region is covered by a lead/scintillating fiber calorimeter (SPACAL) [82] ($154° < \theta < 177.8°$). It consists of an electromagnetic and a hadronic section with a total depth of two hadronic interaction lengths. In the present analysis it is used to measure the hadronic energy flow in the backward direction. The hadronic energy scale uncertainty of the SPACAL is 7%.

4.2.3 Luminosity System

The cross section of a given process $\sigma_{\mathrm{process}}$ is related to the observed number of events of this process N_{process} according to

$$\sigma_{\mathrm{process}} = \frac{N_{\mathrm{process}}}{\mathcal{L}_{\mathrm{int}}}\,, \tag{4.1}$$

where $\mathcal{L}_{\text{int}}$ denotes the integrated luminosity represented by the data set. The measurement of any cross section therefore requires a precise knowledge of $\mathcal{L}_{\text{int}}$. The integrated luminosity can be determined by measuring the event rate of a process with a well known cross section. In the H1 experiment the elastic bremsstrahlung $ep \rightarrow e\gamma p$ (Bethe-Heitler process) is used for this purpose. Both, the scattered positron and the emitted photon, are measured by two detectors installed close to the positron beam in the HERA tunnel (Fig. 4.6). The electron tagger (ET) and the photon detector (PD) are situated at z positions of $-33.4\,\text{m}$ and $-102.8\,\text{m}$ respectively. The uncertainty of the luminosity measurement is 1.5% for the data sample considered in this analysis.

4.2.4 Time of Flight Counters

Background induced by reactions of the proton beam with residual gas particles and interactions with the wall of the beam pipe can be rejected by using time-of-flight (ToF) information. For this purpose scintillators with a time resolution of 2–4 ns are mounted around the beam pipe at both ends of the detector. Based on the precise timing knowledge of the bunch crossings in the detector provided by the HERA machine (HERA clock), this time resolution allows to distinguish between signals from proton induced background and actual collision events at a particular point in the detector.

4.2.5 Trigger

At HERA the positron and the proton bunches collide with a frequency of 10.4 MHz. The frequency by which the various detector components deliver signals is of the order $\sim 10\,\text{kHz}$ [79]. Since the expected rate of events from positron-proton collisions is significantly smaller the largest contribution comes from background processes as e.g. synchrotron radiation from the positron beam, proton gas interactions and stray protons which produce particle showers by hitting the beam pipe.

The task of the trigger system is to reject background events and to select events that originate from positron-proton collisions out of the data flow of signals registered in the various detector components for permanent recording. The H1 trigger system used for the online selection consists of three active levels plus one level which is used in the offline reconstruction step. Events are recorded at a rate of $\approx 10\,\text{Hz}$.

4.3 Reconstruction of the Kinematics

At a fixed center-of-mass energy $\sqrt{s}$ the kinematics of a deep-inelastic scattering event is given by two independent variables. The H1 detector allows to measure the energy and the scattering angle of the positron as well as the energies and angles of the hadronic final state particles. This allows the application of various methods to reconstruct the event kinematics. These methods differ in the resolution of the kinematic variables, since the input quantities are measured at a different precision. Furthermore, even for a perfect measurement, exact agreement between these methods cannot be expected. Different methods are in different ways sensitive to QED corrections, as the emission of photons collinear to the positron beam, which escape through the beam pipe.

The redundancy in the measurement can be used to combine the different variables to optimize the experimental resolution of the kinematic variables and reduce the sensitivity to QED radiation.

4.3.1 The Electron Method

The "Electron Method" [83] is based on the information of the energy E' and the polar angle θ_e of the scattered positron to determine the kinematic variables according to

$$\begin{aligned} Q^2_e &= 2\,E_0\,E'\,(1+\cos\theta_e)\,, \\ y_e &= 1-\frac{E'}{2E_0}(1-\cos\theta_e)\,, \\ x_e &= \frac{Q^2_e}{y_e\,s}\,, \end{aligned} \tag{4.2}$$

where E_0 denotes the positron beam energy. The Electron Method gives a very good resolution of the four-momentum transfer squared Q^2. At small values of y (corresponding to large x_{Bj}) the y and x_{Bj} resolutions decrease.

4.3.2 The Hadron Method

The "Hadron Method" [84] has been proposed to reconstruct the kinematic variables in charged current events where the scattered neutrino can not be detected. It relies solely on the measurement of the energies and the angles of the hadronic final state particles. The kinematic variables are obtained as

$$\begin{aligned} Q^2_{\mathrm{had}} &= \frac{(\sum_{\mathrm{had}} p_x)^2\,+\,(\sum_{\mathrm{had}} p_y)^2}{1-y_{\mathrm{had}}}\,, \\ y_{\mathrm{had}} &= \frac{\sum_{\mathrm{had}}(E-p_z)}{2E_0} \\ x_{\mathrm{had}} &= \frac{Q^2_{\mathrm{had}}}{y_{\mathrm{had}}\,s}\,. \end{aligned} \tag{4.3}$$

The sums run over particles[2] of the hadronic final state (where the scattered positron is excluded). The Hadron Method gives a poor resolution of Q^2 and x_{Bj}.

4.3.3 The Double Angle Method

The "Double Angle Method" [83] uses only the angles of the final state particles. The kinematic variables are given by

$$\begin{aligned} Q^2_{\mathrm{da}} &= 4E_0^2\,\frac{\sin\gamma\,(1+\cos\theta_e)}{\sin\gamma+\sin\theta_e-\sin(\theta_e+\gamma)}\,, \\ y_{\mathrm{da}} &= \frac{\sin\theta_e\,(1-\cos\gamma)}{\sin\gamma+\sin\theta_e-\sin(\theta_e+\gamma)}\,, \\ x_{\mathrm{da}} &= \frac{Q^2_{\mathrm{da}}}{y_{\mathrm{da}}\,s}\,. \end{aligned} \tag{4.4}$$

The angle γ is defined by

$$\cos\gamma = \frac{(\sum_{\mathrm{had}} p_x)^2 + (\sum_{\mathrm{had}} p_y)^2 - (\sum_{\mathrm{had}}(E-p_z))^2}{(\sum_{\mathrm{had}} p_x)^2 + (\sum_{\mathrm{had}} p_y)^2 + (\sum_{\mathrm{had}}(E-p_z))^2}\,, \tag{4.5}$$

where the sums run over all particles of the hadronic final state. The advantage of this approach is the insensitivity to the absolute calorimetric energy calibration. It is, however, sensitive to the relative calibration between different detector components. Since such uncertainties are very hard to determine and quantify, it is nearly impossible to determine the corresponding uncertainties for a measured cross section. We will therefore not use this method in the cross section measurements.

4.3.4 The Sigma Method

The previous methods are all sensitive to the radiation of photons, collinear to the incoming positron. This sensitivity can be reduced by using the "Sigma Method" [85] which exploits the redundancy of the measurements to eliminate the value of the positron beam energy in the formulae. From energy and longitudinal momentum conservation it follows

$$\begin{aligned} \sum_{\text{final state}} (E-p_z) &= \sum_{\text{initial state}} (E-p_z)\,, \\ \Longrightarrow \quad \sum (E-p_z) &\equiv \sum_{\mathrm{had}} (E-p_z) + E'\,(1+\cos\theta_e) = 2\,E_0\,. \end{aligned} \tag{4.6}$$

From transverse momentum conservation we have

$$\left(\sum_{\mathrm{had}} p_x\right)^2 + \left(\sum_{\mathrm{had}} p_y\right)^2 = E'^2 \sin^2\theta_e\,. \tag{4.7}$$

---

[2] The term "particle" refers here either to calorimetric energy clusters or measured track momenta.

Inserting the identities (4.6) and (4.7) in the definition of the Hadron Method (4.3) we obtain the formulae for the Sigma Method

$$\begin{aligned} Q^2_\Sigma &= \frac{E'^2_e \sin^2\theta_e}{1-y_\Sigma}\,, \qquad (4.8)\\ y_\Sigma &= \frac{\sum_{\mathrm{had}}(E-p_z)}{\sum_{\mathrm{had}}(E-p_z)\,+\,E'_e\,(1-\cos\theta_e)}\,,\\ x_\Sigma &= \frac{Q^2_\Sigma}{y_\Sigma\; s}\,. \end{aligned}$$

The so-defined variables Q^2_Σ and x_Σ give a better resolution than those from the Hadron Method.

4.3.5 The Electron-Sigma Method

While the Sigma Method is less sensitive to QED radiation and gives a better x resolution than the Electron Method, it suffers from an inferior resolution in Q^2. An optimized method can therefore be defined by combining the Q^2 from the Electron Method and the x_{Bj} measurement from the Sigma Method in the "Electron-Sigma Method" [86]

$$\begin{aligned} Q^2_{e\Sigma} &= Q^2_e\,, \qquad (4.9)\\ x_{e\Sigma} &= x_\Sigma\,,\\ y_{e\Sigma} &= \frac{Q^2_{e\Sigma}}{x_{e\Sigma}\; s}\,. \end{aligned}$$

This method has been used in a recent H1 structure function measurement at high Q^2 [32, 81] and will also be used in the present analysis. In appendix A we demonstrate its advantage to the Electron Method in the reconstruction of the boost vector to the Breit frame.

4.4 The Unfolding Method

In any experimental measuring device with limited resolution the true value of an observable is distorted and subject to random fluctuations. Further restrictions in the reconstruction of observables may arise e.g. from limitations in the detector acceptance and from inefficiencies in the data selection. Comparisons of such "primary observations" to the predictions of a physical theory require a precise knowledge of the properties of the measuring device, the so-called "detector response function".

Folded with the detector response function the theoretical prediction can be compared to the reconstructed data. Although this approach is straightforward, it prevents comparing measurements of the same observable from different experiments with different measuring devices (in which in general the effects of resolution are different).

A different approach is to "unfold" the data for the detector effects. The unfolded distributions are independent of the measuring device and can therefore be directly compared to theoretical predictions and also between different experiments.

In the following we introduce the unfolding procedure to be used in the present analysis, and describe how the detector response is determined.

4.4.1 The Unfolding Problem

We consider binned distributions where $\hat{\mathcal{O}}_j$ denotes the true value of the j-th bin of an observable. The reconstructed value of the i-th bin of this observable $\mathcal{O}_i$ is related to the true distribution by a folding with the detector response matrix $\mathcal{D}_{ij}$

$$\mathcal{O}_i \; = \; \sum_j \mathcal{D}_{ij} \, \hat{\mathcal{O}}_j \, . \tag{4.10}$$

The response matrix element $\mathcal{D}_{ij}$ represents the conditional probability that an event will be reconstructed in bin i of the observable given that the true value was in bin j. For complicated measuring devices the response matrix can often not be determined analytically. In such a case it is possible to use a model of the detector that simulates the response to single events. A sample of events with similar properties as observed in the data can be generated and passed through the detector simulation. If the correlation between the generated values of the observable and the values reconstructed after the detector simulation is known, the response matrix $\mathcal{D}$ can be determined [87].

In principle the true distribution $\hat{\mathcal{O}}_j$ can then be obtained through the inversion of the matrix $\mathcal{D}_{ij}$. This procedure, however, leads to unstable and oscillating solutions with large errors [87]. A damping of the oscillations (and correspondingly a reduction of the errors) can be achieved by imposing additional restrictions on the solution as e.g. in the unfolding procedures described in [88, 89]. These approaches allow to handle migrations between different bins.

4.4.2 The Bin-by-Bin Correction Method

In most applications it is desirable to have results without significant correlations between single data points. The correlations between bins which arise from migrations of events can be avoided by choosing the bin sizes appropriately large. When migrations between bins are negligible, the off-diagonal elements ($i \neq j$) of $\mathcal{D}_{ij}$ vanish and the solution of (4.10) is simply given by

$$\hat{\mathcal{O}}_i \; = \; C_{i,\,\mathrm{detector}} \cdot \mathcal{O}_i \,, \tag{4.11}$$

where $C_{i,\,\mathrm{detector}} \equiv \mathcal{D}_{ii}^{-1}$. The convolution in (4.10) reduces therefore to a simple bin-by-bin correction. The values of the $C_{i,\,\mathrm{detector}}$ can be determined from the simulated events as the ratios of the generated ($\hat{\mathcal{S}}_i$) and the reconstructed values ($\mathcal{S}_i$) of the observables

$$C_{i,\,\mathrm{detector}} \; = \; \frac{\hat{\mathcal{S}}_i}{\mathcal{S}_i} \,. \tag{4.12}$$

The solution $\hat{\mathcal{O}}_i$ of (4.11) corresponds to the measured observable corrected for detector resolution and acceptance.

The applicability of this method is not restricted to problems where migrations between bins are small. However, in cases where migrations between bins are not negligible this procedure may bias the result if the distribution of the observable in the simulated events differs from the data [87]. To apply this method (at least) one of two conditions should therefore be fulfilled.

- Migrations between bins are small.
- The simulated events describe all details of the reconstructed data sample.

In the present analysis we aim to fulfill both requirements. We will demonstrate that the simulated events describe the reconstructed data (chapter 5) and we will choose the bin widths sufficiently large to keep migrations between bins relatively small (chapter 6).

Furthermore we use two different models with slightly different properties to generate the events. In chapter 5 we show that for most distributions the data are in between the two model predictions. Differences in the corresponding correction factors can thus be regarded as a rough estimate of the uncertainty introduced by the possible bias.

4.4.3 Unfolding Detector Effects and QED Corrections

It may be desirable to unfold the data also for physical effects which are not included in the theoretical predictions to be compared to the results. In our case this concerns higher order QED corrections connected to real photon emissions from the positron (in the initial state or in the final state) and virtual corrections at the leptonic vertex as represented by the diagrams in Fig. 2.8 (a-c). We do not unfold the corrections from the fermionic contributions to the virtual photon self energy (Fig. 2.8 d) which account for the running of the electromagnetic coupling constant since these are included in the theoretical calculations (see section 2.3).

To take into account the mentioned effects we introduce a second correction factor defined as the ratio of the observable in a calculation without QED corrections ($\hat{\mathcal{S}}_{i,\,\mathrm{w/o\,QED\,corr.}}$) and a calculation including QED corrections ($\hat{\mathcal{S}}_{i,\,\mathrm{incl.\,QED\,corr.}}$) but otherwise identical physics assumptions

$$C_{i,\,\mathrm{QED}} \;\equiv\; \frac{\hat{\mathcal{S}}_{i,\,\mathrm{w/o\,QED\,corr.}}}{\hat{\mathcal{S}}_{i,\,\mathrm{incl.\,QED\,corr.}}} \,. \tag{4.13}$$

The unfolding of detector effects and QED corrections is then performed in two steps. Combining (4.12) and (4.13) the total correction factor is given by

$$C_{i,\,\mathrm{total}} \;\equiv\; C_{i,\,\mathrm{detector}} \;\cdot\; C_{i,\,\mathrm{QED}} \,, \tag{4.14}$$

and the corrected data distribution is obtained as

$$\hat{\mathcal{O}}_i \;=\; C_{i,\,\mathrm{total}} \cdot \mathcal{O}_i \,. \tag{4.15}$$

Since the event sample to be subjected to the detector simulation also includes higher order QED corrections, the factors $\hat{\mathcal{S}}_i$ in (4.12) and $\hat{\mathcal{S}}_{i,\,\mathrm{incl.\,QED\,corr.}}$ in (4.13) are defined identically such that they would cancel in the total correction factor (4.14).

However, for practical reasons we use different event samples to determine $\hat{\mathcal{S}}_i$ and $\hat{\mathcal{S}}_{i,\,\mathrm{incl.\,QED\,corr.}}$. The simulation of the detector response is time consuming such that the value of $\mathcal{S}_i$ is determined with non-negligible statistical uncertainties. If $\hat{\mathcal{S}}_i$ is calculated from the same data sample part of the statistical fluctuations cancel in the ratio (4.12). The computation of $\hat{\mathcal{S}}_{i,\,\mathrm{w/o\,QED\,corr.}}$ and $\hat{\mathcal{S}}_{i,\,\mathrm{incl.\,QED\,corr.}}$ does not require the simulation of the detector response and can thus be performed with high statistical precision.

While the total correction factor could in principle be calculated in a single step, the separation in (4.14) allows to disentangle the contributions from detector effects and the QED corrections. This, however, requires a suitable definition of the intermediate level, which includes QED corrections. In the presence of QED corrections (as the emission of real photons from the positron) the event kinematics are not longer uniquely defined. To separate the detector effects from the QED corrections we define the intermediate level according to the resolution and acceptance of the H1 detector at which radiated photons are detected. For this purpose we divide generated events with final state photons, radiated from the positron, into three classes.

- Experimentally, photons with an angle of $\Omega_{e\gamma} < 7^\circ$ to the scattered positron can not be resolved from the positron [90]. In the generated events we therefore recalculate the four-vector of the scattered positron from the sum of the original positron four-vector and the four-vector of the photon if $\Omega_{e\gamma} < 7^\circ$ and exclude the photon from the final state.

- Photons with a polar angle of $\theta_\gamma > 178.5^\circ$ escape the detection in the backward calorimeter through the beam pipe. If the energy of a generated photon with $\theta_\gamma > 178.5^\circ$ is above $E_\gamma = 5\,\mathrm{GeV}$ the event is ignored. This emulates the effect of the selection cut (5.5) on $\sum(E - p_z) > 45\,\mathrm{GeV}$ (see the related discussion in section 5.1.3). If $E_\gamma < 5\,\mathrm{GeV}$ the event is kept but the photon is excluded from the final state.

- In all other cases we have isolated photons which are within the acceptance of the calorimeters. Since we do not attempt to identify these photons in the experiment, we also consider the corresponding generated photons as a part of the hadronic final state.

Based on the re-defined four-vectors of the scattered positron and the hadronic final state the event kinematics is calculated according to the same reconstruction method that is also used to reconstruct the data.

4.4.4 Event Generation and Detector Simulation

To determine the detector response $C_{i,\,\mathrm{detector}}$ we generate two event samples which are both subjected to a detailed simulation of the H1 detector, based on the program GEANT [91]. The events are generated by the Monte Carlo programs LEPTO [65] and ARIADNE [67] which have been introduced in Section 2.3. Both programs are interfaced to the program HERACLES [73] via the program DJANGO [72] to include higher order QED corrections. LEPTO (version 6.5) is used without the soft color interaction model. The LEPTO event sample represents an integrated luminosity of $\mathcal{L}_\mathrm{int} \simeq 87\,\mathrm{pb}^{-1}$ using parton distributions from the CTEQ4L parameterization [77].

The event sample for ARIADNE (version 4.08) is generated using parton distributions from the MRSH parameterization [92] and corresponds to an integrated luminosity of $\mathcal{L}_\mathrm{int} \simeq 162\,\mathrm{pb}^{-1}$. Further ARIADNE events are generated at $Q^2 > 1000\,\mathrm{GeV}^2$ corresponding to $\mathcal{L}_\mathrm{int} \simeq 392\,\mathrm{pb}^{-1}$.

To investigate the probability with which photoproduction events are misidentified as deep-inelastic scattering events, we have generated photoproduction events using the generator PYTHIA [93]. The PYTHIA event sample consists of so-called “direct” and “resolved” photoproduction events corresponding to an integrated luminosity of $\mathcal{L}_\mathrm{int} \simeq 100\,\mathrm{pb}^{-1}$.

The integrated luminosities of the simulated Monte Carlo event samples are at least a factor of three above the integrated luminosity of the H1 data of $\mathcal{L}_\mathrm{int} \simeq 33\,\mathrm{pb}^{-1}$ used in the present analysis.

To determine the QED corrections we have generated the same LEPTO and ARIADNE event samples as above, respectively with and without the inclusion of QED corrections. Each of these single event samples corresponds to $\mathcal{L}_\mathrm{int} \simeq 1000\,\mathrm{pb}^{-1}$.

5

Data Selection

In this chapter we describe the selection of deep-inelastic scattering events at large four-momentum transfer and the reconstruction of hadronic jets in the Breit frame. The global selection of DIS events (which is based on standard reconstruction methods) is only discussed briefly. Emphasis is put on the details related to the jet selection and to the study of various categories of distributions, such as kinematic event quantities, general hadronic final state properties and properties of single jets.

Distributions of simulated events from Monte Carlo event generators are compared to the data. We intend to show that the data are technically well understood. We demonstrate that the Monte Carlo event simulations give a sufficiently good description of the detector calibration and of all event properties, to be used in the unfolding procedure of the data (according to the criteria discussed in the previous chapter).

5.1 Basic Selection Criteria

The data employed in this analysis have been taken by the H1 experiment in the HERA running periods of the years 1995–1997. The selection of deep-inelastic scattering events follows closely the one used in a recent measurement of the inclusive ep cross section at large four-momentum transfer [32]. We have benefited very much from the detailed studies which have been performed in this context, documented in detail in the Ph.D. thesis of B. Heinemann [81]. Here we will only give a brief discussion of the basic selection criteria and document the corresponding control distributions only for the jet sub-sample. Although the selection cuts are discussed one after the other, at each step the control distributions are shown for the data sample with all selection cuts applied (except where noted).

The cuts, applied in the selection of the data can be grouped in two classes: Phase space cuts and technical cuts. The first class contains the kinematic cuts that define the phase space of the final (corrected) observables. These are the cuts in the kinematic variables y and Q^2 (reconstructed by the Electron-Sigma Method which utilizes information from the scattered positron and the hadronic final state) and the jet selection cuts as introduced in section 2.4 and summarized in table 5.1. The second class contains cuts on the event quality,

DIS event selection		$0.2 < y < 0.6$ $150 < Q^2 < 15\,000\,\mathrm{GeV}^2$
global jet selection	(all jet cross sections)	$-1 < \eta_{\mathrm{jet,\,lab}} < 2.5$
incl. jet cross section	incl. $k_\perp$ algo. / Aachen algo. (E_T recomb. scheme)	$E_{T,\,\mathrm{Breit}} > 7\,\mathrm{GeV}$
dijet cross section	incl. $k_\perp$ algo. / Aachen algo. (E_T recomb. scheme)	$E_{T,1,\,\mathrm{Breit}} + E_{T,2,\,\mathrm{Breit}} > 17\,\mathrm{GeV}$ $E_{T,\,\mathrm{Breit}} > 5\,\mathrm{GeV}$
	excl. $k_\perp$ algo. / Cambridge algo. (E recomb. scheme)	(reference scale)$^2 = 100\,\mathrm{GeV}^2$ $y_{\mathrm{cut}} = 1$
three-jet cross section	incl. $k_\perp$ algo. (E_T recomb. scheme)	$E_{T,\,\mathrm{Breit}} > 5\,\mathrm{GeV}$ $M_{\mathrm{3jet}} > 25\,\mathrm{GeV}$
four-jet cross section	incl. $k_\perp$ algo. (E_T recomb. scheme)	$E_{T,\,\mathrm{Breit}} > 5\,\mathrm{GeV}$ $M_{\mathrm{4jet}} > 25\,\mathrm{GeV}$

Table 5.1: A summary of the phase space definitions for the jet cross section measurements. The detailed definitions are given in section 2.4.

which are designed to improve the experimental resolution and to reduce the influence of badly reconstructed events and background processes. The fractional signal that is lost by these cuts is corrected for in the unfolding procedure. Only for some cuts (where explicitly stated) the corrections have been determined and directly applied to the data.

5.1.1 Run Selection and Trigger Requirement

The analysis includes all data taken while the main detector components were fully operational. These include the main calorimeters (LAr and SPACAL), the tracking system (CJC1, CJC2, CIP, COP), the luminosity system and the time of flight counters. Runs, in which coherent noise was detected in the LAr calorimeter are excluded. The resulting data set corresponds to an integrated luminosity of $\mathcal{L}_{\mathrm{int}} = 33\,\mathrm{pb}^{-1}$ (the years 1995, 1996, 1997 contribute $3.8\,\mathrm{pb}^{-1}$, $7.9\,\mathrm{pb}^{-1}$, $21.3\,\mathrm{pb}^{-1}$ respectively).

Neutral current events at high Q^2 are triggered by the positron trigger of the LAr calorimeter. The investigations in [81] have shown that for the present data sample (where the positron energy is $E' \gtrsim 13\,\mathrm{GeV}$) the trigger efficiency is 100% with an uncertainty of 0.5%.

To reduce contributions from background we require that the timing signal of the interaction (delivered by the CJC) lies within $\pm 20\,\mathrm{ns}$ of the nominal interaction time of the current bunch crossing or one bunch crossing before or after that. In [81] it has been shown that this cut reduces the signal by 0.4% (for which we reweight the remaining events).

5.1.2 Event Vertex and Identification of the Scattered Positron

The selection of neutral current DIS events is based on the identification of the scattered positron and the reconstruction of the z-position of the event vertex.

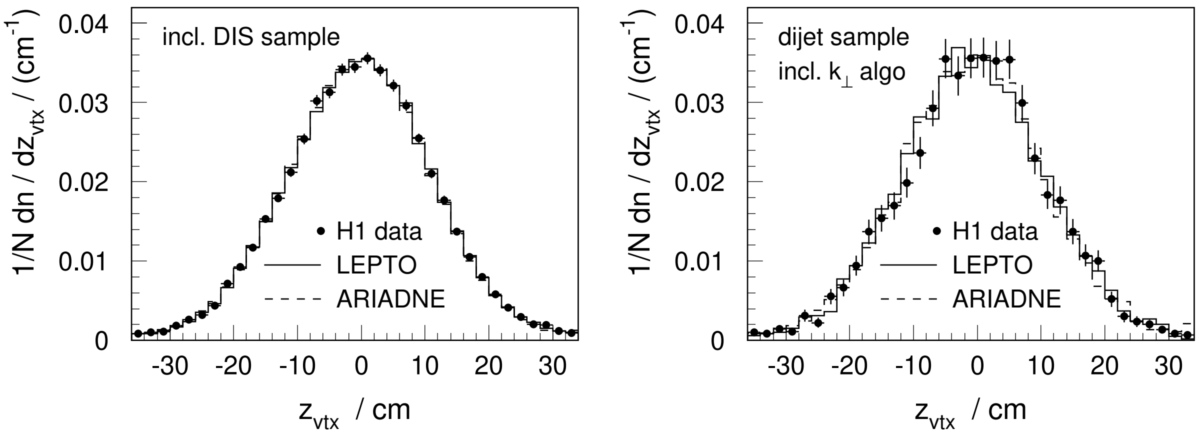

Figure 5.1: The distribution of the reconstructed z-position of the event vertex, for the inclusive DIS event sample (left) and for the dijet event sample (right).

In the present analysis we require that the z-position of the event vertex, reconstructed using central or forward tracks, lies within $\pm 35\,\mathrm{cm}$ of its nominal position at $-1\,\mathrm{cm}$. The distribution of the z-vertex position is shown in Fig. 5.1 for the inclusive DIS event sample (left) and for the dijet sample (right), together with the distributions of the simulated events, which have been reweighted to give an optimized description of the z-vertex distribution. The vertex finding efficiency is 100% and well described by the simulation [81].

In events at high Q^2 the positron is scattered with high energy under a large polar angle and therefore expected to produce a compact and isolated energy cluster with large transverse momentum in the electromagnetic part of the LAr calorimeter [94]. We select events in which the cluster of a positron candidate fulfills these requirements (specified in detail in [81]). If the polar angle of the positron cluster lies within the acceptance of the central tracker ($\theta_{\mathrm{cluster}} > 35°$) we require a track pointing to the positron cluster with a distance of closest approach (DCA) $d_{\mathrm{DCA}} < 12\,\mathrm{cm}$ (when extrapolated to the calorimeter surface). The investigations performed in [81] have shown that the requirement of a track-link introduces a 2.2% larger inefficiency in the data than in the simulation. We take this into account by applying a corresponding correction factor to the simulation.

The positron energy is taken from the calorimetric energy measurement. If a track is matched to the positron cluster, the polar and azimuthal angle are taken from the track measurement (or otherwise from the cluster position).

The standard reconstruction corrects for the energy loss in the dead material in front of the calorimeter and for losses in the cracks between the calorimeter modules. A high precision in the energy measurement, however, requires to limit the size of these corrections by excluding certain crack regions, based on the impact position of the positron in the calorimeter. These are the regions of $\pm 2°$ in the azimuthal angle around the eight ϕ-cracks (see Fig. 4.5) and $\pm 5\,\mathrm{cm}$ around the z-crack at $z = +20\,\mathrm{cm}$ between the CB2 and CB3 wheels of the LAr calorimeter (see Fig. 4.4). Furthermore in the backward part of the BBE wheel (see Fig. 4.4) the electromagnetic shower of the positron is not fully contained in the calorimeter. Therefore we exclude the region $z < -180\,\text{cm}$. Within the remaining acceptance region the positron finding efficiency is very high ($> 99\%$) and well modeled by the simulation [81].

In three regions in the z-ϕ plane the positron trigger is not fully efficient. Events with positrons in these regions are therefore excluded. In total we apply the following cuts on the impact point of the positron (z_e, ϕ_e) in the calorimeter

$$\text{z-crack} \qquad +15\,\text{cm} < z_e < +25\,\text{cm}\,, \tag{5.1}$$

$$\text{BBE acceptance} \qquad z_e > -180\,\text{cm}\,, \tag{5.2}$$

$$\text{ϕ-cracks} \qquad \phi_e \in (n \cdot 45^\circ) \pm 2^\circ \qquad (n = 0, 1, \cdots, 7)\,, \tag{5.3}$$

$$\begin{array}{lrcl} \text{ineff. trigger} & -60\,\text{cm} < z_e < 20\,\text{cm} & \text{and} & -135^\circ < \phi_e < -112.5^\circ\,, \\ & -90\,\text{cm} < z_e < -60\,\text{cm} & \text{and} & 135^\circ < \phi_e < 157.5^\circ\,, \\ & -120\,\text{cm} < z_e < 20\,\text{cm} & \text{and} & 90^\circ < \phi_e < 112.5^\circ\,. \end{array} \tag{5.4}$$

We correct for the event loss due to cuts (5.3) and (5.4) by using the symmetry in ϕ and reweight the remaining events corresponding to the fraction of the excluded ϕ range (which depends on z).

In Fig. 5.2 the distributions of the energy, the polar angle and the azimuthal angle of the positron candidates are displayed. The latter shows the effect of the cuts in the z-ϕ plane. While the distributions of the energy and the azimuthal angle are well described by the simulation, we observe differences in the polar angle spectrum for both models. This is directly connected to the fact that the Q^2 dependence of the dijet cross section is not described by LEPTO and ARIADNE (as will be discussed later). We note, however, that the data distribution is always between both model predictions.

5.1.3 Reconstruction of the Hadronic Final State

When a positron candidate has been accepted, all corresponding calorimetric cell energies, clusters and the associated track are excluded from the further reconstruction of the hadronic final state. The same applies to all tracks and clusters within a radius of $\Delta R = 0.5$ (in the η, ϕ plane) around the reconstructed positron direction.

The hadronic final state is then reconstructed by combining the calorimetric energy measurement and the momenta of low momentum tracks according to a procedure that avoids the double counting of energies [32]. For this purpose all central tracks with a transverse momentum of $p_T < 2$ GeV are considered. The axis of each accepted track is then extrapolated to the LAr calorimeter. If the energy in the electromagnetic (hadronic) part of the LAr calorimeter in a cylinder of 15 cm (25 cm) radius around this axis is smaller than the corresponding track energy it is excluded from the measurement. If the total energy in the cylinders is greater than the track energy, only the calorimetric energy measurement is used.

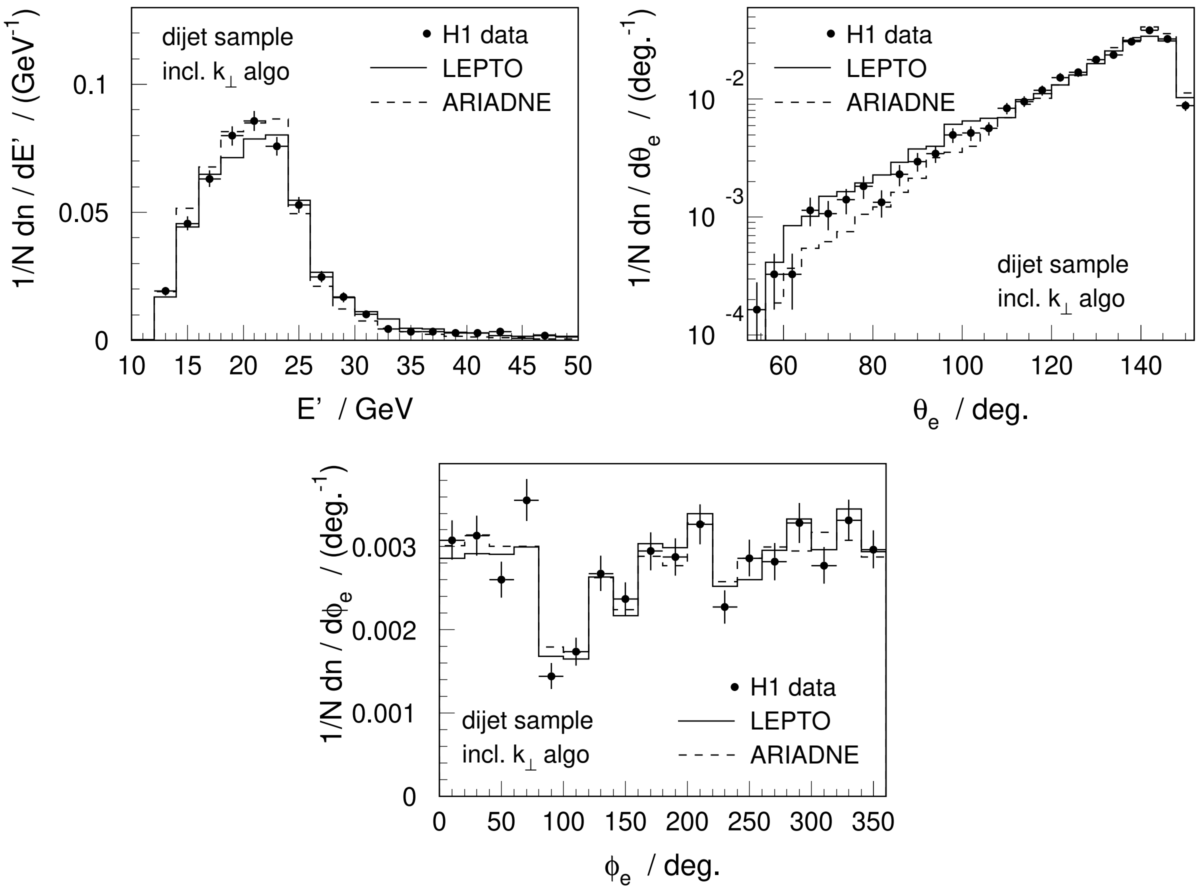

Figure 5.2: The distributions of the energy (left), the polar angle (right) and the azimuthal angle (center) of the positron candidates in the dijet sample for the inclusive $k_\perp$ algorithm.

The fractional contributions from the calorimeters and the trackers to the hadronic final state are shown in Fig. 5.3 for the final dijet sample where all selection cuts are applied. On the left are the different contributions to the transverse energy of the hadronic final state as a function of the total transverse energy. The contribution from the SPACAL is small (below 2%) and the contribution from the track measurement decreases from 30% to 8% towards larger $\sum E_T$. The right plot shows the same for the variable $y_{\rm had}$ as reconstructed by the Hadron Method according to (4.3). This variable is sensitive to the longitudinal energy flow of the hadronic final state, especially in the backward direction. Correspondingly the contribution of the SPACAL is slightly larger in this distribution (typically 4% and at most 6%). The track contribution is $\approx 20\%$, independently of $y_{\rm had}$. The fractional energy contributions from the different detector components are well modeled by the simulated events.

From (4.6) we expect that in a deep-inelastic scattering event the sum of all $(E - p_z)$ in the final state (including the scattered positron) should be equal to 55 GeV if all energy in

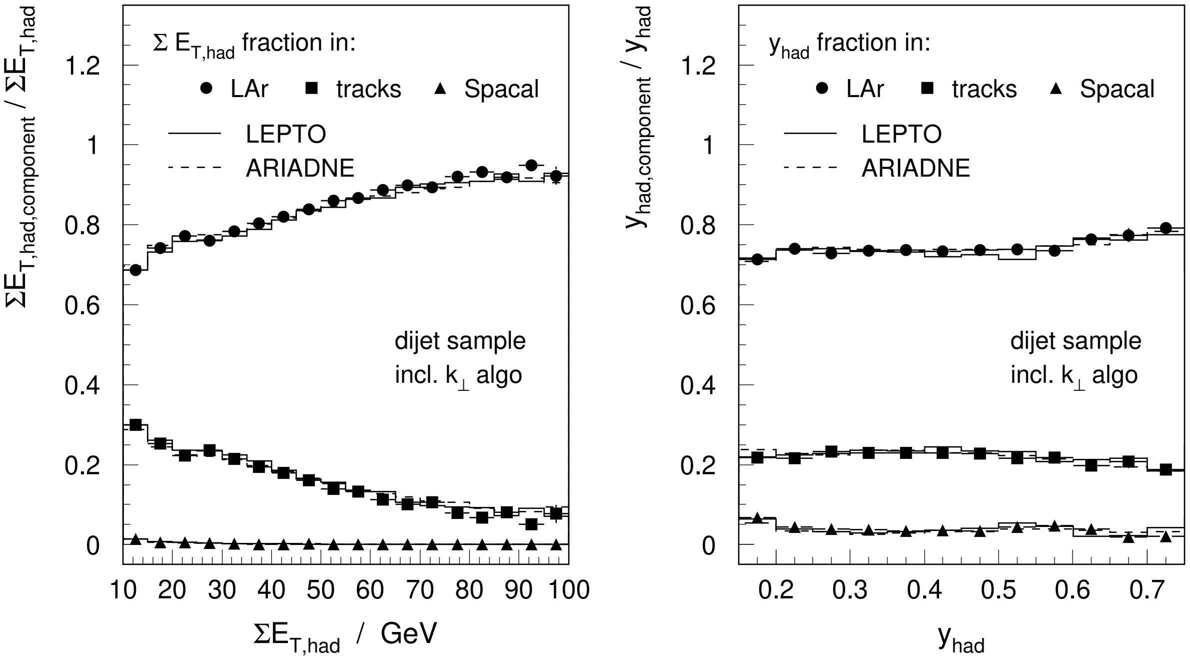

Figure 5.3: The fractional contributions from the single detector components to the reconstructed transverse energy of the hadronic final state (left) and to the reconstructed variable y_{had} in the dijet event sample (right).

the event is measured correctly. When particles in the event have escaped through the beam pipe in negative z-direction, the $\sum(E-p_z)$ is lowered by twice their energy. This is e.g. the case in photoproduction events where the positron is scattered at $\theta_e \to 180°$ and a particle from the hadronic final state is accepted as the positron candidate. In cases where photons are radiated collinear to the initial state positron, they also escape undetected through the beam pipe and the sum is reduced by twice the photon energy. We require $\sum(E-p_z)$ to be within ±10 GeV around its expectation value

$$45\,\mathrm{GeV} < \sum(E-p_z) < 65\,\mathrm{GeV}\,. \tag{5.5}$$

For perfectly measured events this corresponds to a cut against collinear radiated photons of energies $E_\gamma > 5\,\mathrm{GeV}$. The distribution of $\sum(E-p_z)$ is shown in Fig. 5.4 for the inclusive DIS sample (left) and for the dijet sample (right). In the dijet sample the distribution is peaked more sharply and, unlike in the inclusive DIS sample, the cut affects only small tails. Both the data and the simulated distributions are peaked at the nominal value of 55 GeV.

Having defined the hadronic final state, we can calculate the event kinematics using the Electron-Sigma Method, as introduced in (4.10), and apply the phase space cuts on the kinematic variables

$$0.2 < y_{e\Sigma} < 0.6 \qquad \text{and} \qquad 150 < Q^2_{e\Sigma} < 15\,000\,\mathrm{GeV}^2\,. \tag{5.6}$$

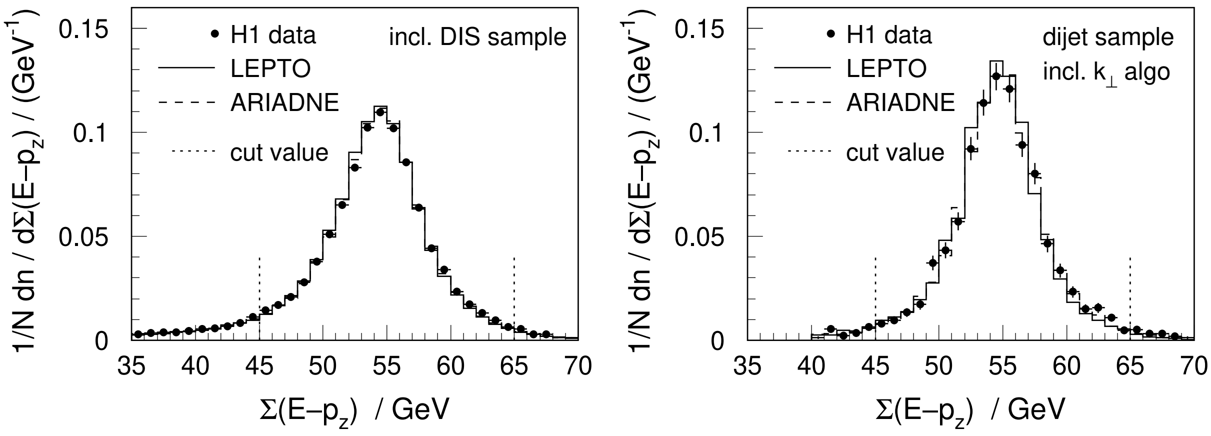

Figure 5.4: The distribution of $\sum(E - p_z)$ of the final state (including the positron) in the inclusive DIS sample (left) and in the dijet sample (right).

After all selection cuts are applied the event sample contains 30 617 deep-inelastic scattering events. The subsequent jet analyses are based on this event sample.

5.1.4 Jet Selection

In this analysis we measure the jet cross sections of four different processes: The inclusive jet cross section, the dijet, the three-jet and the four-jet cross section. Four different jet clustering algorithms are used. For the reasons discussed in chapter 3 the central analysis is performed with the inclusive $k_\perp$ jet algorithm. Therefore most of the studies presented here are shown for this choice (except in cases where the conclusions are different for the other jet algorithms).

As discussed in section 2.1 the clustering of the particles to jets is performed in the Breit frame which is defined by $2x_{\mathrm{Bj}}\vec{p} + \vec{q} = \vec{0}$. The event is rotated in the x-y plane of the Breit frame such that the scattered positron points in the positive x-direction (i.e. $\phi_{e,\,\mathrm{Breit}} = 0°$). To reconstruct the boost vector we need the kinematic variables x_{Bj} and Q^2, as well as the direction of $\vec{q}$. The latter is obtained from the azimuthal angle ϕ_e of the scattered positron in the laboratory frame and the variables x_{Bj} and Q^2 are reconstructed by the Electron-Sigma Method. In appendix A we show that using this reconstruction method the boost vector is less affected by radiative QED corrections than with the Electron Method.

Table 5.1 gives an overview on the parameters that define the jet phase space (described in more detail in section 2.4). These are specific for the single jet algorithms introduced in section 2.2. For all jet algorithms we apply the same cut on the pseudorapidity region in the laboratory frame within which jets are accepted. For this purpose the four-vectors of the jets are boosted from the Breit frame back to the laboratory frame where we demand

$$-1 < \eta_{\mathrm{jet,\,lab}} < 2.5 \tag{5.7}$$

	inclusive jet cross section		incl. dijet cross section
incl. $k_\perp$ algorithm	10 432 jets	(in 7 263 events)	2 855 dijet events
Aachen algorithm	10 097 jets	(in 7 065 events)	2 715 dijet events
excl. $k_\perp$ algorithm	—		2 771 dijet events
Cambridge algorithm	—		2 138 dijet events

incl. three-jet cross section	incl. $k_\perp$ algorithm	666 three-jet events
incl. four-jet cross section	incl. $k_\perp$ algorithm	84 four-jet events

Table 5.2: Statistics of the jet selection

for all jets. In addition to the cuts on the jets phase space listed in table 5.1 (which are applied in the Breit frame), we also require a minimum jet energy measured in the detector of

$$E_{\mathrm{jet,\,lab}} > 4\,\mathrm{GeV} \tag{5.8}$$

for experimental reasons. This cut affects only a few jets at high Q^2 (see Fig. 5.5) where (due to the larger transverse boost) the jet energies in the laboratory frame and in the Breit frame can be very different. According to the classification made above this cut is a "technical" cut which is corrected for.

For the inclusive jet cross section we count all jets in the event sample which pass the selection cuts. A single event may therefore give multiple contributions to the distributions. The dijet event sample consists of all events which have at least two jets that pass the selection cuts. For the three-jet (four-jet) event sample we require correspondingly events with at least three (four) accepted jets (we are measuring *inclusive* multi-jet cross sections).

The number of events finally obtained for the individual data samples (when all selection cuts are applied) are listed in table 5.2. In the inclusive jet sample many events contribute with more than one jet. 60.5% of the events in the sample for the inclusive $k_\perp$ algorithm have only a single jet, 35.6% have two jets, 3.5% have three jets and 0.4% have four jets (i.e. jets of $E_T > 7\,\mathrm{GeV}$ within the angular acceptance region).

5.2 The Inclusive Jet Sample

In the following sections we show distributions of the selected jet events. We give an overview of the basic properties of the jet samples and study how well the simulated events describe the data. In this section we investigate the inclusive jet sample. The dijet and the three-jet samples are discussed in the next sections.

5.2.1 Angular and Energy Distributions of Jets

The detector response to a hadronic jet is related to the primary observables: Energy and angle (or rather pseudorapidity) of the jet in the laboratory frame. Distributions of both

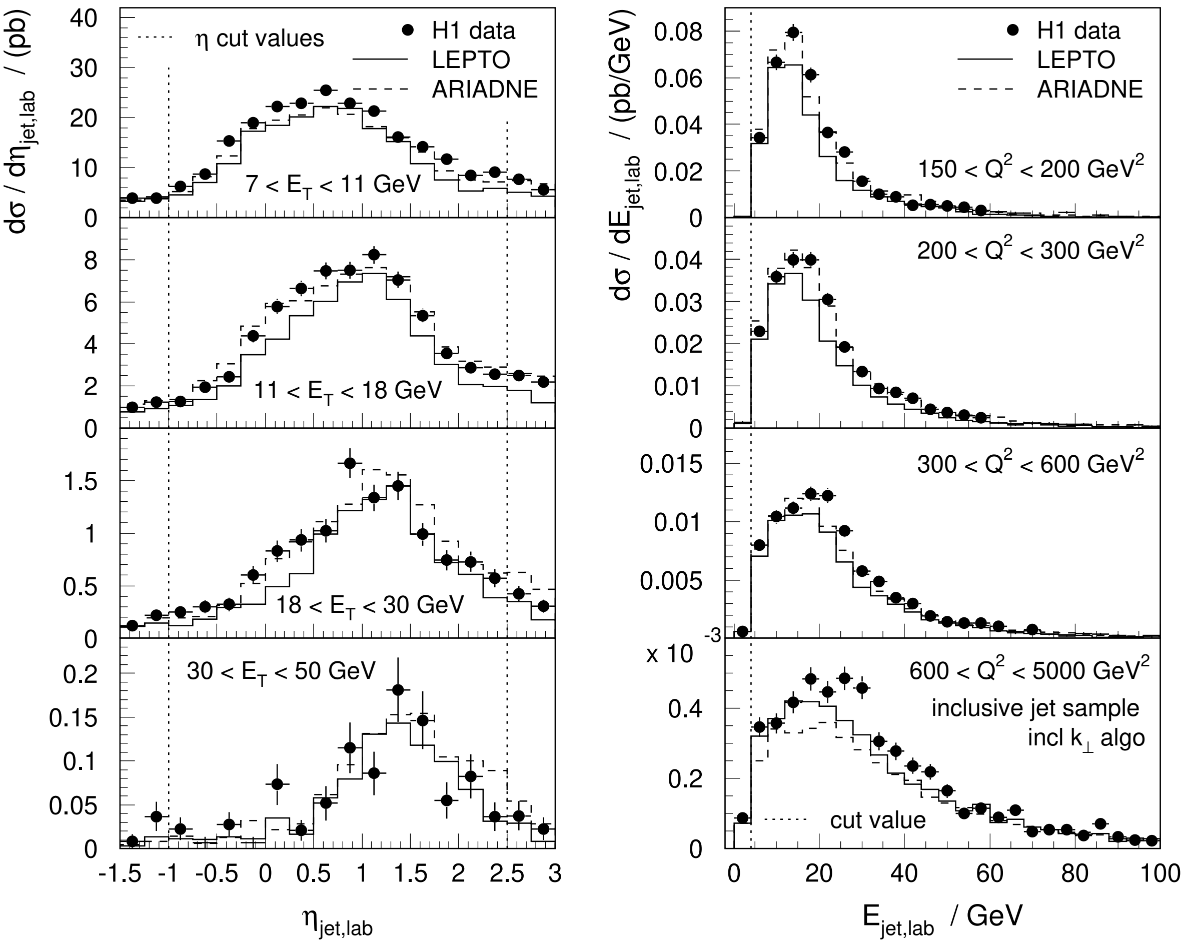

Figure 5.5: Angular and energy distributions of the inclusive jet sample in the laboratory frame, measured with the inclusive $k_\perp$ algorithm.

quantities are shown in Fig. 5.5 for the inclusive jet sample. The pseudorapidity distribution (left) is shown in different regions of the transverse jet energy in the Breit frame E_T. The E_T regions correspond to the bins in which the cross section is measured. Towards higher E_T the pseudorapidity distribution is slightly shifted to the forward direction. In all E_T regions the bulk of the data are in the central part of the angular acceptance region and the cuts on the pseudorapidity only affect the tails of the distribution. The measured energy distribution of the jets (right) is shown in different regions of Q^2. At large Q^2 we observe a spectrum of higher jet energies. ARIADNE is very close to the data at smaller Q^2, but shows deviations at high Q^2. The simulated events give a good description of the shape of the pseudorapidity distribution, also outside the analysis range.

The distributions of the jet pseudorapidities and the transverse jet energies in the Breit frame (where the jets are recombined) are shown in Fig. 5.6. We observe a shift in the jet pseudorapidity spectrum in the Breit frame (left) in the proton direction at larger E_T. The transverse jet energies (right) are shown in different Q^2 regions for the final E_T bins and

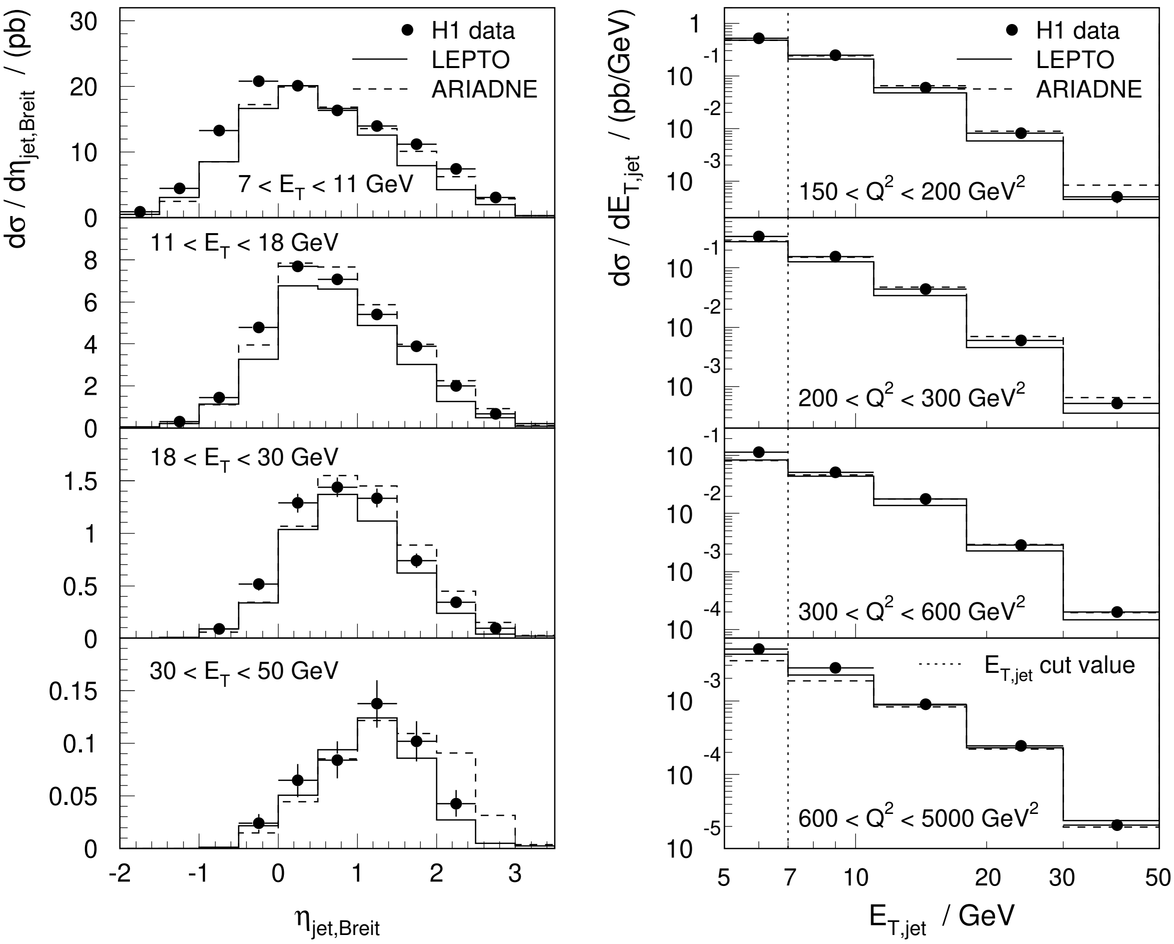

Figure 5.6: Angular and transverse energy distributions of the inclusive jet sample in the Breit frame, measured with the inclusive $k_\perp$ algorithm.

an additional bin extending down to $E_T = 5\,\text{GeV}$. Both distributions are reasonably well described by the simulation.

5.2.2 Internal Jet Structure

Two observables, related to the internal structure of jets, have been defined in section 2.4.2 and are studied here for the inclusive jet sample. The jet shape $\psi(r)$, which is the fractional transverse jet energy inside a cone of radius r around the jet axis, is shown as a function of r in Fig. 5.7 (top) in different regions of E_T. The curvature of $\psi(r)$ as a function of r is strongly dependent on E_T. At fixed r the value of $\psi(r)$ increases with rising E_T, i.e. the jets become more collimated.

The average number of subjets $\langle N_{\text{subjet}}(y_{\text{cut}})\rangle$ within a jet is shown in Fig. 5.7 (bottom) as a function of the subjet resolution parameter y_{cut}. The value of y_{cut} specifies at which relative squared transverse momentum structures within a jet are resolved. Within a given

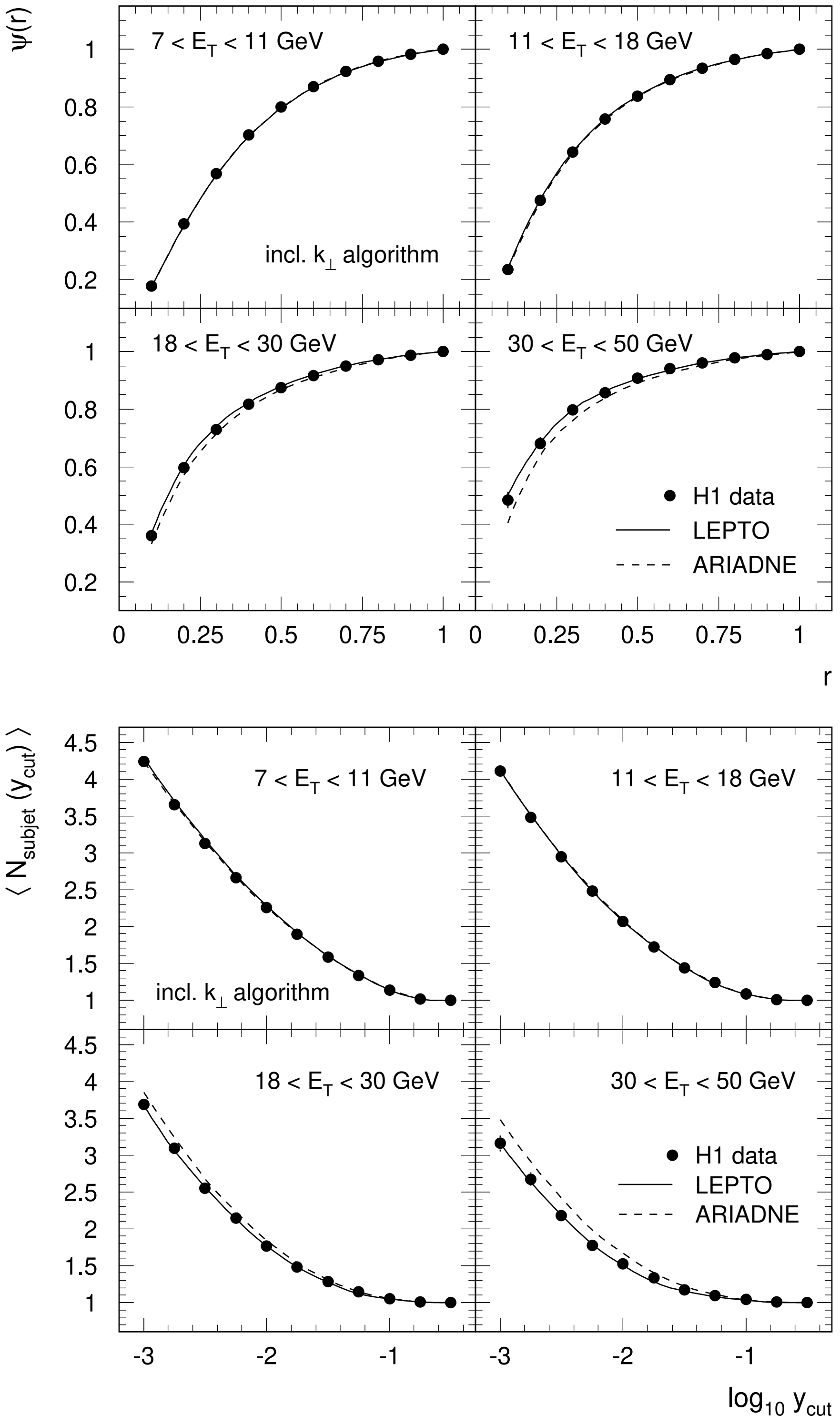

Figure 5.7: Jet shapes (top) and subjet multiplicities (bottom), measured with the inclusive $k_\perp$ algorithm in different E_T regions in the Breit frame.

E_T range the subjet multiplicity increases towards smaller y_{cut}. For a fixed value of y_{cut} we observe a decrease of $\langle N_{\mathrm{subjet}}(y_{\mathrm{cut}})\rangle$ towards larger E_T, indicating more collimated jets. Although the subjet multiplicities are sensitive to a different aspect of the jet broadening than the jet shapes, the findings are the same for both.

While the basic E_T dependence is reproduced by both models, LEPTO and ARIADNE, the latter shows a too fast decrease of the jet width with E_T, leading to a worse description of the high E_T data. LEPTO gives a good description of the data over the whole E_T range.

5.3 The Dijet Sample

In this section we study properties of dijet events. Starting from kinematic variables, jet angles and energies, we put the main focus on distributions that characterize the dijet system itself or its properties relative to the total hadronic final state.

5.3.1 Distributions of the Event Kinematics

The differential cross section in dependence of y and Q^2 is shown in Fig. 5.8 for the dijet samples of both $k_\perp$ algorithms. For comparison the y distribution is also shown for the inclusive DIS sample. Within the range $0.2 < y < 0.6$ used in the analysis we see a similar shape for both jet algorithms which is also similar to the shape of the inclusive DIS sample. Only at values of $y < 0.25$ the behavior is different. While the spectrum for the exclusive algorithm keeps rising towards small y as does the inclusive DIS cross section, the y distribution for the inclusive algorithm decreases again. This effect is connected to the different selection criteria of both jet definitions and is modeled by the simulation.

The distributions on the right side show the dijet cross sections as a function of Q^2. We observe a decrease of nearly four orders of magnitude over the range $150 < Q^2 < 15\,000\,\mathrm{GeV}^2$. Neither model can describe this shape. LEPTO shows a smaller Q^2 dependence and describes the absolute cross section only at high Q^2, ARIADNE gives a better description of the lower Q^2 range, but falls off too fast towards higher Q^2. The data lie always between both models.

In Fig. 5.8 we have compared the absolute model predictions of the cross sections to the data. In the following we will only compare distributions normalized to the number of events which enter the distribution, such that we can test whether the simulated events are able to describe the shapes.

5.3.2 Angular and Energy Distributions of Jets

In Fig. 5.9 the pseudorapidity distributions of the jets are shown in the laboratory frame (top) and in the Breit frame (bottom) for the backward (left) and for the forward jet (right). As in the case of the inclusive jet distributions, the dijet pseudorapidity distributions in the laboratory frame have already fallen off where the angular acceptance cuts are applied.

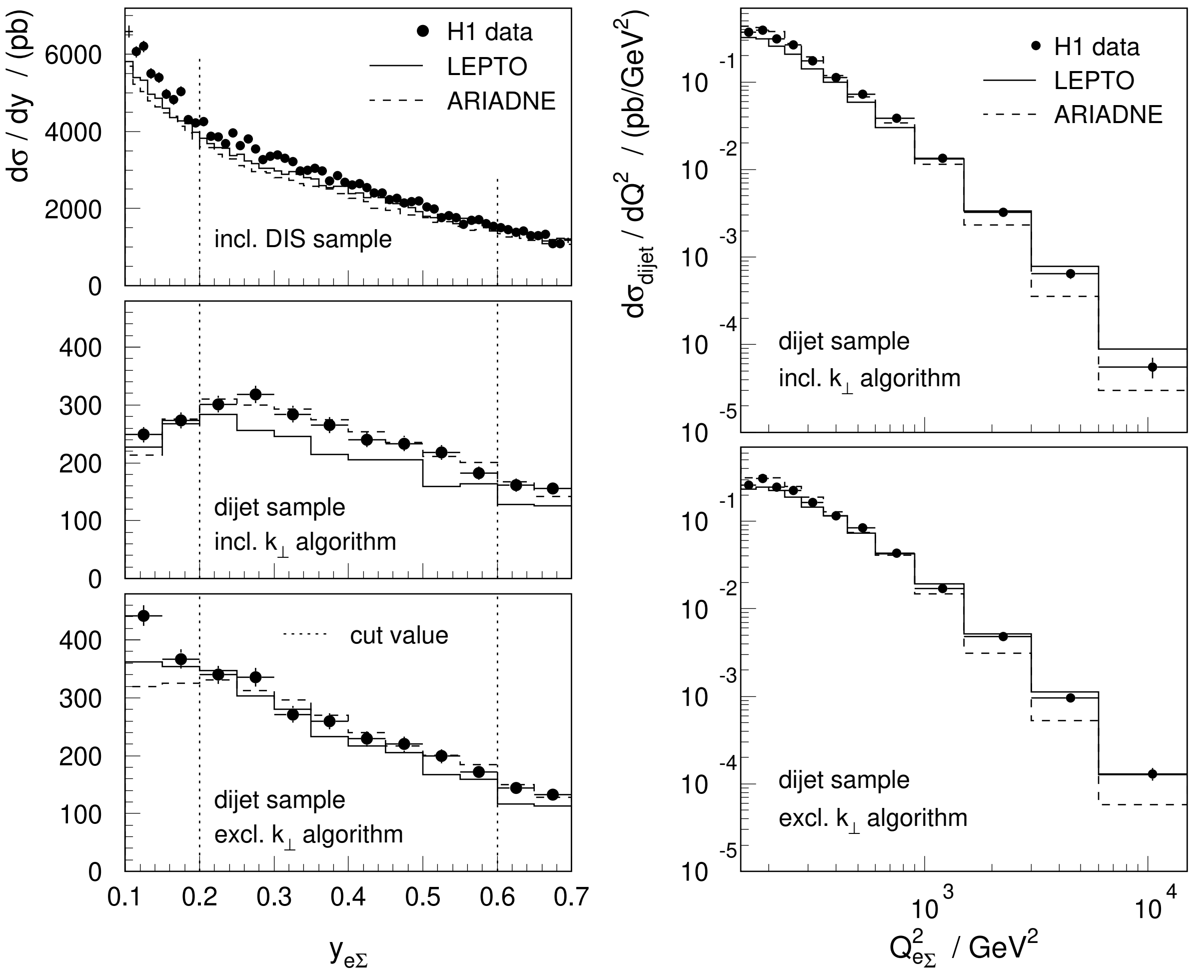

Figure 5.8: Distributions of the kinematic variables y and Q^2 in the dijet sample for both $k_\perp$ ordered jet algorithms. The y distribution is also shown for the inclusive DIS sample.

The simulations describe both distributions reasonably well. The same is true for the distributions in the Breit frame. Here we see that most of the jets are produced at positive pseudorapidities, i.e. in the so-called “target hemisphere” of the Breit frame.

The energy distributions of the jets as measured in the laboratory frame are shown separately for the jet of lowest (highest) energy in the left (right) plot in the top of Fig. 5.10. The less energetic jet has typically an energy of more than 10 GeV, the higher energetic jet more than 20 GeV.

The lower part of Fig. 5.10 displays the transverse energy spectrum of the lower E_T jet in the Breit frame (left) and the invariant dijet mass distribution (right). It is seen that the transverse jet energy cut $E_T > 5\,\mathrm{GeV}$ has only a small effect after the hard cut $E_{T,1}+E_{T,2} > 17\,\mathrm{GeV}$ is applied. The dijet mass spectrum covers a range $15 \lesssim M_{\mathrm{jj}} \lesssim 100\,\mathrm{GeV}$ and is well described by LEPTO and ARIADNE. The same holds for the other distributions. Only at lower jet energies in the laboratory frame a small deviation between the data and

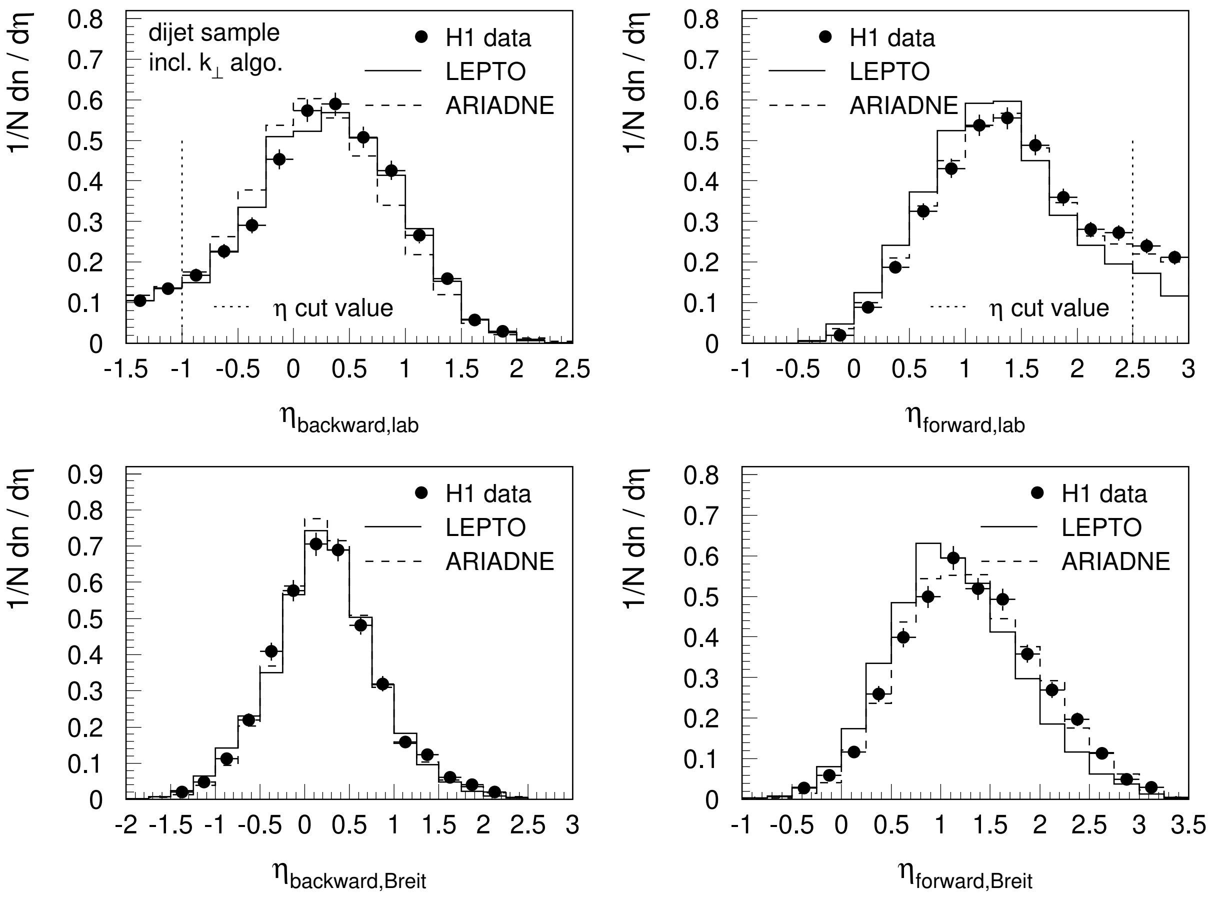

Figure 5.9: Angular jet distributions in the dijet event sample for the inclusive $k_\perp$ algorithm. Shown are the jet pseudorapidities in the laboratory frame (top) and in the Breit frame (bottom) for the backward (left) and the forward jet (right).

the simulation is seen.

5.3.3 Dijet Variables

While inclusive jet production is fully described by the angles and the transverse jet energies, dijet production is characterized by additional variables, connected to the properties of the dijet system. In the leading order picture the variable ξ (as introduced in section 2.4) represents the proton momentum fraction carried by the struck parton. To obtain an optimized reconstruction of ξ we rewrite the formula as

$$\xi \;\equiv\; x_{\rm Bj}\,(1+\frac{M_{jj}^2}{Q^2}) \;=\; x_{\rm Bj}+\frac{M_{jj}^2}{y\,s}\,. \tag{5.9}$$

We use the right hand expression to reconstruct ξ and take $x_{\rm Bj}$ as usual from the Electron-Sigma Method. For the reconstruction of the variable y we use the Hadron Method. Although

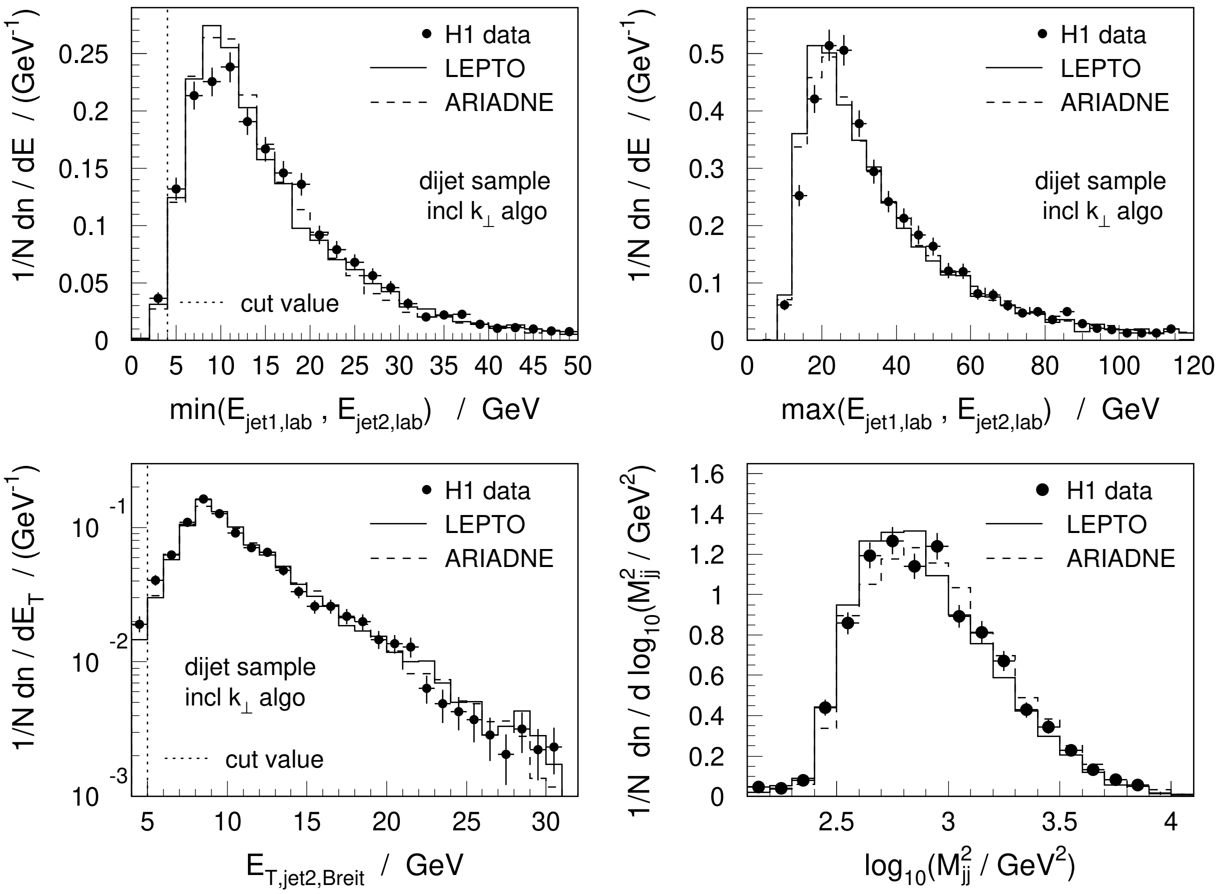

Figure 5.10: Distributions of jet energies in the dijet sample for the inclusive $k_\perp$ algorithm. Shown are the jet energies in the laboratory frame (top), the transverse energy of the lower E_T jet in the Breit frame (bottom, left) and the invariant dijet mass spectrum (bottom, right).

the variable y_{had} itself is less well reconstructed, the mismeasurement in y_{had} cancels partially with those in the hadronic energies from which the invariant dijet mass is derived. The variables ξ and x_p (see section 2.4) are then reconstructed according to

$$\xi_{\mathrm{reco}} = x_{e\Sigma} + \frac{M_{jj}^2}{y_{\mathrm{had}}\, s}, \qquad x_p = \frac{x_{e\Sigma}}{\xi_{\mathrm{reco}}}. \tag{5.10}$$

The distributions of both variables are shown in the top row of Fig. 5.11. The ξ range covers parton momentum fractions between $10^{-2} \lesssim \xi \lesssim 3\cdot 10^{-1}$. The ξ distribution is well described by LEPTO and ARIADNE but both models show some discrepancies in the distribution of x_p. While LEPTO's spectrum is slightly shifted towards larger x_p, ARIADNE is shifted to smaller values. The data curve lies between both model predictions.

The bottom row of Fig. 5.11 shows the distributions of η' and η_{Boost}. According to the definitions in section 2.4 these variables are reconstructed from the difference and the sum of

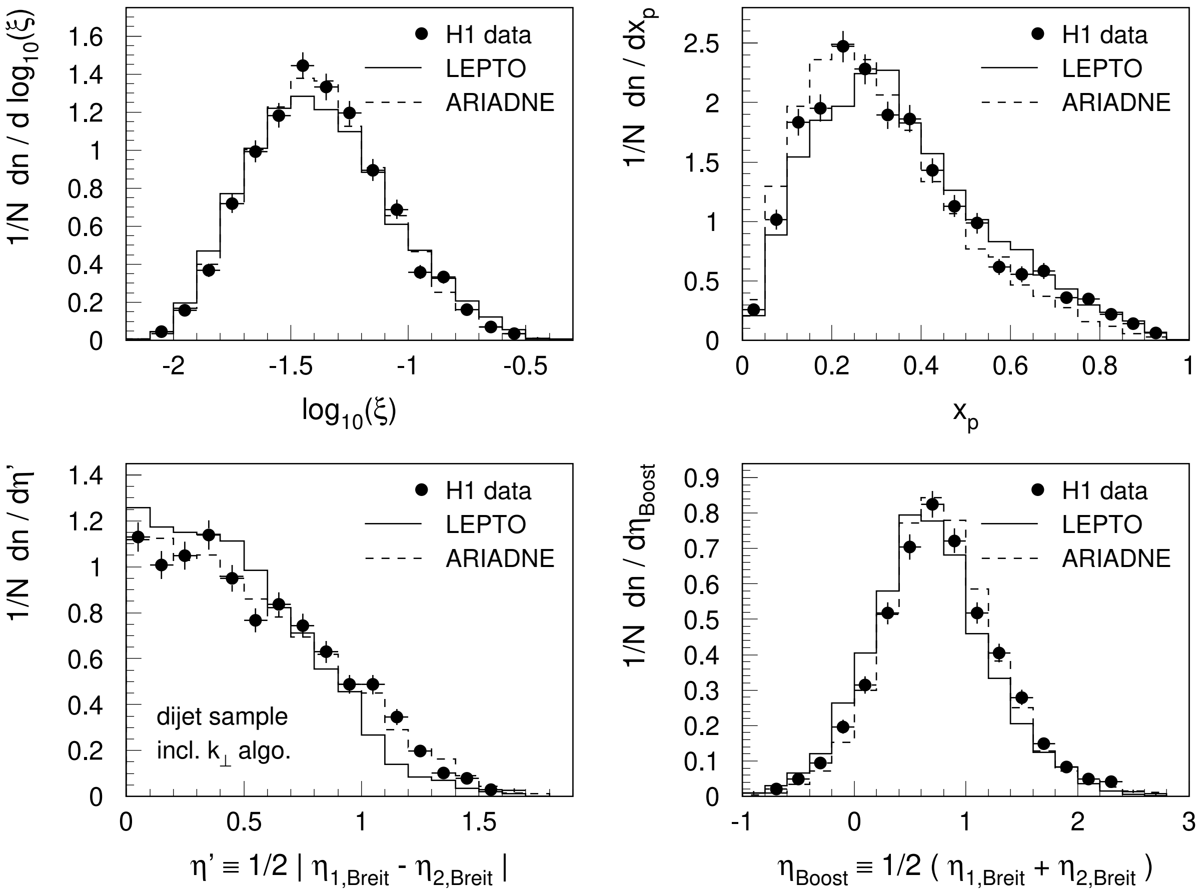

Figure 5.11: Distributions of the dijet variables ξ, x_p, η' and η_{Boost} for the inclusive $k_\perp$ algorithm.

the jet pseudorapidities in the Breit frame. They characterize respectively the jet pseudorapidity in the dijet center-of-mass frame (η') and the pseudorapidity difference corresponding to the longitudinal boost from the dijet center-of-mass frame to the Breit frame (η_{Boost}).

The distribution of the jet pseudorapidities in the dijet center-of-mass frame η' is limited to values $\eta' \lesssim 1.8$ (an effect of the hard transverse jet energy cuts). The distribution of η_{Boost} is approximately symmetrically distributed around a center value of $\langle \eta_{\mathrm{Boost}} \rangle \simeq 0.7$, i.e. the Breit frame is on average shifted by $\Delta\eta = 0.7$ relative to the dijet center-of-mass frame. Both distributions are reasonably well described by the simulated events.

In the leading order picture, pairs of jets are produced back-to-back in the x-y plane of the Breit frame ($\Delta\phi_{\mathrm{jet,jet}} = 180°$) and with equal transverse energies ($\Delta E_T = 0$). This picture is modified when higher order corrections are considered.

Further changes may be introduced by errors in the measurement leading e.g. to an increase of the E_T imbalance. In the top row of Fig. 5.12 distributions of both ΔE_T (left) and $\Delta\phi$ (right) are shown. The difference in the transverse jet energies is normalized to the transverse jet energy of the highest E_T jet.

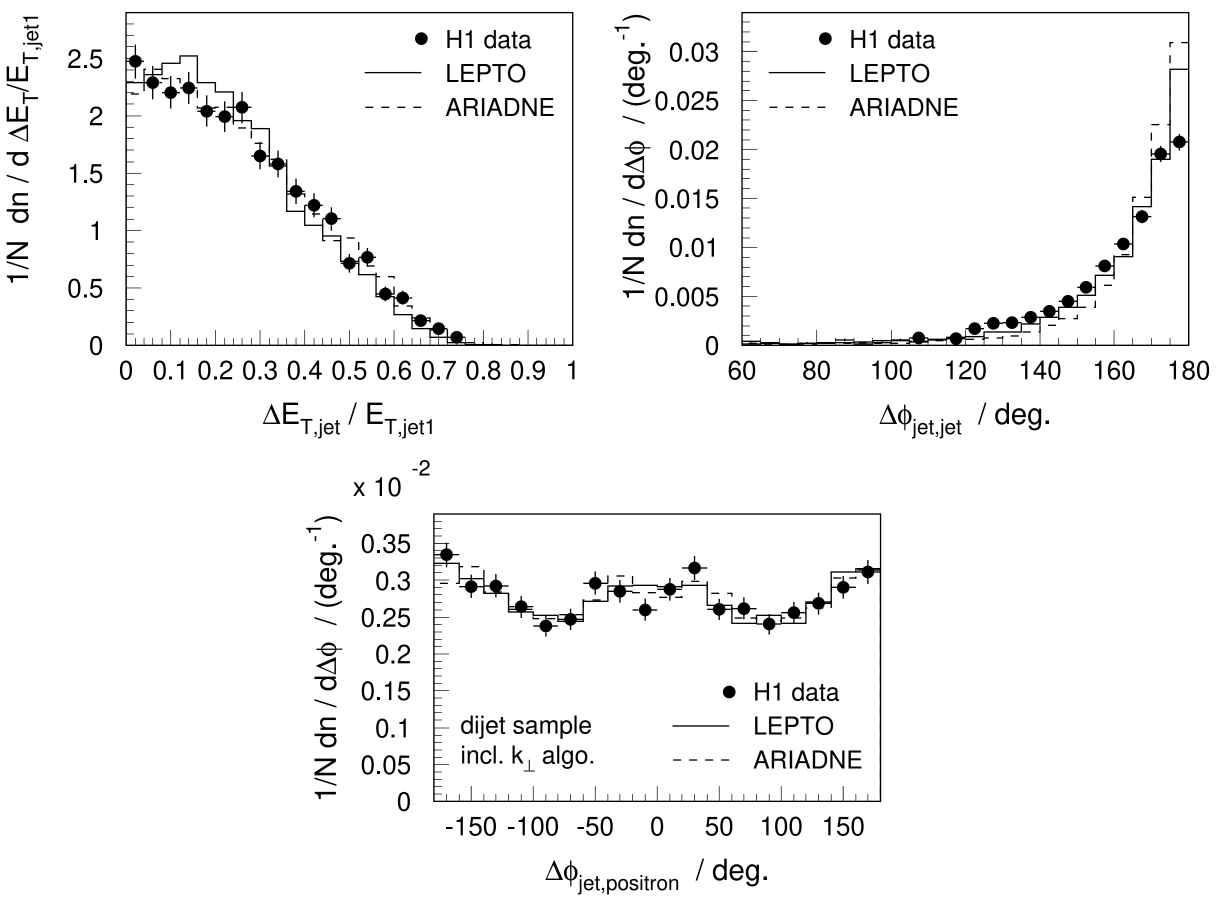

Figure 5.12: Distributions of the imbalance of the transverse jet energies, the difference in the jet azimuthal angles and the azimuthal angle between the jets and the scattered positron in the Breit frame.

The normalized transverse jet energy imbalance is on average 0.25 and is well described by both Monte Carlo simulations. The difference in the azimuthal jet angles shows a peak at $\Delta\phi = 180^\circ$ and a strong decrease towards smaller values. The simulated events give only a poor description of this distribution. They overestimate the peak and, consequently, underestimate the tail.

A further quantity that we study here is the azimuthal angle between the scattered positron and the jets in the Breit frame (both jets in the event enter this distribution). Although the leading order matrix elements predict a certain modulation of this distribution, the observed variation is more connected to the restricted jet pseudorapidity acceptance in the laboratory frame [95]. The modulation is well described by both Monte Carlo simulations.

Dijet production in deep-inelastic scattering involves multiple hard scales. On one hand there are scales that characterize the two-jet final state, as the average transverse energy of the two jets $\overline{E}_T$ in the Breit frame or the invariant mass of the dijet system M_{jj}. On the other hand there is the virtuality of the exchanged photon Q^2. In Fig. 5.13 we show distributions

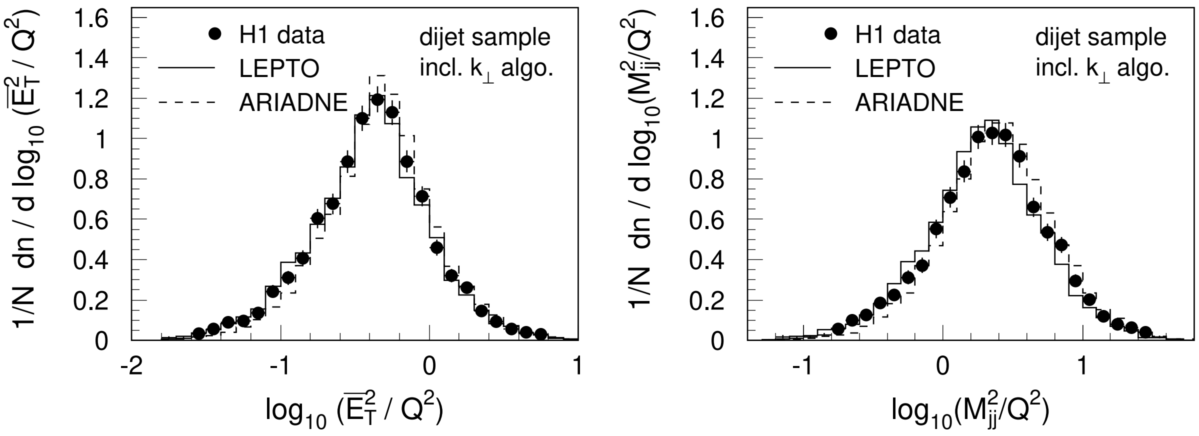

Figure 5.13: Ratios of process relevant hard scales in dijet production.

of the ratios of these scales. Both distributions are well described by the simulated events.

5.3.4 The Dijet System and the Hadronic Final State

Our last investigations on the dijet event samples concern dimensionless variables that relate the jet energies to the total energy of the hadronic final state.

The variable x_γ measures the fractional longitudinal energy in the backward direction contained in the jets. It is defined as the ratio of the $(E-p_z)_{\text{dijets}}$ carried by the dijet system and the $\sum(E-p_z)_{\text{had}}$ carried by the total hadronic final state[1]

$$x_\gamma \equiv \frac{(E-p_z)_{\text{dijets}}}{\sum(E-p_z)_{\text{had}}}\,. \tag{5.11}$$

The x_γ distribution is shown for both $k_\perp$ algorithms in Fig. 5.14. One sees clearly the differences arising from the inclusive and the exclusive clustering procedures. The exclusive $k_\perp$ algorithm assigns each particle in the event either to one of the hard jets or to the proton remnant. Particles in the backward region are usually closer to the hard jets and are therefore mostly included in the multi-jet system. Hence they give no contribution to the backward energy flow outside the jets and the x_γ distribution for the exclusive $k_\perp$ algorithm is sharply peaked at $x_\gamma = 1$ (Fig. 5.14, right).

In the inclusive jet definitions particles may be preclustered to “protojets” which are later not clustered to the two highest E_T jets. These particles (and especially those in the backward region) produce a tail in the measured x_γ distribution, as seen in Fig. 5.14 (left). The x_γ distribution for the inclusive $k_\perp$ algorithm is peaked at $x_\gamma \simeq 0.9$ and has a much larger tail towards smaller x_γ.

---

[1] In photoproduction events (at $Q^2 \simeq 0\,\text{GeV}^2$) the variable x_γ is sensitive to the energy of the photon remnant and can therefore be directly related to the energy fraction of the quasi real photon that enters the hard process.

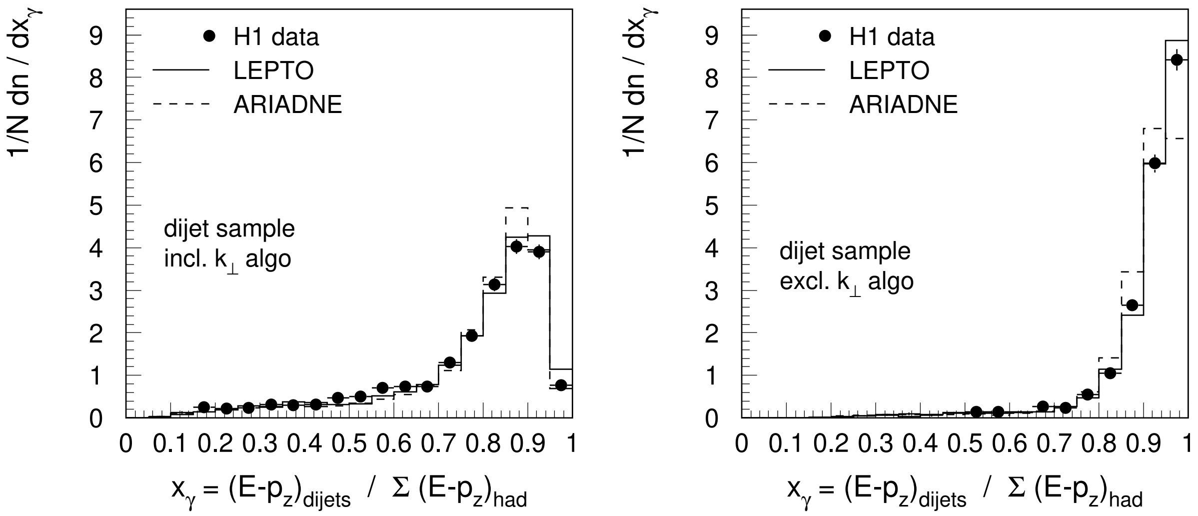

Figure 5.14: Distribution of the variable x_γ which is defined as the fractional $\sum(E - p_z)$ of the hadronic final state carried by the dijet system.

Two further variables h_1 and h_2 are defined as the fraction of the total transverse energy in the Breit frame carried by respectively the leading jet or the dijet system. They are defined as

$$h_1 \equiv \frac{E_{T,1}}{\sum E_{T,\,\mathrm{Breit}}} \qquad \text{and} \qquad h_2 \equiv \frac{E_{T,1} + E_{T,2}}{\sum E_{T,\,\mathrm{Breit}}} \,. \tag{5.12}$$

In Fig. 5.15 the differential distributions of h_1 (top) and h_2 (middle) are presented for the inclusive (left) and for the exclusive $k_\perp$ algorithm (right). For both algorithms similar distributions are observed. The highest E_T jet contains on average 42% of the transverse energy in the Breit frame, while the dijet system contains on average more than 70%.

The average values $\langle h_1 \rangle$ and $\langle h_2 \rangle$ are displayed as a function of the total hadronic final state energy in the range of $15 < \sum E_{T,\,\mathrm{Breit}} < 100\,\mathrm{GeV}$ in Fig. 5.15 (bottom). For both algorithms only small dependences are seen[2].

The simulated events from both generators are able to describe qualitatively the features of all distributions, including the dependence of the x_γ spectrum on the jet definition. LEPTO gives a good quantitative description of the amount of energy outside the jets. ARIADNE predicts slightly more energy outside the jets, in the backward region (showing as a shift in the x_γ spectrum) and also for the transverse component (showing as a shift in the $h_{1,2}$ spectra).

---

[2] The increased averages at small $\sum E_{T,\,\mathrm{Breit}}$ for the inclusive $k_\perp$ algorithm are only a phase space effect. The requirement $E_{T,1} + E_{T,2} > 17\,\mathrm{GeV}$ restricts e.g. h_1 to a value of one if $\sum E_{T,\,\mathrm{Breit}} \simeq 17\,\mathrm{GeV}$.

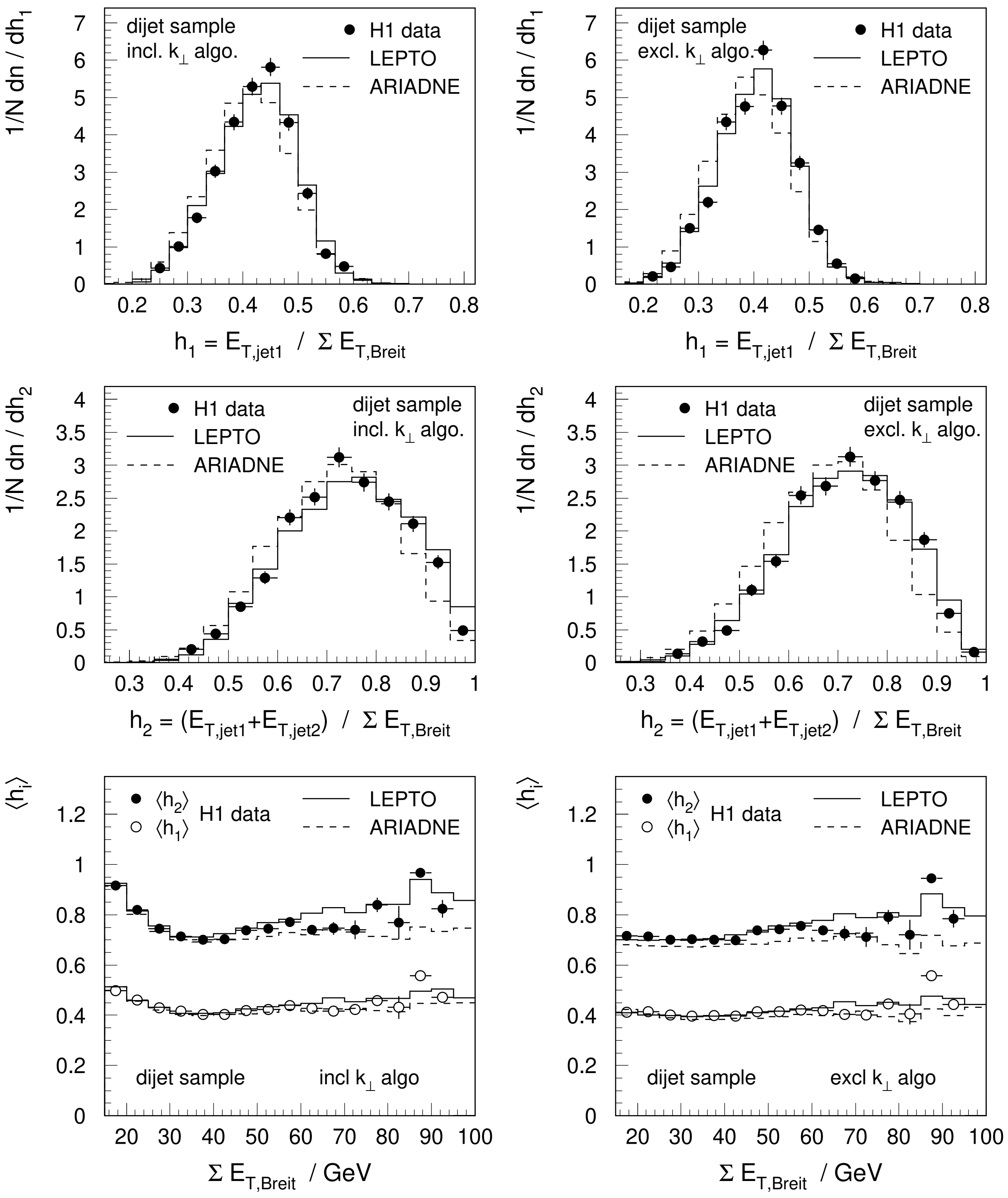

Figure 5.15: Distributions of the fractional transverse energy of the hadronic final state in the Breit frame carried by the jets, for the inclusive (left) and for the exclusive $k_\perp$ algorithm (right). Shown is the fractional contribution of the first jet h_1 (top) and the fractional contribution of both jets h_2 (middle). The bottom plots show the average values of h_1 and h_2 as a function of the total transverse energy of the hadronic final state in the Breit frame.

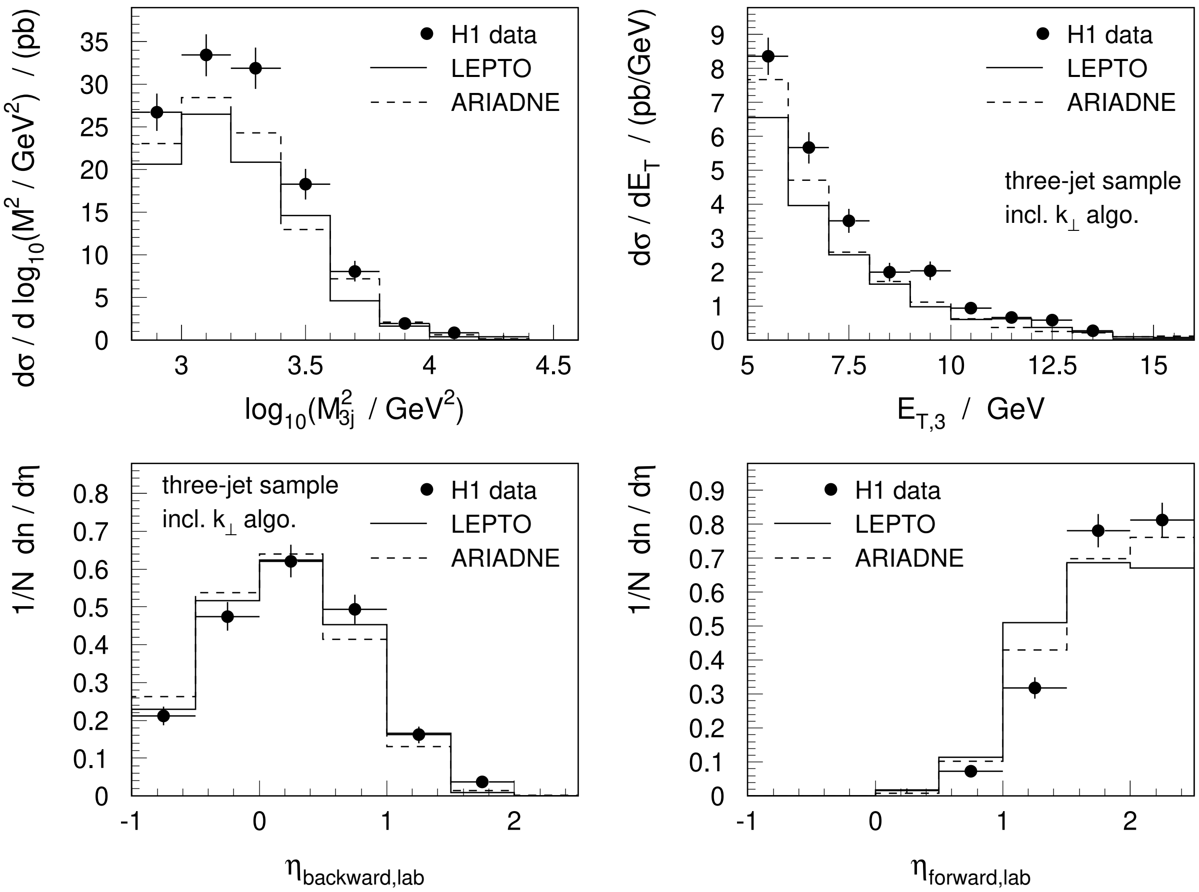

Figure 5.16: Distributions of three-jet events. Shown are the three-jet cross sections (top) as a function of the invariant three-jet mass M_{3j} (left) and the transverse energy of the third jet $E_{T,3}$ in the Breit frame (right). The bottom plots show the normalized pseudorapidity spectra of the most backward (left) and the most forward jet (right) in the laboratory frame.

5.4 The Three-Jet Sample

Finally we take a brief look at distributions of three-jet events. A detailed analysis of three- and four-jet production has been performed in collaboration with A. Heister and is documented in his Diploma thesis [96]. Here we will only show selected distributions.

In the upper plots of Fig. 5.16 the three-jet cross section is shown as a function of the invariant mass of the three-jet system M_{3j} (left) and of the transverse energy of the third jet $E_{T,3}$ in the Breit frame (right). The simulated events give a good description of the shapes of these distributions, but they fail to describe the absolute production rate by approximately 20%. Since the LEPTO prediction for the dijet cross section is also slightly below the data (Fig. 5.8) the fractional contribution of three-jet events to the dijet sample is still well described (Fig. 3.13 in [96]).

The normalized pseudorapidity spectra of the most backward (forward) jet in the laboratory frame are shown in the left (right) plot in the bottom of Fig. 5.16. These distributions are also well described by the simulated events.

Both models LEPTO and ARIADNE only include the QCD matrix elements of $\mathcal{O}(\alpha_s)$. The production of a third jet originates therefore only in the parton cascade (i.e. the parton shower in LEPTO and the dipole cascade in ARIADNE). Since these parton cascades are based on soft and collinear approximations it is an interesting observation that both give such a good description of the three-jet cross section, even at large three-jet masses and high transverse energies of the third jet.

5.5 The Calibration of the Hadronic Energy Scale

The experimental uncertainties in the measurement of the positron energy and the scattering angle have been determined for the measurement of the inclusive neutral current cross section [32]. Details on the procedure can be found in [81]. While these results can directly be applied in the present analysis, this is not the case for the hadronic energy calibration. In this section we estimate this uncertainty.

The calibration of the hadronic energy scale has been performed by comparing the transverse momentum of the precisely calibrated positron to that of the hadronic system in the inclusive neutral current event sample [81]. Calibration constants have been determined for each electromagnetic and hadronic wheel using the ratio of the transverse momenta of the hadronic system and the scattered positron. The final calibration is obtained by applying an additional overall correction factor depending on the transverse momentum $p_{T,\,\mathrm{had}}$ of the hadronic final state and the angle γ (as defined in (4.5)). Using this calibration procedure, the uncertainty in the hadronic energy measurement is quoted to be 2% [32]. This value is obtained from the quadratic sum of an uncorrelated uncertainty of 1.7% and a correlated uncertainty of 1%, originating from the calibration method and from the uncertainty of the reference scale, given by the positron energy.

For the present jet analyses we apply the same (wheel dependent) correction as in the inclusive analysis. The $p_{T,\,\mathrm{had}}$ dependent correction is not applied, since in a multi-jet sample the angle γ does not represent the direction of the actual energy flow in the detector and in addition the total transverse momentum can be very different from the local transverse momenta of the single jets.

We study here the quality of the calibration (without the $p_{T,\,\mathrm{had}}$ dependent part) to estimate the uncertainty induced in the present analysis. For this purpose we use the kinematics of the scattered positron for comparisons to the hadronic final state properties. In Fig. 5.17 we compare the transverse momenta p_T (top) and the variable y (bottom), as reconstructed respectively from the hadronic final state and from the positron, for the inclusive event sample (left) and for the dijet sample (right). The distributions of both ratios are peaked closely to the value of one, and the simulations give a good description of all distributions.

To look into further detail, we study these ratios for the dijet sample as a function

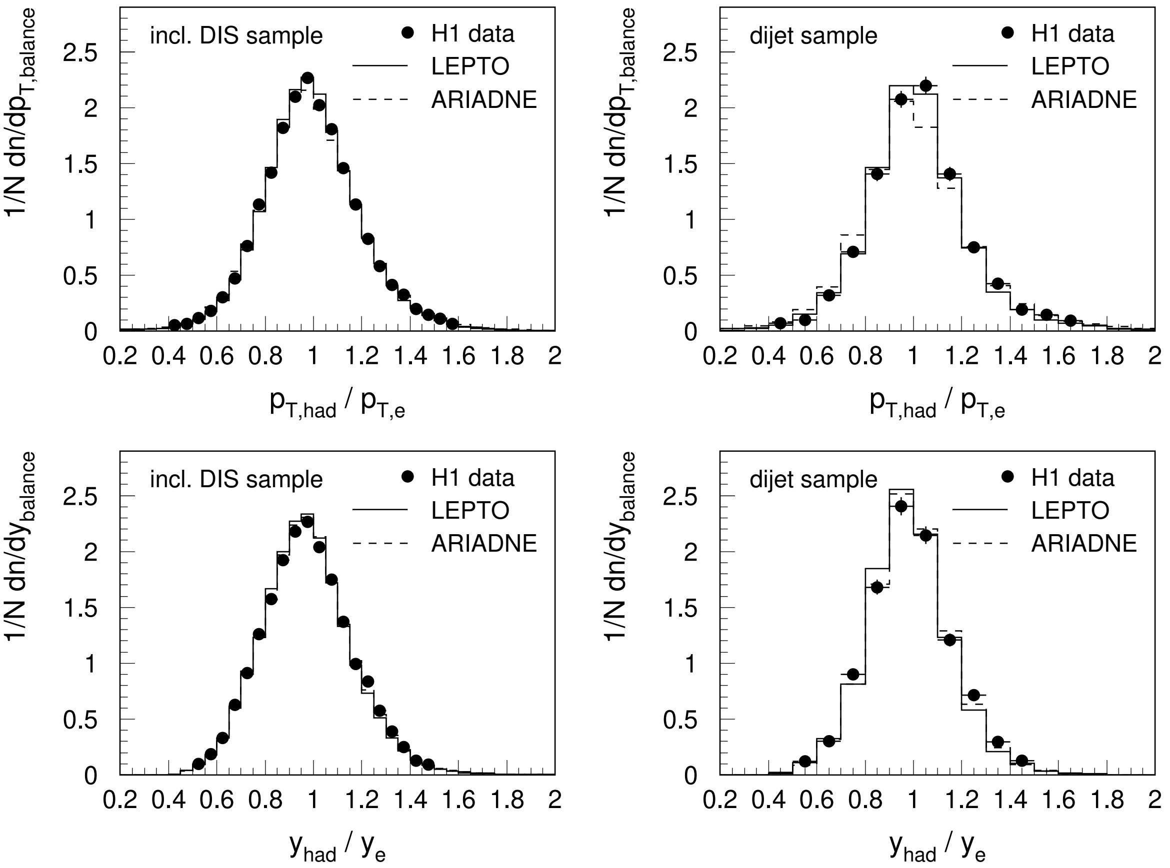

Figure 5.17: The distributions of the p_T-balance (top) and the y-balance (bottom) between the positron and the hadronic final state for the inclusive event sample (left) and for the dijet event sample (right) as measured using the inclusive $k_\perp$ algorithm.

of the angle of the hadronic energy in the detector. For the inclusive event sample such comparisons are usually performed as a function of the angle γ which indicates the direction of the hadronic energy flow in the calorimeter. In a multi-jet sample, however, the angle γ has no direct interpretation. The standard procedure is here adapted to the multi-jet analysis, by using a subsample of the dijet events in which both jets lie approximately in the same pseudorapidity region in the detector (namely within $\Delta\eta_{\mathrm{dijet,\,lab}} < 1$). In this subsample the average pseudorapidity $\overline{\eta}_{\mathrm{dijet,\,lab}}$ of both jets is a good representation of the direction of the energy flow in the event.

In Fig. 5.18 (left) we show the average values of the p_T-balance (top) and the y-balance (bottom) as a function of $\overline{\eta}_{\mathrm{dijet,\,lab}}$. Both average values are always in the range of $+5\%$ and -4% and decreasing slightly with $\overline{\eta}_{\mathrm{dijet,\,lab}}$. To make the relative deviation between the simulation and data visible we have displayed the corresponding ratios of data over Monte Carlo simulation on the right side. The agreement is better than 2% over the whole range. The leftmost and the rightmost bins have limited significance due to their large statistical

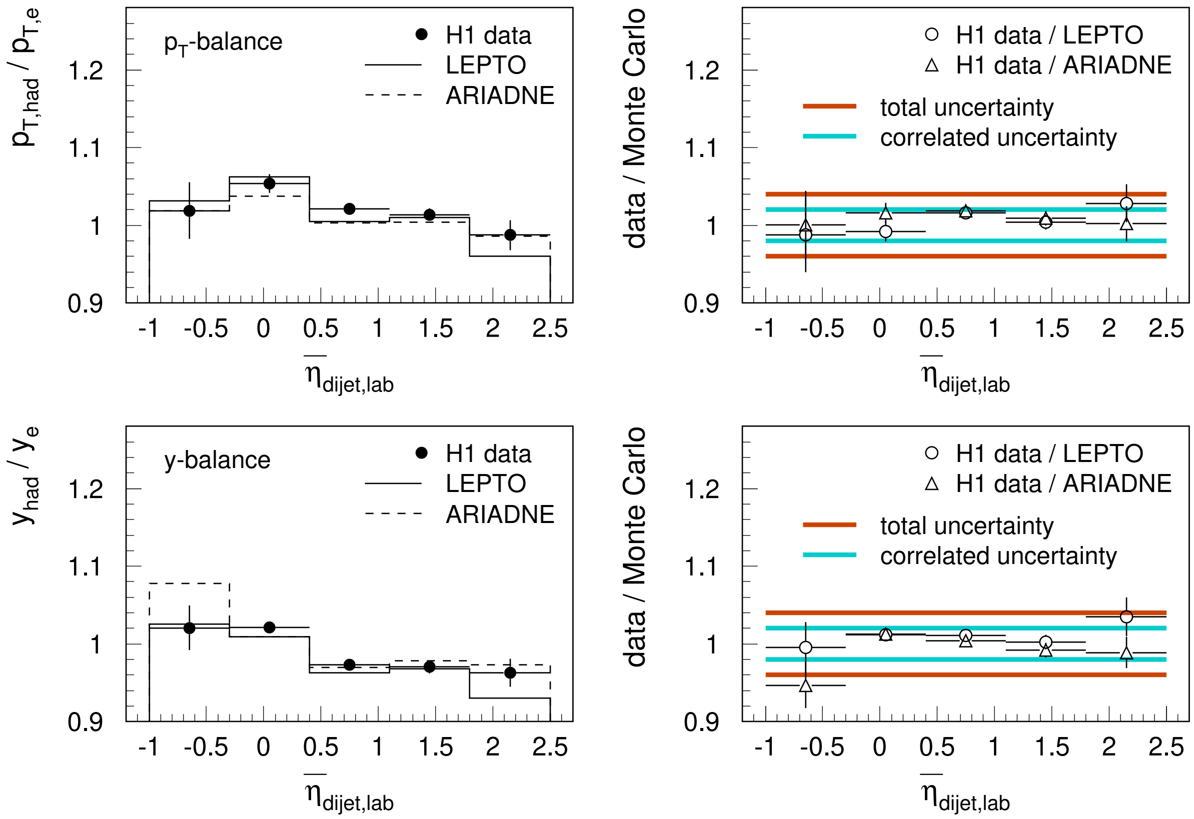

Figure 5.18: Hadronic final state calibration studies for a subset of the dijet sample where $\Delta\eta_{\mathrm{jet,lab}} < 1$. Shown is the p_T-balance (top) and the y-balance (bottom) as a function of the average pseudorapidity of the dijet system (left) and the ratio of the data and the simulation (right).

errors (the amount of events with two very forward or backward jets is small). In some cases these ratios are, however, close to the value of 2%, such that a quoted value of 2% might underestimate the true uncertainty. We therefore decide to quote a larger uncertainty of 4% of which 2% are considered as correlated and 3.4% as uncorrelated (such that the quadratic sum is equal to 4%). This should be a conservative estimate of the uncertainty of the present hadronic energy calibration.

5.6 Photoproduction Background

Background from photoproduction events (where the scattered positron is not detected in the detector) may contribute to the measured jet event samples when a hadronic final state particle is misidentified as a positron candidate and further hadronic activity passes the jet selection criteria. The size of this background has been estimated using events simulated by the event generator PYTHIA corresponding to an integrated luminosity of $\mathcal{L}_{\mathrm{int}} \simeq 100\,\mathrm{pb}^{-1}$.

The estimated contribution of photoproduction events to the dijet cross section is below one per mil for all jet algorithms. The contribution to the inclusive jet cross section is 2.5 per mil. The largest contribution in a single bin is never above 5 per mil. Due to the very small contributions these values fluctuate strongly between different bins, such that a statistical subtraction is neither meaningful nor statistically justified. We therefore decide to neglect this small effect.

6

Unfolding the Data

To unfold the data by applying bin-by-bin correction factors which are determined from simulated event samples (as described in section 4.4) two conditions have to be fulfilled: The simulation has to give a reasonable description of properties of the data sample and the bin widths have to be chosen such that migrations between bins are sufficiently small.

In the previous chapter we have shown that the simulated events are able to describe most details of the hadronic final state, including the properties of single jets and the multi-jet system. The simulation can therefore be used in the unfolding procedure of the data.

In this chapter we use the simulation to study the resolution of the observables and to choose the bin widths such that migrations between different bins are small, i.e. that the bin purities and efficiencies are sufficiently large. We determine the correction functions for detector effects and the QED corrections. The different sources of experimental uncertainties are studied to determine the corresponding uncertainties in the cross section measurement. Finally we redo the analysis, using the Electron Method for the kinematic reconstruction to test the stability of the results.

6.1 Resolution and Migration Studies

The following criteria have been used to chose the bins in which the cross sections are measured (the quoted numbers are given for the dijet sample of the inclusive $k_\perp$ algorithm, which consists of 2855 events).

- We require that bin purities and efficiencies are typically above 50%. Bin purities and efficiencies are defined as the number of events that enter the same bin of a distribution on generator and on reconstructed level, divided by the number of all events that are reconstructed, respectively generated in this bin[1]. For the determination of these we have to consider migrations between bins as well as migrations in and out of the event (or jet) sample.

---

[1] In the inclusive jet sample this definition does not apply to events, but to single jets.

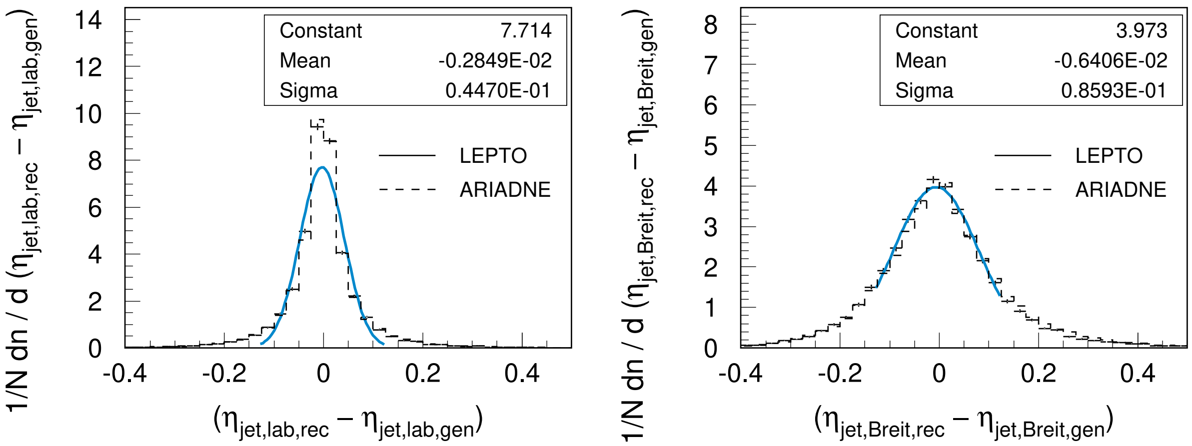

Figure 6.1: The resolution of the jet pseudorapidity in the laboratory frame (left) and in the Breit frame (right) for the inclusive jet sample obtained using the inclusive $k_\perp$ algorithm.

- If allowed by the resolution, the bins of the distributions should have approximately the same statistics, with a typical number of events per bin of approximately 150. This leads to a statistical error of about 8% which is smaller than the expected systematic uncertainties and allows to have approximately 19 bins for each observable.

- The data are divided into four regions of Q^2, such that each region contains approximately 700 events. Differential distributions can therefore have five bins if no further restrictions apply, e.g. from limited resolution.

- In the case of steeply falling distributions (e.g. the E_T spectrum) where the resolution does not allow to have equal statistics in all bins, we choose the bins such that no bin has less than 20 events (corresponding to a statistical error of 22%).

All resolution studies are shown here for the inclusive $k_\perp$ algorithm which is our choice for the central results of the analysis. The most important observables in the QCD analysis are the differential inclusive jet cross section w.r.t. E_T and the differential dijet cross section w.r.t. ξ. For these two observables we will present a detailed migration study.

The resolutions of the observables are always shown in bins of the reconstructed value. To guide the eye we have overlaid fits of a Gaussian in the central region of the distributions (the fit parameters are displayed in the plots). The bin boundaries finally chosen are listed together with the results in the appendix D.1.

6.1.1 The Inclusive Jet Sample

The inclusive jet cross section is measured as a function of the transverse jet energy in different Q^2 regions. The limiting factor in the choice of the binning is the E_T resolution. To determine the E_T resolution a matching criterion must be introduced, according to which a reconstructed jet is identified with a generated jet (e. g. based on the spatial distance). If no generated jet can be matched with a reconstructed jet, the reconstructed jet is considered as "background" and the purity of the jet sample is reduced. In the case that no reconstructed jet is matched with a generated jet, this reduces the efficiency of the jet finding.

The matching criterion that we use is based on the distance ΔR in the plane of pseudorapidity and azimuthal angle between the axis of a generated and a reconstructed jet. To match two (generated and reconstructed) jets we require that the reconstructed jet axis lies within a cone of $\Delta R = 0.6$ around the axis of a generated jet in the detector[2]. The chosen value of ΔR is, of course, arbitrary. We can see, however, in Fig. 6.1 (left) that the resolution of the pseudorapidity measurement in the detector is very good (better than $\Delta\eta = 0.05$). Therefore all further conclusions do not change e.g. if we vary ΔR by ± 0.3.

The resolution of the jet pseudorapidity in the Breit frame is shown in Fig. 6.1 (right). We notice that the resolution in the Breit frame is worse than in the laboratory frame ($\Delta\eta_{\text{Breit}} \simeq 0.09$), due to the event-wise uncertainty in the reconstruction of the boost vector. However, as in the laboratory frame, the difference between the generated and the reconstructed value is peaked close to zero. Hence, on average, the boost does not introduce any bias, which would be seen as a shift in the distribution.

In Fig. 6.2 (top) we display the ratio of the reconstructed and the generated transverse jet energy E_T in different regions of E_T. It is seen that in all cases the curves are peaked within $\pm 2\%$ around one, with a resolution that improves from 18% to 8% from lower to higher E_T. The simulations by LEPTO and ARIADNE predict the same behavior. We have also investigated the Q^2 dependence of the resolution, integrating over E_T (not shown here). The resolution is always 16% and no Q^2 dependence is seen.

The lower plot in Fig. 6.2 gives the complete information on the migrations in the inclusive jet sample. The axis labels 1–4 correspond to the four different E_T bins in each Q^2 range. Bin number 0 contains those reconstructed (generated) jets which are not matched with a generated (reconstructed) jet. If an event does not pass the kinematic cuts on one level (or the technical cuts on reconstructed level) it falls in bin No. -1. Based on this information all purities and efficiencies can be calculated[3]. For the bin sizes chosen here we obtain purities between 52% and 77% and efficiencies of 49%–64% (improving towards higher E_T). These values are sufficiently high to apply the bin-by-bin correction procedure. The off-diagonal elements in the migration plot (Fig. 6.2, bottom) are small enough to consider the single bins as uncorrelated.

---

[2] The matching of jets is done in the laboratory frame, such that uncertainties in the boost to the Breit frame do not affect the matching. Whenever these uncertainties affect the E_T or the $\eta_{\text{jet, Breit}}$ reconstruction this can be seen in the corresponding resolution plots.

[3] The event loss due to cuts (5.3) and (5.4) is not included in the migration tables and in the quoted efficiencies. Since these cuts only affect a well defined fraction of the event sample and the remaining events are correspondingly reweighted, their effect is not regarded as an inefficiency.

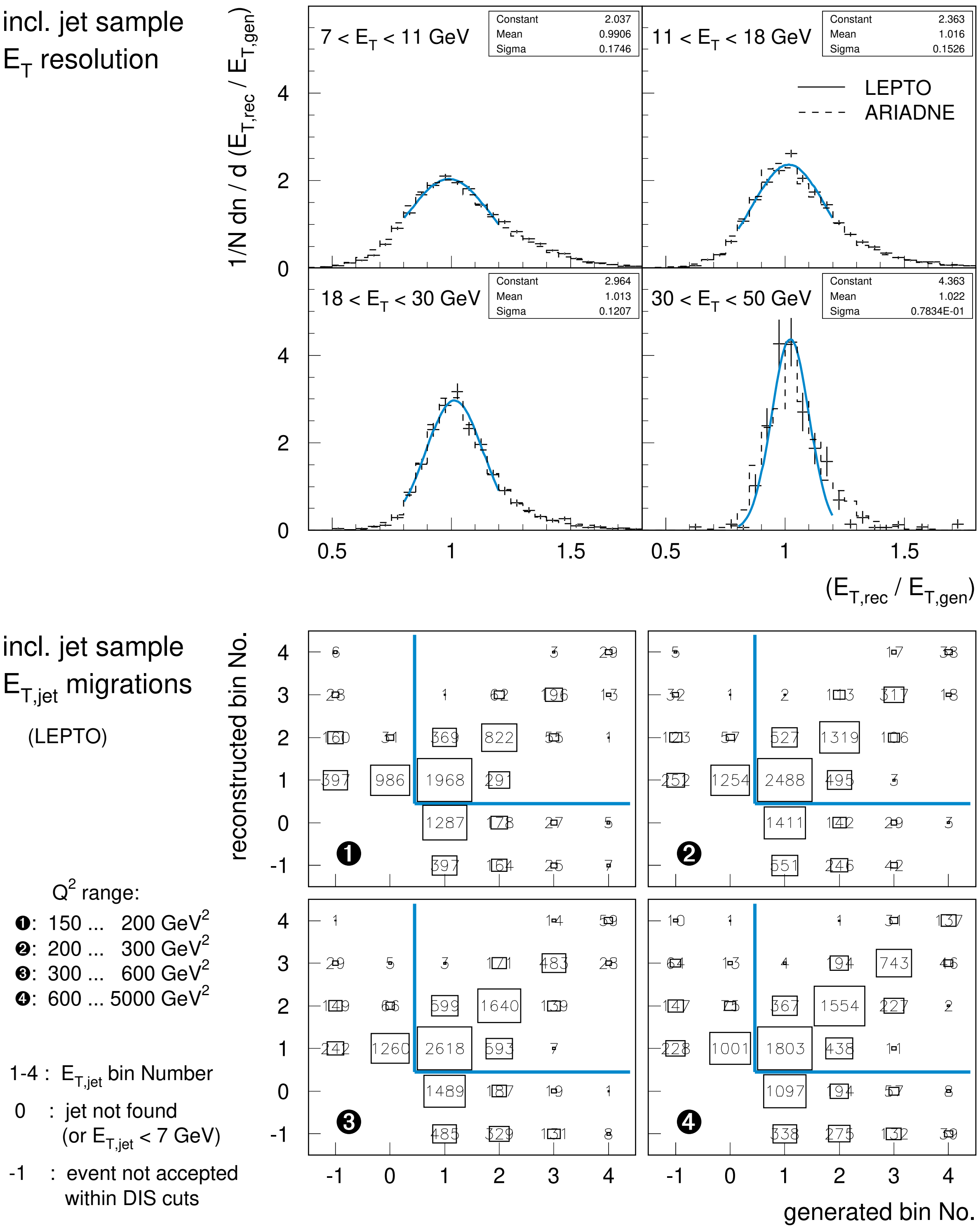

Figure 6.2: Resolution and migration studies for the inclusive jet cross section using the inclusive $k_\perp$ algorithm. Shown is the E_T resolution in different bins of the reconstructed E_T (top) and the migrations between different E_T bins in the four Q^2 regions (bottom).

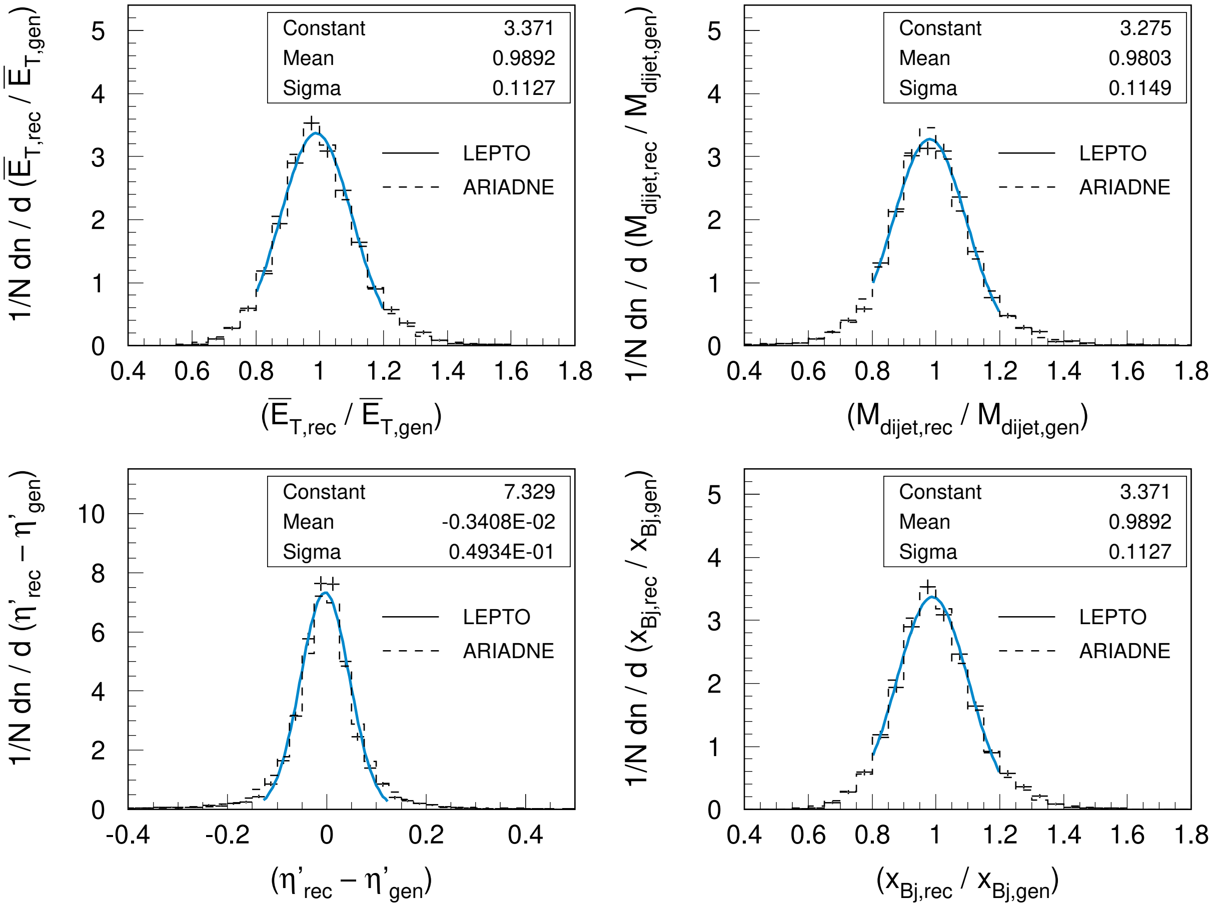

Figure 6.3: The resolution of the average transverse energy $\overline{E}_T$, the invariant mass M_{jj}, the variable η' of the dijet system and the Bjorken scaling scaling variable $x_{\rm Bj}$ in the dijet event sample for the inclusive $k_\perp$ algorithm.

6.1.2 The Dijet Event Sample

The dijet cross sections are measured as functions of various variables. Most distributions are presented in different regions of Q^2 (only the η' dependence is, in addition, also measured in different $\overline{E}_T$ regions). The resolution of most variables is independent of Q^2, as in the cases of the average transverse energy of the dijet system $\overline{E}_T$, the invariant dijet mass M_{jj}, the pseudorapidity difference η' and the Bjorken scaling variable $x_{\rm Bj}$. For these variables the resolution is shown in Fig. 6.3, integrated over the total Q^2 range. The resolution is defined as the ratio of the respective variables using all events which are classified as dijet events on generator level, as well as on detector level. The only exception is the variable η' for which the resolution is defined as the *difference* of the reconstructed and the generated value. The resolution of η' is $\Delta\eta' \simeq 0.05$, while the other variables have a resolution of $\simeq 11.5\%$ (independently of Q^2). All distributions are nicely peaked at one or zero, respectively.

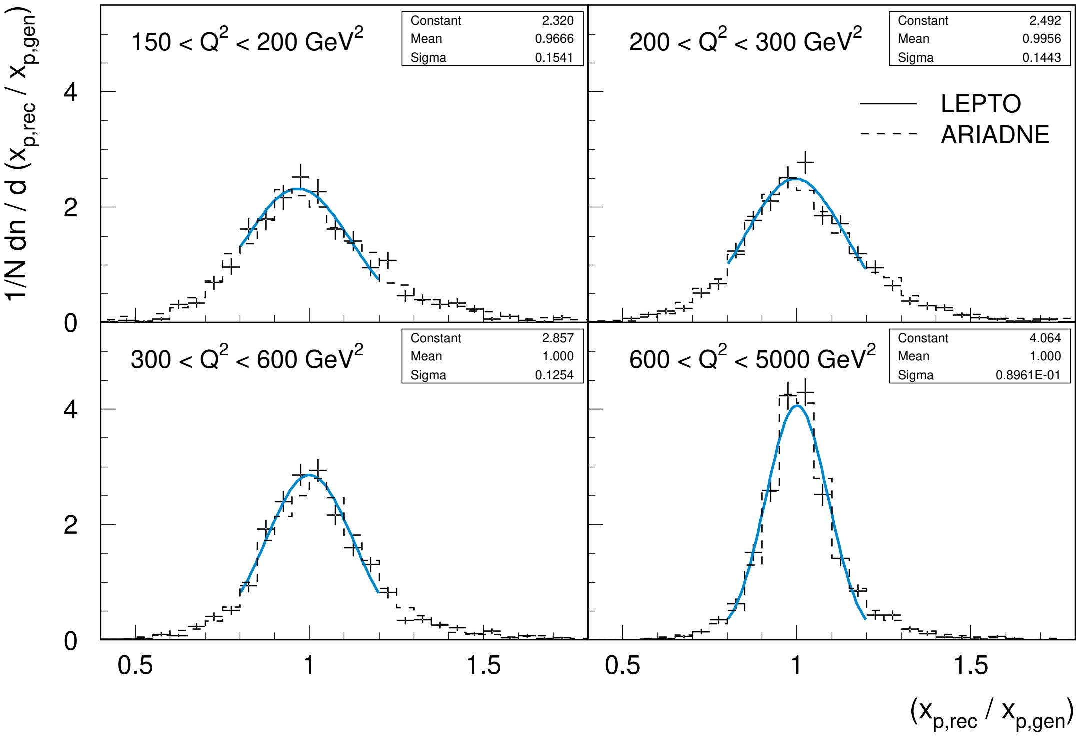

Figure 6.4: The resolution of the partonic scaling variable x_p in the dijet event sample for the inclusive $k_\perp$ algorithm in four regions of Q^2.

A Q^2 dependence is observed in the resolution of the variables x_p and ξ, as displayed in Figs. 6.4 and 6.5 (top). The resolution for both variables improves from 15% at lower Q^2 to 9% at the highest Q^2. Both variables are on average reconstructed with an accuracy better than 1% in most Q^2 regions.

The migrations between the final ξ bins is shown in the bottom of Fig. 6.5. The presentation is identical to the one for the inclusive jet cross section: The ξ bins in the analysis are labeled by numbers 1–5 (the highest Q^2 range has only 4 ξ bins). Bin No. 0 contains events which were (either on detector level or on generator level) not classified as dijet events while events that were not selected as DIS events are counted in bin No. −1.

For the chosen binning we obtain bin purities between 50% and 86%, except for bin No. 1 in the lowest Q^2 range where the purity is 41%. The efficiencies are slightly smaller (in the range of 44% and 73%). The migrations in the distributions of the other observables (not shown here) have also been investigated. All bin widths have been chosen such that the bin purities and efficiencies are in the same range as those shown here.

As for the inclusive jet cross section, we therefore conclude that the bin widths are chosen appropriately to unfold the data using the bin-by-bin correction procedure and to neglect correlations between different bins in the final QCD analysis.

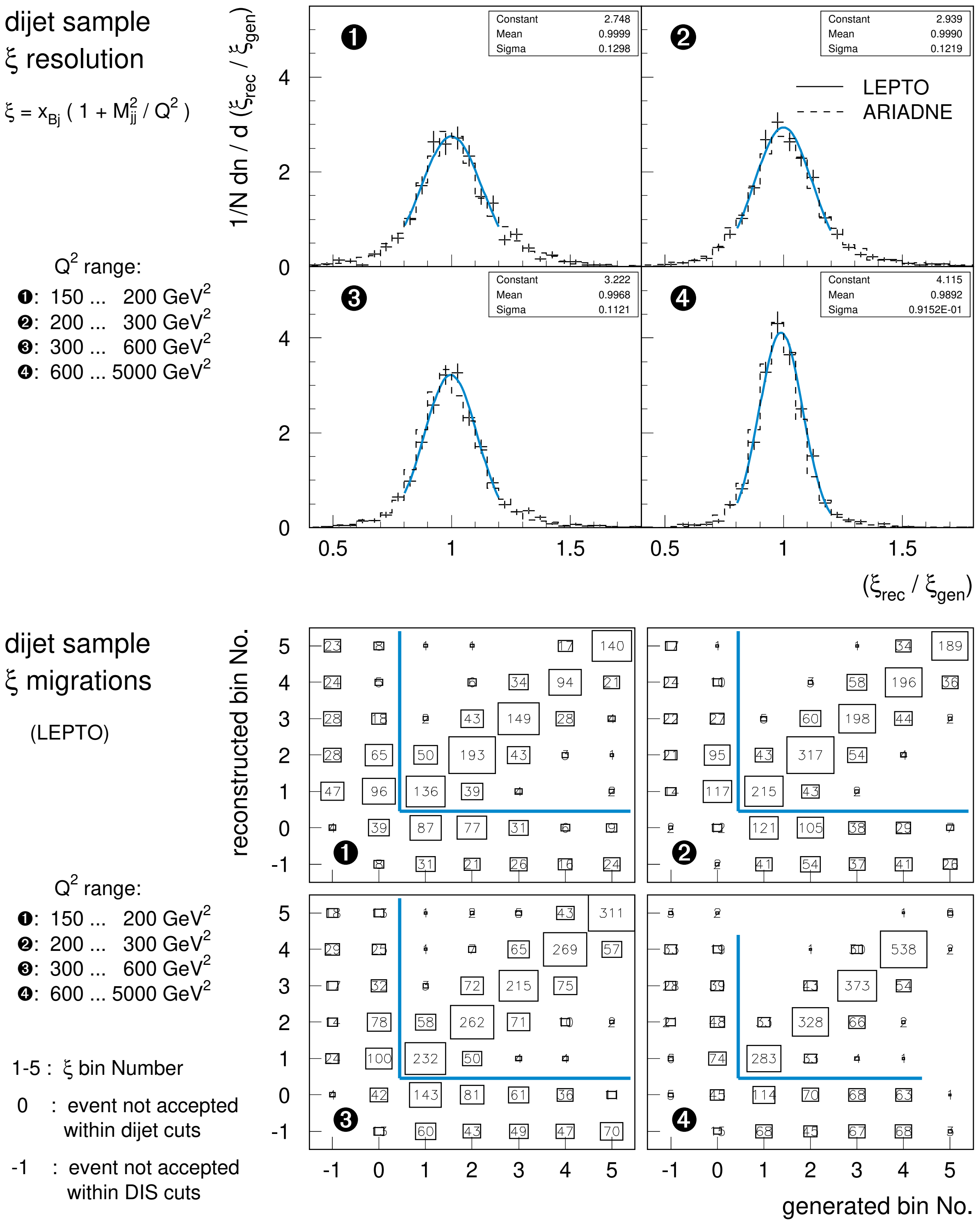

Figure 6.5: Resolution and migration studies for the dijet cross section using the inclusive $k_\perp$ algorithm. Shown is the resolution of the variable ξ in different regions of Q^2 (top) and the migrations between different ξ bins in the four Q^2 regions (bottom).

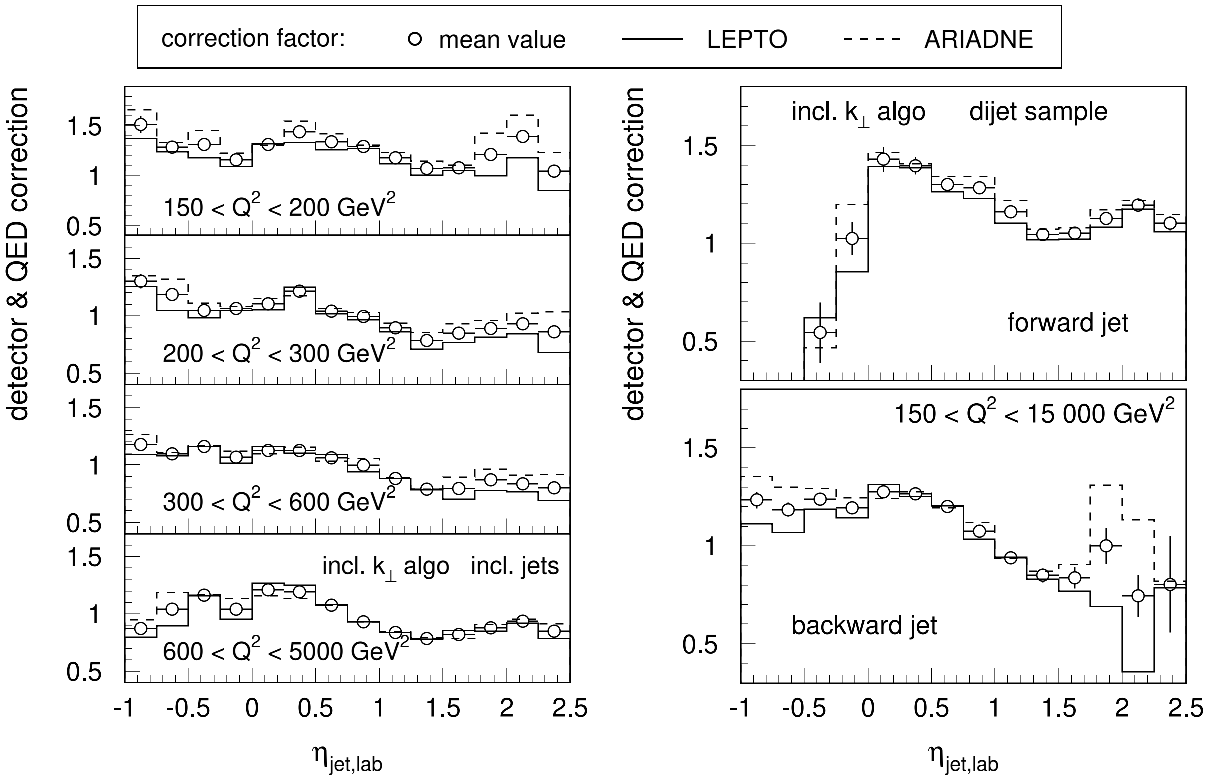

Figure 6.6: The dependence of the correction function on the jet pseudorapidity in the laboratory frame, for the inclusive jet cross section (left) in different Q^2 ranges, and for the dijet cross section (right) separately for the forward (top) and backward jet (bottom) in the laboratory frame.

6.2 Correction Functions

The distributions of all observables will be corrected for effects of limited detector resolution and acceptance, as well as for inefficiencies of the selection. Furthermore we correct for higher order QED processes (but not for the running of the electromagnetic coupling constant). All results represent therefore the values of the corresponding observables at the level of "stable" hadrons (hadrons with a lifetime above $3 \cdot 10^{-10}$ sec), if higher order QED corrections are excluded.

In the previous chapter we have shown that the simulated events from both LEPTO and ARIADNE give a reasonable description of many properties of the selected data samples. Although not both of them could describe all distributions, in most cases at least one of them was able to describe the basic features. On this basis we decide to use these event simulations to determine the correction functions for our cross section measurements. From the remarks made above, it is clear that there is no reason to prefer one or the other simulation. It is indeed helpful to see whether the small differences in the distributions lead to a difference in the estimated correction functions.

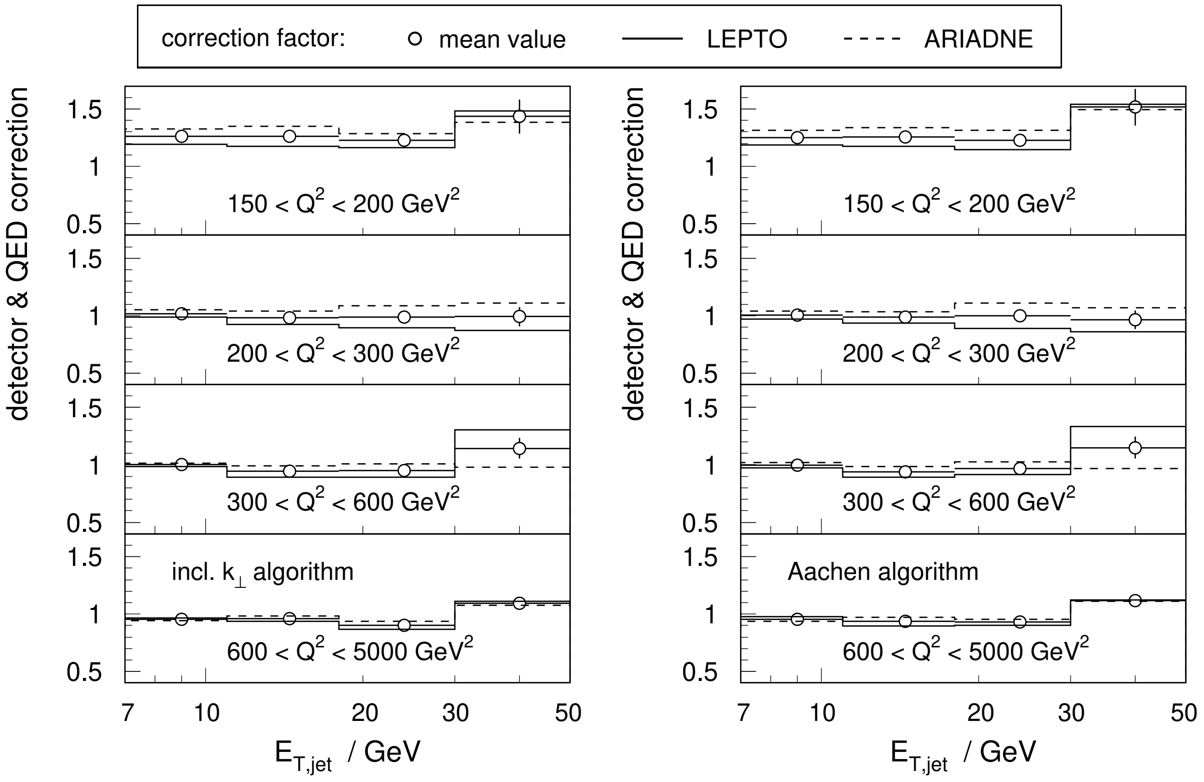

Figure 6.7: The correction functions for the E_T dependence of the inclusive jet cross section, for the inclusive $k_\perp$ algorithm (left) and for the Aachen algorithm (right).

We have seen that in most cases where differences between both models are observed, the data distribution is in between both model predictions. We therefore determine the correction functions for our analysis from the mean value of both estimates, and consider the difference between the mean value and the single values as the intrinsic uncertainty, arising from the insufficient description of the data by (at least one of) the models.

In the following we show the combined correction functions, including the detector and the QED corrections. For demonstration purposes we show in one case the single contributions as well. We give a comprehensive overview on the correction functions for the most important observables.

6.2.1 Inclusive Jet Cross Section

Before we discuss the correction functions for the final observables, we look at the correction as a function of the jet pseudorapidity η in the laboratory frame (Fig. 6.6). In the left plot we show the correction for the inclusive jet sample in four different regions of Q^2. The correction functions vary within ±20% around one. Only in the lowest Q^2 region the average correction is +25%, due to cut (5.2) on the z-impact position of the positron, which requires this acceptance correction.

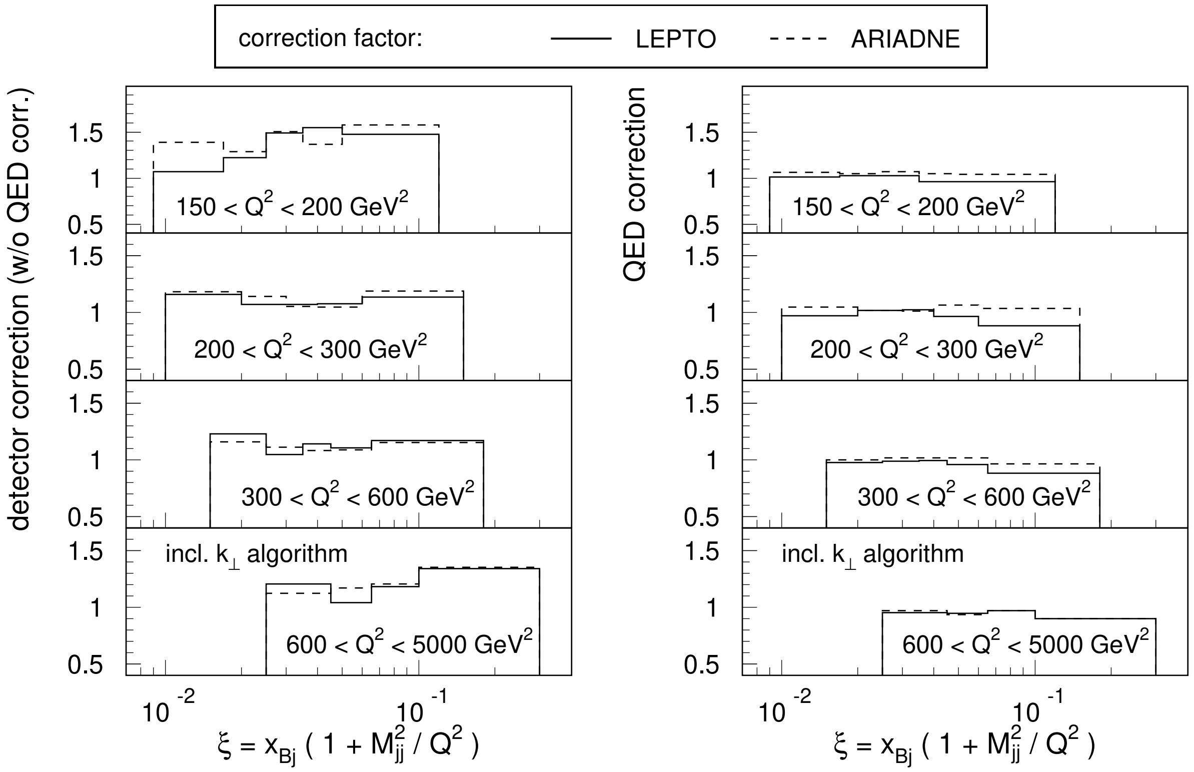

Figure 6.8: The correction functions for the ξ distribution of the dijet cross section for the inclusive $k_\perp$ algorithm, separated in the detector correction (left) and the QED correction (right).

In all Q^2 regions the correction functions show a slight η dependence. A very similar behavior is seen in the correction functions of the dijet cross section, shown in Fig. 6.6 (right) separately for the forward (top) and the backward jet (bottom), here integrated over Q^2. This pseudorapidity dependence is seen in both model estimates, which agree in all general characteristics. ARIADNE predicts corrections slightly higher than LEPTO, especially in the forward and in the backward region, where the differences can be as large as 20%. Since the bulk of the jets are, however, in the central detector region (see Fig. 5.5), the differences for integrated distributions are small.

The correction functions for the inclusive jet cross section are shown in Fig. 6.7 for the inclusive $k_\perp$ algorithm (left) and for the Aachen algorithm (right). For both jet algorithms the correction functions are flat in E_T, only in the highest E_T bin an increase is seen. The model dependence is in most cases below 10%.

6.2.2 Dijet Cross Section

For the ξ distribution we show the single contributions to the total correction factor in Fig. 6.8: The detector correction (left) and the QED correction (right). It is seen that the

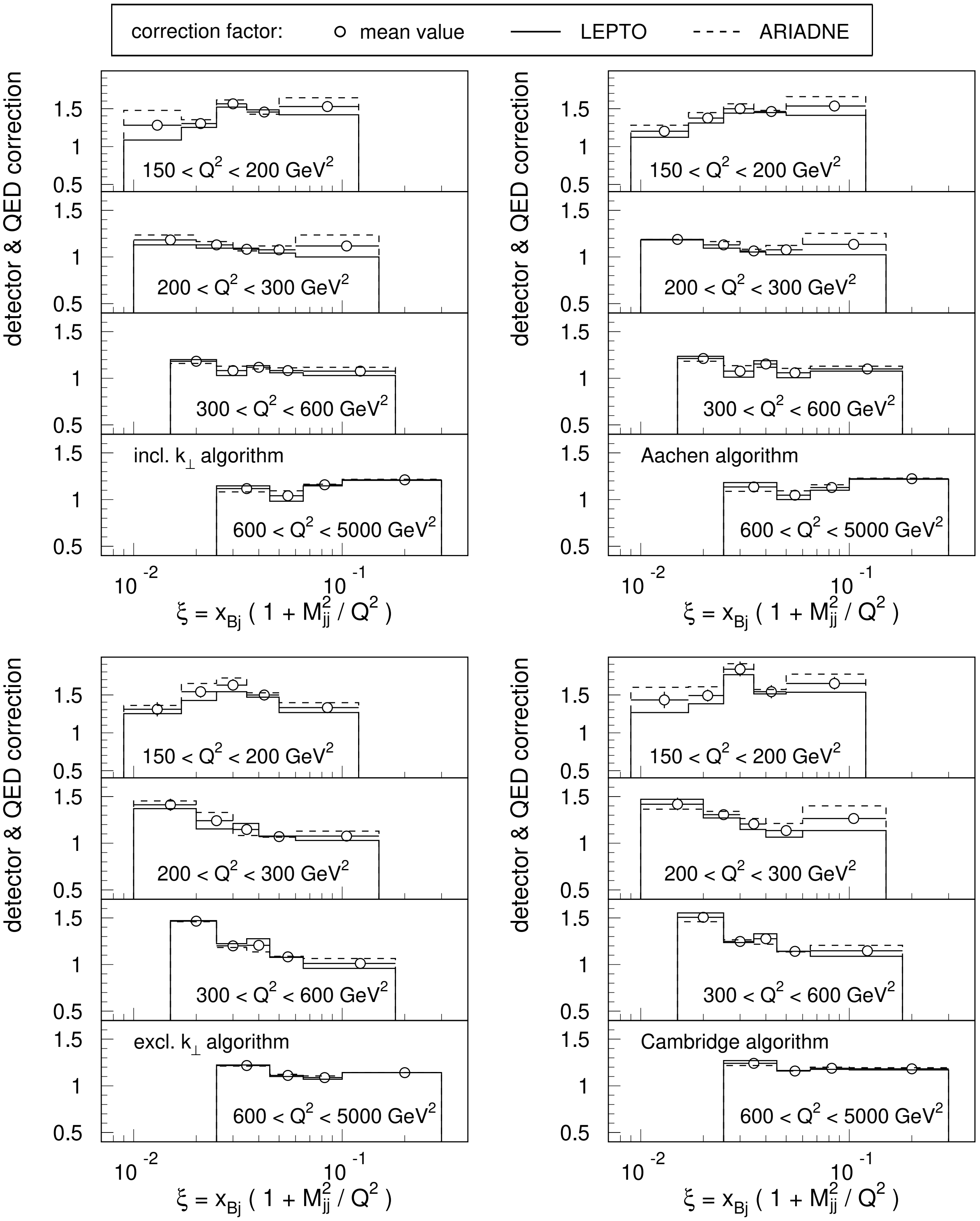

Figure 6.9: The correction functions for the ξ distribution of the dijet cross section for four different jet algorithms.

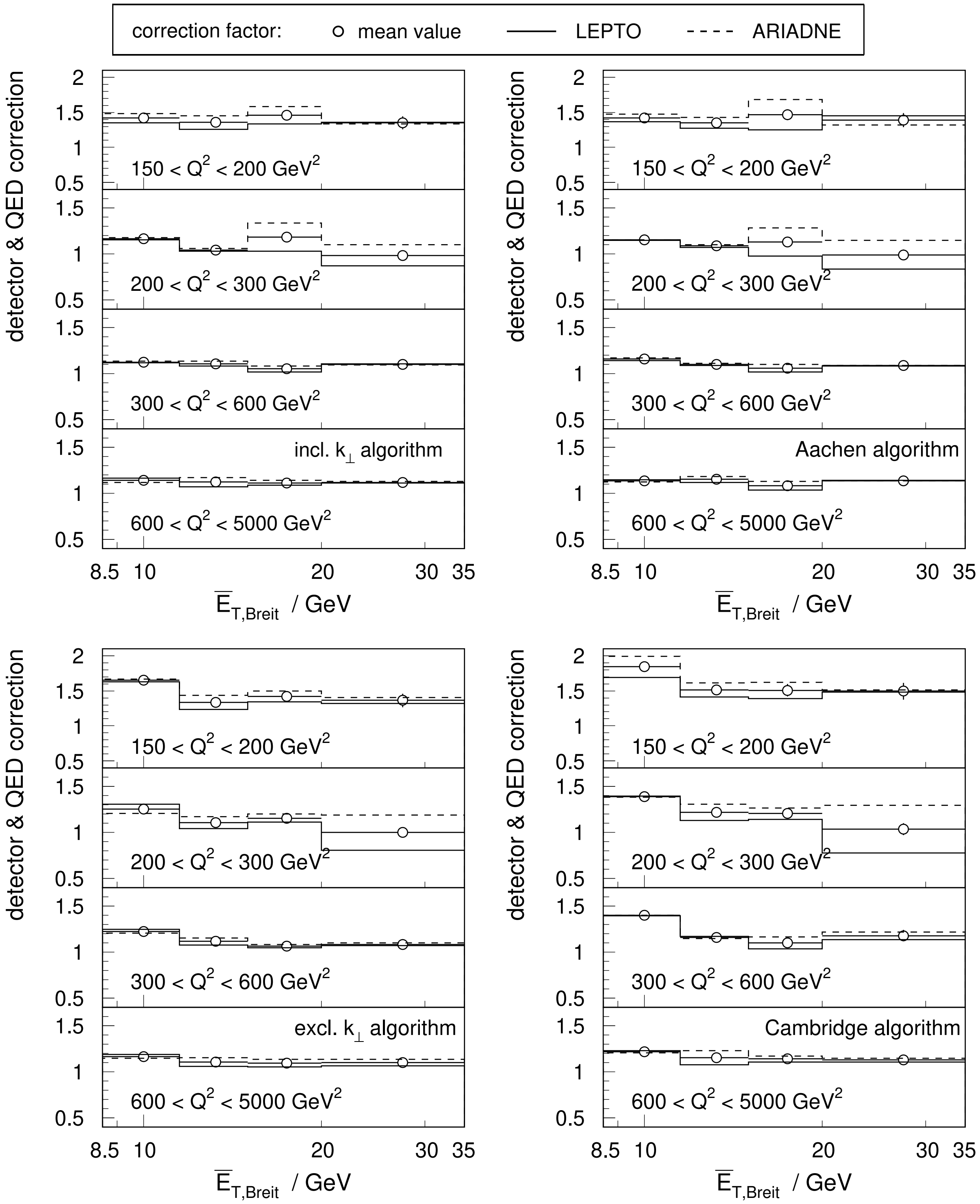

Figure 6.10: The correction functions for the $\overline{E}_T$ distribution of the dijet cross section for four different jet algorithms.

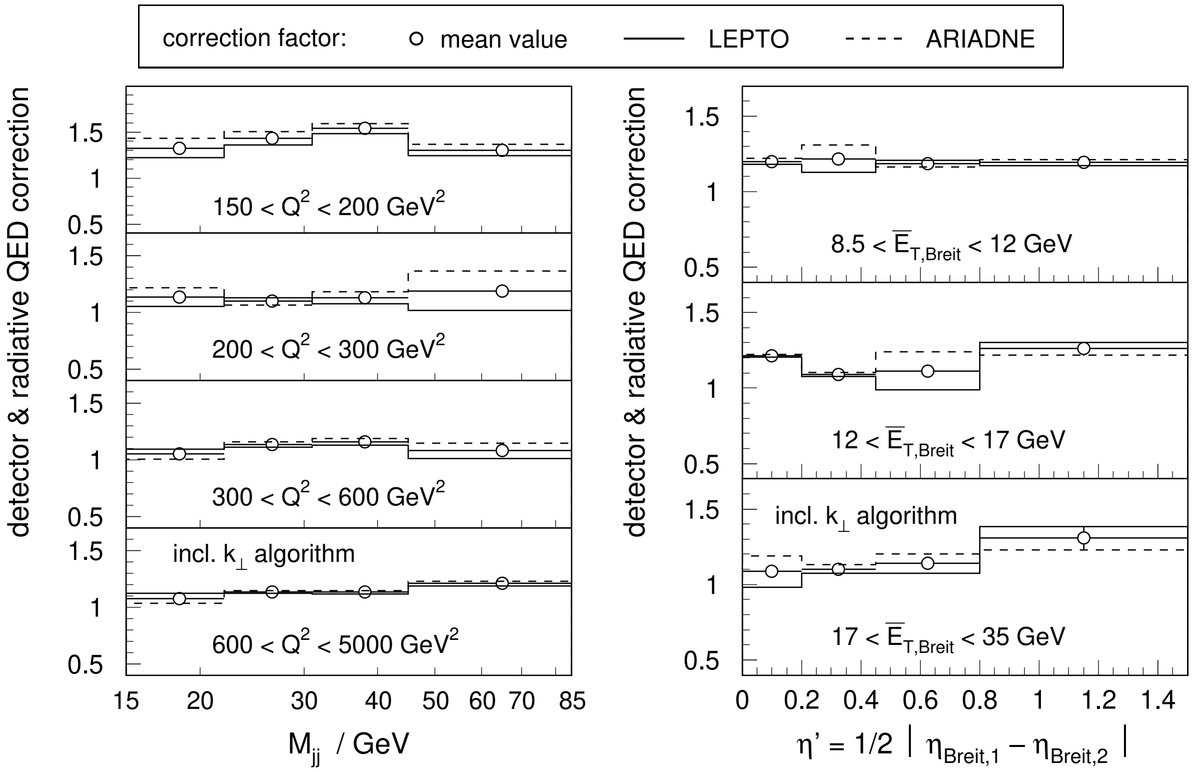

Figure 6.11: The correction functions for the dijet cross section as a function of the invariant dijet mass M_{jj} (left) and the variable η' (right) using the inclusive $k_\perp$ algorithm .

QED corrections are very small and flat in all Q^2 regions, such that the size of the total correction reflects mostly the size of the detector correction.

The total correction functions for the ξ distributions are given in Fig. 6.9 for all four jet algorithms. Both exclusive jet algorithms (bottom) exhibit sightly larger corrections compared to the inclusive algorithms (top). In Fig. 6.10 the correction functions for the $\overline{E}_T$ distributions are displayed (for the four jet algorithms) and Fig. 6.11 shows the correction functions for the dijet mass distribution (left) and for the variable η' (right), for the inclusive $k_\perp$ algorithm.

In all cases the correction functions show a reasonably small model dependence. The size of the corrections is for the inclusive jet algorithms (inclusive $k_\perp$ and Aachen algorithms) typically below 20%, except at $Q^2 < 200\,\mathrm{GeV}^2$, where we correct for the acceptance cut (5.2). The observables obtained from the exclusive jet algorithms (exclusive $k_\perp$ and Cambridge algorithm) have slightly higher corrections, especially at lowest ξ and at lowest E_T, but still have a small model dependence.

6.3 Experimental Uncertainties

Various sources contribute to the uncertainties of the measured jet cross sections. In the following we discuss which sources are correlated and which are uncorrelated between the single data points and how the single contributions are evaluated.

Statistical Uncertainties

Statistical uncertainties arise from the limited amount of events used in the determination of a quantity. In this analysis they enter at three places: (i) the limited amount of data in the reconstructed distributions, (ii) the limited number of simulated events, used to determine the detector correction functions, (iii) the number of generated events, used to determine the size of the QED corrections. All three contributions are added in quadrature for each bin. Due to their statistical nature they are uncorrelated between different bins.

While the size of (i) is largest, (ii) gives further contributions, which are only slightly smaller since the luminosity of the simulated events is a factor of three (five) larger for LEPTO (ARIADNE) compared to the data. The statistical uncertainty from (iii) is always negligible, compared to the (i) and (ii), due to the very large luminosities of the generated event samples (see section 4.4.4).

Uncertainty in the Luminosity Determination

For the present data set the uncertainty in the luminosity determination is 1.5%. This introduces a corresponding overall normalization uncertainty, which is correlated between all data points.

Model Dependence of the Correction Functions

In section 6.2 we have described the correction procedure, in which the correction functions are determined as the mean value of the estimates from LEPTO and ARIADNE. The uncertainty, arising from the model dependence is taken to be the difference between the mean value and the single model estimates (i.e. half the spread between both models).

Since we do not observe a general trend, we assume a fraction of $1/\sqrt{2}$ of the spread to be correlated and a further fraction of $1/\sqrt{2}$ to be uncorrelated between the single data points, such that the quadratic sum is equal to the total quoted uncertainty.

Uncertainties in the Positron Reconstruction

In the present analysis we use the calibration of the positron energy which has been developed for the measurement of the inclusive neutral current cross section [32]. Details on the procedure can be found in [81]. Here we only summarize the final results on the achieved precision, which depend on the calorimeter wheel in which the impact point $z_{\rm imp}$ of the positron lies.

The uncertainty of the positron energy is 1% in the backward part ($z_{\rm imp} < -145\,{\rm cm}$), 0.7% in the CB1 and CB2 wheels ($-145\,{\rm cm} < z_{\rm imp} < 20\,{\rm cm}$), 1.5% for $20\,{\rm cm} < z_{\rm imp} < 100\,{\rm cm}$ and 3% in the forward part ($z_{\rm imp} < 100\,{\rm cm}$). These values are obtained by the quadratic sum of uncorrelated uncertainties and a correlated uncertainty, which is 0.5% in the whole LAr calorimeter.

The uncertainty in the positron track measurement is taken to be ±3 mrad for the polar and for the azimuthal angle (the latter enters through the reconstruction of the boost vector to the Breit frame, as described in section 5.1.4). While the uncertainty in the polar angle is considered to be correlated between the data points, we consider the uncertainty in the azimuthal angle reconstruction as uncorrelated.

Uncertainties in the Hadronic Final State Measurement

The uncertainties in the measurement of the hadronic final state comprise three different contributions: The hadronic energy scale uncertainty of the LAr calorimeter, which is ±4% for the present analysis (as described in section 5.5), and the uncertainties in the measurement of the track momenta and in the hadronic energy scale of the SPACAL, which are ±3% and ±7%, respectively [32, 81]. As in [32, 81] we treat the uncertainties from the track momenta and the SPACAL energy scale as uncorrelated between the data points. From the 4% uncertainty of the hadronic energy scale of the LAr calorimeter we consider 2% to be correlated and the rest (when added in quadrature) of 3.4% as uncorrelated.

Evaluation of the Size of the Uncertainties

To determine the contributions from the different sources to the uncertainties of the measured jet cross sections, we have varied all single sources by one standard deviation upwards and downwards, and have redone the data selection. Since most of the variations are small, the variations in the data sample are often caused by to purely statistical event fluctuations. Therefore we have redone the selection procedure also for the LEPTO simulation which has a higher statistics. The variations are consistent with those seen in the data. Due to the higher statistics we quote the relative change of the LEPTO event sample as the relative uncertainty of the measured cross sections.

The largest uncertainties come from the hadronic energy scale of the LAr calorimeter and from the measurement of the track momenta. For these contributions we quote the observed (and in general asymmetric) variations, when the corresponding sources are varied by one standard deviation upwards and downwards. The contributions from all other sources are relatively small such that statistical fluctuations may sometimes lead to an underestimation of the true uncertainty. In order not to underestimate these uncertainties and to be conservative, we quote a symmetric uncertainty of the size of the larger relative change when the sources are varied by one standard deviation upwards or downwards.

The model dependence of the correction functions has been presented in all plots in the previous section. In Figs. 6.12 and 6.13 we show the other contributions, connected to the

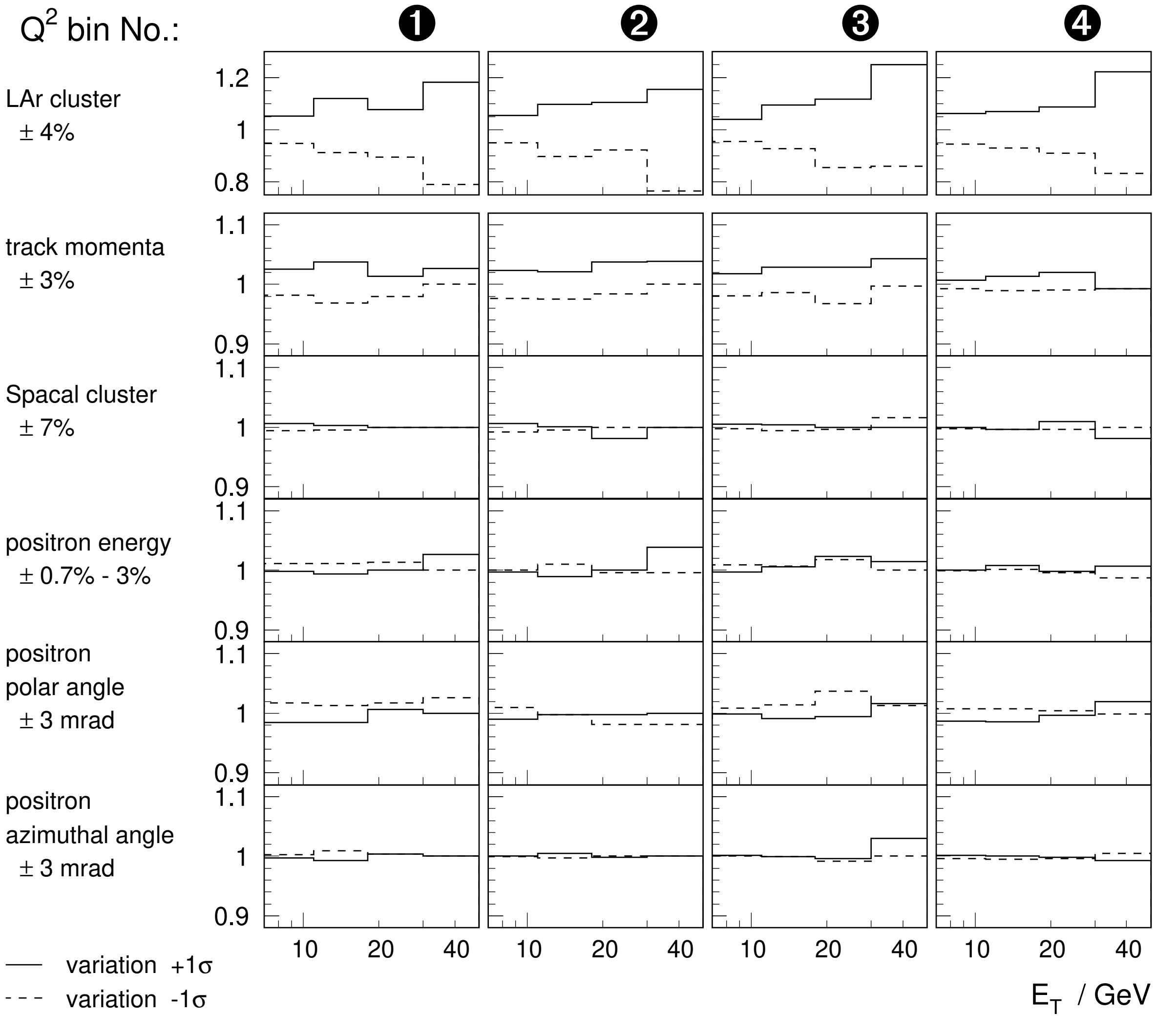

Figure 6.12: The relative experimental uncertainties for the inclusive jet cross section measured using the inclusive $k_\perp$ algorithm as a function of the transverse jet energy in different regions of Q^2. Shown are the relative variations of the cross section w.r.t. to the central result when the single sources are varied by one standard deviation.

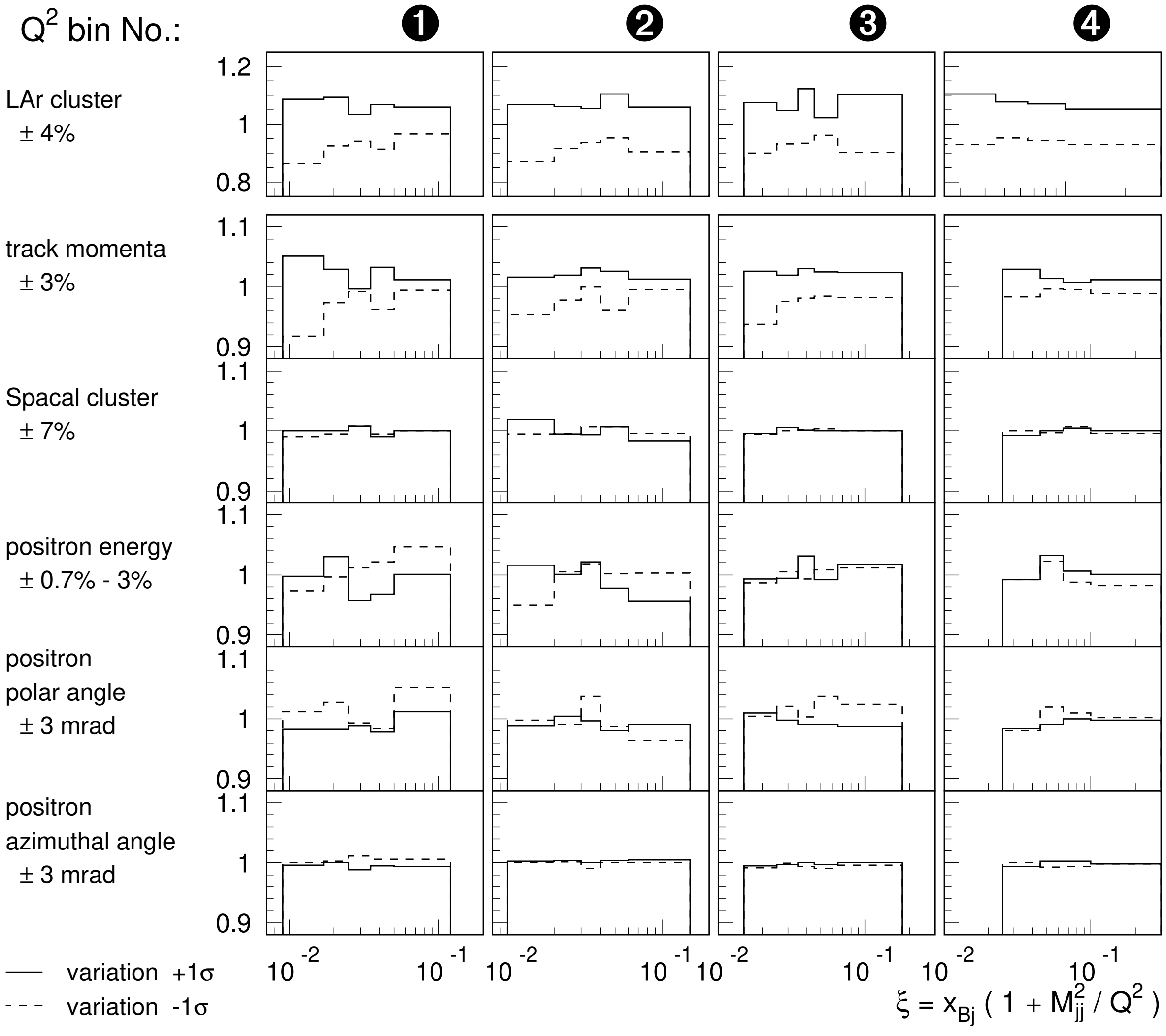

Figure 6.13: The relative experimental uncertainties for the dijet cross section measured using the inclusive $k_\perp$ algorithm as a function of the reconstructed parton momentum fraction ξ in different regions of Q^2. Shown are the relative variations of the cross section w.r.t. to the central result when the single sources are varied by one standard deviation.

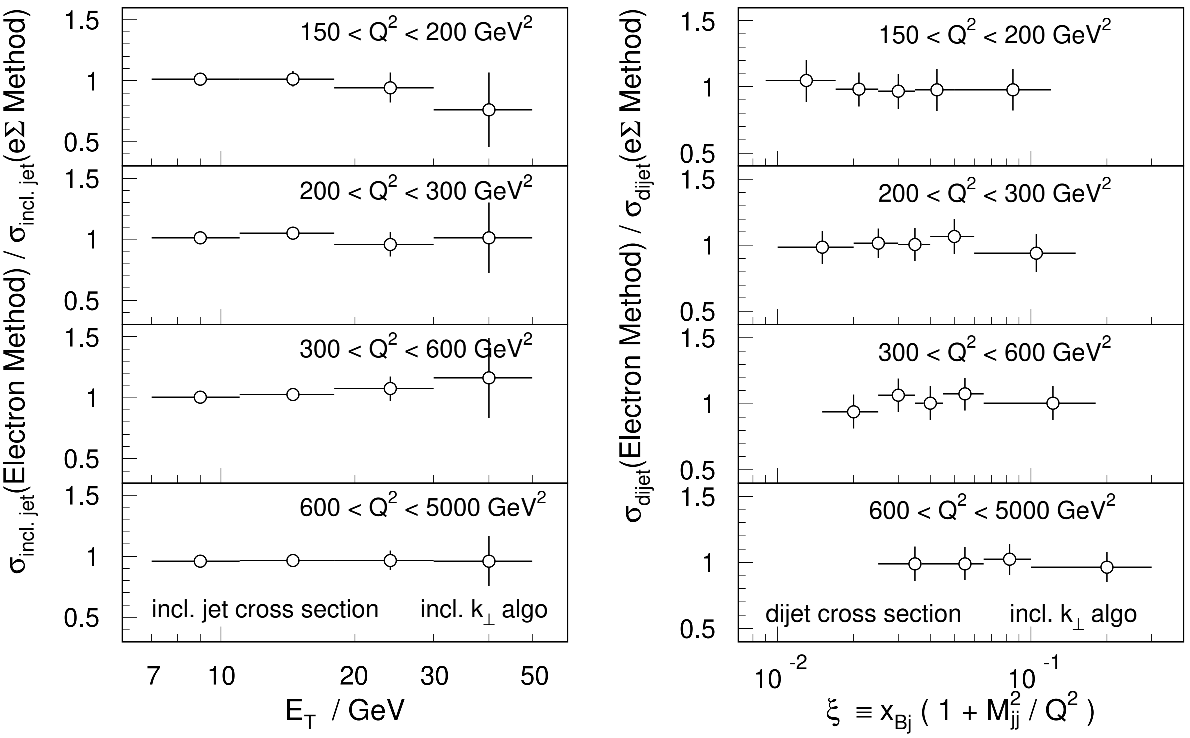

Figure 6.14: The relative change in the corrected cross sections when using the Electron Method instead of the Electron-Sigma Method, for the E_T distribution of the inclusive jet cross section (left) and the ξ distribution of the dijet cross section (right).

uncertainties in the calibration, for the E_T dependence of the inclusive jet cross section and the ξ dependence of the dijet cross section. A complete list of the total uncertainties of all measured cross sections can be found in appendix D.1.

A Different Reconstruction of the Kinematics

We have performed a further consistency test by using the Electron Method instead of the Electron-Sigma Method to reconstruct the event kinematics, and have redone the whole analysis. The ratio of both results is displayed in Fig. 6.14. The error bars represent the statistical uncertainties of the ratio, which are, however, overestimated since both data samples are highly correlated. For the ξ distribution (right) both results agree within less than 5%, which is compatible with both, the statistical uncertainties and the quoted model dependence. The same is true for the E_T distribution (left), with the exception of two of the highest E_T bins where the deviations are larger. In these bins, however, other uncertainties are larger than the observed change: The model dependence of the correction, the hadronic energy scale of the LAr calorimeter, and the statistical uncertainties. Therefore we do not consider the changes as additional uncertainties, but as a different appearance of uncertainties that we already account for.

7

Experimental Results

In this chapter we present the results of the measurements. All observables have been corrected for detector effects and for QED corrections (but neither for the running of the electromagnetic coupling constant nor for the contributions from Z^0 exchange). Furthermore we have not applied any corrections for non-perturbative contributions ("hadronization corrections"). In the presentation the statistical uncertainties are indicated by the inner error bars, while the total error bar represents the quadratic sum of the statistical and all systematic uncertainties.

The central results of the analysis are the inclusive jet and the dijet cross sections at large momentum transfer Q^2, for which the experimental analysis procedure has been described in detail in the two previous chapters. These results will later be used in the QCD analysis.

Two further analyses have been performed in collaboration with Arno Heister and Lars Sonnenschein and are documented in their respective Diploma theses [96, 97]. These analyses have investigated the production rates of higher jet multiplicities (three- and four-jet cross sections) and the internal structure of jets (jet shapes and subjet multiplicities). From these analyses we will present here only some of the main results.

7.1 The Inclusive Jet Cross Section

The inclusive jet cross section is measured for two jet algorithms, the inclusive $k_\perp$ algorithm and the Aachen algorithm (as defined in section 2.2) in the Breit frame, in the phase space given by

$$0.2 < y < 0.6\,, \quad 150 < Q^2 < 5000\,\mathrm{GeV}^2\,, \quad E_{T,\mathrm{jet,\,Breit}} > 7\,\mathrm{GeV}\,, \quad -1 < \eta_{\mathrm{jet,\,lab}} < 2.5\,. \quad (7.1)$$

The analysis is based on data taken in the years 1995–1997 by the H1 experiment, corresponding to an integrated luminosity of $\mathcal{L}_{\mathrm{int}} = 33\,\mathrm{pb}^{-1}$.

The results are presented in Fig. 7.1 double differentially as a function of the transverse jet energy in the Breit frame E_T in different regions of Q^2 (the numerical values can be found in appendix D.1).

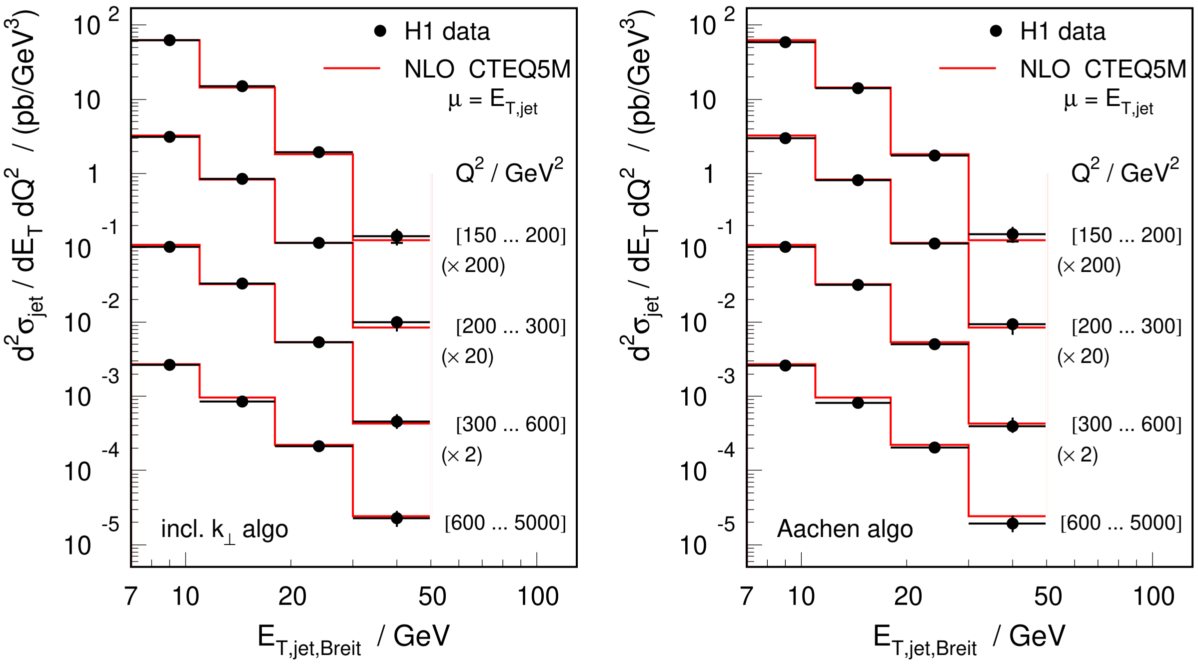

Figure 7.1: The inclusive jet cross section as a function of the transverse jet energy in different regions of Q^2 for the inclusive $k_\perp$ algorithm (left) and for the Aachen algorithm (right). The perturbative QCD prediction in NLO is compared to the measurement.

The data for the inclusive $k_\perp$ algorithm (left) and for the Aachen algorithm (right) cover a range of transverse jet energies squared ($49 < E_T^2 < 2500\,\mathrm{GeV}^2$) that is similar to the range of the four-momentum transfers squared ($150 < Q^2 < 5000\,\mathrm{GeV}^2$) of the event sample. The cross sections for both jet algorithms are of the same size and show a slightly harder E_T spectrum towards larger Q^2.

The inclusive jet cross sections measured are compared to the predictions of perturbative QCD in next-to-leading order in the strong coupling constant[1]. This direct comparison is meaningful since non-perturbative contributions are seen to be always below 10% (see section 3.1). Over the whole range of Q^2 and E_T the perturbative calculation gives a good description of the data.

7.2 The Dijet Cross Section

The dijet cross section is measured for the four jet algorithms introduced in section 2.2: Two inclusive jet algorithms (inclusive $k_\perp$ and Aachen algorithm) and two exclusive jet algorithms

---

[1] The calculations are performed using the program DISENT [60] for the parton distributions from the CTEQ5M parameterization and the corresponding value of $\alpha_s(M_Z) = 0.118$ which is evolved according to the 2-loop solution of the renormalization group equation. The renormalization scale is set to the transverse jet energy $\mu_r^2 = E_T^2$, and the factorization scale to the average E_T of the total jet sample $\mu_f^2 = 200\,\mathrm{GeV}^2$.

(exclusive $k_\perp$ and Cambridge algorithm). While the inclusive and exclusive $k_\perp$ algorithms cluster particles in the order of smallest relative transverse momenta ($k_\perp$), the Aachen and the Cambridge algorithms perform the clustering in the order of smallest angles between particles. The results have been obtained in the phase space

$$0.2 < y < 0.6\,, \qquad 150 < Q^2 < 15\,000\,\mathrm{GeV}^2 \qquad (10 < Q^2 < 70\,\mathrm{GeV}^2)\,. \tag{7.2}$$

The analysis at $Q^2 > 150\,\mathrm{GeV}^2$ is based on the H1 data taken in the years 1995–1997, corresponding to an integrated luminosity of $\mathcal{L}_{\mathrm{int}} = 33\,\mathrm{pb}^{-1}$. The measurement at $10 < Q^2 < 70\,\mathrm{GeV}^2$ uses the H1 data from 1994, corresponding to an integrated luminosity of $\mathcal{L}_{\mathrm{int}} = 2\,\mathrm{pb}^{-1}$ and is performed for the inclusive $k_\perp$ algorithm only[2].

The jet phase space (as motivated in section 2.4) is defined differently for the inclusive and for the exclusive jet algorithms by

$$\begin{aligned} \text{inclusive jet algorithms:} \quad & E_{T,1,\mathrm{Breit}} + E_{T,2,\mathrm{Breit}} > 17\,\mathrm{GeV}\,, \quad E_{T,\mathrm{jet,\,Breit}} > 5\,\mathrm{GeV}\,, && (7.3)\\ \text{exclusive jet algorithms:} \quad & (\text{reference scale})^2 = 100\,\mathrm{GeV}^2\,, \quad y_{\mathrm{cut}} = 1\,, && (7.4)\\ \text{always:} \quad & -1 < \eta_{\mathrm{jet,\,lab}} < 2.5\,. \end{aligned}$$

In all cases we measure *inclusive* dijet cross sections, i.e. cross sections for the production of two or more jets within the acceptance region. The dijet cross sections are measured for a large set of variables, where all variables characterizing the dijet system are calculated from the two jets with highest $E_{T,\mathrm{jet,\,Breit}}$. The numerical values of the differential dijet cross sections can be found in appendix D.1.

In Fig. 7.2 we display the single differential dijet cross section measured with the inclusive $k_\perp$ algorithm as a function of Q^2 in the range $10 < Q^2 < 15\,000\,\mathrm{GeV}^2$. The results for the other jet algorithms are shown in Fig. 7.3 at $150 < Q^2 < 15\,000\,\mathrm{GeV}^2$.

The dijet cross sections measured are compared to the perturbative QCD predictions in next-to-leading order[3] (full line) and, in addition, to the product of the next-to-leading order prediction and the hadronization correction (dashed line), the latter being estimated by the HERWIG model (Fig. 3.1). While the hadronization corrections have only a small effect for the inclusive jet algorithms, they lower the perturbative cross section for the exclusive algorithms by up to 30% at $Q^2 = 150\,\mathrm{GeV}^2$. However, when these non-perturbative corrections are considered, the dijet cross sections for all four jet algorithms are described by the theoretical curves. Only towards small Q^2 values ($Q^2 < 70\,\mathrm{GeV}^2$) deviations are seen and the theory curve is below the data. In this kinematic range the next-to-leading order corrections to the dijet cross section are very large (up to a factor of two at $Q^2 = 10\,\mathrm{GeV}^2$, see

---

[2] This part of the analysis has been performed at an early stage of the present work, where it was not recognized that the data would not be useful in the QCD analysis, due to the very large theoretical uncertainties in the low Q^2 region. For completeness we have nevertheless included the results in the following comparisons. Details of the experimental procedure are described in [98, 99].

[3] The calculation has been performed as described for the inclusive jet cross section, with the only exception that here the renormalization scale is set to the average transverse energy of the dijet system $\mu_r = \overline{E}_T$.

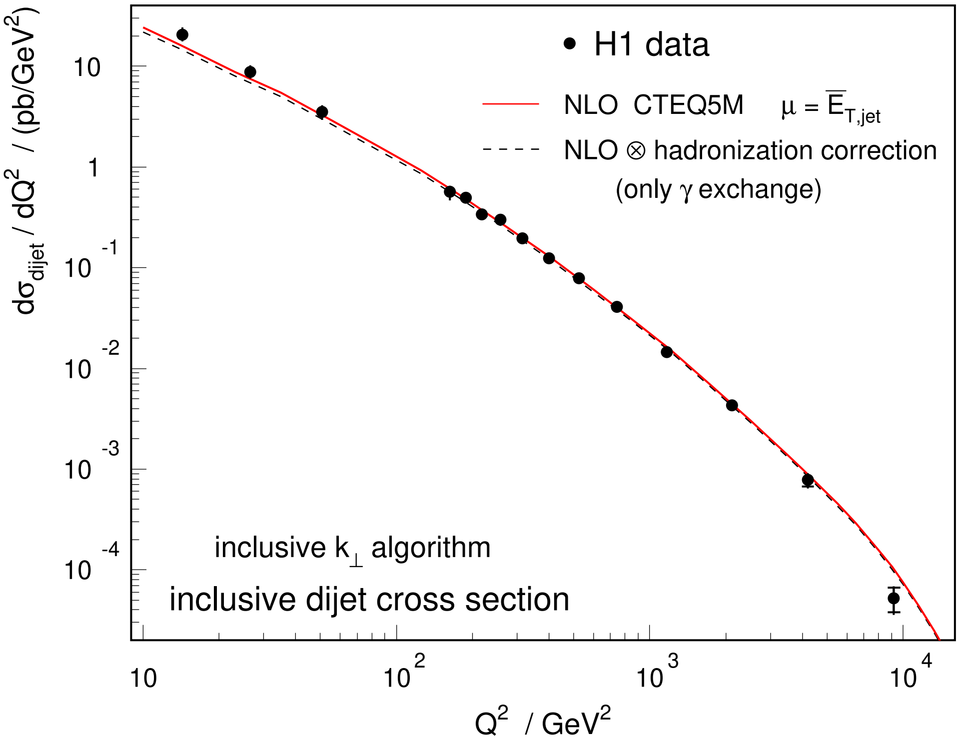

Figure 7.2: The dijet cross section measured with the inclusive $k_\perp$ algorithm as a function of Q^2. The data are compared to the perturbative QCD prediction in NLO (solid line) and to a theoretical prediction where non-perturbative corrections are included (dashed line) as described in the text.

Fig. 3.8). In a phase space where NLO corrections are sizeable, we also expect contributions from higher orders to become relevant.

Deviations between data and theory are also seen at the highest Q^2 point ($6000 < Q^2 < 15\,000\,\mathrm{GeV}^2$), where corrections due to Z° exchange (which are not included in the NLO calculation by DISENT) become sizable (see Fig. 3.7). For this reason we perform all further comparisons between data and theory only for $Q^2 < 5000\,\mathrm{GeV}^2$ where the corresponding effects are negligible.

In the following a more detailed look into differential dijet distributions for the four jet algorithms is given. In Figs. 7.4 – 7.7 we present the dijet cross section as a function of the average transverse jet energy $\overline{E}_T$, the invariant dijet mass M_{jj}, the jet pseudorapidity in the dijet center-of-mass frame η' and the reconstructed parton momentum fraction ξ. These distributions are shown in different regions of Q^2, except for the η' distribution, which is presented in regions of different $\overline{E}_T$. As for the Q^2 distribution in Fig. 7.3, we compare all results to the perturbative QCD prediction in next-to-leading order, and to a theory curve that includes non-perturbative corrections. In general we see a very good description of all distributions measured. Before we discuss details of the single observables, we summarize some general features.

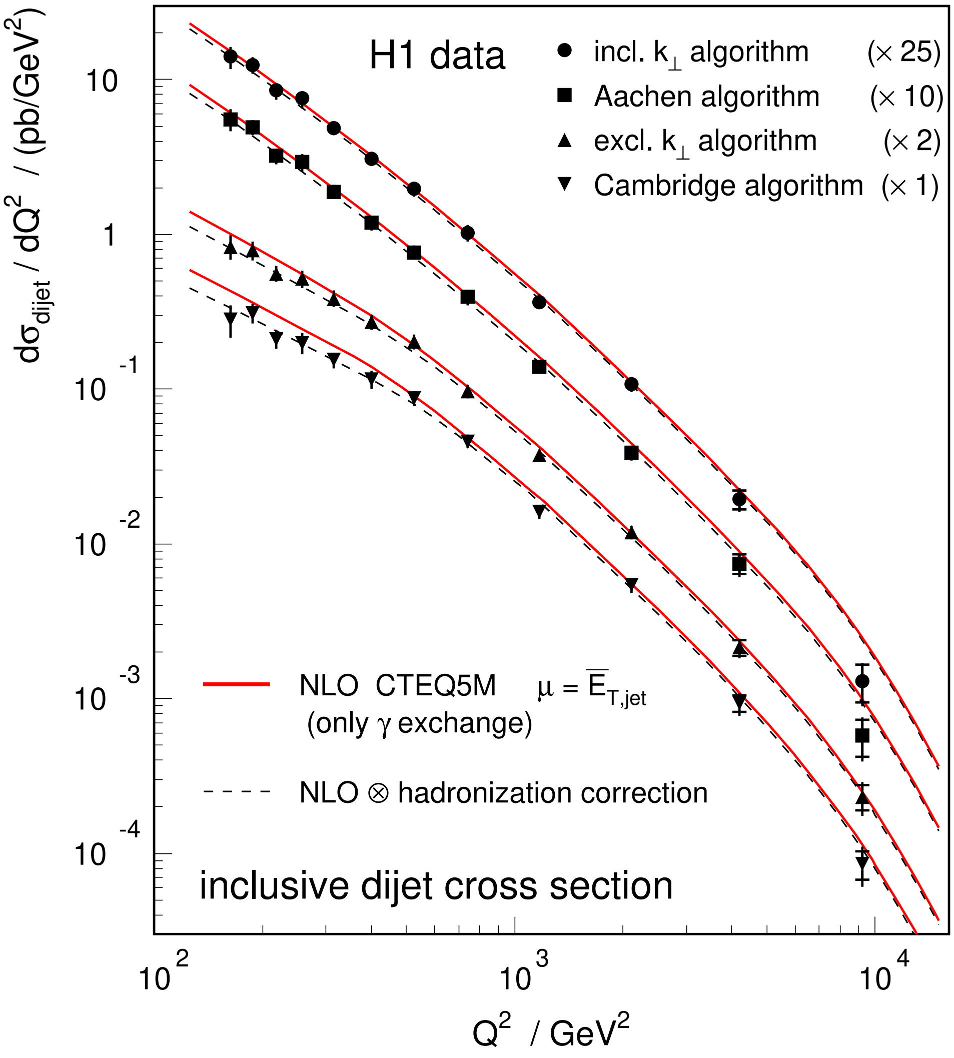

Figure 7.3: The dijet cross section as a function of Q^2 for four jet algorithms. The data are compared to the perturbative QCD predictions in NLO (solid line) and to a theoretical prediction where non-perturbative corrections are included (dashed line) as described in the text.

The low Q^2 data The data at lower momentum transfers $Q^2 < 70\,\mathrm{GeV}^2$, which are only measured for the inclusive $k_\perp$ algorithm (top left), are significantly above the theoretical predictions. This has to be seen, however, in the context of the very large NLO corrections (up to a factor of two at $Q^2 = 10\,\mathrm{GeV}^2$, see Fig. 3.8). The largest discrepancies are seen at smallest $\overline{E}_T$ and smallest M_{jj} and, correspondingly, at smallest ξ. At large values of $\overline{E}_T > 20\,\mathrm{GeV}$ or $M_{jj} > 40\,\mathrm{GeV}$ the low Q^2 data are reasonably well described by the perturbative calculation.

The inclusive jet definitions The dijet cross sections for both inclusive jet definitions, the inclusive $k_\perp$ algorithm (top left) and the Aachen algorithm (top right) are always of similar size and shape. This is, of course, expected since at next-to-leading order both definitions are identical and the predicted hadronization corrections are small for both. In all cases already the perturbative prediction gives a good description of the data.

The exclusive jet definitions The dijet cross sections, measured with the exclusive $k_\perp$ algorithm (bottom left) and the Cambridge algorithm (bottom right) also show very similar shapes, but are of slightly different size. For both exclusive algorithms some regions of phase space have large non-perturbative contributions (above 60%). These are the regions of small transverse jet energies and small dijet masses (and, correspondingly, small ξ values). In these regions the perturbative predictions alone are obviously not able to describe the data. Within the estimated size of the non-perturbative corrections, however, theory and data are mostly consistent, except in those regions where these corrections are too large. This may confirm our arguments from section 3.1 that the hadronization corrections, as estimated by parton-cascade models, are only reliably for comparisons to NLO calculations if the size of these corrections is small.

The distribution of the average transverse energy $\overline{E}_T$ of the dijet system (Fig. 7.4) is similar to the E_T distribution of the inclusive jet sample (Fig. 7.1). For all algorithms we observe a harder $\overline{E}_T$ spectrum towards larger Q^2. The same is seen in the distribution of the dijet mass (Fig. 7.5) which fall more steeply towards higher masses at lower Q^2.

The jet pseudorapidity in the dijet center-of-mass frame is given by the variable η', which is reconstructed from the difference of the jet pseudorapidities in the Breit frame. The η' distribution is shown in Fig. 7.6 in different regions of $\overline{E}_T$. We see that at higher $\overline{E}_T$ large values of η' are more strongly suppressed, such that the fraction of jets produced centrally in the dijet center-of-mass frame is larger at high $\overline{E}_T$.

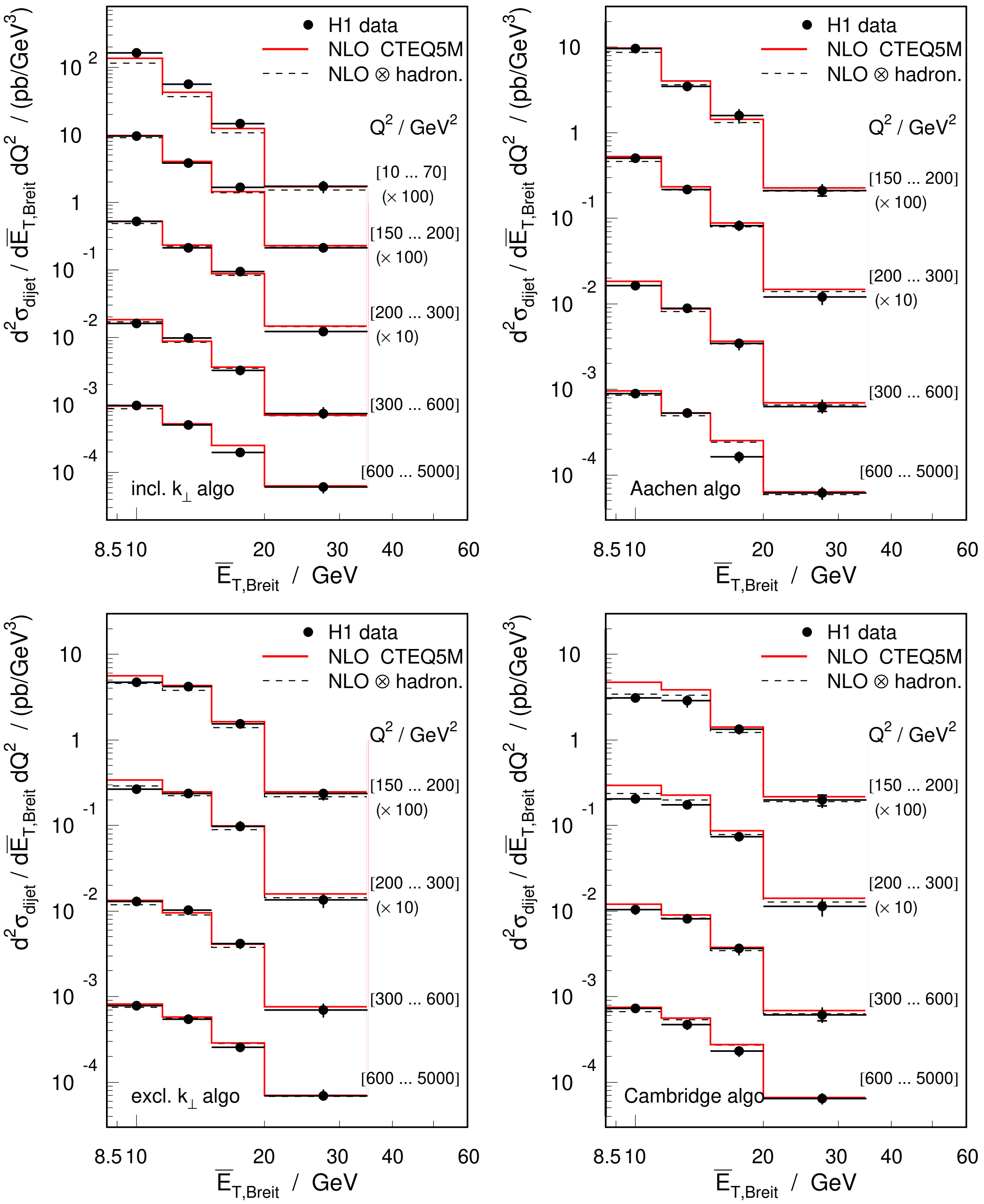

Figure 7.4: The dijet cross section as a function of the average transverse jet energy in the Breit frame in different regions of Q^2 for the inclusive $k_\perp$ algorithm (top left), the Aachen algorithm (top right), the exclusive $k_\perp$ algorithm (bottom left) and the Cambridge algorithm (bottom right). The data are compared to the perturbative QCD predictions in NLO (solid line) and to a theoretical prediction where non-perturbative corrections are included (dashed line) as described in the text.

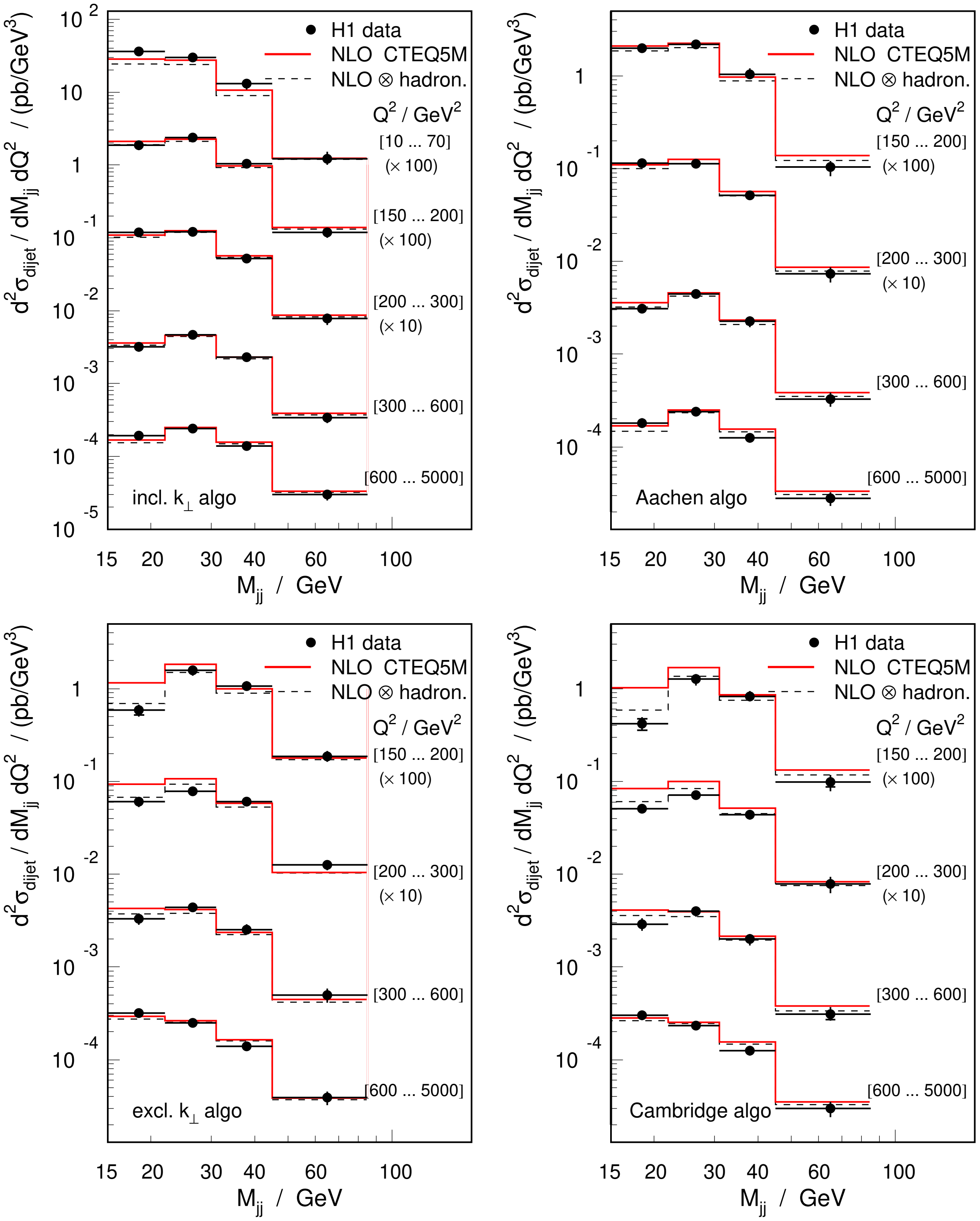

Figure 7.5: The dijet cross section as a function of the invariant dijet mass in different regions of Q^2 for the inclusive $k_\perp$ algorithm (top left), the Aachen algorithm (top right), the exclusive $k_\perp$ algorithm (bottom left) and the Cambridge algorithm (bottom right). The data are compared to the perturbative QCD predictions in NLO (solid line) and to a theoretical prediction where non-perturbative corrections are included (dashed line) as described in the text.

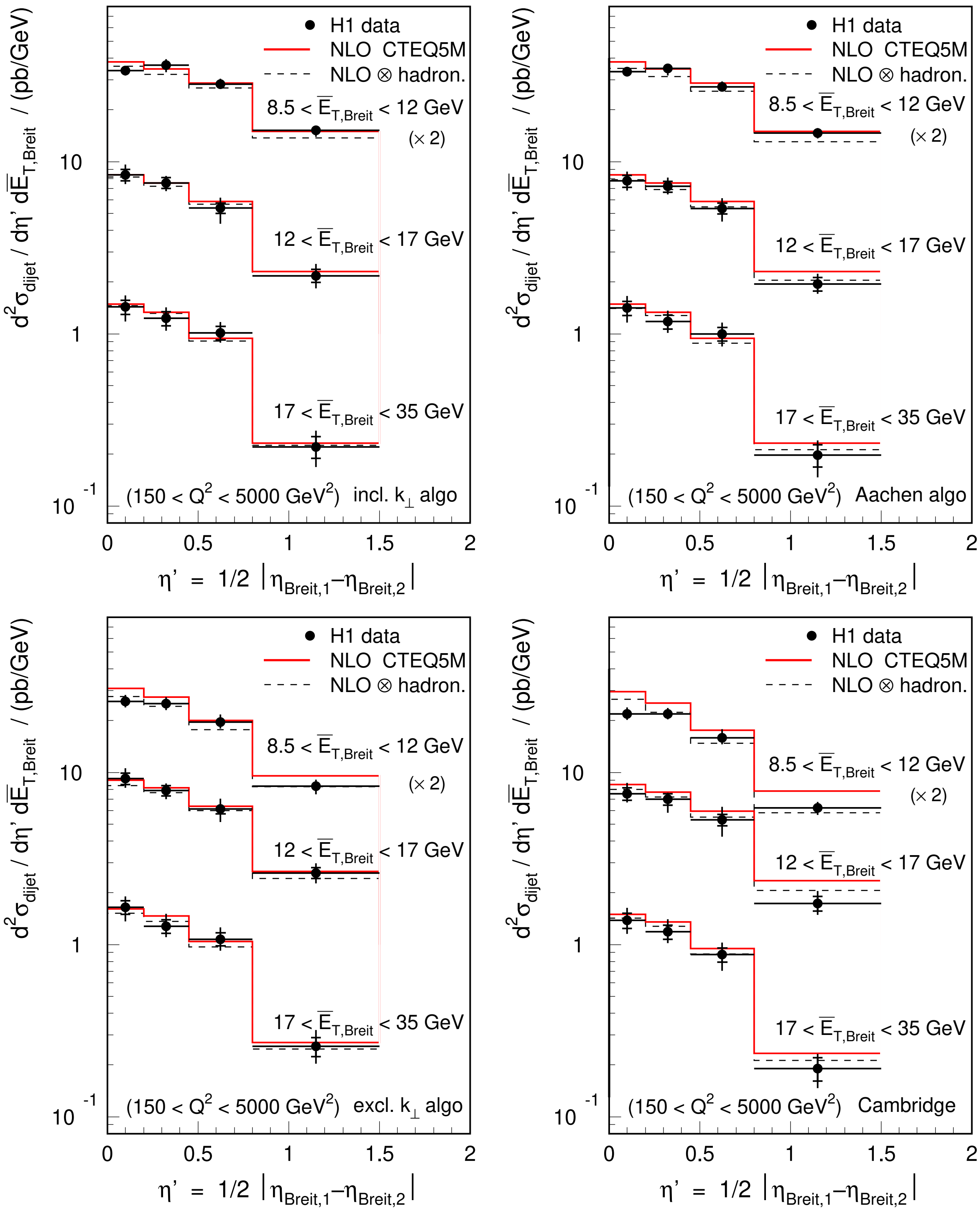

Figure 7.6: The dijet cross section as a function of the jet pseudorapidity in the dijet center-of-mass frame. The data are measured in different regions of $\overline{E}_T$ for the inclusive $k_\perp$ algorithm (top left), the Aachen algorithm (top right), the exclusive $k_\perp$ algorithm (bottom left) and the Cambridge algorithm (bottom right). The data are compared to the perturbative QCD predictions in NLO (solid line) and to a theoretical prediction where non-perturbative corrections are included (dashed line) as described in the text.

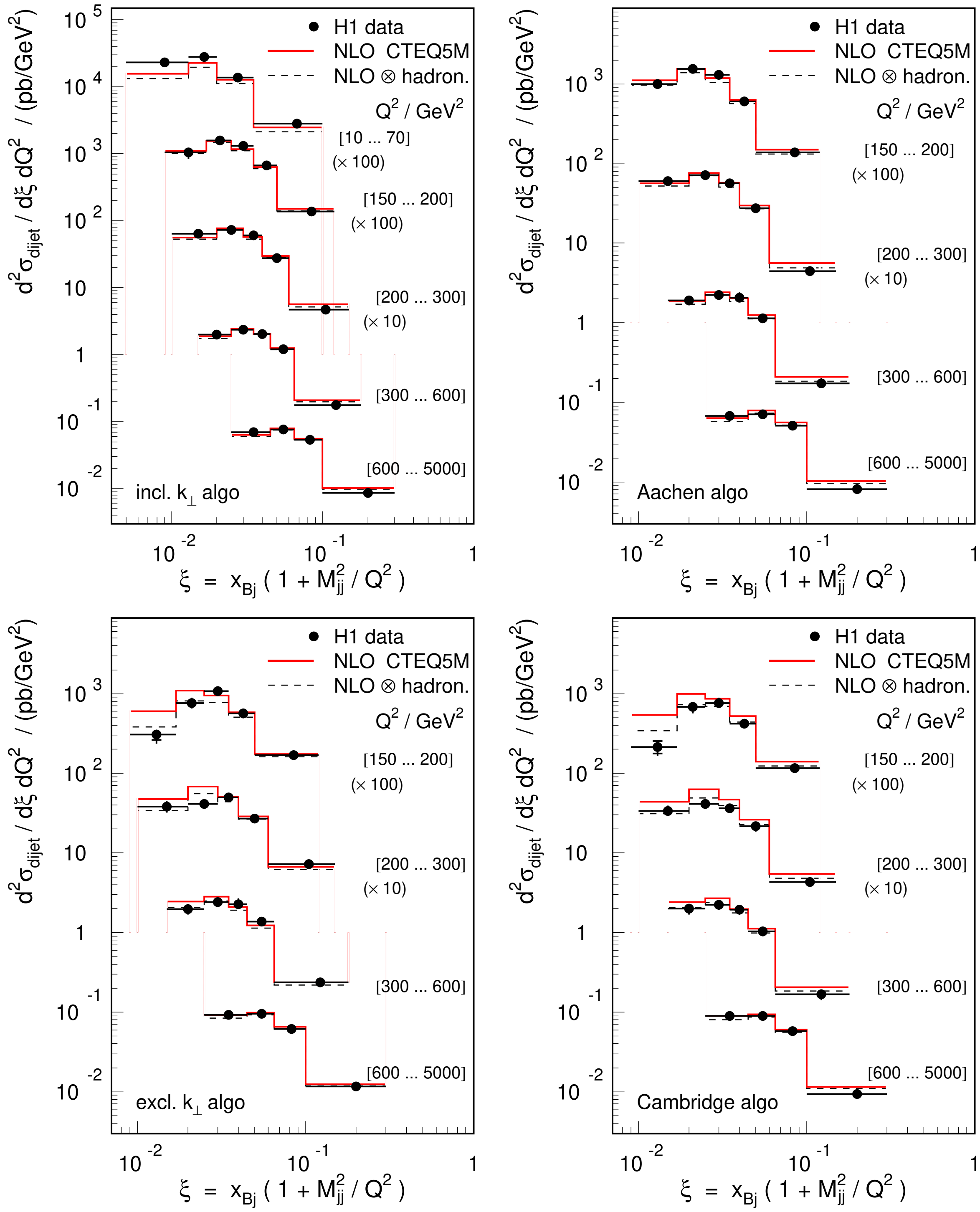

Figure 7.7: The dijet cross section as a function of the reconstructed parton momentum fraction ξ. The data are measured in different regions of Q^2 for the inclusive $k_\perp$ algorithm (top left), the Aachen algorithm (top right), the exclusive $k_\perp$ algorithm (bottom left) and the Cambridge algorithm (bottom right). The data are compared to the perturbative QCD predictions in NLO (solid line) and to a theoretical prediction where non-perturbative corrections are included (dashed line) as described in the text.

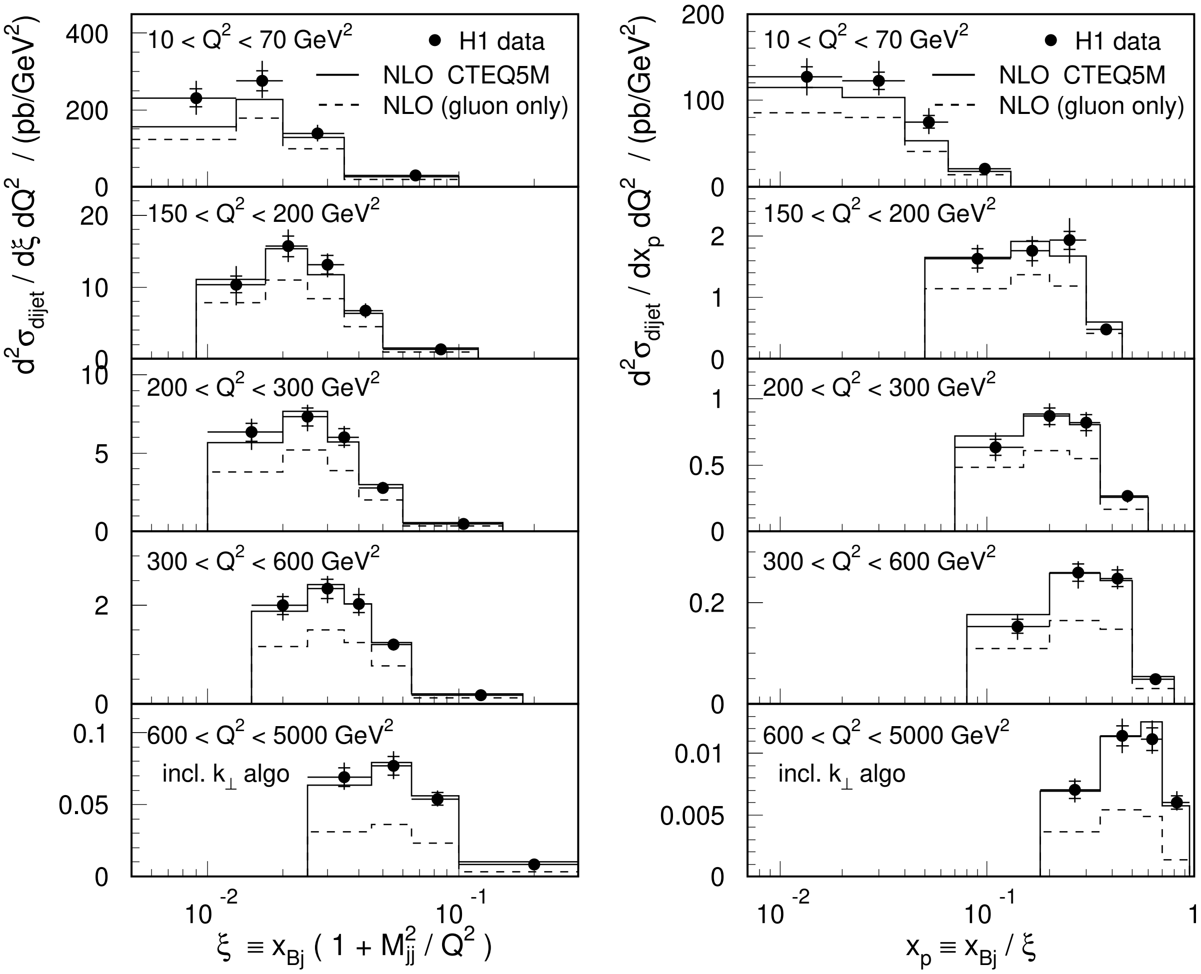

Figure 7.8: The dijet cross section for the inclusive $k_\perp$ algorithm as a function of the variables ξ (left) and x_p (right). The perturbative QCD prediction in NLO (solid line) is compared to the measured dijet cross section. In addition the contribution from gluon induced processes is shown (dashed line).

The variable ξ represents (in the leading order approximation) the fraction of the proton momentum carried by the incoming parton. The dijet cross section in bins of ξ is therefore directly proportional to the size of the parton densities at a specific parton momentum fraction. In Fig. 7.7 the ξ distributions are shown for the four jet algorithms. At $Q^2 > 150\,\mathrm{GeV}^2$ the dijet data are sensitive to partons of momentum fractions $0.01 \lesssim \xi \lesssim 0.2$, increasing with increasing Q^2.

Due to its direct sensitivity to the parton densities the ξ distribution is of special importance in the QCD analysis, for the determination of the gluon density in the proton. For this reason we display the distributions of ξ and further variables now in a different representation for the inclusive $k_\perp$ algorithm, showing also the fractional contribution from gluon induced processes to all distributions. The data are here compared to the perturbative next-to-leading calculation only.

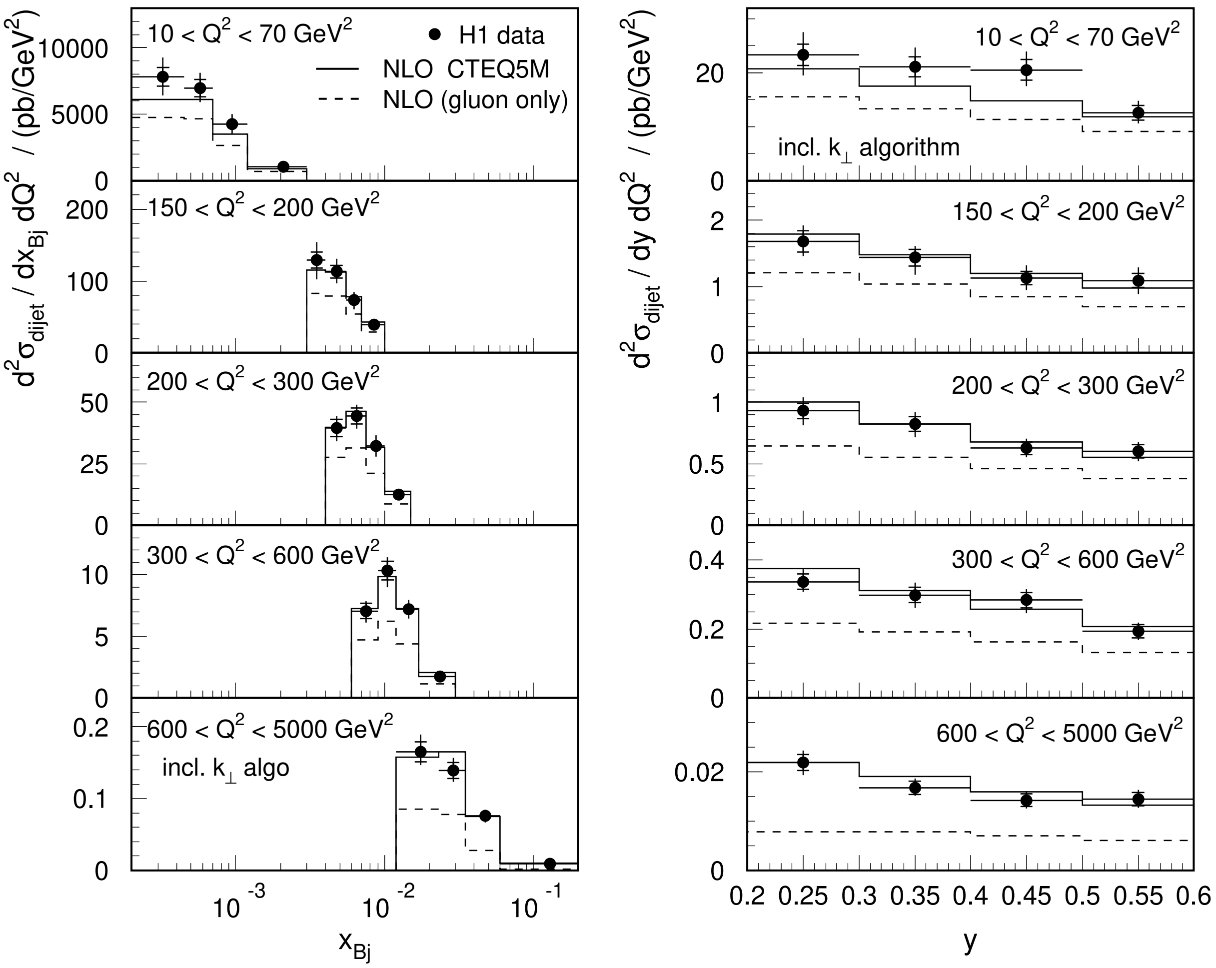

Figure 7.9: The dijet cross section for the inclusive $k_\perp$ algorithm as a function of the kinematic variables x_{Bj} (left) and y (right). The perturbative QCD prediction in NLO (solid line) is compared to the measured dijet cross section. In addition the contribution from gluon induced processes is shown (dashed line).

In Fig. 7.8 (left) we show again the ξ distribution for the inclusive $k_\perp$ algorithm. The gluon induced contribution to the dijet cross section is indicated by the dashed line. This contribution can be seen to decrease strongly with increasing Q^2 and with increasing ξ. In this and the following distributions we see that the theory gives a good description of the data, independent of the size of the fractional gluon contribution. This may give confidence that the agreement between theory and data is not accidental, but that perturbative QCD is able to describe jet production in deep-inelastic scattering, such that these data can be used for the determination of parameters, as e.g. α_s or the gluon density in the proton.

The distribution of the partonic scaling variable x_p is shown in the right plot in Fig. 7.8. It is defined as the ratio of the Bjorken scaling variable x_{Bj} and the parton momentum fraction ξ. We observe a strong increase of x_p towards larger Q^2. While in the inclusive deep-inelastic scattering cross section the variable x_{Bj} is directly related to the momentum

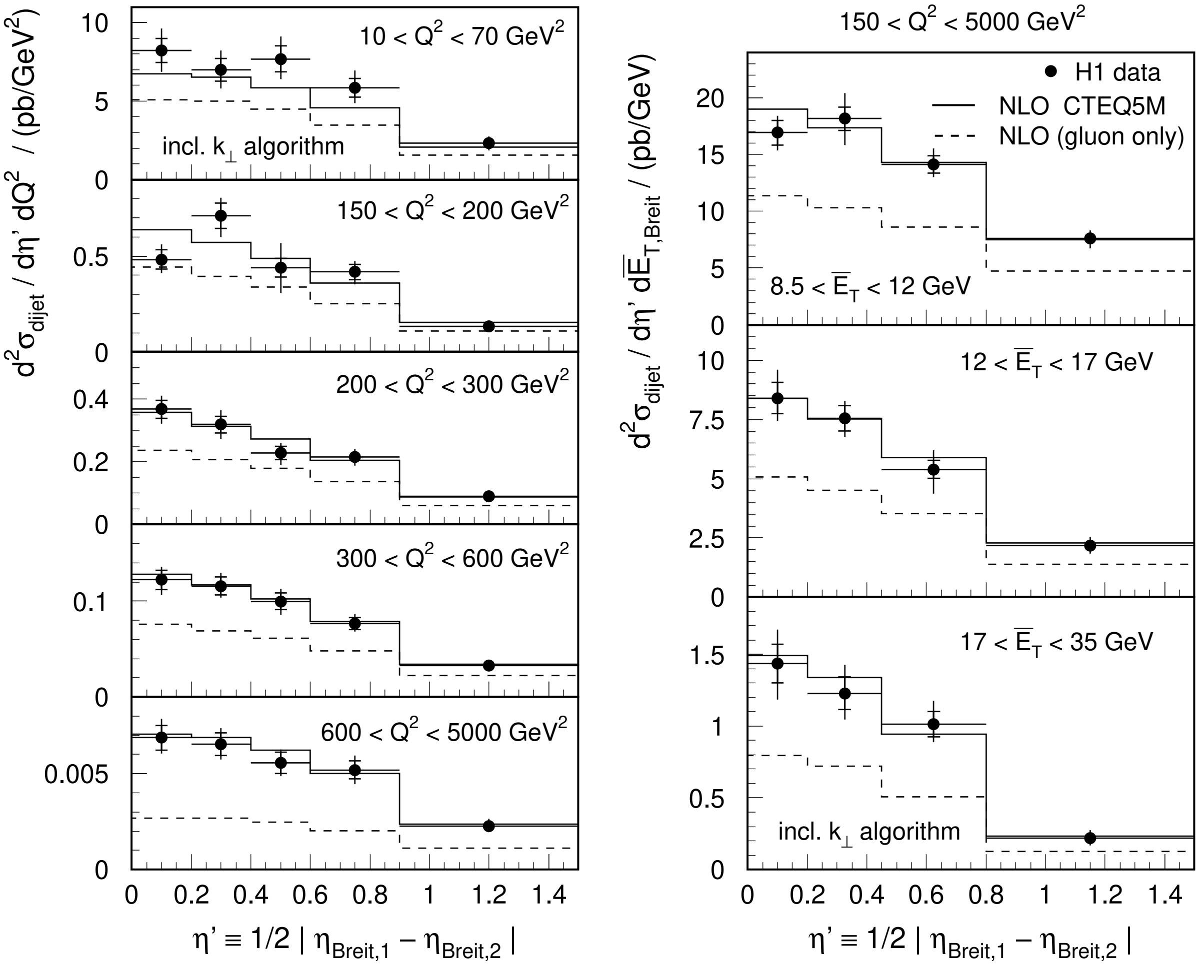

Figure 7.10: The dijet cross section for the inclusive $k_\perp$ algorithm as a function of the jet pseudorapidity η' in different regions of Q^2 (left) and $\overline{E}_T$ (right). The perturbative QCD prediction in NLO (solid line) is compared to the measured dijet cross section. In addition the contribution from gluon induced processes is shown (dashed line).

fraction of the incoming parton, the x_p distribution demonstrates that this is not longer the case in dijet production, where $x_{\rm Bj}$ can be very different from ξ (by a factor of 100 at small Q^2).

Variables connected to the event kinematics are shown in Fig. 7.9. The accessible range of the Bjorken scaling variable $x_{\rm Bj}$ (left) shows a strong Q^2 dependence, varying over three decades within the range $2 \cdot 10^{-4} < x_{\rm Bj} < 2 \cdot 10^{-1}$ for $10 < Q^2 < 5000\,{\rm GeV}^2$. The inelasticity variable y shows a slight decrease towards larger values in all Q^2 regions, with an almost constant gluon fraction within the single Q^2 ranges.

The variable η' (already discussed before in Fig. 7.6) is shown in Fig. 7.10 in different regions of Q^2 (left) and in regions of $\overline{E}_T$ (right). In contrast to the $\overline{E}_T$ dependence of the η' distribution we do not observe any change with Q^2. It is again visible that the gluon fraction decreases towards larger Q^2, while it is only weakly depending on $\overline{E}_T$.

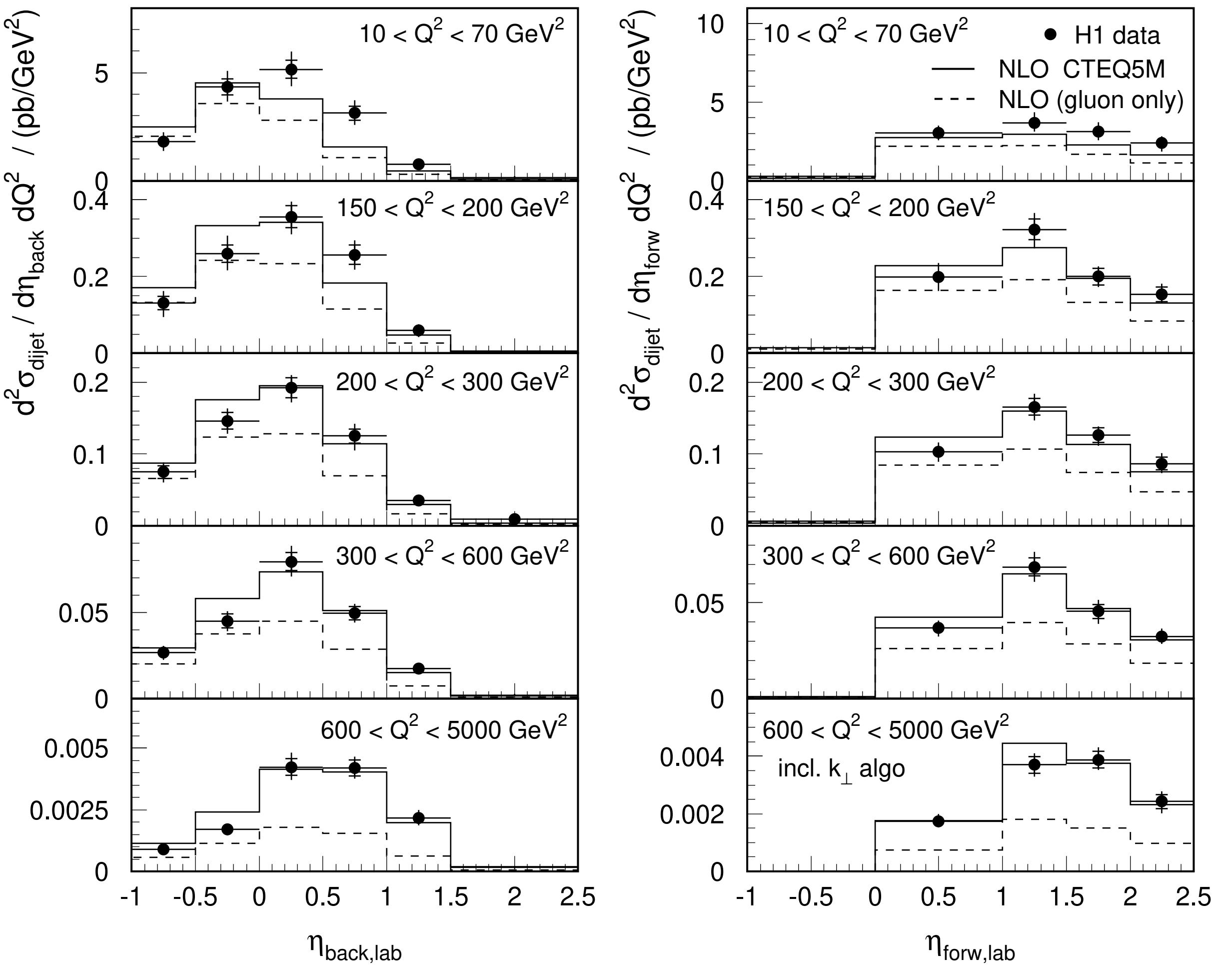

Figure 7.11: The dijet cross section for the inclusive $k_\perp$ algorithm as a function of the pseudorapidity of the backward (left) and the forward jet (right) in the laboratory frame. The perturbative QCD prediction in NLO (solid line) is compared to the measured dijet cross section. In addition the contribution from gluon induced processes is shown (dashed line).

The last dijet distributions shown here, are mainly presented to study how well the variables are described by theory that define the angular acceptance region of the dijet event sample. In Fig. 7.11 we display the jet pseudorapidity distributions in the laboratory frame, for the backward jet (left) and for the forward jet (right). At $Q^2 < 70\,\mathrm{GeV}^2$ we see that the deviations between data and theory are connected to jets, produced towards the proton (i.e. the forward) direction. These are the only distribution for the low Q^2 data, in which one sees a clear difference which does not only affect the size of the cross section, but also the shape of the distribution.

At higher Q^2 the data are well described by the theory, such that we do not have to worry that any conclusion (or result of the QCD fit) may be an artifact, depending on the angular acceptance region chosen in the analysis.

7.3 Three-Jet and Four-Jet Cross Sections

The measurements of the three-jet and the four-jet cross sections have been performed in collaboration with Arno Heister. Preliminary results of the three-jet analysis have been published in a conference contribution by the H1 collaboration [100]. A detailed description of the analysis is given in Arno Heister's Diploma thesis [96]. The analysis is based on data taken in the years 1995–1997 by the H1 experiment, corresponding to an integrated luminosity of $\mathcal{L}_{\text{int}} = 33\,\text{pb}^{-1}$. The kinematic range is given by

$$0.2 < y < 0.6\,, \qquad 150 < Q^2 < 5000\,\text{GeV}^2\,. \tag{7.5}$$

Jets are defined by the inclusive $k_\perp$ jet algorithm in the Breit frame. Only jets are considered which satisfy

$$E_{T,\text{jet, Breit}} > 5\,\text{GeV}\,, \quad \text{and} \quad -1 < \eta_{\text{jet, lab}} < 2.5\,. \tag{7.6}$$

To measure the three-jet (four-jet) cross section we select events with, at least, three (four) jets with the additional requirement

$$M_{3\,\text{jet}} > 25\,\text{GeV}\,, \quad \text{and} \quad M_{4\,\text{jet}} > 25\,\text{GeV} \quad \text{respectively}\,, \tag{7.7}$$

where the invariant multi-jet mass $M_{\text{n}\,\text{jet}}$ is calculated from the three (four) highest E_T jets.

Fig. 7.12 shows the three-jet and the four-jet cross sections as a function of Q^2 (left), the invariant multi-jet mass (right) and the average transverse jet energy of the multi-jet system in the Breit frame (bottom). The results are compared to perturbative QCD calculations[4] in leading order (i.e. $\mathcal{O}(\alpha_s^2)$ and $\mathcal{O}(\alpha_s^3)$, respectively). In addition we show the product of the leading order calculation and the expected hadronization corrections[5]. The hadronization corrections to the three-jet cross section are on average 20% and the corrections to the four-jet cross section are 50%, both decreasing towards higher invariant jet masses and transverse jet energies.

While the perturbative QCD prediction is in most bins slightly above the data, we obtain a good description when we consider the non-perturbative corrections. Only at the smallest Q^2 and $M_{3\,\text{jet}}$ the theory curve for the three-jet cross section is below the data.

Further results from this analysis on three-jet and four-jet production, including cross sections for different variables, as well as angular jet distributions in the multi-jet center-of-mass frame can be found in [96, 100].

---

[4] The calculations have been performed by the program MEPJET [57], using CTEQ5L parton distributions with the corresponding value of $\alpha_s(M_Z) = 0.127$ which is evolved according to the 1-loop solution of the renormalization group equation. The renormalization and factorization scales are set to the average transverse jet energy of the three-jet (four-jet) system in the Breit frame $\mu_r = \mu_f = \overline{E}_T$. The calculation of the three-jet cross section includes quark mass effects, which lower the results by approximately 3%.

[5] The hadronization corrections have been estimated in [96] using the models HERWIG and LEPTO which agree within a few percent for all distributions shown.

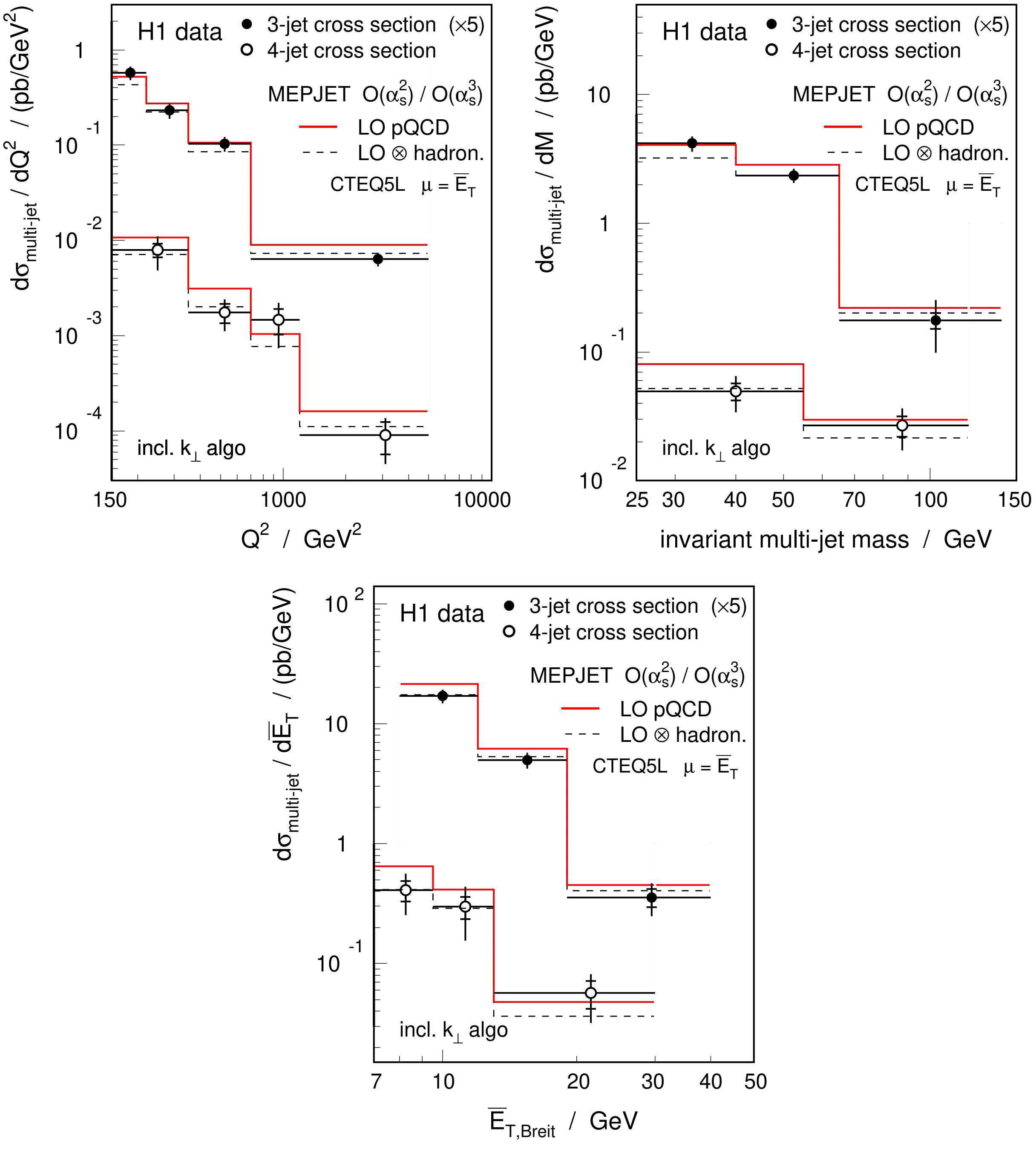

Figure 7.12: The three-jet and the four-jet cross sections, measured using the inclusive $k_\perp$ jet algorithm as a function of Q^2 (left), the invariant three-jet mass (right) and the average transverse energy $\overline{E}_T$ of the multi-jet system in the Breit frame (bottom). The data are compared to the perturbative QCD prediction in leading order (solid line) and to a prediction including hadronization corrections (dashed line) as described in the text.

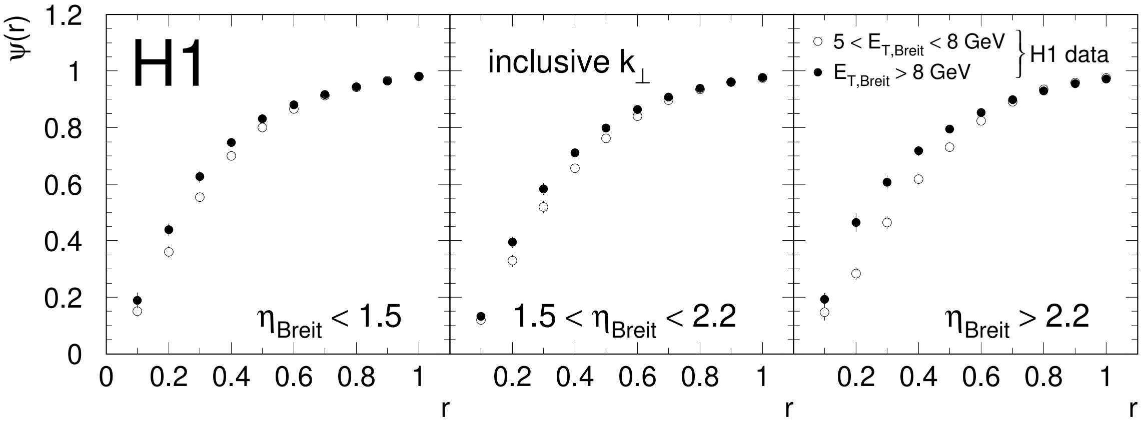

Figure 7.13: Jet shapes measured in an inclusive dijet sample for the inclusive $k_\perp$ algorithm. The jet shapes are compared for different transverse jet energies in three different ranges of the pseudorapidity in the Breit frame $\eta_{\mathrm{jet,\,Breit}}$.

7.4 Internal Jet Structure

The internal structure of jets is studied in terms of jet shapes and subjet multiplicities (the exact definitions of the observables are given in section 2.4). We have already presented jet shapes and subjet multiplicities for jets in the inclusive jet sample in section 5.2.2, where *reconstructed* data distributions have been compared to the Monte Carlo simulation. These distributions are, however, not corrected for detector effects and are only intended to test the simulation.

A full analysis of internal jet structure, providing corrected data distributions, has been performed in collaboration with Lars Sonnenschein and is published in [101]. A detailed description of the experimental procedure can be found in Lars Sonnenschein's Diploma thesis [97]. Here we only give a brief description of the main results.

The analysis is based on H1 data taken in the year 1994, corresponding to an integrated luminosity of $\mathcal{L}_{\mathrm{int}} \simeq 2\,\mathrm{pb}^{-1}$. The measurement is performed in the phase space given by

$$y > 0.15\,, \qquad Q^2 > 10\,\mathrm{GeV}^2\,, \qquad E' > 11\,\mathrm{GeV}\,, \qquad \theta_e > 156^\circ\,. \tag{7.8}$$

We have measured the internal structure of jets in an inclusive dijet sample, employing the inclusive $k_\perp$ algorithm in the Breit frame[6]. The jet phase space is defined by

$$E_{T,\mathrm{jet,\,Breit}} > 5\,\mathrm{GeV} \qquad \text{and} \qquad -1 < \eta_{\mathrm{jet,\,lab}} < 2\,. \tag{7.9}$$

The jet shapes and the subjet multiplicities are presented in Figs. 7.13 and 7.14 in three different regions of the jet pseudorapidity $\eta_{\mathrm{jet,\,Breit}}$. In each $\eta_{\mathrm{jet,\,Breit}}$ region the distributions for jets of different transverse energies E_T in the Breit frame are shown.

---

[6] Further results, obtained with a cone jet algorithm can be found in references [97, 101].

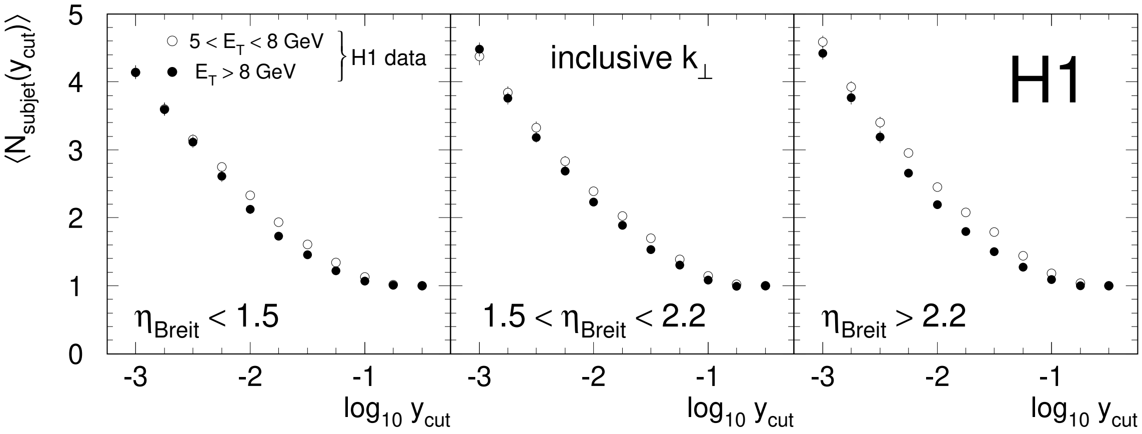

Figure 7.14: The average number of subjets measured in an inclusive dijet sample for the inclusive $k_\perp$ algorithm. The subjet multiplicities are compared for different transverse jet energies in three different ranges of the pseudorapidity in the Breit frame $\eta_{\mathrm{jet,\,Breit}}$.

Jet Shapes

The jet shape $\psi(r)$ is defined as the average fractional transverse jet energy contained in a cone of radius r (in η-ϕ space), around the jet axis. In Fig. 7.13 the $\psi(r)$ distribution is shown as a function of the cone radius r. At fixed r the jets of higher E_T have larger values of $\psi(r)$, indicating that these jets are more collimated.

We also observe a dependence of the jet shape on $\eta_{\mathrm{jet,\,Breit}}$ which is more pronounced for jets of lower E_T. The jets at larger $\eta_{\mathrm{jet,\,Breit}}$ (i.e. towards the proton direction) are seen to be broader than backward jets (towards the photon direction).

In a recent analysis the OPAL collaboration has presented a measurement of jet shapes in dijet production in $\gamma\gamma$ collisions [102]. A comparison of these results and our results has been made in [103] and it is seen that the jets from both processes have very similar shapes.

Subjet Multiplicities

The average number of subjets $\langle N_{\mathrm{subjet}}(y_{\mathrm{cut}})\rangle$ is shown in Fig. 7.14 as a function of the subjet resolution parameter y_{cut}, which specifies the relative squared transverse momentum at which local structures (i.e. subjets) within the jet are resolved. The region of larger y_{cut} is sensitive to perturbative processes whereas non-perturbative contributions become increasingly important with decreasing y_{cut}. The subjet multiplicity therefore allows to study the transition from perturbative to non-perturbative processes, while the jet shape is influenced by both perturbative and non-perturbative processes over the whole r range.

At a fixed value of y_{cut} the jets of higher E_T have a smaller average number of subjets, and jets towards the proton direction have a larger number of subjets. Although the jet shapes and the subjet multiplicities are sensitive to different aspects of the jet broadening,

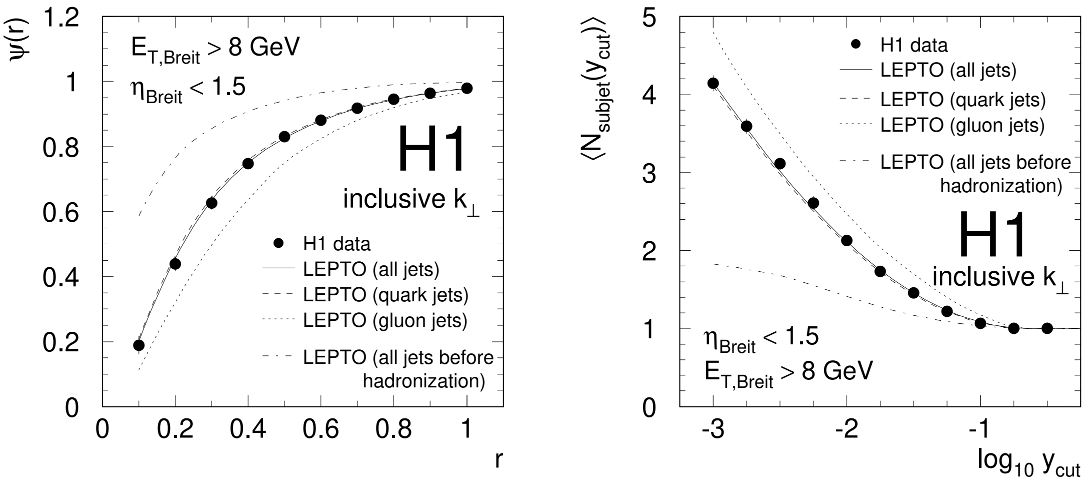

Figure 7.15: A comparison of the measured jet shape (left) and the average number of subjets (right) with the predictions of the Monte Carlo generator LEPTO for the total jet sample (solid line), as well as for the jet subsamples consisting only of quark (dashed line) and gluon induced jets (dotted line). In addition, also the predictions for the observables before hadronization are included (dashed-dotted line).

consistent conclusions can be drawn for both observables: The jet broadening increases at lower E_T and towards the proton direction.

The data at higher E_T and smallest $\eta_{\text{jet, Breit}}$ are compared to the predictions of LEPTO[7] in Fig. 7.15. Although in previous analyses of DIS jet data in similar kinematic regions (see e.g. [104, 105]) QCD models like LEPTO, based on leading order matrix elements combined with parton showers, were not able to describe the jet rates (respectively the jet cross sections), LEPTO gives a good description of the internal structure of these jets.

Also included in Fig. 7.15 is the LEPTO prediction of the observables before hadronization (i.e. for jets on “parton-level”). We see that these jets are significantly narrower and that the largest fraction of the broadness develops during the hadronization process. It is therefore surprising that basic characteristics of the perturbative phase are still visible after hadronization, as we will show in the following.

Within a model based on leading order matrix elements combined with parton showers, we can distinguish whether a jet is induced by a quark or by a gluon. Technically this is done by comparing the direction of a selected jet to the direction of a quark or a gluon emerging from the matrix element. The LEPTO predictions for quark and gluon induced jets are both included in Fig. 7.15. It is seen that (within this model!) gluon jets are significantly broader than quark jets, a feature that is preserved after hadronization.

In the LEPTO prediction (as well as in next-to-leading order calculations) the boson-

---

[7] The LEPTO [65] predictions have been obtained without the “Soft Color Interaction” model, using the CTEQ4L parton distributions [77].

gluon fusion process accounts for 80% of all dijet events in this event sample while only 20% of the events are from QCD-Compton processes.. Correspondingly 90% of the jets are quark induced. Therefore the total jet sample mainly reflects the properties of quark jets.

Given that these model predictions give a reasonable description of the observed jet structure we conclude that the jets measured are consistent with being mainly induced by quarks, i.e. that the dijet event sample is dominated by the boson-gluon fusion process.

Due to the large size of the non-perturbative contributions, as visible in Fig. 7.15, we consider a comparison to perturbative QCD predictions in fixed order α_s for these observables not to be meaningful.

7.5 Summary

We have presented measurements of jet observables in the Breit frame in deep-inelastic scattering over a large range of four-momentum transfers $10 < Q^2 < 15\,000\,\mathrm{GeV}^2$ and transverse jet energies $50 \lesssim E_T^2 \lesssim 2500\,\mathrm{GeV}^2$. A large variety of observables has been employed for detailed tests of the theoretical predictions.

The Central Analysis

What we call "central analysis" contains the results that we will use in the following QCD analysis. The **inclusive jet cross section** and **the dijet cross section** have been measured for a comprehensive set of variables at **large momentum transfers** $Q^2 > 150\,\mathrm{GeV}^2$ where the perturbative QCD predictions in next-to-leading order are seen to have small uncertainties. These results have been obtained using the **inclusive $\boldsymbol{k_\perp}$ ordered jet clustering algorithm** for which hadronization corrections are small (always below 10%). The theoretical predictions give a good description of the data over the whole phase space, in regions which are dominated by boson-gluon fusion, as well as in regions dominated by the QCD-Compton process. This central analysis has been extended in various respects.

Different Jet Definitions

The measurements of the inclusive jet and the dijet cross section have been repeated using different types of jet definitions. Switching to an **angular ordered jet clustering algorithm** ("Aachen algorithm") leads to very similar cross sections. While the perturbative NLO predictions are identical for this definition, the measured cross sections are slightly smaller (by a few percent). This is perfectly consistent with the prediction of slightly larger hadronization corrections (also a few percent) for this jet definition.

We have also redone the analysis using **exclusive jet clustering algorithms**, i.e. jet definitions which cluster all final state particles into the hard jets (or the proton remnant). A $k_\perp$ ordered and an angular ordered jet definition ("Cambridge algorithm") have been used. Both of these algorithms have significantly larger hadronization corrections (up to 30% at $Q^2 = 150\,\mathrm{GeV}^2$) than the inclusive jet algorithms. However, the model estimates of these corrections can account for the observed differences to the perturbative QCD predictions in next-to-leading order. The combined theoretical predictions (i.e. perturbative and non-perturbative contributions) give a good description of the dijet data, also for these jet definitions.

Higher Jet Multiplicities

One part of the analysis is dedicated to the production rates of higher jet multiplicities. Differential cross sections have been measured in **three-jet production** and in **four-jet production** as functions of the momentum transfer Q^2, the average transverse jet energy $\overline{E}_T$ in the Breit frame and the invariant three-jet and four-jet mass $M_{\mathrm{n\,jet}}$. These multi-jet cross sections are subject to relatively large hadronization corrections (20% for the three-jet cross section and 50% for the four-jet cross section). For these observables perturbative QCD calculations are only available in leading order (i.e. $\mathcal{O}(\alpha_s^2)$ and $\mathcal{O}(\alpha_s^3)$ for the three-jet, respectively the four-jet cross section). When these leading order predictions are combined with the estimated hadronization corrections they give a good description of the data.

Internal Jet Structure

The internal structure of jets has been investigated in terms of **jet shapes** and **subjet multiplicities**. For both quantities we observe a decrease of the jet broadness with increasing transverse jet energy. In the range of the transverse jet energies studied here, both observables are dominated by non-perturbative processes, and are well described by models combining parton showers and phenomenological hadronization models.

Extension to low Q^2

The dijet analysis at high Q^2 has also been extended to the region of $10 < Q^2 < 70\,\mathrm{GeV}^2$. In this region (where hadronization corrections for the inclusive $k_\perp$ algorithm are still below 10%) the perturbative QCD prediction in next-to-leading order is no longer able to describe the size of the measured dijet cross section (except maybe at $\overline{E}_T > 20\,\mathrm{GeV}$ or $M_{jj} > 40\,\mathrm{GeV}$).

In this kinematic region, however, next-to-leading order corrections are very large (up to a factor of two at $Q^2 = 10\,\mathrm{GeV}^2$) and terms of higher orders in α_s are likely to be non-negligible.

The exact numerical values of the inclusive jet cross sections and the dijet cross sections are listed in appendix D.1.

Part III

Interpretation: Direct Determination of the Strong Coupling Constant and the Gluon Density in the Proton in a QCD Fit to Jet Cross Sections

8

Outline of the QCD Analysis

Before we interpret the measurements in the framework of perturbative QCD, we introduce various strategies of performing the QCD analysis and describe the physical goals and the physical and technical choices that we have made.

8.1 Where We Stand

As a first step we briefly recall the results from part one and part two and discuss what has been obtained by now experimentally and theoretically.

Theoretically – a priori

We have compared properties of different jet observables to identify those for which the theory is most predictive. Requiring small hadronization corrections and a small renormalization scale dependence, we find that for the inclusive $k_\perp$ algorithm the theoretical predictions are safe at large momentum transfers $Q^2 \gtrsim 100\,\mathrm{GeV}^2$ for sufficiently large transverse jet energies. In this region we expect the theory to describe the production of jets in deep-inelastic scattering. In the region of $Q^2 \lesssim 100\,\mathrm{GeV}^2$ the uncertainties of perturbative calculations become large and the influence of non-perturbative corrections becomes increasingly important. It can therefore not be expected that theory and data agree in this kinematic region.

Experimentally

The measurement has provided us many distributions of the inclusive jet cross section and the dijet cross section for different jet definitions. For all distributions the full list of uncertainties is available for all different sources as well as all correlations. The most important distributions are those which can be directly related to the parameters which we intend to determine in the subsequent QCD analysis. These are the differential jet cross sections as a function of the energy scales E_T and Q^2 (available for both the inclusive jet and the dijet cross section) and the dependence on the reconstructed parton momentum fraction ξ (dijet cross section).

Theoretically – a posteriori

Using parton density functions obtained in global fits to DIS structure function data and Drell-Yan data and a value of $\alpha_s(M_Z)$ as e.g. determined in e^+e^- collisions, the theory describes the jet data in the phase space region $Q^2 > 100\,\mathrm{GeV}^2$ where it is expected (from a priori arguments) to be reliable. Only in the region $Q^2 < 100\,\mathrm{GeV}^2$ we see discrepancies between theory and data which are increasing towards smaller Q^2.

The good agreement in the region of $Q^2 > 100\,\mathrm{GeV}^2$ is seen in all differential distributions. We mean that the theory is "in principle" able to describe the DIS jet data. By "in principle" we mean that theory would give a perfect description if the "true" values of the free parameters (α_s and parton densities) were known. We therefore intend to use the distributions measured and fit the free parameters of the theory: $\alpha_s(M_Z)$, the gluon and the quark densities in the proton.

Additional Data Set: The Inclusive Reduced *ep* Cross Section

As we will show below, a consistent determination of the gluon density from the jet cross sections requires the knowledge of the quark densities from additional data. For this purpose we include data on the inclusive *ep* cross section in the QCD analysis. The data are taken from a recent publication by the H1 collaboration [32] in which the inclusive reduced double differential *ep* cross section ($\mathrm{d}^2\sigma_{\mathrm{DIS}}/\mathrm{d}x_{\mathrm{Bj}}\mathrm{d}Q^2$) is measured within the range $150 < Q^2 < 30\,000\,\mathrm{GeV}^2$. Since the present jet cross section measurements are based on similar analysis methods the correlations between the experimental uncertainties of both data sets can be taken into account in the statistical analysis.

8.2 The Parameters in the QCD Fits

The free parameters in a perturbative QCD calculation of cross sections in deep-inelastic scattering are the parton density functions and the strong coupling constant α_s. In this section we discuss in what way the cross sections measured are sensitive to these parameters. We also specify the assumptions needed to determine these parameters in the QCD analysis.

To visualize the sensitivity of the perturbative cross sections to the different parameters of the theory we look at the relations in the leading order approximation[1]. In leading order the inclusive *ep* cross section and the jet cross section can be written in the symbolic form

$$\begin{aligned} \text{inclusive DIS:} \qquad & \tilde{\sigma}_{\text{incl. DIS}} & \propto \quad & q\,, \\ \text{jets in DIS:} \qquad & \sigma_{\text{jet}} & \propto \quad & \alpha_s \cdot (c_g\, g \; + \; c_q\, q)\,. \end{aligned} \tag{8.1}$$

In these formulae g denotes the gluon density in the proton and q a specific sum of the quark densities over all flavors (see the discussion in section 8.2.2). The coefficients c_g and c_q are

---

[1] The inclusion of next-to-leading order corrections changes these relations slightly but it does not affect our discussion in principle. In the QCD analysis the NLO corrections are, of course, fully considered.

predicted by perturbative QCD. From the relations (8.1) one sees that the quark densities are directly constrained by the inclusive *ep* cross section. Using the jet cross section we can then determine either one of the gluon density or α_s. For a simultaneous determination of both additional information is needed, e.g. a measurement of the jet cross section in a different kinematic region where the perturbative prediction is given by

$$\sigma'_{\rm jet} \propto \alpha_s \cdot (c'_g\, g \,+\, c'_q\, q) \qquad \text{with} \qquad \frac{c'_g}{c'_q} \neq \frac{c_g}{c_q}\,. \tag{8.2}$$

This is in fact the case for the inclusive jet and the dijet cross section in different regions of Q^2, as shown in Figs. 3.6 and 7.8 where the fractional gluon induced contributions vary strongly with Q^2.

Using jet cross sections in different Q^2 regions therefore yields a third equation allowing to determine the three independent parameters simultaneously. However, the gluon and the quark densities are not single parameters in the fit but functions of the momentum fraction x. It has to be checked whether the data can constrain the functional forms of the parton distributions and α_s simultaneously.

8.2.1 α_s and the Choice of the Renormalization Scale

The value of the strong coupling constant $\alpha_s(\mu_r)$ is a function of the renormalization scale μ_r. Since the dependence of $\alpha_s(\mu_r)$ on μ_r is predicted by perturbative QCD the value at any scale can be calculated from the value at a specified scale $\mu_{r,0}$. We choose $\mu_{r,0}$ as the mass of the Z^0 boson $\mu_{r,0} = M_Z = 91.187\,\text{GeV}$ [21] and compute the μ_r dependence using the exact numerical solution of the renormalization group equation (1.6) at four-loop accuracy[2]. The fitted parameter is $\alpha_s(M_Z)$. We will now explain how we choose the renormalization scales at which the perturbative cross sections are calculated.

In the calculation of the inclusive *ep* cross section we identify the renormalization scale μ_r^2 with the four-momentum transfer Q^2, the only hard scale appearing in the calculation.

In jet production a further hard scale is given by the transverse jet energy E_T in the Breit frame. This scale is *directly* related to the jet production vertices in the Feynman diagrams and specifies the physical scale at which hard QCD radiation is resolved. This scale $\mu_r = E_T$ is usually chosen in the computations of jet cross sections in $\bar{p}p$ collisions, i.e. processes which are very similar to jet production in *ep* collisions in the Breit frame.

In section 3.2 we have compared properties of the perturbative predictions for different choices of the renormalization scale ($\mu_r^2 = E_T^2$, Q^2, $E_T^2 + Q^2$) and have seen that in most regions of phase space the perturbative calculations have the smallest scale dependences and

---

[2] One may prefer to use the 2-loop solution because the perturbative cross sections are computed at next-to-leading order accuracy. However, in Fig. 1.4 we have shown that within the range of scales considered here ($7\,\text{GeV} < \mu_r < M_Z$) the difference between both formulae is always below three per mil and therefore negligible for our purposes.

smallest NLO corrections for the choice $\mu_r^2 = E_T^2$. For these reasons we decide to use the renormalization scale $\mu_r^2 = E_T^2$ for the central results. We will also study the influence of using the scale $\mu_r^2 = Q^2$ on the results (and their scale dependence).

8.2.2 Parton Density Functions

Linear Combinations of Parton Densities

As we have discussed above, our goal is a combined fit of the gluon and the quark densities in the proton. These comprise eleven different parton types: the gluon (g) and the quark flavors up (u), down (d), strange (s), charm (c), bottom (b) as well as the five corresponding anti-quarks[3] It is obvious that the data sets considered here are not sufficient to constrain all of these quark distributions simultaneously. However, using the relations between the perturbative coefficients of the different quark flavors we can replace the ten different quark flavors by two linear combinations. The following steps are based on the standard model prediction that the electromagnetic coupling of the photon to quarks is proportional to their electrical charge squared, irrespective of their flavor. Therefore two assumptions have to be made.

- Neglect of Z^0 exchange
  The phase space considered in this analysis is restricted to four-momentum transfers $Q^2 < 1000\,\mathrm{GeV}^2$ (inclusive *ep* cross section) and $Q^2 < 5000\,\mathrm{GeV}^2$ (jet cross sections). In this kinematic range the contributions from Z^0 exchange and γZ^0 interference are negligible (as shown in section 3.2) and it is safe to only consider photon exchange.
- Neglect of quark masses
  For the calculation of the inclusive *ep* cross section at $Q^2 > 150\,\mathrm{GeV}^2$ quark masses can be safely neglected. The effects of quark masses for the dijet cross section have been investigated in section 3.2 using a leading order calculation and were found to be small.

Neglecting quark masses and taking only photon induced processes into account the perturbative coefficients for the quarks fulfill the following relations

$$c_u = c_c = c_t \;=\; c_{\bar{u}} = c_{\bar{c}} = c_{\bar{t}} \quad \text{and} \quad c_d = c_s = c_b \;=\; c_{\bar{d}} = c_{\bar{s}} = c_{\bar{b}} \; . \tag{8.3}$$

Only three coefficients are independent. We choose these as c_g, c_Σ and c_Δ, given by linear combinations of the single flavor coefficients:

$$\begin{aligned} c_G &\equiv c_{\text{gluon}} \, , \\ c_\Sigma &\equiv 1/3\,(4\,c_d - c_u)\, , \\ c_\Delta &\equiv 3\,(c_u - c_d)\, . \end{aligned} \tag{8.4}$$

---

[3] In the range of four-momentum transfers and transverse jet energies considered here there are no contributions from the top quark.

These coefficients have been chosen such that they correspond to the following linear combinations of parton densities[4]

$$
\begin{aligned}
\text{Gluon:} \quad & x\,G(x) &\equiv\;& x\,g(x)\,, \\
\text{Sigma:} \quad & x\,\Sigma(x) &\equiv\;& x \sum_a \left(q_a(x) + \bar{q}_a(x)\right), \\
\text{Delta:} \quad & x\,\Delta(x) &\equiv\;& x \sum_a e_a^2 \left(q_a(x) + \bar{q}_a(x)\right), \qquad (8.5)
\end{aligned}
$$

where the sums run over all quark flavors a and e_a denotes the electrical charge of the quark. Using (8.3) and the definitions (8.4) and (8.5) it can easily be verified that

$$c_G G(x) \,+\, c_\Sigma \Sigma(x) \,+\, c_\Delta \Delta(x) \;=\; c_g g(x) \,+\, \sum_a c_a q_a(x)\,. \qquad (8.6)$$

We will now discuss at which order of α_s these parton densities contribute to the different processes under consideration. A selection of Feynman diagrams of different orders in α_s is shown in Fig. 8.1. From the left to the right they correspond to processes of order $\mathcal{O}(\alpha_s^0)$, $\mathcal{O}(\alpha_s^1)$ and $\mathcal{O}(\alpha_s^2)$.

- **The Δ Quark Density**
  The Δ density is defined as the sum over the single quark densities weighted with their electrical charges squared. $\Delta(x)$ enters the cross section whenever the incoming quark couples directly to the photon (via its electrical charge). It contributes to the inclusive *ep* cross section and to the jet cross section at all orders of α_s.

- **The Gluon Density**
  The gluon density is probed in processes of order $\mathcal{O}(\alpha_s^1)$ and higher. It does not contribute to the inclusive *ep* cross section at leading order, but at next-to-leading order and beyond. The jet cross sections, however, are sensitive to the gluon density at leading order and beyond.

- **The Σ Quark Density**
  The Σ density is defined as the sum of the quark densities of all flavors (not weighted with their electrical charge). It is therefore relevant in all processes where the incoming quark does not couple directly to the photon, as e.g. shown in the bottom of Fig. 8.1. These processes are at least of order $\mathcal{O}(\alpha_s^2)$. The Σ density does not contribute to the inclusive *ep* cross section up to next-to-leading order. It enters only the jet cross sections via the next-to-leading order corrections. At large Q^2 these contributions are, however, very small (4.5% for the dijet cross section at $150 < Q^2 < 200\,\mathrm{GeV}^2$, decreasing to 2% at $600 < Q^2 < 5000\,\mathrm{GeV}^2$).

---

[4] We do not explicitly display here the dependence on the factorization scale.

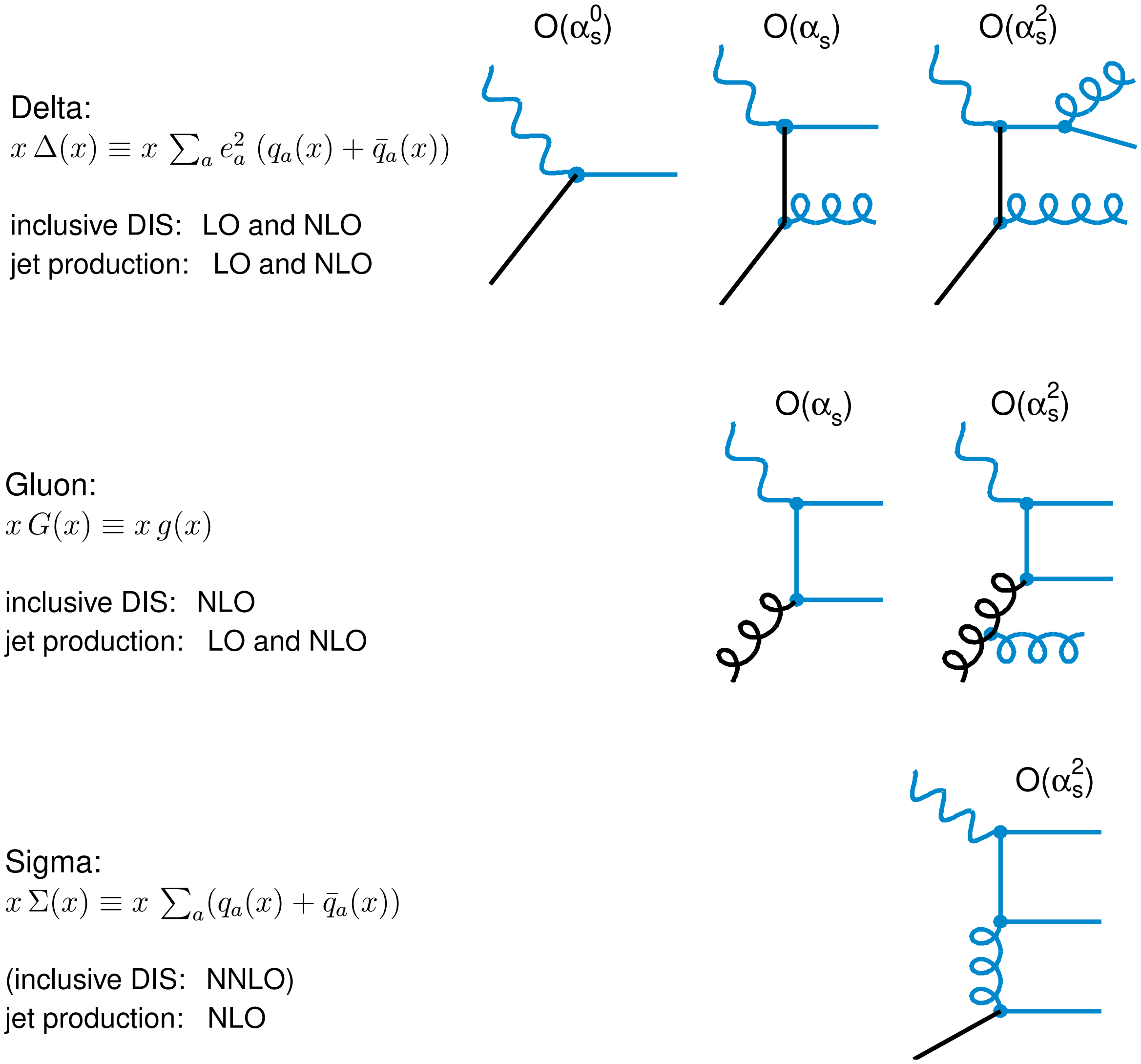

Figure 8.1: Examples of Feynman diagrams in different orders of α_s describing the coupling of the virtual photon to the different parton densities.

At orders $\mathcal{O}(\alpha_s^0)$ and $\mathcal{O}(\alpha_s^1)$ the contributions from different quark flavors are proportional to their electrical charge squared. This leads to the relation

$$c_u = 4\,c_d \qquad (\text{at } \mathcal{O}(\alpha_s^0) \text{ and } \mathcal{O}(\alpha_s^1))\,. \tag{8.7}$$

The coefficient c_Σ in (8.4) vanishes therefore at orders $\mathcal{O}(\alpha_s^0)$ and $\mathcal{O}(\alpha_s^1)$, and the only contributions to the cross sections are from the gluon density $xG(x)$ and $x\Delta(x)$. The quark density $x\Sigma(x)$ starts to contribute at order $\mathcal{O}(\alpha_s^2)$. The following table gives an overview of the order at which the parton densities contribute to the different processes (up to NLO).

	LO	NLO
$\tilde{\sigma}_{\text{incl. DIS}}$	$x\Delta(x)$	$x\Delta(x),\ xG(x)$
σ_{jets}	$xG(x),\ x\Delta(x)$	$xG(x),\ x\Delta(x),\ x\Sigma(x)$

In summary we state that we can reduce the number of parton densities in the QCD analysis by building suitable linear combinations of the quark densities. We are left with three different parton densities: the gluon density, the quark density $x\Delta(x)$ and the quark density $x\Sigma(x)$. Up to NLO the latter does not contribute to the inclusive *ep* cross section. It enters the jet cross sections only via the NLO corrections giving only small contributions. We therefore conclude that taking the $x\Sigma(x)$ from the results of global fits is only a weak assumption in our QCD analysis which will not bias our results. We are then left with two parton densities that account (up to NLO) for the inclusive *ep* cross section and for more than 95% of the jet cross section: the gluon density $xG(x)$ and the quark density $x\Delta(x)$.

This justifies the picture of a single quark density that we have used in the beginning of this section in (8.1).

Choice of the Factorization Scale

In principle the same arguments invoked in the choice of the renormalization scale μ_r apply also to the factorization scale μ_f for the inclusive *ep* cross section and for the jet cross section. However, we make a different choice for the following reasons.

We have combined the different parton flavors into three independent parton density functions $xG(x, \mu_f)$, $x\Delta(x, \mu_f)$ and $x\Sigma(x, \mu_f)$. These three parton densities are, however, only independent as long as no evolution between different scales μ_f is performed. The evolution of the gluon density is coupled to the evolution of $x\Sigma(x, \mu_f)$. Furthermore, since $x\Delta(x, \mu_f)$ is not an eigenstate of the DGLAP evolution operators the evolution requires its decomposition into a non-singlet and a singlet (i.e. $x\Sigma(x, \mu_f)$). This introduces an additional dependence between both quark densities. To avoid mixing between the different parton densities we do not evolve the parton distributions to different scales but perform the perturbative calculations at a fixed value of the factorization scale $\mu_f = \mu_0$. We will now discuss under which circumstances this procedure is justified.

The jet cross sections are sensitive to the parton distributions in the x-range of $0.008 \lesssim x \lesssim 0.3$. In this x-range the factorization scale dependence of the parton density functions is very small (Fig. 1.8). The remaining μ_f^2 dependence (given by the DGLAP evolution equations) is largely compensated by a corresponding term $\propto \alpha_s \ln(\mu_f^2/\mu_0^2)$ in the perturbative coefficients. The perturbative cross sections therefore depend only very weakly on the choice of the factorization scale. The difference between using a fixed factorization scale μ_0^2 and performing the full DGLAP evolution at a scale μ_f^2 is of higher order in α_s, and enters through terms of order $\mathcal{O}(\alpha_s^2 \ln^2(\mu_f^2/\mu_0^2))$. However, if the scale μ_f^2 is close to the fixed scale μ_0^2 (such that $\ln(\mu_f^2/\mu_0^2) \lesssim 1$), these terms are small.

We therefore decide to use a fixed value of the factorization scale of the order of the average transverse jet energies in the dijet and the inclusive jet cross section $\mu_f^2 = \mu_0^2 = 200\,\mathrm{GeV}^2 \simeq \langle E_T^2 \rangle$. It has been shown in Fig. 3.12 that the factorization scale dependence of the dijet cross section is below 2% when varying this scale by a factor of four in both directions.

It is customary to evaluate the inclusive *ep* cross sections at a factorization scale of the order of the four-momentum transfer Q^2. However, whereas the recent H1 measurements [32] are performed over the large range $150 < Q^2 < 30000\,\mathrm{GeV}^2$, we restrict our QCD analysis to a subset of these data in the range of $150 < Q^2 < 1000\,\mathrm{GeV}^2$ for which $\mu_f^2 = 200\,\mathrm{GeV}^2$ is a reasonable choice.

Parameterization of the x-Dependence

The parton distributions are functions of the parton momentum fraction x. Neither the shape nor the amplitude of the x-dependence are predicted by perturbative QCD. To fit these functions to the data we have to assume a functional form that can be parameterized by a (small) number of parameters. The functional forms have to be chosen such that they do not restrict the possible solutions. We will use different functional forms which were already used in the global fits [29, 77, 30, 106]. The following parameterizations for the parton densities are used in our analysis

$$\begin{array}{rrcl}
\text{3 parameters} & xP(x) & = & A\,x^b\,(1-x)^c\,, \\
\text{4 parameters} & xP(x) & = & A\,x^b\,(1-x)^c\,(1+dx)\,, \\
\text{5 parameters (I)} & xP(x) & = & A\,x^b\,(1-x)^c\,(1+dx^e)\,, \\
\text{5 parameters (II)} & xP(x) & = & A\,x^b\,(1-x)^c\,(1+d\sqrt{x}+ex)\,,
\end{array} \tag{8.8}$$

where $xP(x)$ stands for $xG(x)$ or $x\Delta(x)$. While the form of the parameterizations with three and four parameters are unique there are two different forms for the five parameter ansatz.

8.3 Strategies for the QCD Analysis

Any QCD analysis of a limited data set must address the question of how much external information should be used. If the amount of external information is large one can expect to obtain a higher precision of the results, but has to take into account that the analysis results are not independent of the external information. The uncertainties of the external information have to be appropriately propagated into the uncertainty of the result.

If one aims for a completely independent determination of all parameters, one has to ensure that the available data are able to constrain all parameters simultaneously.

Different strategies shall be discussed which differ in the amount of external information included in the analysis. We start with a simple one-parameter fit to determine $\alpha_s(M_Z)$ using the knowledge of parton distributions from global analyses. A more elaborate strategy will aim at the determination of gluon and quark densities while $\alpha_s(M_Z)$ is taken to be the world average value within its uncertainty. The third step will be the simultaneous determination of $\alpha_s(M_Z)$, the gluon and the quark densities, relying on no external information at all.

8.3.1 Determination of α_s

The technically simplest procedure is to reduce the QCD analysis to the fit of a single free parameter ($\alpha_s(M_Z)$) while maximizing the external input (the parton densities). Corresponding analyses of jet data have been performed in *ep* collisions [3, 4, 5, 107, 108, 109] and in $\bar{p}p$ collisions [110]. In this approach the parton distributions are assumed to be "well-known" from independent measurements. In practice we will take the knowledge on the parton distributions from the results of global analyses. This approach has several shortcomings, connected to the following three points.

- **The Validity of the Assumption**
  In global analyses parton density functions are basically fitted to DIS structure function data. These data are however only indirectly sensitive to the gluon density, and give only constraints at small x where the scaling violations of the structure functions are large. The gluon density at moderate x (to which our jet data are sensitive) is only obtained from extrapolations and from additional constraints as e.g. momentum sum rules. One can hardly consider this as "well-known".

- **Consistency of the Procedure**
  The second shortcoming of this method concerns the self consistency of the $\alpha_s(M_Z)$ result. The parton distributions obtained in global fits depend on an initial assumption on $\alpha_s(M_Z)$. The resulting value of $\alpha_s(M_Z)$ therefore also depends on this initial assumption. If the result comes out different from the initial assumption the analysis is inconsistent. Consistency is only achieved if the result is equal to the initial assumption. Many recent global fits have therefore provided sets of parton distributions for different assumptions on $\alpha_s(M_Z)$ [30, 77, 106]. Using these sets of parton distributions the influence of the initial assumption on $\alpha_s(M_Z)$ can be tested.

- **Propagation of Uncertainties**
  It is straightforward to propagate the experimental and theoretical uncertainties into the $\alpha_s(M_Z)$ result. This is, however, not the case for the uncertainties connected to the parton distributions. No global analysis has yet provided an error analysis of the fit results. The uncertainty coming in from the parton distributions is usually estimated by using the fit results from different groups (CTEQ, MRST, GRV). However, these groups are using nearly the same data sets, and the fits are based on similar assumptions. The spread between these results (which are all "best fits") does therefore not

> cover the range of possible variations and does not reflect the true uncertainty of the parton distributions.
>
> Only the CTEQ collaboration has performed a study [111] of the uncertainty in the gluon distribution. The global analysis was repeated for different parameterizations of the gluon density, allowing also the quality of the fits to degrade. Only extreme fits were discarded that showed clear disagreement with one or more data sets. While this study is a first step towards the estimation of uncertainties, it can still not replace a proper error analysis.

The consequence for an $\alpha_s(M_Z)$ determination along these lines is that an important part of the uncertainties, coming from insufficient knowledge of the parton densities, can not be determined. It is highly questionable whether the parton distributions are really "well-known" in the relevant x-range, especially when comparing their uncertainty to the uncertainty of the world average value of $\alpha_s(M_Z)$. It seems to be more reasonable to take external knowledge of parameters which are better known (i.e. $\alpha_s(M_Z)$) from independent processes and to fit those parameters which are less constrained by other data (i.e. the gluon density). This approach will be discussed in the next subsection.

Although the present approach can not be seen as an independent α_s determination, it may still demonstrate consistency. The advantage of this approach is that all freedom in the comparison of theory with data is absorbed into the value of the single parameter $\alpha_s(M_Z)$. This allows to study the effects of different physical and technical assumptions in the QCD fit and their influence on the result. The α_s analysis in section 9.1 is based on this approach and will be used to perform detailed studies.

8.3.2 Independent Determination of Gluon and Quark Densities

The value of $\alpha_s(M_Z)$ has been determined independently of the proton structure, for example in jet production in e^+e^- annihilation [22, 112]. A determination of the parton densities in the proton for a fixed value of $\alpha_s(M_Z)$ will therefore not lead to a circular argument as discussed above for the α_s analysis. The uncertainty of the world knowledge on $\alpha_s(M_Z)$ is known (e.g. from the studies in [22]) and can be propagated into the uncertainty of the resulting parton densities. This approach has been applied in previous determinations of the gluon density in the proton from HERA jet data [113, 114, 115]. However, in these analyses the quark content of the proton was fixed and taken from global analyses which leads to similar conceptual problems as discussed above for the α_s determination.

We will avoid such inconsistencies in our QCD analysis by fitting simultaneously the gluon and quark densities. The fit is capable to constrain both if we include additional H1 data on the inclusive *ep* cross section in the fit because these data are directly sensitive to the quark densities (see the next section)[5].

---

[5] A similar approach has been followed in a previous analysis by G. Lobo [116].

8.3.3 Simultaneous Determination of $\alpha_s(M_Z)$, the Gluon and the Quark Densities

The final aim of the present analysis is an independent, simultaneous fit of all free parameters, $\alpha_s(M_Z)$, the gluon and the quark densities, without relying on any external assumptions. Such a direct, simultaneous determination has never been attempted before using data from a single experiment. This procedure is fully independent of any external input and can thus provide new, independent information and demonstrate in which way the data are sensitive to the single parameters and their correlation.

However, while the QCD fits in the two previous approaches are likely to converge, this can not trivially be expected here. It remains to be checked whether the present jet data are really able to constrain $\alpha_s(M_Z)$ and the gluon density simultaneously.

8.4 Correlated Uncertainties between Data Points

Before we perform the QCD analysis according to the three strategies outlined above, we give an overview of the different sources of correlated uncertainties (experimental and theoretical ones). In table 8.1 all sources are listed with the information whether they are correlated between both data sets. The correlations are taken into account in the definition of the χ^2 variable as given in (B.16) in appendix B.

The single sources of experimental uncertainties for the jet cross sections have been discussed in section 6.3 and the uncertainties for the inclusive *ep* data are treated in [32]. The theoretical uncertainties for the jet cross sections are evaluated as discussed in section 3.3 (the renormalization and factorization scale dependence and the uncertainties in the hadronization corrections). The scale dependence is used to estimate the possible size of higher order corrections. Since higher order effects may be different for different processes, we assume the renormalization scale dependences of the inclusive *ep* cross section and of the jet cross sections to be uncorrelated.

Additional sources of uncertainties become relevant whenever external information is included in the QCD analysis. In the cases where we set the value of the strong coupling constant to the world average value $\alpha_s(M_Z) = 0.119$ we assume an uncertainty of ± 0.004 [22]. Whenever the parton density functions are taken from global fit results we use the parameterization CTEQ5M [29] for the central analysis because it gives the best description of the recent measurement of the inclusive *ep* cross section by the H1 collaboration [32]. The corresponding analysis steps are repeated using all parameterizations from other recent global fits (including the gluon uncertainty study by the CTEQ collaboration [111]). Due to the lack of a more realistic estimate we will quote the largest deviation from the central result as the uncertainty.

	source of correlated uncertainties	reduced inclusive DIS cross section	inclusive jet and dijet cross section
experimental	luminosity	×	×
	model dependence of detector correction		×
	positron energy	×	×
	positron polar angle	×	×
	LAr cluster energy	×	×
	LAr noise	×	
	photoproduction background	×	
theoretical	renormalization scale (inclusive DIS)	×	
	renormalization scale (jets)		×
	factorization scale (jets)		×
	hadronization corrections		×
external (if not fitted)	$\alpha_s(M_Z)$	0.119 ± 0.004	
	parton density functions	spread of recent global fits	

Table 8.1: The different sources of uncertainties which are correlated between the different data points.

9

Results of the QCD Analysis

We have now compiled all information required to perform the QCD analysis.

- The results of the inclusive jet and the dijet cross sections have been presented in chapter 7. The uncertainties and their correlations between the different data points are discussed in section 6.3 and listed in appendix D.1.
- The data on the inclusive reduced *ep* cross section are taken from a recent H1 analysis [32]. For these data all uncertainties and their correlations between different data points are published. Since the jet analysis presented here is based on similar analysis methods, the correlations of the uncertainties between both data sets are also known (see section 8.4) and can be taken into account.
- Detailed investigations of the renormalization and factorization scale dependence of the perturbative QCD predictions and the size and uncertainties of non-perturbative corrections as predicted by different models have been performed in chapter 3 for the jet cross sections. In section 3.3 we have discussed how the corresponding uncertainties, which both contribute to the theoretical uncertainties of the fit results, are defined

In the fits the inclusive reduced *ep* cross section is directly compared to the perturbative QCD predictions, while the jet cross sections are compared to the product of the perturbative predictions and the non-perturbative (hadronization) corrections. The latter are taken to be the average value from the model predictions of HERWIG, LEPTO and ARIADNE (the values are listed in appendix D.1). Further tools needed in the QCD fit are presented in the appendices:

- A method for the fast evaluation of the perturbative QCD predictions in next-to-leading order (for the jet cross sections and for the inclusive reduced *ep* cross section) needed in the iterative fitting procedure, is introduced in appendix C.
- In appendix B we introduce a definition of χ^2 which takes into account the correlations of uncertainties between the data points by fitting a parameter for each source of uncertainty (formula (B.16)). Using this definition each fit takes into account the size

and the correlations of *all* uncertainties of the data points and therefore returns the values of the fit parameters with their total uncertainty. The individual uncertainty components (experimental and theoretical) are evaluated according to the procedure described in appendix B.5.

The perturbative QCD predictions are calculated in next-to-leading order in the $\overline{\mathrm{MS}}$ scheme using the program DISENT [60]. The free parameters in the fits are:

- The value of the strong coupling constant at the scale of the mass of the Z^0 boson ($M_Z = 91.187\,\mathrm{GeV}$ [21]) which is evolved to the process relevant energy scales using the numerical 4-loop solution (1.2) of the renormalization group equation.
- The gluon density and a linear combination of the quark densities (the sum over all quark flavors, weighted with the squared electric charge). Their x dependence is parameterized using the formulae (8.9). The error bands are determined as described in appendix B.5.

The results of the QCD fits are presented in the next sections, following the three strategies outlined in section 8.3. In all cases we present the main result together with detailed studies of the stability of the fit under variations of technical parameters and also the dependence of the result on the choice of the data sets used in the fit.

9.1 Determination of $\alpha_s(M_Z)$

As a first step we fit the QCD predictions to the jet cross sections using parameterizations for the parton distributions from global fits. The single free parameter which we determine in the fit is the value of the strong coupling constant. All α_s fit results presented hereafter consider all experimental and theoretical uncertainties. The effect of uncertainties of the parton distributions is discussed separately.

The central value of $\alpha_s(M_Z)$ is obtained from a fit to the double differential inclusive jet cross section $\mathrm{d}^2\sigma_{\mathrm{jet}}/\mathrm{d}E_T\mathrm{d}Q^2$, measured with the inclusive $k_\perp$ algorithm. For this algorithm the hadronization corrections are smallest (section 3.1). For the central result we use the parton distributions from the CTEQ5M parameterization [29], the renormalization scale is chosen to be $\mu_r = E_T$ and the factorization scale is set to the fixed value of $\mu_f = \sqrt{200}\,\mathrm{GeV}$ (the average E_T of the jet sample). The effect of choosing a different value for μ_r are studied.

The studies of the stability of the results include fits to the inclusive jet cross section measured with the Aachen jet algorithm, fits to the double differential dijet cross section $\mathrm{d}^2\sigma_{\mathrm{dijet}}/\mathrm{d}\overline{E}_T\mathrm{d}Q^2$ using four different jet algorithms and fits to other double differential dijet distributions.

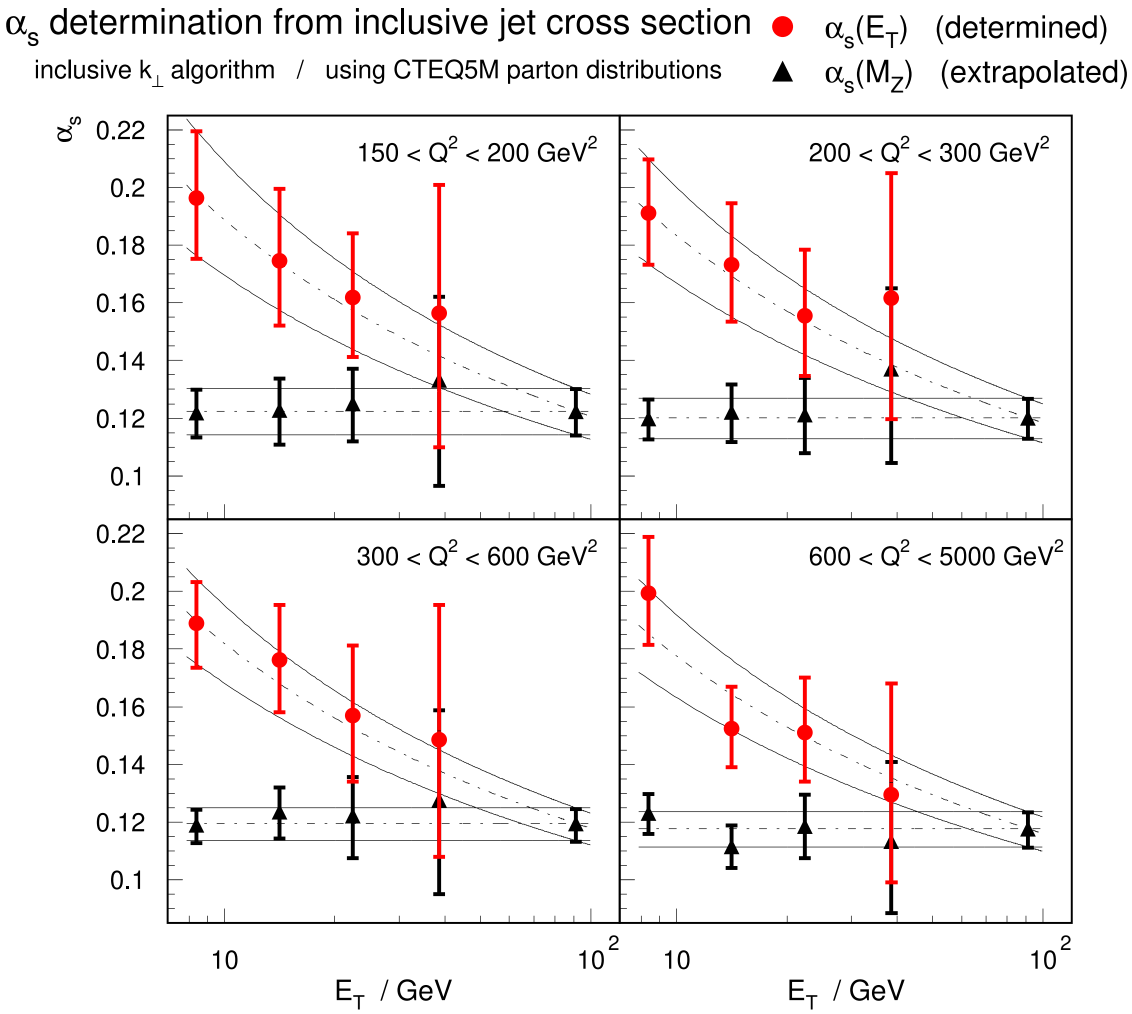

Figure 9.1: Determination of α_s from the inclusive jet cross section using the inclusive $k_\perp$ algorithm at a renormalization scale $\mu_r = E_T$. Displayed are the results of the fits to the single data points in each Q^2 region at each E_T value (circles). The single values are extrapolated to the Z^0 mass (triangles). A combined fit yields a result for $\alpha_s(M_Z)$ (rightmost triangle) for each Q^2 region. The upper curves indicate the prediction of the renormalization group equation for the energy evolution of the combined fit results and their uncertainties.

9.1.1 Fits to Single Data Points

Before carrying out combined fits to groups of data points we test the consistency of the data by performing QCD fits separately to all sixteen single data points of the double differential inclusive jet cross section. The fit results are displayed in Fig. 9.1 for the four regions of Q^2. In each fit we extract a result for $\alpha_s(E_T)$ (circles) which is presented at the average E_T of the corresponding data point. The individual results are subsequently evolved to $\alpha_s(M_Z)$ (triangles). Combined fits to all data points in the same Q^2 regions are performed, leading to a combined result of $\alpha_s(M_Z)$ for each Q^2 region (rightmost triangles). The three upper curves in the plots indicate the evolution of the combined result (dashed-dotted curve) and its uncertainties (solid curves) according to the renormalization group equation. The single $\alpha_s(E_T)$ values are consistent with the predicted scale dependence of α_s and all combined $\alpha_s(M_Z)$ results are compatible with each other. The combined results of the Q^2 regions are (for $\mu_r = E_T$)

$$\begin{aligned}
150 < Q^2 < 200\,\mathrm{GeV}^2 &: \quad \alpha_s(M_Z) = \; 0.1224\,^{+0.0052}_{-0.0054}\,(\mathrm{exp.})\,^{+0.0060}_{-0.0063}\,(\mathrm{th.})\,, \\
200 < Q^2 < 300\,\mathrm{GeV}^2 &: \quad \alpha_s(M_Z) = \; 0.1201\,^{+0.0043}_{-0.0044}\,(\mathrm{exp.})\,^{+0.0052}_{-0.0057}\,(\mathrm{th.})\,, \\
300 < Q^2 < 600\,\mathrm{GeV}^2 &: \quad \alpha_s(M_Z) = \; 0.1196\,^{+0.0037}_{-0.0038}\,(\mathrm{exp.})\,^{+0.0040}_{-0.0047}\,(\mathrm{th.})\,, \\
600 < Q^2 < 5000\,\mathrm{GeV}^2 &: \quad \alpha_s(M_Z) = \; 0.1177\,^{+0.0048}_{-0.0048}\,(\mathrm{exp.})\,^{+0.0035}_{-0.0043}\,(\mathrm{th.})\,. \qquad (9.1)
\end{aligned}$$

While the experimental uncertainties are of the same size for all $\alpha_s(M_Z)$ values, the theoretical uncertainties shrink slightly towards larger Q^2. This is a consequence of the reduced renormalization scale dependence of the jet cross section at higher Q^2 (shown in Fig. 3.10).

9.1.2 Combined Fit – Central $\alpha_s(M_Z)$ Result

Having convinced ourselves that our data are consistent over the whole range of Q^2 and E_T we can now attempt to make combined fits to groups of data points. To study the E_T dependence of $\alpha_s(E_T)$, we combine the four data points of the same E_T at different Q^2 and extract four values of $\alpha_s(E_T)$ (circles in Fig. 9.2). The single values are evolved to $\alpha_s(M_Z)$ (triangles below). A combined fit to all 16 data points gives $\chi^2/\mathrm{N.d.f.} = 3.81/15$ and leads to the final result for $\alpha_s(M_Z)$ (rightmost triangle)

$$\alpha_s(M_Z) \;=\; 0.1181\;\pm 0.0030\,(\mathrm{exp.})\,^{+0.0039}_{-0.0046}\,(\mathrm{th.}) \qquad\qquad (\mu_r = E_T)\,. \qquad (9.2)$$

The upper curves in Fig. 9.2 indicate the prediction of the renormalization group equation for the evolution of the final result and its uncertainties (the contribution from the uncertainty of the parton distributions is discussed later). A detailed overview of the numerical values of the results is given in appendix D.2. The contributions from the single sources of uncertainties to the result (9.2) are listed in table D.1, and table D.2 gives the same information for the four individual $\alpha_s(E_T)$ values. The fitted values of the parameters of the correlated uncertainties are listed in table D.7.

The largest contribution to the experimental uncertainty comes from the hadronic energy scale of the LAr calorimeter. The theoretical uncertainty comprises at equal parts of the uncertainty of the hadronization corrections and the renormalization scale dependence. The contribution from the renormalization scale dependence is $(^{+0.0025}_{-0.0034})$ (corresponding to a variation by a factor of two around the choice $\mu_r = E_T$ as described in section 3.3).

The result (9.2) is in good agreement with the current world average value of $\alpha_s(M_Z) = 0.119 \pm 0.004$ [22].

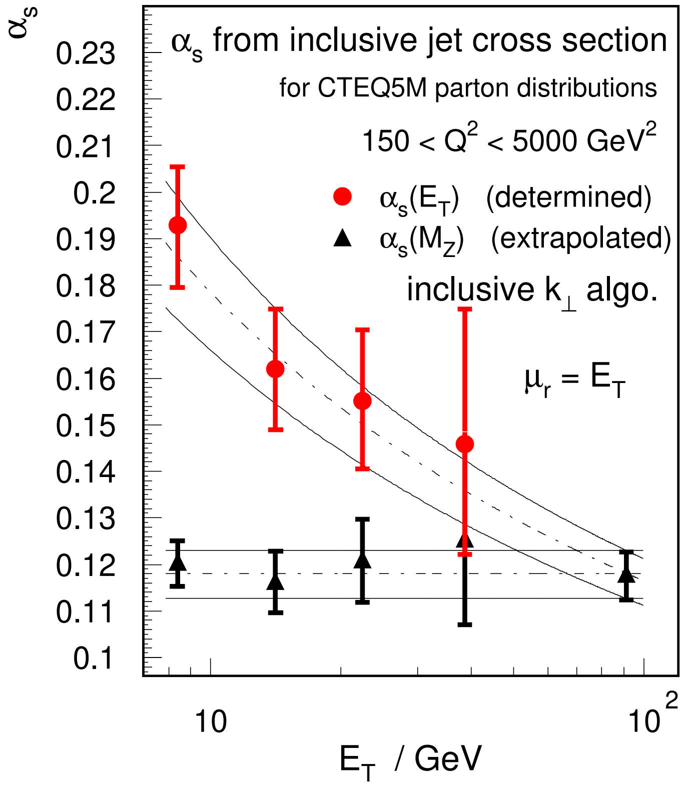

Figure 9.2: Determination of α_s from the inclusive jet cross section using the inclusive $k_\perp$ algorithm for a renormalization scale $\mu_r = E_T$. The results are shown for each E_T value (circles). The single values are extrapolated to the Z^0-mass (triangles). The final result for $\alpha_s(M_Z)$ (rightmost triangle) is obtained in a combined fit. The upper curves indicate the prediction of the renormalization group equation for the evolution of the combined fit result and its uncertainty.

9.1.3 Choice of a Different Renormalization Scale

Another possible choice of the renormalization scale in the theoretical calculation is the four-momentum transfer Q. Analogous to the procedure applied in section 9.1.2 we perform an α_s determination for the renormalization scale $\mu_r = Q$ and obtain the results shown in Fig. 9.3. In this case we combine the data points at the same Q but different E_T and obtain four single values of $\alpha_s(Q)$ (circles) which we evolve to $\alpha_s(M_Z)$ (triangles below). A combined fit to the 16 data points gives $\chi^2/\text{d.o.f.} = 4.17/15$ and a combined value of $\alpha_s(M_Z)$ (rightmost triangle) of

$$\alpha_s(M_Z) \;=\; 0.1221 \pm 0.0034\,(\text{exp.})\,^{+0.0054}_{-0.0059}\,(\text{th.}) \qquad\qquad (\mu_r = Q)\,. \tag{9.3}$$

Comparing this result with the one obtained for $\mu_r = E_T$ in (9.2), we note that the central value is shifted by +0.0040 (the single contributions to the uncertainty are listed in table D.1). In addition, we observe an increased theoretical uncertainty for the choice $\mu_r = Q$ which is

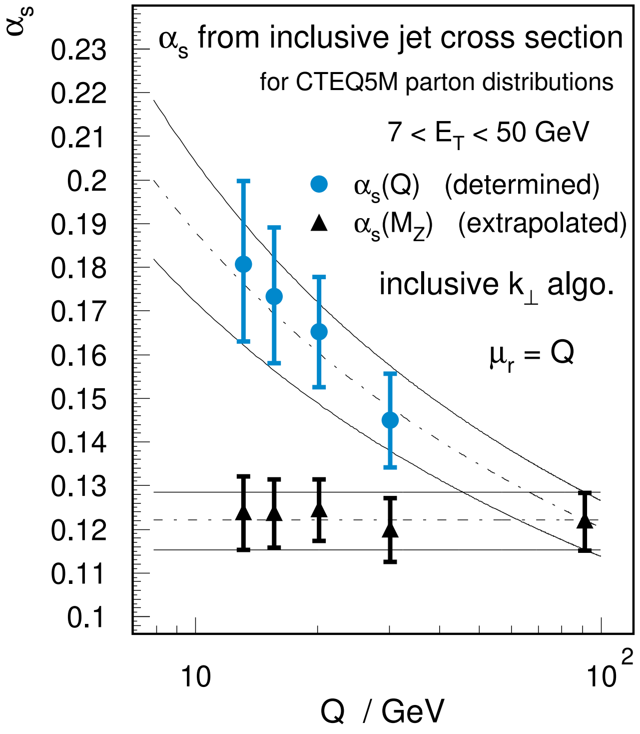

Figure 9.3: Determination of α_s from the inclusive jet cross section using the inclusive $k_\perp$ algorithm for a renormalization scale $\mu_r = Q$. The results are shown for each Q value (circles). The single values are extrapolated to the Z^0-mass (triangles). A final result of $\alpha_s(M_Z)$ (rightmost triangle) is obtained from a combined fit. The upper curves indicate the prediction of the renormalization group equation for the evolution of the combined fit result and its uncertainty.

directly connected to a stronger renormalization scale dependence of the perturbative NLO calculation for $\mu_r = Q$ (compared to $\mu_r = E_T$). The renormalization scale dependence gives a contribution to the uncertainty of $\left({}^{+0.0044}_{-0.0049}\right)$ which can by itself account for the difference between the two results.

9.1.4 Variations of Parton Distributions

The need to use parton distributions determined in other processes by the global fits is the strongest limitation of the approach chosen to determine α_s.

In section 8.3 we have already discussed the problem of how to determine the uncertainties of the parton distributions which then have to be propagated into the uncertainty of the α_s result. Furthermore we have addressed the question of the consistency of the whole approach since the parton densities obtained in global fits already depend on an initial assumption on $\alpha_s(M_Z)$.

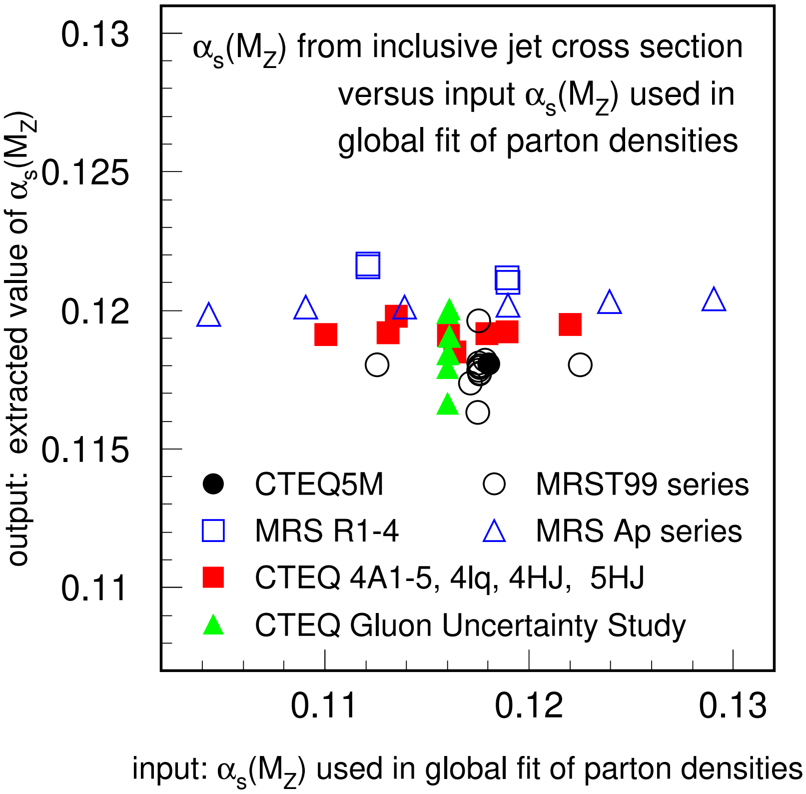

Figure 9.4: Dependence of the $\alpha_s(M_Z)$ fit result (for $\mu_r = E_T$) on the parton distributions used in the fit. The results are displayed as a function of the $\alpha_s(M_Z)$ value used in the global fits of the parton distributions. The correlation is shown for a comprehensive collection of different global fits.

The central fit results are obtained for the parton distributions from the CTEQ5M parameterization [29]. We redo the QCD fits using all parameterizations from recent global fits which have been performed in next-to-leading logarithmic accuracy in the $\overline{\text{MS}}$-scheme[1]. These include all sets from the fits CTEQ5 [29], CTEQ4 [77], MRST99 [30], MRSR [117], MRSAp [106] and the sets from the gluon uncertainty study [111] by the CTEQ collaboration. The fits CTEQ4, MRST99 and MRSAp have provided sets of parton distributions for different assumptions on $\alpha_s(M_Z)$. Using these sets of parton distributions, we study the dependence of our results on the initially assumed $\alpha_s(M_Z)$.

The $\alpha_s(M_Z)$ results obtained for the different parton distributions are shown in Fig. 9.4 as a function of the $\alpha_s(M_Z)$ value used in the global fit. The range of the variations is small and no significant correlation is seen. Using the default set from MRST99 we obtain nearly the same result ($\alpha_s(M_Z) = 0.1179$) as for CTEQ5M.

---

[1] The parameterization from GRV98 [31] could not be used since the charm and the bottom quark densities are not provided in the code.

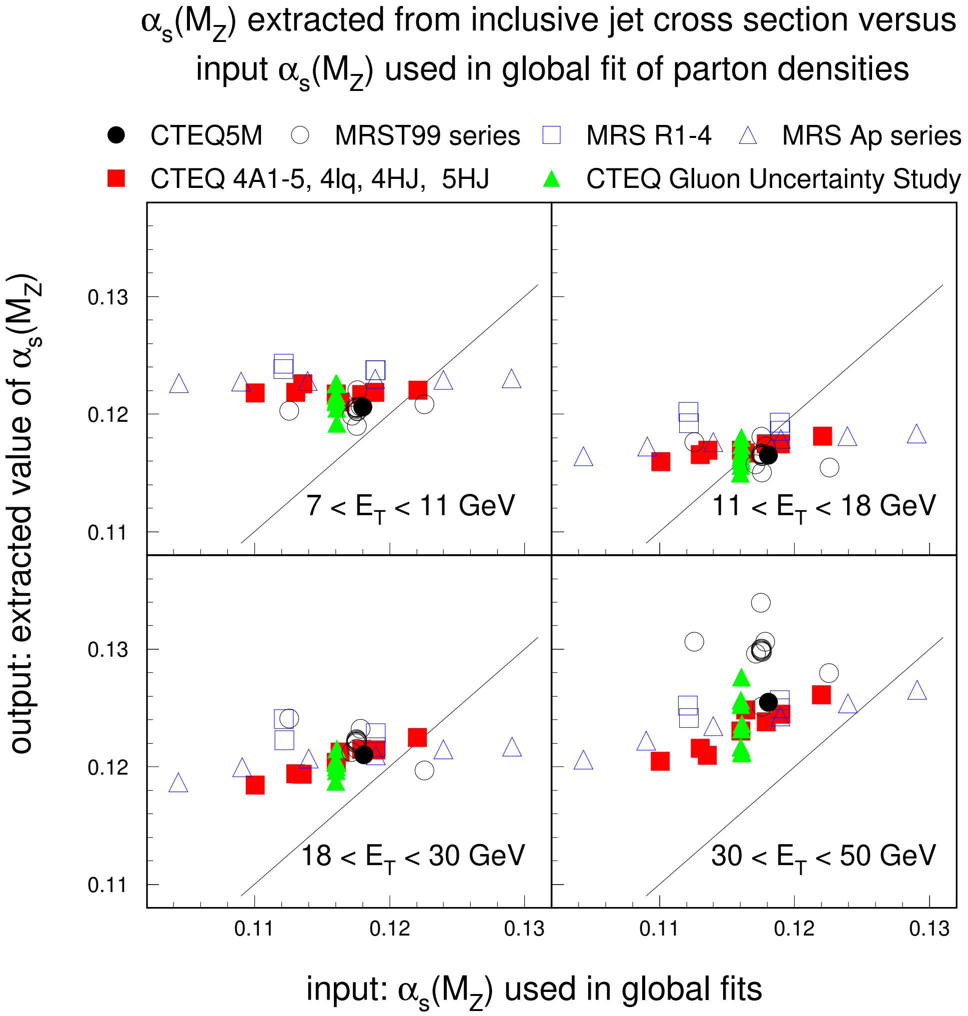

Figure 9.5: Dependence of the $\alpha_s(M_Z)$ fit result on the $\alpha_s(M_Z)$ value used in the global fits of the parton distributions, separately for each E_T bin.

The largest deviations from the central result (9.2) are obtained with the MRSR3 parameterization (+0.0036) and for the set MRST99(g↓) (−0.0017). We quote this spread as the corresponding uncertainty of our result which is then given by

$$\alpha_s(M_Z) \;=\; 0.1181 \pm 0.0030\,(\text{exp.})\,{}^{+0.0039}_{-0.0046}\,(\text{th.})\,{}^{+0.0036}_{-0.0017}\,(\text{pdf}) \qquad (\mu_r = E_T)\,. \tag{9.4}$$

The small dependence of our result on the $\alpha_s(M_Z)$ value used in the global fit is in contrast with the observation made by the CDF Collaboration in an α_s analysis of the high E_T inclusive jet cross section in $\bar{p}p$ collisions [110]. The CDF $\alpha_s(M_Z)$ result depends strongly on the $\alpha_s(M_Z)$ assumption in the global fits. To investigate the origin of this deviating result we study the correlation separately within the regions of different E_T. We redo the fits of the four $\alpha_s(M_Z)$ values in the four different E_T regions in Fig. 9.2 using all parton distributions described above. The correlations of these results with the input $\alpha_s(M_Z)$ values are shown in Fig. 9.5.

In both lower E_T regions we observe the same behavior as in the combined fit: The variations are small and not correlated with the input $\alpha_s(M_Z)$ value. At higher E_T, however, the range of the variations becomes larger. For the CTEQ4 series (filled squares) and for the MRSAp series (open triangles) we observe a positive correlation between the $\alpha_s(M_Z)$ result and the initial assumption. A different tendency is seen for the MRST99 series, where input and output $\alpha_s(M_Z)$ values are clearly anti-correlated.

These (anti-)correlations are strongest in the highest E_T region ($30 < E_T < 50\,\mathrm{GeV}$) where also the absolute variation between the different parameterizations is largest. The inclusive jet data in this E_T range are sensitive to parton momentum fractions in the range $0.1 \lesssim x \lesssim 0.4$ (see Fig. 3.6). The most likely explanation for this behavior in our opinion is that in this region of high x the parton densities are only weakly constrained by the data used in the global fits. Different assumptions in the fitting procedure may therefore lead to large differences in the results of the global fits.

However, our data points at high E_T have large statistical uncertainties and therefore only a small influence on the combined $\alpha_s(M_Z)$ fit result. This is reflected in the weak dependence of the combined fit result on the input $\alpha_s(M_Z)$ seen in Fig. 9.4.

9.1.5 Testing the Stability of the Result

Fit to the Inclusive Jet Cross Section Measured using the Aachen Algorithm

To test the stability of the central fit result we perform the same QCD fits to other jet distributions. In the first variation we use again the double differential inclusive jet cross section $\mathrm{d}^2\sigma_{\mathrm{jet}}/\mathrm{d}E_T\mathrm{d}Q^2$, now measured using the Aachen jet algorithm. Following the exact same procedure as described in section 9.1.2 we obtain the results shown in Fig. 9.6. Performing the same variations of the parton distributions the result for the Aachen algorithm is

$$\alpha_s(M_Z) \;=\; 0.1172 \pm 0.0032\,(\mathrm{exp.})\,{}^{+0.0046}_{-0.0053}\,(\mathrm{th.})\,{}^{+0.0036}_{-0.0017}\,(\mathrm{pdf}) \qquad (\mu_r = E_T)\,, \tag{9.5}$$

in perfect agreement with the result obtained for the inclusive $k_\perp$ algorithm in (9.4).

Fits to the Dijet Cross Section Measured using Different Jet Algorithms

The analysis that we have performed for the inclusive jet cross section can also be made for the dijet cross section. The dijet cross section has also been measured double differentially as a function of Q^2 and $\overline{E}_T$ (the average transverse energy of the dijet system). In addition to the inclusive $k_\perp$ algorithm and the Aachen algorithm we have also used the exclusive $k_\perp$ algorithm and the Cambridge algorithm for this measurement. Setting the renormalization scale to $\mu_r = \overline{E}_T$ we have performed the same fits as for the inclusive jet cross section. The corresponding fit results are displayed in Fig. 9.7 for the four different jet algorithms.

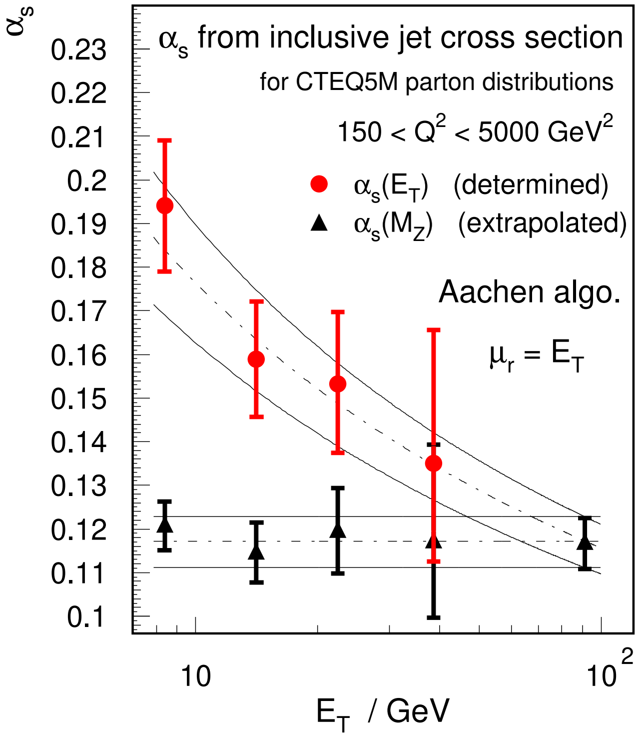

Figure 9.6: Determination of α_s from the inclusive jet cross section using the Aachen algorithm for a renormalization scale $\mu_r = E_T$. The results are shown for each E_T value (circles). The single values are extrapolated to the Z^0-mass (triangles). A final result for $\alpha_s(M_Z)$ (rightmost triangle) is obtained from a combined fit. The upper curves indicate the prediction of the renormalization group equation for the evolution of the combined fit result and its uncertainty.

The combined results of these fits are directly compared to each other in Fig. 9.8 and the numerical values are listed in table D.3 in the appendix.

All $\alpha_s(M_Z)$ results are in good agreement with each other. The results for both exclusive jet algorithms have larger theoretical uncertainties due to the larger hadronization corrections[2]. Only the result for the Cambridge algorithm is somewhat low compared to the other jet algorithms (although still consistent within its uncertainties). For the Cambridge algorithm, however, the hadronization corrections are large (between 10% and 25%) such that the model estimates may not be reliable (see the related discussion in section 3.1).

---

[2] In section 3.3 we have motivated our assumption that the uncertainty is proportional to the estimated size of the hadronization corrections.

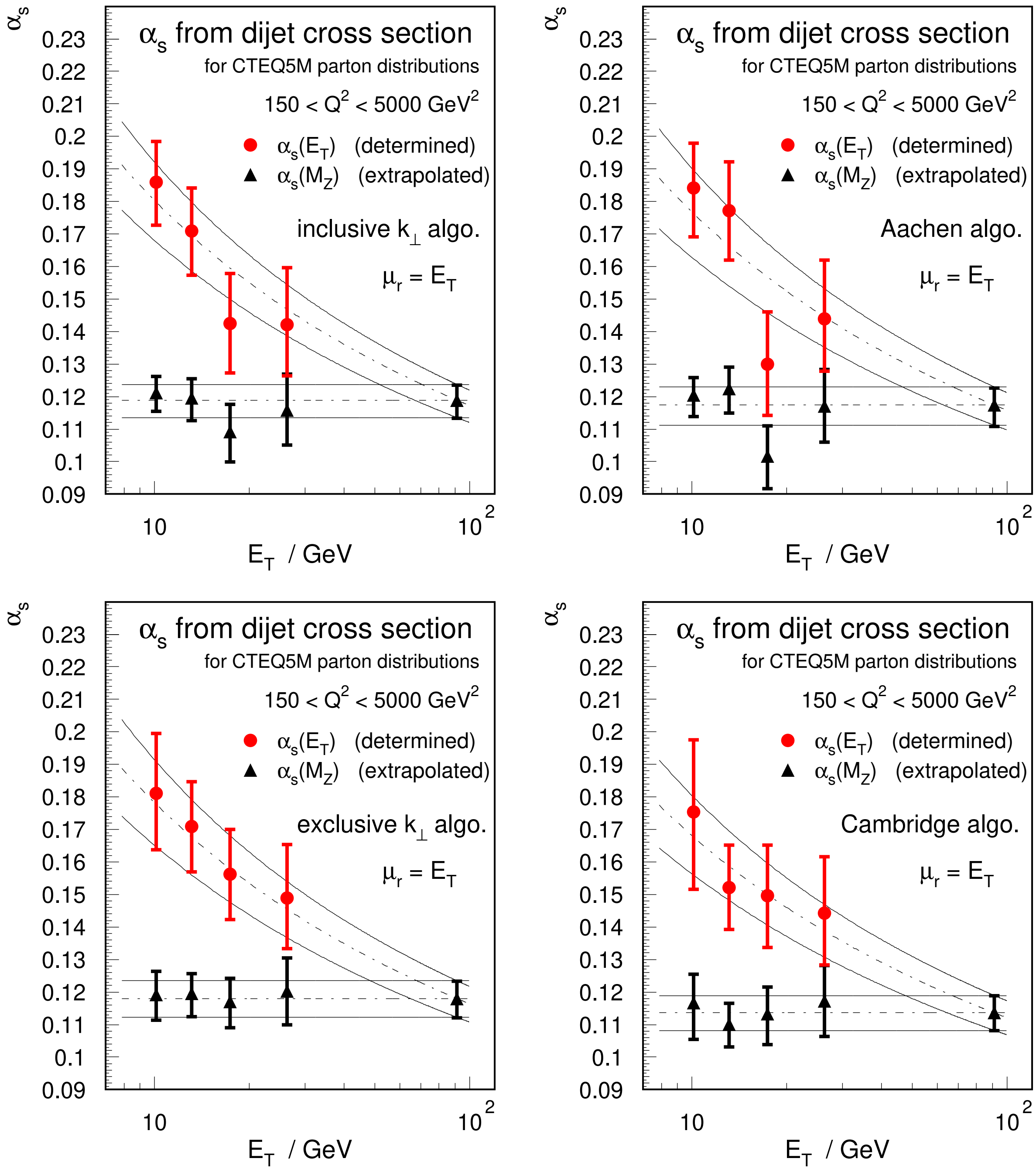

Figure 9.7: Determination of α_s from the dijet cross section measured with four different jet algorithms at a renormalization scale $\mu_r = \overline{E}_T$. The results for $\alpha_s(E_T)$ are obtained in different $\overline{E}_T$ regions (circles) and are subsequently evolved to the Z^0 mass (triangles). A combined fit yields2 a result for $\alpha_s(M_Z)$ (rightmost triangle).

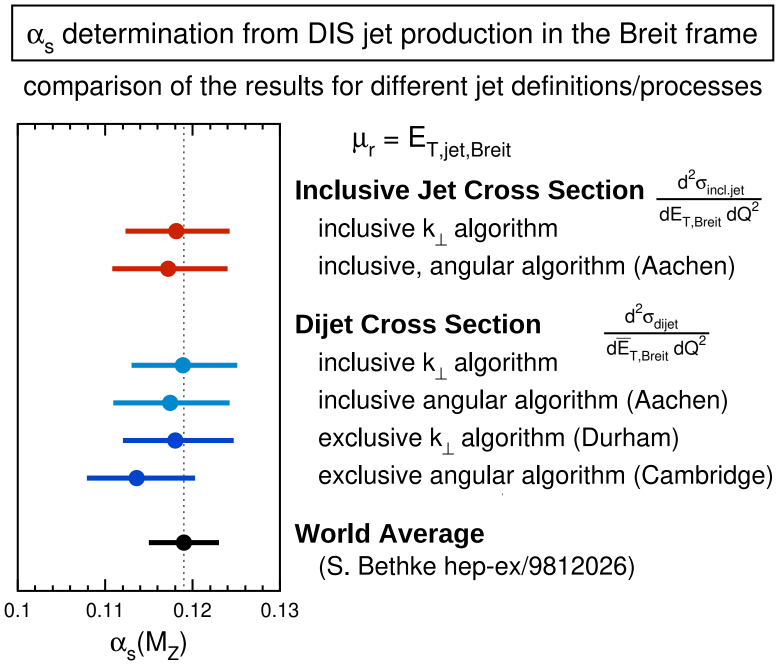

Figure 9.8: The $\alpha_s(M_Z)$ results from the fits to the double differential cross section $\mathrm{d}^2\sigma/\mathrm{d}E_T\mathrm{d}Q^2$ in inclusive jet production and in dijet production for different jet definitions.

Fits to Different Dijet Distributions

As a further consistency test we perform fits to the other dijet distributions measured using the inclusive $k_\perp$ algorithm. The $\alpha_s(M_Z)$ results from these fits are summarized in Fig. 9.9 and listed in table D.4. All results are seen to be consistent with each other deviating by maximally ${}^{+0.0037}_{-0.0008}$ from our central result (9.4).

Using a Different χ^2 Definition

The central $\alpha_s(M_Z)$ result in (9.4) is obtained in a fitting procedure by minimizing the variable χ^2 as defined in (B.16). Correlations between uncertainties are taken into account by fitting corresponding parameters for each source. In appendix B we have given the reasons why we prefer this definition for our purposes, one argument being the possibility of taking into account the asymmetry of uncertainties.

We however wish to demonstrate that the results do not depend too strongly on the exact definition. We have therefore repeated the fit using a χ^2 definition based on the covariance matrix as introduced in (B.11) and (B.15). Since this definition can only handle symmetric uncertainties we redefine all uncertainties to be symmetric by taking the average of the positive and the negative uncertainty. Repeating the procedure from section 9.1.2 we obtain an $\alpha_s(M_Z)$ result of

$$\alpha_s(M_Z) \;=\; 0.1184 \pm 0.0031\,(\text{exp.}) \pm 0.0039\,(\text{th.})\,{}^{+0.0036}_{-0.0017}\,(\text{pdf}) \qquad (\text{cov. matrix})\,, \qquad (9.6)$$

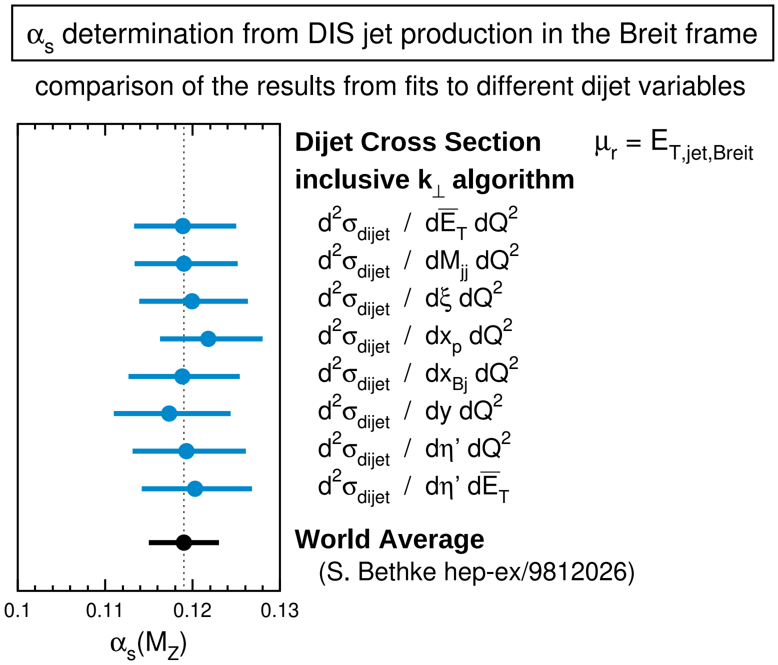

Figure 9.9: The $\alpha_s(M_Z)$ results from the fits to different double differential dijet cross sections measured with the inclusive $k_\perp$ jet algorithm.

which is very close to the central result in (9.4). The uncertainties are also similar in size (the experimental and the theoretical uncertainties are here symmetric by definition).

9.1.6 Summary of the α_s Fits

We have performed various QCD fits in which we have extracted $\alpha_s(M_Z)$ from different jet distributions measured using different jet algorithms. The main results displayed in Figs. 9.8 and 9.9 are seen to be consistent with each other and with the current world average value [22].

We do not consider an averaging of the different results to be meaningful. Correlations are only known for the experimental, but not for the theoretical uncertainties. The renormalization scale dependence for example is assumed to be an estimate of the possible size of higher order corrections. Since different jet definitions may have different higher order corrections one can not make any assumptions on their correlations. Similar statements apply to the uncertainty of the hadronization corrections, since the applicability of the hadronization models (which are not matched to the NLO calculation; see section 3.3) may vary for different jet algorithms.

We therefore prefer to quote the value obtained with the jet algorithm with the smallest hadronization corrections, i.e. the inclusive $k_\perp$ algorithm as the main result. We extract four values of $\alpha_s(E_T)$ for the four bins in E_T which are found to be consistent with the running of α_s as predicted by the renormalization group equation (Fig. 9.2). In a combined fit of all data points we obtain the result

$$\alpha_s(M_Z) = 0.1181 \pm 0.0030\,(\text{exp.})\,^{+0.0039}_{-0.0046}\,(\text{th.})\,^{+0.0036}_{-0.0017}\,(\text{pdf}) \qquad (\mu_r = E_T)\,. \tag{9.7}$$

This result is extracted for a renormalization scale of $\mu_r = E_T$. The theoretical uncertainty includes the effect of the variation between $\mu_r = 0.5 E_T$ and $\mu_r = 2 E_T$. The choice of $\mu_r = Q$ leads to an $\alpha_s(M_Z)$ result which is by $+0.0040$ higher. The renormalization scale dependence of the result increases from $^{+0.0025}_{-0.0034}$ (for $\mu_r = E_T$) to $^{+0.0044}_{-0.0049}$ (for $\mu_r = Q$) such that both results are still consistent. Because of the reduced scale dependence we consider the perturbative calculation to be more reliable for $\mu_r = E_T$ and therefore decide to quote this as the main result of the analysis.

We may compare this result to the published results from earlier analyses performed in dijet production in deep-inelastic scattering by the H1 and the ZEUS collaborations[3]:

$$\begin{aligned}
\text{ZEUS [5]}: \quad \alpha_s(M_Z) &= 0.117 \pm 0.005(\text{stat.})\,^{+0.004}_{-0.005}(\text{exp.}) \pm 0.007(\text{th.})\,,\\
\text{H1 [3]}: \quad \alpha_s(M_Z) &= 0.117 \pm 0.003(\text{stat.})\,^{+0.009}_{-0.013}(\text{exp.\&th.}) + 0.006(\text{jet algorithm})\,,\\
\text{H1 [4]}: \quad \alpha_s(M_Z) &= 0.118 \pm 0.002(\text{stat.})\,^{+0.007}_{-0.008}(\text{exp.})\,^{+0.007}_{-0.006}(\text{th.})\,.
\end{aligned}$$

It is obvious that the present analysis is able to reduce the uncertainty of the result very significantly. Progress has been made in the statistical, the experimental and the theoretical contribution.

The main cause for the progress in all three contributions is the high statistics of the H1 data taken in 1995-1997 ($\mathcal{L}_{\text{int}} = 33\,\text{pb}^{-1}$ as compared to $\mathcal{L}_{\text{int}} \simeq 7\,\text{pb}^{-1}$ in the older H1 analyses and $\mathcal{L}_{\text{int}} = 3.2\,\text{pb}^{-1}$ for the ZEUS result). The reduction of the statistical uncertainty to ± 0.0007 (see table D.2) however, is only one aspect.

The high statistics available now has been used to improve the calibration of the hadronic energy scale [32, 81] which helped to reduce the corresponding uncertainty. Furthermore an improved jet definition (the previous analyses were all performed using the modified JADE jet algorithm [46, 47]) and harder cuts on the transverse jet energies helped to reduce experimental uncertainties (the model dependence of the detector correction) as well as theoretical uncertainties (the size of the hadronization corrections).

A major advantage of the present analysis is the large variety of measured jet distributions which confirm the stability of the fit results with respect to the choice of variables employed for the QCD fits. This demonstrates the good overall agreement between theory and data over a wide kinematic range.

---

[3] The H1 result [4] uses a different definition of the experimental uncertainties which includes the uncertainties in the model estimates of the hadronization corrections as well as the uncertainties in the parton distributions. In our analysis the former is included in the theoretical uncertainty and the latter is quoted separately. In the estimate of the theoretical uncertainty of the ZEUS result the renormalization scale was varied only in the range $0.63Q < \mu_r < 1.41Q$ while the H1 analyses used $0.5Q < \mu_r < 2Q$ (as we do in our analysis). In contrast to the present analysis these earlier analyses did not take into account QED corrections.

9.2 Determination of the Gluon and the Quark Densities

In the second part of the QCD analysis we determine the gluon density $xg(x)$ and the charge weighted sum of the quark densities $x\Delta(x) = x\sum_i e_i^2(q_i(x) + \overline{q}_i(x))$ in the proton, while fixing the value of the strong coupling constant to the current world average value of $\alpha_s(M_Z) = 0.119 \pm 0.004$ [22]. The QCD predictions are fitted to the inclusive jet cross section, to the dijet cross section and to recently published H1 data on the inclusive reduced ep cross section $\tilde{\sigma}(x_{\mathrm{Bj}}, Q^2)$.

Our primary interest lies in the result for the gluon density to which the jet cross sections are *directly* sensitive. The inclusive reduced ep cross section is only included to constrain the quark densities from which we can determine the quark induced fraction of the jet cross sections. This approach therefore allows a *consistent* determination of the gluon density in the proton by considering the correlation with the quark densities.

For the reasons described in section 8.2.2 we perform the fit of $xg(x)$ and $x\Delta(x)$ at a fixed factorization scale of $\mu_f = \sqrt{200}\,\mathrm{GeV}$. This value is of the order of the average transverse jet energies E_T of the jet data and of the four-momentum transfer Q of the inclusive ep data (to achieve this we use only the inclusive ep data within $150 < Q^2 < 1000\,\mathrm{GeV}^2$). The small contributions of the quark singlet density $x\Sigma(x) = x\sum_i(q_i(x) + \overline{q}_i(x))$ to the NLO corrections of the jet cross sections are evaluated using the CTEQ5M parameterization[4].

The renormalization scale is set to $\mu_r = Q$ for the inclusive ep cross section and to $\mu_r = E_T$ for the jet cross sections (we will also show the result for the choice $\mu_r = Q$).

9.2.1 The Central Result for the Gluon and the Quark Densities

For the central result we perform a fit to the inclusive ep cross section, to the inclusive jet cross section $\mathrm{d}^2\sigma_{\mathrm{jet}}/\mathrm{d}E_T\mathrm{d}Q^2$ and to the dijet cross section $\mathrm{d}^2\sigma_{\mathrm{dijet}}/\mathrm{d}\xi\mathrm{d}Q^2$ (the latter measured using the inclusive $k_\perp$ algorithm). The gluon and the quark distributions are parameterized according to the 4-parameter formula in (8.9). The fit yields $\chi^2/\mathrm{d.o.f.} = 61.16/105$.

In Fig. 9.10 we present both the fitted gluon (left) and quark densities (right). The error bands include all experimental and theoretical uncertainties as well as the uncertainty of $\alpha_s(M_Z)$. The resulting parameters of the parton densities can be found in the tables D.5 and D.6 in the appendix D.2 together with the uncertainties of the parton densities at specific x-values, corresponding to the error bands in Fig. 9.10. The fitted values of the parameters

---

[4] As described in section 8.2.2 the quark singlet does not contribute to the inclusive ep cross section at next-to-leading order and contributes only marginally to the jet cross sections via the next-to-leading order corrections (below 5% at $Q^2 = 150\,\mathrm{GeV}^2$ and decreasing towards higher Q^2). These contributions are evaluated using the parameterization from CTEQ5M. We have verified that (due to the small size of these contributions) all results are stable if we use other parameterizations. Using e.g. the parameterizations that caused the largest changes in the α_s results in the previous section (MRSR3 and MRST99(g$\downarrow$)) leads to a change in the gluon density below two per mil over the whole x-range and to a change of $x\Delta(x)$ below 0.1 per mil.

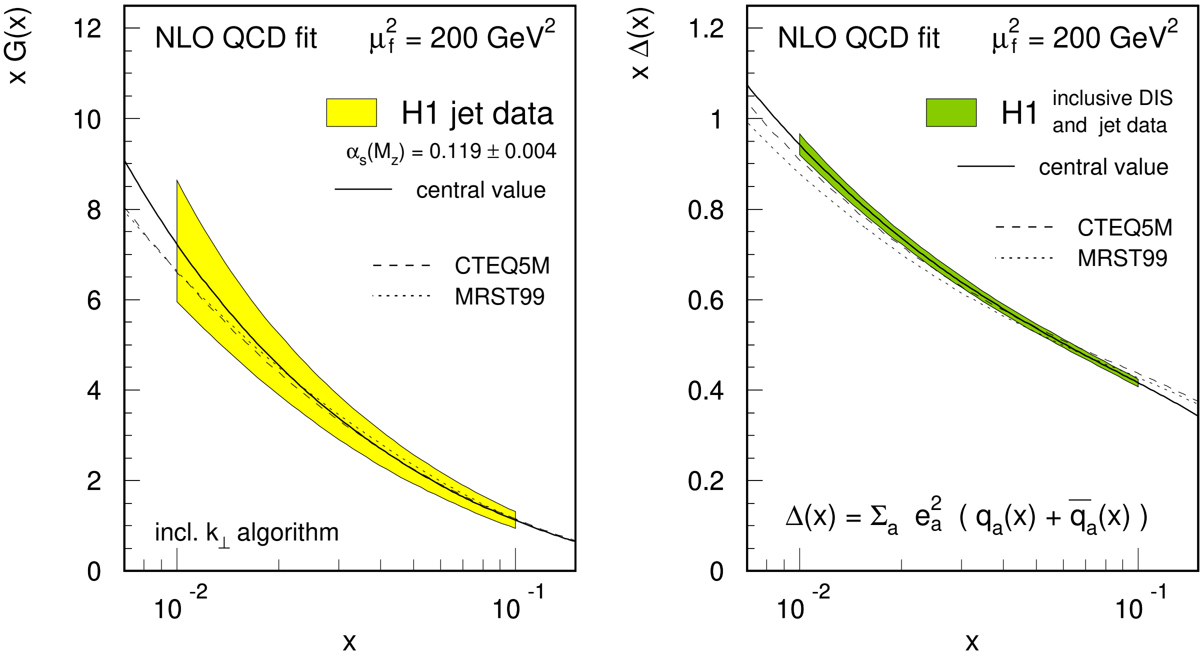

Figure 9.10: The gluon density $xg(x)$ (left) and the quark density $x\Delta(x)$ (right) in the proton, determined in a combined QCD fit to the inclusive reduced ep cross section, the inclusive jet cross section and the dijet cross section. The jet cross sections are measured using the inclusive $k_\perp$ jet algorithm. The error bands include the experimental and the theoretical uncertainties as well as the uncertainty of $\alpha_s(M_Z)$.

for the correlated uncertainties are listed in table D.7.

In Fig. 9.10 the results for the gluon density and the quark density are compared to the results from global analyses. For $x \gtrsim 0.02$ the gluon result is very close to the parameterizations from CTEQ5M and MRST99. Only at smaller x-values our result is slightly larger (8% at $x = 0.01$), but still compatible within its uncertainty. The fitted quark density, however, differs significantly from the global fit results (which also differ from each other by the same amount) and in addition shows a different x dependence.

The gluon density shown in Fig. 9.10 has an uncertainty of ≈ 18% over the whole x range. However, some part of the uncertainty is anti-correlated between the values at different x. We have therefore also determined the integral of the gluon density over the range $0.01 < x < 0.1$ and obtain

$$\begin{aligned} \int_{0.01}^{0.1} \mathrm{d}x \; x\, G(x, \mu_f^2 = 200\,\mathrm{GeV}^2) &= 0.229 \;^{+0.034}_{-0.032}(\mathrm{tot.})\,, \\ &= 0.229 \;^{+0.016}_{-0.015}(\mathrm{exp.}) \;^{+0.019}_{-0.021}(\mathrm{th.}) \;^{+0.022}_{-0.018}(\Delta\alpha_s)\,, \end{aligned} \tag{9.8}$$

with a precision of ≈ 15%. This result means that (at $\mu_f^2 = 200\,\mathrm{GeV}^2$) 23% of the proton momentum is carried by gluons with a momentum fraction in the range $0.01 < x < 0.1$.

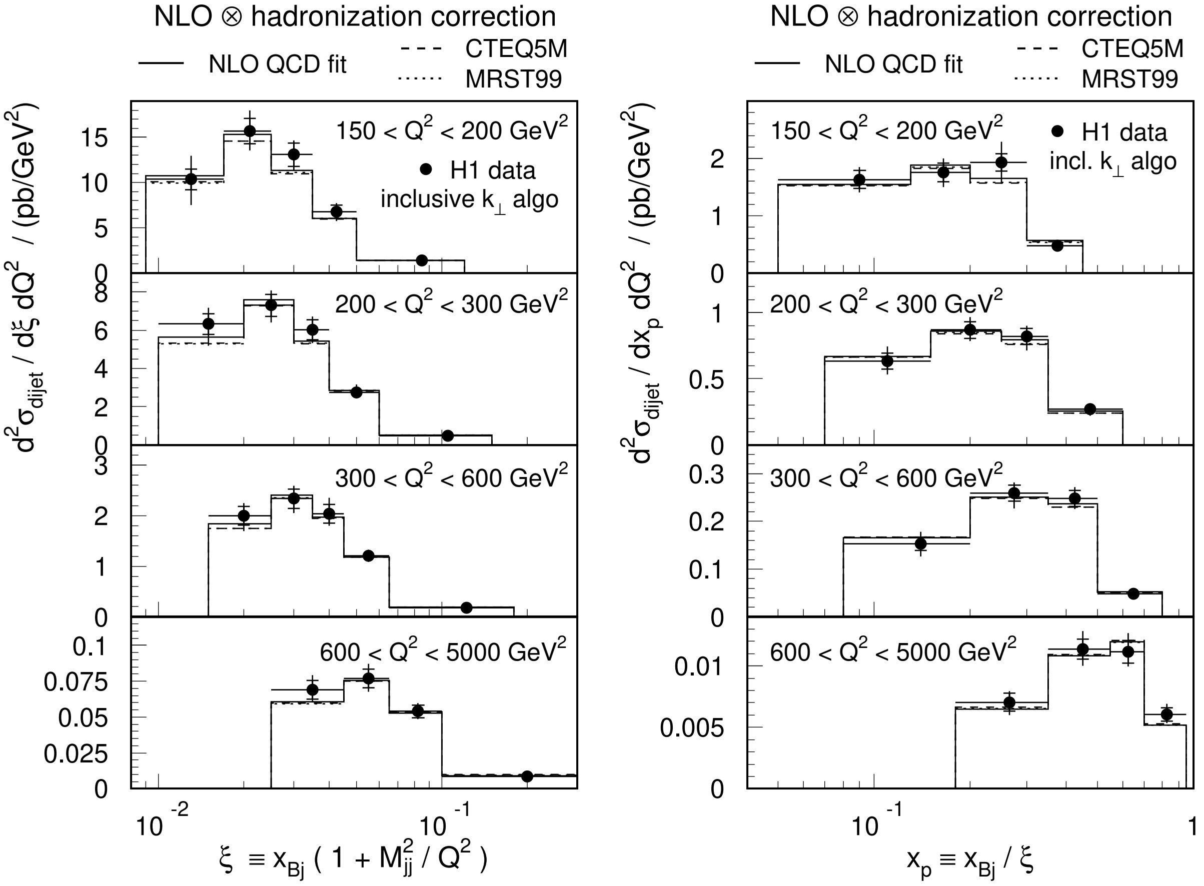

Figure 9.11: The dijet cross section measured double differentially as a function of Q^2 and the variables ξ (left) and x_p (right) using the inclusive $k_\perp$ algorithm. The data are compared to the QCD predictions (including hadronization corrections) using the parton distributions from the NLO QCD fit result (solid line) and the parameterizations from CTEQ5M (dashed line) and MRST99 (dotted line).

This result is in good agreement with the results from global fits for which the integral has the values

$$\text{CTEQ5M: } 0.226\,, \qquad \text{MRST99: } 0.232\,, \qquad \text{GRV98HO: } 0.235\,. \tag{9.9}$$

Using the fitted parton distributions (and $\alpha_s(M_Z) = 0.119$) we compare the theoretical calculations to two differential dijet cross sections (Fig. 9.11) and to the inclusive reduced ep cross section (Fig. 9.12) within the Q^2 range in which the fits are performed. For the inclusive ep cross section we obtain a significantly improved description as compared to the calculations using the CTEQ5M or MRST99 parameterizations. The corresponding differences in the dijet distributions are almost imperceptible.

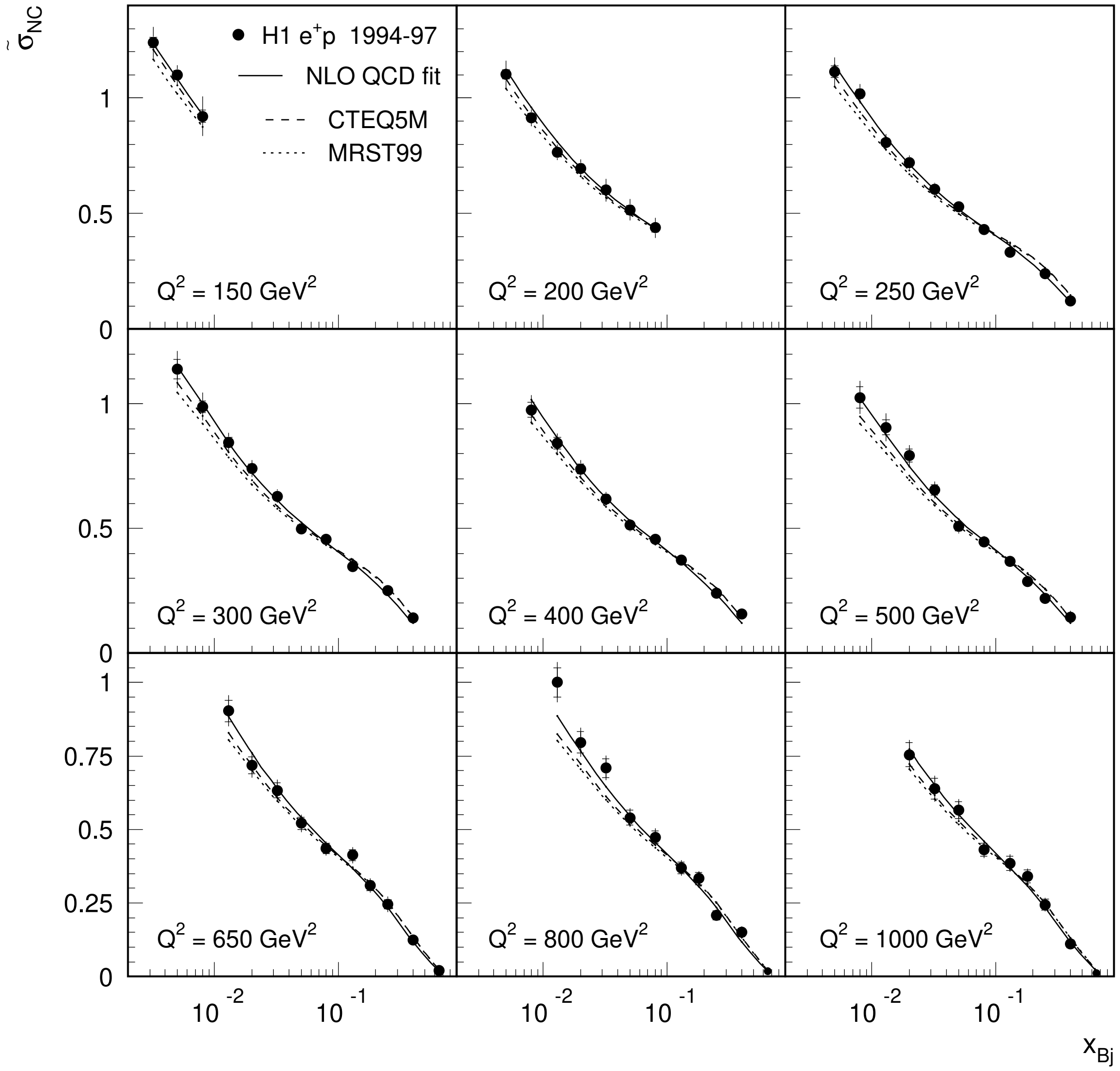

Figure 9.12: The reduced inclusive DIS cross sections measured in the H1 experiment. The data are compared to the QCD predictions in the range $150 < Q^2 < 1000\,\mathrm{GeV}^2$ using either the parton distributions from our NLO QCD fit (solid line) or the parameterizations from recent global analyses (dashed and dotted lines).

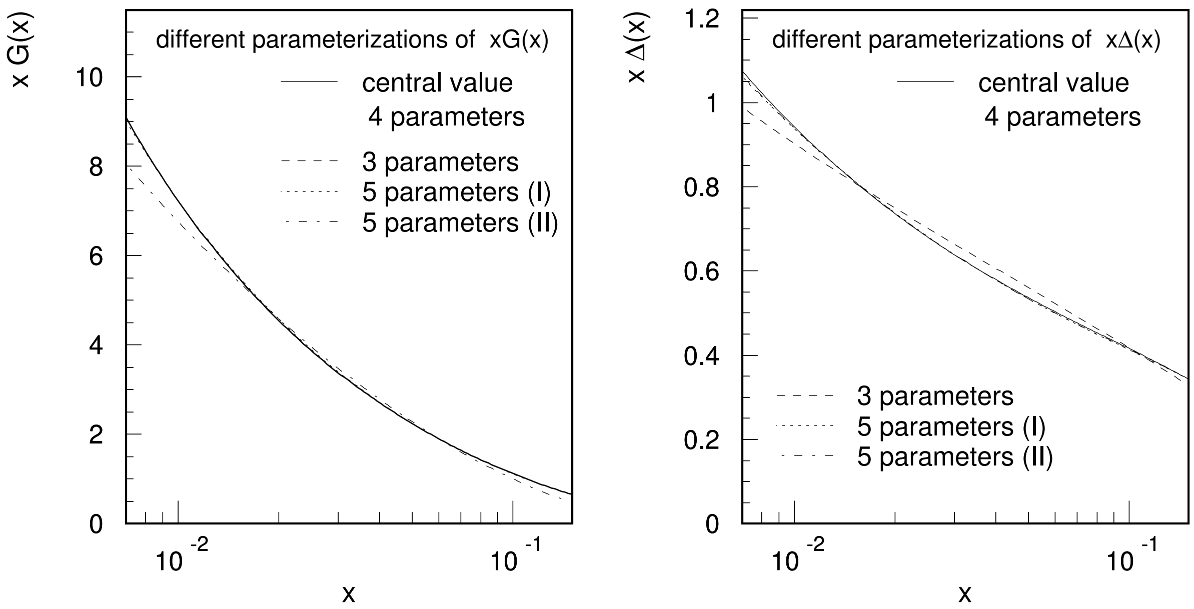

Figure 9.13: The fit results for the gluon density (left) and the quark density (right) for different parameterizations of the x-dependence.

9.2.2 Tests of the Stability of the Results

Dependence of the Result on the Fit Procedure

To test the influence of the specific functional form of the parameterization on the fit results we repeat the fits using the other parameterizations from (8.9). In Fig. 9.13 the corresponding fit results are shown for the gluon density (left) and for the quark density (right). The fitted gluon density does not change when we use the three-parameter formula or the first five-parameter formula. Only for the second five-parameter formula the lowest x-region is slightly reduced (by 8% at $x = 0.01$). For the quark density we obtain stable results with four or more parameters while the three-parameter formula seems not to be flexible enough: The fit result comes out very different and describes the data significantly worse (χ^2/d.o.f. is increased by 0.45!). We conclude that the four-parameter formula employed here is flexible enough not to introduce any bias in the fit results.

As a further check we investigate whether the fit results change when subsets of the data are excluded from the fitting procedure. For this purpose we repeat the fit excluding the data above (or below) $Q^2 = 300\,\mathrm{GeV}^2$. The results of these fits are shown in Fig. 9.14 for the gluon density (left) and for the quark density (right) in comparison with the main result (solid line). Although the uncertainties of these results (not shown here) are larger than the result from the fit to the whole data set, their central values are in good agreement with the main result. This demonstrates that the data are consistent over the whole Q^2 range.

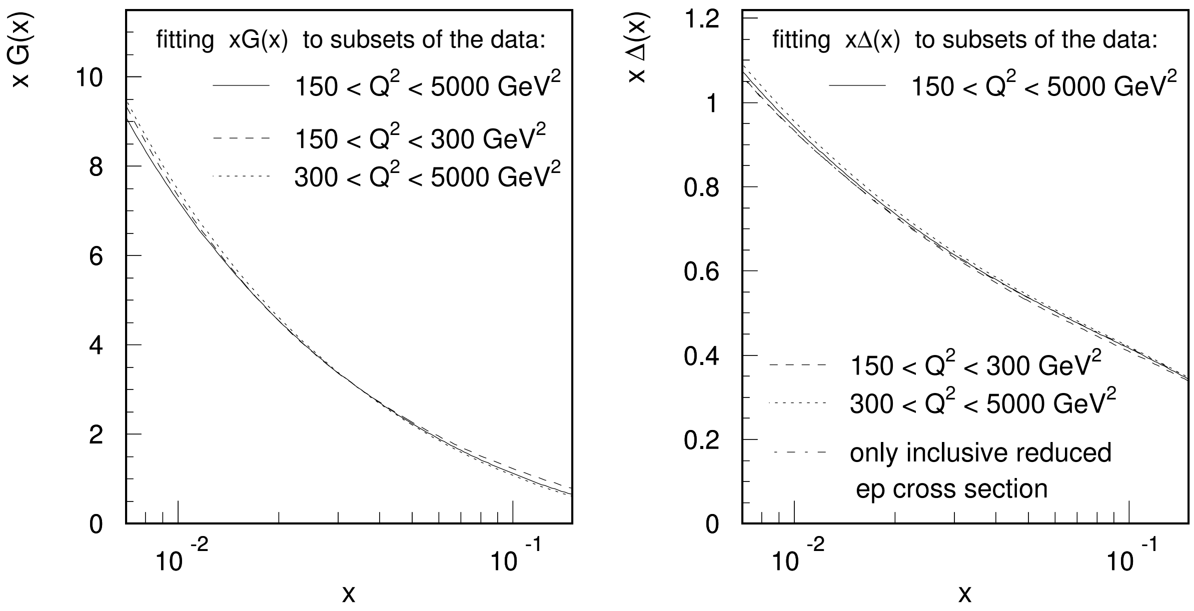

Figure 9.14: The fit results for the gluon density (left) and the quark density (right) from fits to subsets of the data sample.

To show that the quark density is completely determined by the inclusive reduced *ep* cross section we perform a further fit in which the jet data are excluded. The result of this fit is also shown in Fig. 9.14 (dashed-dotted line) and hardly distinguishable from the main result.

Usage of a Different Renormalization Scale

When the perturbative QCD calculations of the jet cross sections are performed at a renormalization scale $\mu_r = Q$ we obtain a slightly larger result for the gluon density as is shown in Fig. 9.15 (left). The quark results (not shown here) are not influenced by this choice. The effect of the increased gluon density is similar to the effect observed in the α_s determination (section 9.1.3). Since the perturbative predictions are slightly lower, the fitted parameters tend to be correspondingly higher.

Usage of a Different Jet Algorithm

The inclusive jet cross section and the dijet cross sections have also been measured using the Aachen jet algorithm. Employing these distributions, we repeat the central fits from section 9.2.1 (under otherwise unchanged conditions). The fit result for the gluon density is displayed in Fig. 9.15 (right). No difference from the result obtained for the inclusive $k_\perp$ algorithm is seen.

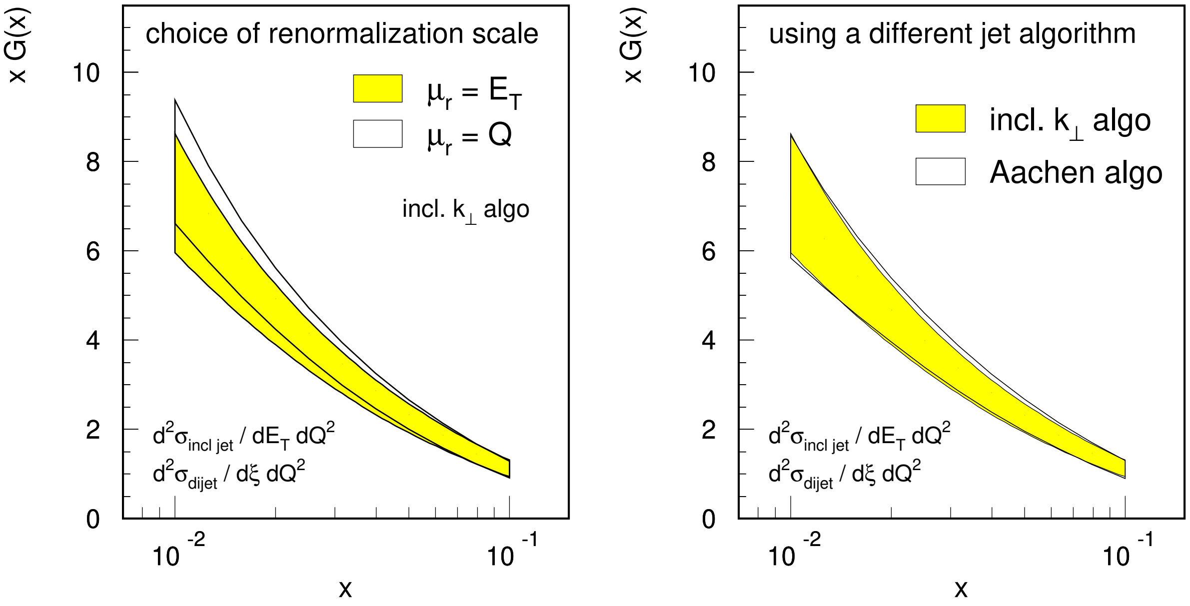

Figure 9.15: The dependence of the fitted gluon density on the choice of the renormalization scale at which the jet cross sections are evaluated (left) and on the jet definition (right).

Fits to Different Dijet Distributions

So far we have only used the measurements performed with the inclusive jet definitions. The exclusive jet definitions were only employed for measurements of the dijet cross section.

To investigate the influence of the jet algorithm on the results we repeat the combined fits to the inclusive reduced *ep* cross section and to the two dijet cross sections $\mathrm{d}^2\sigma_{\rm dijet}/\mathrm{d}\overline{E}_T\mathrm{d}Q^2$ and $\mathrm{d}^2\sigma_{\rm dijet}/\mathrm{d}\xi\mathrm{d}Q^2$ for all jet algorithms. The results for the gluon density from these fits are displayed in Fig. 9.16 as error bands. The additional lines represent the results from further fits to other dijet variables. Since different jet variables are in different ways sensitive to the x-dependence of the parton densities we observe some deviations between the single fit results which become larger towards $x \approx 0.01$ where the data used are no longer sensitive.

For the inclusive jet algorithms (top) the deviations between the fits to different variables are small compared to the size of the error band over the whole x range. The results for the gluon density obtained with the exclusive jet algorithms (bottom) are slightly lower. For these algorithms the deviations between the fits to the different variables are larger, but still within the error bands.

A direct comparison of the combined fits for the different jet algorithms (the error bands in Fig. 9.16) to our main result (from Fig. 9.10) is given in Fig. 9.17. All results are found to be compatible and the variations of the single results are well contained in the quoted error band.

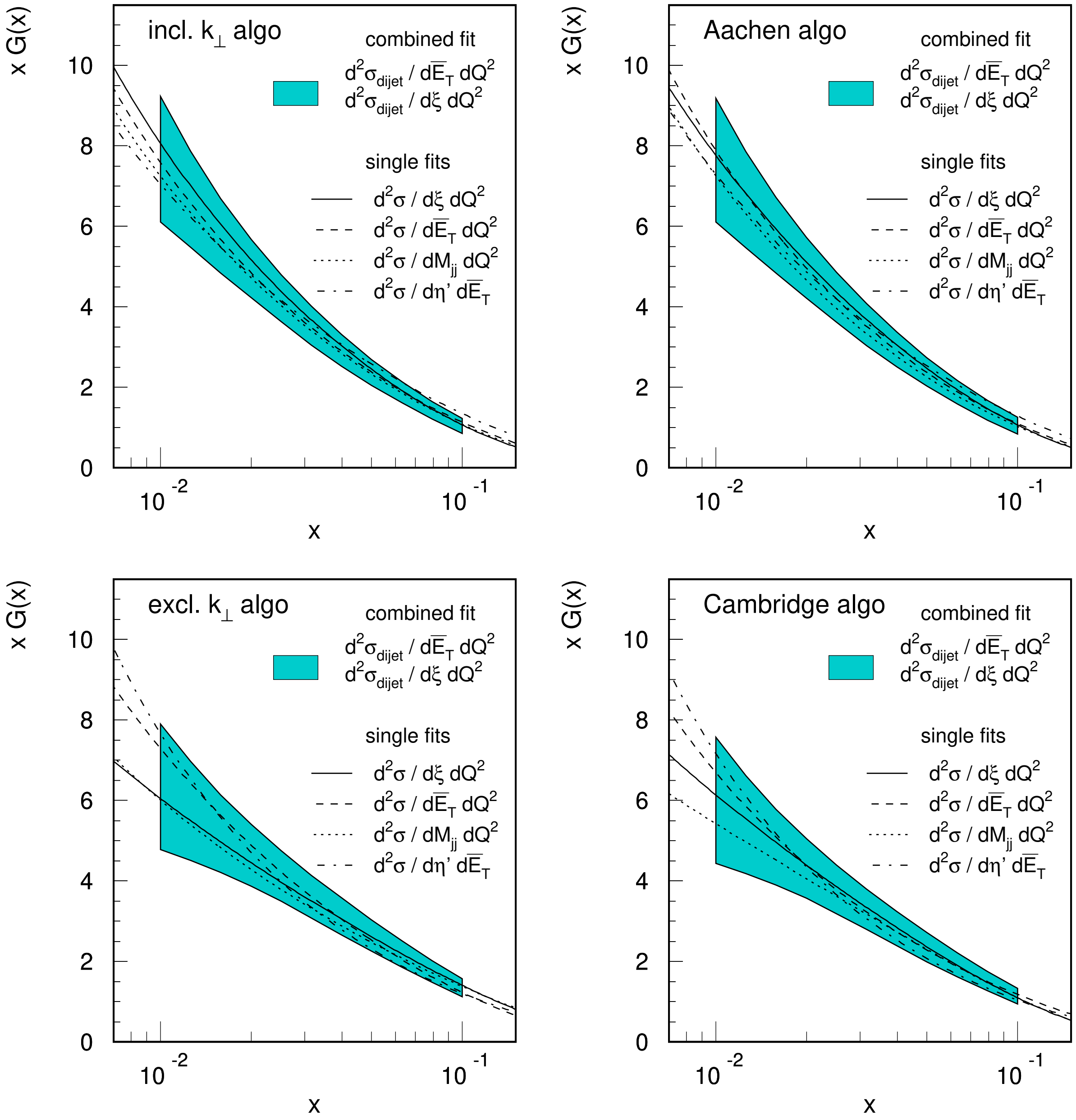

Figure 9.16: The gluon density $xg(x)$ in the proton, determined in QCD fits to the inclusive reduced *ep* cross section and to the dijet cross section, measured using different jet algorithms. The error bands include the experimental and the theoretical uncertainties and the uncertainty of $\alpha_s(M_Z)$. Further fits to different distributions are performed of which only the central values are shown.

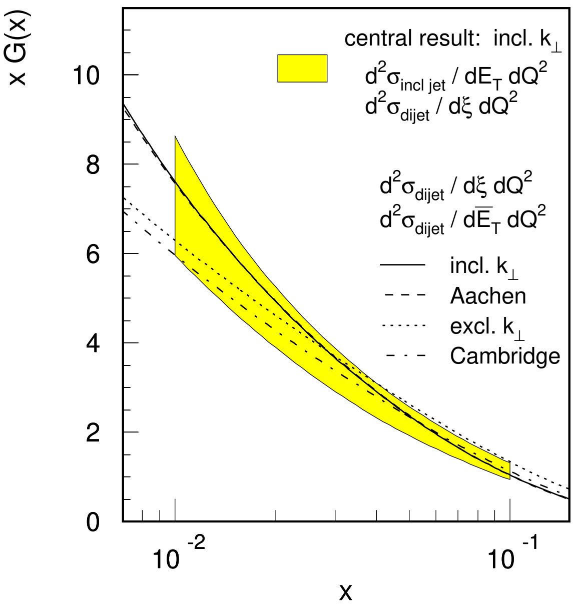

Figure 9.17: A comparison of the central fit result for the gluon density (error band) along with the results of fits to the dijet distributions obtained using different jet algorithms (lines).

9.2.3 Summary of the Results on the Gluon and the Quark Densities

Using the combined jet data from the inclusive jet and the dijet cross section and the H1 results from the inclusive reduced *ep* cross section we have performed a QCD fit to determine the gluon density together with the quark densities in the proton at moderate momentum fractions ($0.01 < x < 0.1$). We have shown that the results remain stable when using different jet distributions and jet algorithms in the fits. The extracted gluon density is in good agreement with the global fit results from CTEQ5M and MRST99.

Evaluating the jet cross sections at a renormalization scale of $\mu_r = Q$ (instead of $\mu_r = E_T$) we obtain a result for the gluon density which is slightly larger (approx. 9% at $0.01 < x < 0.02$), but still consistent with the global fit results within the uncertainty.

9.3 Simultaneous Determination of $\alpha_s(M_Z)$, the Gluon and the Quark Densities

In the previous two parts of the QCD analysis we have either determined $\alpha_s(M_Z)$ or the gluon density while the respective other parameter was fixed and taken from external input (world average or global fits). In the third step of the QCD analysis we will perform a simultaneous fit of the gluon and the quark densities as well as $\alpha_s(M_Z)$.

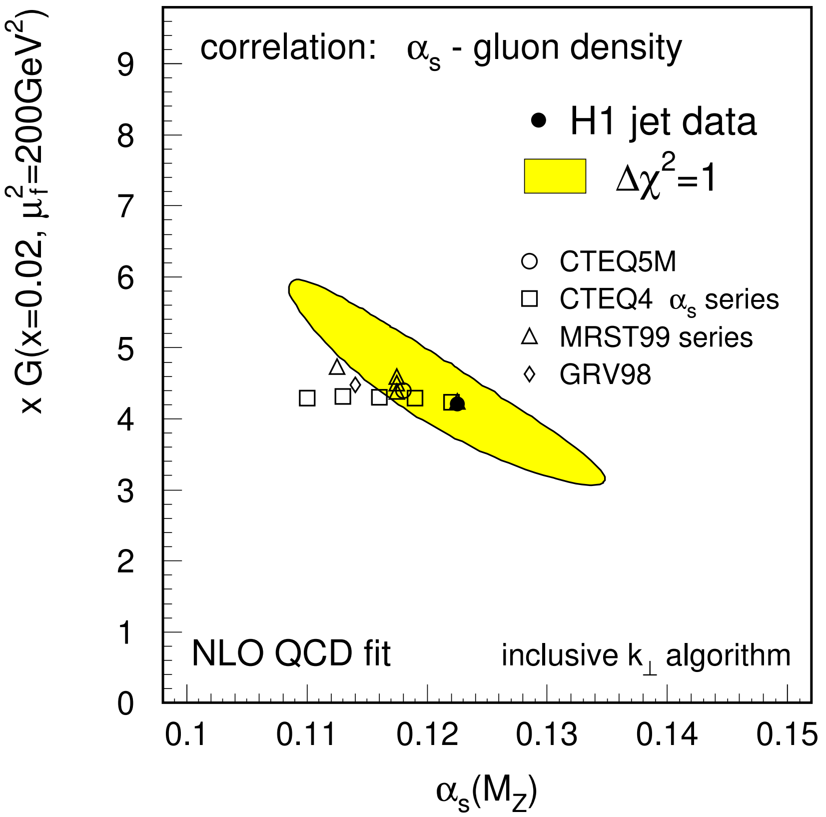

Figure 9.18: The correlation of the fit results for $\alpha_s(M_Z)$ and the gluon density at $x = 0.02$ determined in a simultaneous QCD fit to the inclusive reduced *ep* cross section, the inclusive jet cross section and the dijet cross section. The jet cross sections are measured using the inclusive $k_\perp$ jet algorithm. The error ellipse includes the experimental and the theoretical uncertainties.

9.3.1 The Central Result

The central result is obtained in a fit to the data sets used already in the previous section, the inclusive *ep* cross section, the inclusive jet cross section $\mathrm{d}^2\sigma_{\mathrm{jet}}/\mathrm{d}E_T\mathrm{d}Q^2$ and the dijet cross section $\mathrm{d}^2\sigma_{\mathrm{dijet}}/\mathrm{d}\xi\mathrm{d}Q^2$ (the jet cross sections having been measured with the inclusive $k_\perp$ algorithm). The gluon and the quark distributions are parameterized according to the 4-parameter formula in (8.9). The simultaneous fit yields $\chi^2/\mathrm{d.o.f.} = 61.10/104$ and a result for the quark distributions identical to the one obtained in the fit with a constrained $\alpha_s(M_Z)$ (section 9.2).

We display the result of this simultaneous fit as a correlation plot between $\alpha_s(M_Z)$ and the gluon density evaluated at $x = 0.02$ (a value which is well contained in the range in which our data are sensitive) in Fig. 9.18. The central fit result is indicated by the full marker and the error ellipse is the contour along which the χ^2 of the fit is by one larger than the minimum (including experimental and theoretical uncertainties). The contour is of a narrow

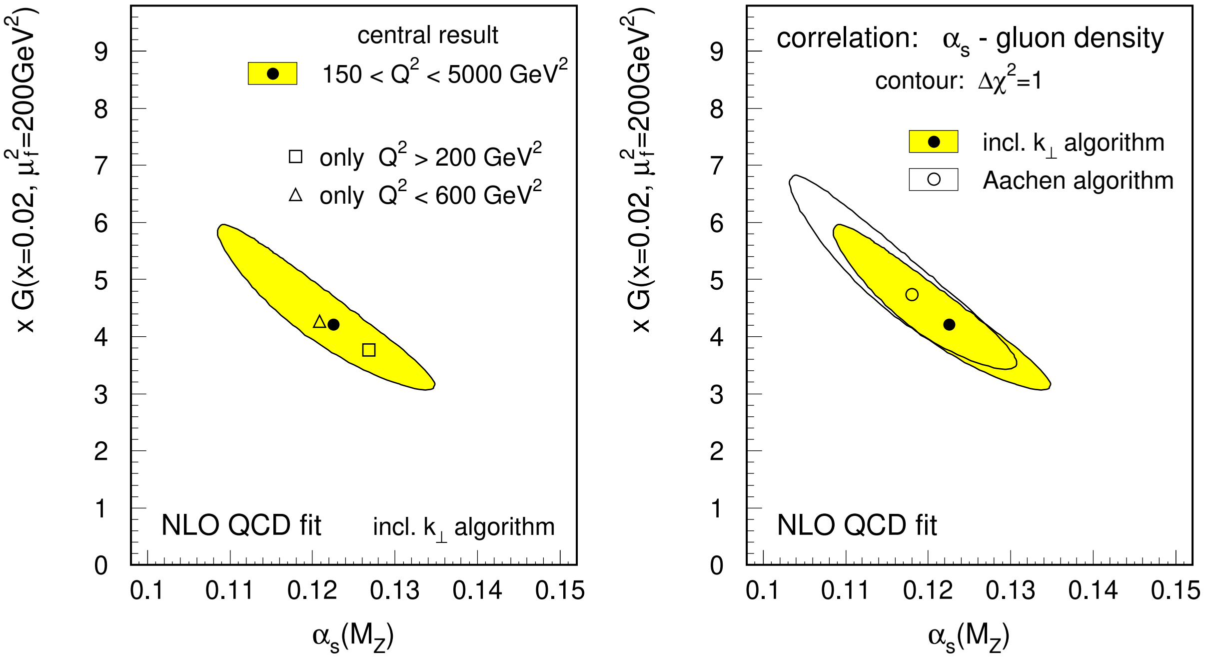

Figure 9.19: The correlation between the fit results for $\alpha_s(M_Z)$ and the gluon density evaluated at $x = 0.02$. The results from fits to different subsets of the data sample (left) and from fits to the data measured using different jet algorithms (right) are compared.

and prolate shape showing that our data are very sensitive to the product $\alpha_s \cdot xg(x)$ but do not yet allow to determine both parameters simultaneously at such high precision.

Also included in Fig. 9.18 are the results from global fits. While no anti-correlation between α_s and the gluon density is seen in the CTEQ4 series, the MRST99 series shows an anti-correlation which is smaller than the one seen in our fit result. Consistency between our result and the global fits is only seen for sets of parton distributions extracted for $\alpha_s(M_Z) \gtrsim 0.117$.

9.3.2 Tests of the Stability of the Result

To test the stability of the fit result we repeat the QCD fit using only data from specific regions of Q^2. In Fig. 9.19 (left) we show the central results from two fits in which we exclude respectively the data at $Q^2 < 200\,\mathrm{GeV}^2$ (rectangle) and those at $Q^2 > 600\,\mathrm{GeV}^2$ (triangle).

Furthermore we perform a fit where the data obtained using the inclusive $k_\perp$ algorithm are replaced by the corresponding distributions measured using the Aachen algorithm. The correlation plot of this result is represented in Fig. 9.19 (right) by an open marker and a white error ellipse and compared to the central result.

The results of all these variations are consistent with the central result. Although the values of $\alpha_s(M_Z)$ and $xg(x)$ fluctuate slightly, the fit results lie always in the central region of the contour.

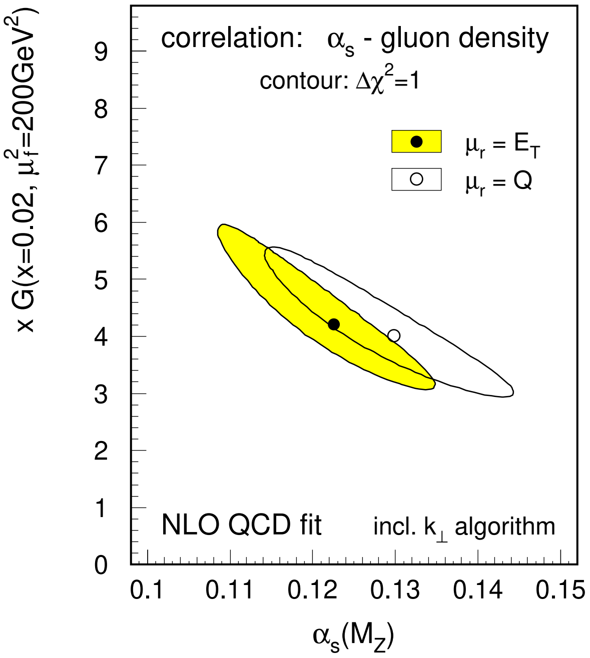

Figure 9.20: The correlation of the fit results for $\alpha_s(M_Z)$ and the gluon density at $x = 0.02$ determined in a QCD fit to the inclusive reduced *ep* cross section, the inclusive jet cross section and the dijet cross section. The fit result for the choice $\mu_r = E_T$ (shaded ellipse) for the renormalization scale in the perturbative calculations of the jet cross sections is compared to that for $\mu_r = Q$.

9.3.3 Choice of a Different Renormalization Scale

As we have done in the previous parts of the QCD analysis, we repeat this fit using a renormalization scale $\mu_r = Q$ in the perturbative calculations of the jet cross sections. The fit result is compared to the result obtained for $\mu_r = E_T$ in Fig. 9.20. The fit result is shifted to slightly higher values of $\alpha_s \cdot xg(x)$ in consistency with the observations made in the previous fits (Figs. 9.3 and 9.15).

9.4 Summary and Comparison to other Results

We have used the jet cross sections measured at high four-momentum transfers Q^2 and large transverse jet energies E_T to determine the free parameters of perturbative QCD calculations to which the jet cross sections are *directly* sensitive, the strong coupling constant and the gluon density in the proton.

process	experiment	$\alpha_s(M_Z)$	theory
DIS – jets	this analysis	$0.1181\ ^{+0.0061}_{-0.0058}$	NLO
DIS – scaling violations	CCFR [119]	$0.119\ \pm 0.0045$	NLO
DIS – GLS sum rules	CCFR [120]	$0.114\ ^{+0.010}_{-0.012}$	NLO
e^+e^- – jets	OPAL [121]	$0.1187\ ^{+0.0034}_{-0.0019}$	NLO + resummed
$e^+e^- - \Gamma(Z^0 \to \text{had.})$	LEP combined [22]	$0.122\ \pm 0.005$	NNLO
τ decays	OPAL [122]	$0.1219\ \pm 0.0020$	NNLO
τ decays	ALEPH [123]	$0.1202\ \pm 0.0027$	NNLO
world average [22]		$0.119\ \pm 0.004$	

Table 9.1: Comparison of the $\alpha_s(M_Z)$ result obtained in this analysis with results determined from other processes. The last column indicates the type of theoretical approximation under which the results are extracted.

Determination of the Strong Coupling Constant

Following a standard approach in which the gluon and the quark densities are taken from the results of global fits, we have determined the strong coupling constant α_s in a NLO QCD fit to the inclusive jet cross section. Using a renormalization scale of $\mu_r = E_T$ we have extracted four values of $\alpha_s(E_T)$ which are consistent with the running of α_s as predicted by the renormalization group equation. A combined fit yields the result

$$\alpha_s(M_Z) \;=\; 0.1181 \pm 0.0030\,(\text{exp.})\,^{+0.0039}_{-0.0046}\,(\text{th.})\,^{+0.0036}_{-0.0017}\,(\text{pdf}) \qquad (\mu_r = E_T)\,.$$

The uncertainty is dominated by the theoretical contributions from the renormalization scale dependence and the uncertainty of the hadronization corrections (the factorization scale dependence is negligible).

In table 9.1 we have compared this result with other $\alpha_s(M_Z)$ results determined from different processes (some values are still preliminary)[5] and with the current world average value. Our result is found to be consistent with the other results and competitive in precision.

Direct Determination of the Gluon and the Quark Densities

We have extracted the gluon and the quark densities in the proton in a NLO QCD fit to the jet cross sections measured in this analysis and to a recent H1 measurement of the inclusive reduced ep cross section [32] fixing $\alpha_s(M_Z)$ at the current world average value of $\alpha_s(M_Z) = 0.119 \pm 0.004$ [22]. This direct determination yields a result for the gluon density in a range of moderate momentum fractions $0.01 < x < 0.1$ shown in Fig. 9.21 as a function of x. The integral over this x range is found to be

$$\int_{0.01}^{0.1} \mathrm{d}x\; x\, G(x, \mu_f^2 = 200\,\mathrm{GeV}^2) \;=\; 0.229\,^{+0.034}_{-0.032}\,. \tag{9.10}$$

---

[5] The selection of the results quoted here is arbitrary. A comprehensive overview can be found in [22, 21], a detailed discussion of $\alpha_s(M_Z)$ determinations in deep-inelastic scattering is given in [118].

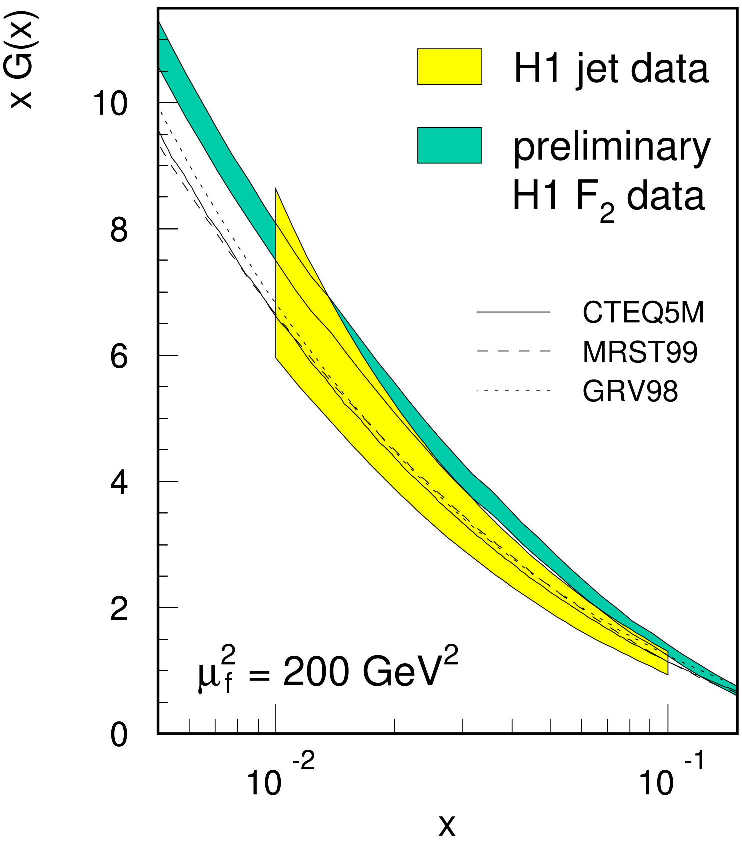

Figure 9.21: A comparison of the gluon density determined in this analysis from jet data to the preliminary H1 result from a fit to structure function data and to the results from recent global analyses.

This result is in very good agreement with the results from recent global analyses (CTEQ5M, MRST99, GRV98) which also include data sets with *direct* sensitivity to the gluon density (prompt photon and jet data). At $x > 0.02$ the result is not consistent with the preliminary H1 result from a fit to structure function data. This discrepancy is currently not understood.

It should, however, be mentioned that the determination of the gluon density from jet cross sections is straightforward and transparent insofar as a change in the gluon density is here *directly* related to a change in the theoretical predictions. In the H1 result obtained from the fit to structure function data only it is not immediately clear which data points (or which properties of the distributions) constrain the gluon density at moderate x with the high precision reflected in the small error band. It seems to be more important to understand why the H1 result is not compatible with the global fit results which also include (parts of) the HERA structure function data and for which they obtain good χ^2 values. The discrepancy does not necessarily represent an inconsistency of the data but could also be attributed to the fit procedure, which can have a significant effect especially in cases where the data are not directly sensitive to the gluon density. This discussion is, however, beyond the scope of the present work. It should be mentioned again at this point that the present analysis arrives at a best fit for the gluon density which is entirely consistent with the results from global analyses (which include H1 structure function data, but not the jet cross sections used here).

Another direct determination of the gluon density in the proton from $D^\star$ production in deep-inelastic scattering and in photoproduction has recently been published by the H1 collaboration [124]. The result was obtained at $\mu_f^2 = 25\,\mathrm{GeV}^2$ in the range $0.001 < x < 0.04$ with uncertainties significantly larger than those of the present analysis. A direct comparison of both results is not possible since they have been extracted at different factorization scales.

The quark densities are determined at high precision and seen to be inconsistent with the global fit results. Our result shows a stronger x-dependence in the range $0.01 < x < 0.1$ and is 3.5% (6.5%) larger than the fit result from CTEQ5M (MRST99) at $x = 0.01$.

Simultaneous Determination of the Strong Coupling Constant, the Gluon and the Quark Densities

In a final step we have performed a NLO QCD fit to the jet data and to the inclusive reduced *ep* cross section for a simultaneous determination of $\alpha_s(M_Z)$, the gluon and the quark densities. We have shown that the simultaneous determination of the gluon density $xg(x)$ and $\alpha_s(M_Z)$ is possible using the jet cross sections measured in this analysis. A stable fit result is obtained and the central values of $\alpha_s(M_Z)$ and $xg(x)$ are consistent with the current world knowledge.

The anti-correlation between $\alpha_s(M_Z)$ and $xg(x)$ is, however, large and our present jet data are not yet sensitive to constrain both with a high precision. On the other hand, our data give strong constraints on the product $\alpha_s \cdot xg(x)$ and will therefore have significant impact if they are included in combined analyses together with other data sets with additional (and different) sensitivity to α_s and the gluon density.

Summary and Outlook

We have used jet cross sections in deep-inelastic positron-proton collisions to perform tests of Quantum Chromodynamics and to determine the strong coupling constant $\alpha_s(M_Z)$ and the gluon density in the proton. The investigations presented in this thesis mark a significant progress in the analysis of jet production in deep-inelastic scattering. Using the high available statistics delivered by HERA in the years 1994–1997 a large variety of jet distributions has been measured using different jet definitions. Over wide regions of phase space an excellent agreement between theory and data is seen. The determination of theoretical parameters has led to significantly improved results compared to previous work (extraction of $\alpha_s(M_Z)$) as well as to novel results (the first simultaneous determination of $\alpha_s(M_Z)$ and the gluon density in the proton). We have demonstrated the consistency of the results from jet production in deep-inelastic scattering with those obtained in other processes on a new quantitative level which represents an important test of perturbative QCD.

The Measurement

The analysis is based on data recorded by the H1 experiment at HERA in the years 1994–1997 at a center-of-mass energy of $\sqrt{s} = 300\,\text{GeV}$, corresponding to an integrated luminosity of $\mathcal{L}_{\text{int}} = 35\,\text{pb}^{-1}$. Jet observables are measured in deep-inelastic scattering (DIS) in the kinematic region of four-momentum transfers $10 < Q^2 < 15\,000\,\text{GeV}^2$ and transverse jet energies $50 \lesssim E_T^2 \lesssim 2500\,\text{GeV}^2$ in the Breit frame using $k_\perp$ and (for the first time in DIS) angular ordered jet algorithms. The inclusive jet and the dijet cross sections are measured double differentially, the latter for a comprehensive set of jet variables. Three-jet and four-jet cross sections are measured single differentially and the internal structure of jets in dijet production is investigated using jet shapes and subjet multiplicities.

Predictions of perturbative QCD in next-to-leading order (NLO) of α_s are compared to the inclusive jet and the dijet cross sections measured. Using parton density functions obtained in global fits and the world average value of $\alpha_s(M_Z)$ we observe an excellent agreement between theory and data for those jet observables for which non-perturbative corrections are small (as estimated by phenomenological hadronization models) and the perturbative predictions are reliable (i.e. where NLO corrections are small).

At small four-momentum transfers $10 < Q^2 < 70\,\mathrm{GeV}^2$ the NLO calculation can no longer describe the size of the measured dijet cross section. In this kinematic region NLO corrections are, however, large (up to a factor of two) and contributions from higher orders in α_s can be sizable.

The QCD Analysis

The QCD analysis is based on the inclusive jet and the dijet cross sections measured using the inclusive $k_\perp$ algorithm at large four-momentum transfers $Q^2 > 150\,\mathrm{GeV}^2$ and on additional data on the inclusive *ep* cross section from a recent measurement by the H1 collaboration. Since both measurements are using similar experimental techniques the full correlations between the uncertainties of all data points are taken into account in the fitting procedure.

In the first step we determine α_s following a standard approach in which the gluon and the quark densities are taken from the results of global fits. Four values of $\alpha_s(E_T)$ are extracted from the inclusive jet cross section at different scales $\mu_r = E_T$. The results are consistent with the running of α_s as predicted by the renormalization group equation. A combined fit yields a result of

$$\alpha_s(M_Z) \;=\; 0.1181\,^{+0.0061}_{-0.0058}\,,$$

which is compatible with the current world average value of $\alpha_s(M_Z)_{\mathrm{world}} = 0.119 \pm 0.004$ and has a significantly higher precision than earlier $\alpha_s(M_Z)$ results determined in jet production in DIS.

In the second step we determine the gluon density in the proton in a consistent way, i.e. simultaneously with the quark densities, assuming the world average value of $\alpha_s(M_Z)$. The gluon and the quark densities are determined at a factorization scale $\mu_f^2 = 200\,\mathrm{GeV}^2 \simeq \langle E_T^2\rangle$ in the $\overline{\mathrm{MS}}$-scheme. The results are presented as a function of the momentum fraction x in the range $0.01 < x < 0.1$. The integral of the gluon density $xG(x)$ in this x range is determined as

$$\int_{0.01}^{0.1} \mathrm{d}x\; x\,G(x, \mu_f^2 = 200\,\mathrm{GeV}^2) = 0.229\,^{+0.034}_{-0.032}\,.$$

This integral and also the x dependence of the distribution are in good agreement with the results from global fits.

In the third step of the QCD analysis we make a simultaneous fit of $\alpha_s(M_Z)$, the gluon and the quark densities avoiding any external input. We demonstrate that we obtain a stable fit result for all of these parameters using the inclusive jet and the dijet cross sections, together with the inclusive *ep* cross section. This analysis constitutes the first simultaneous, *direct* determination of α_s and the gluon density in the proton.

The results are consistent with current world knowledge. The anti-correlation between $\alpha_s(M_Z)$ and the gluon density is, however, large and we see that the present data are not yet sensitive to constrain both with a high precision. On the other hand, our data give strong constraints on the product $\alpha_s \cdot xG(x)$ and will therefore have significant impact if they are included in combined analyses together with other data sets with additional (and different) sensitivity regarding α_s and $xG(x)$.

Outlook

At present the uncertainties of the results from experimental and theoretical sources are of similar size. Further improvement will therefore require progress on both. It is likely that the large luminosities expected in the future will allow to perform extended studies resulting in an improved calibration of the hadronic energy measurement which is currently the source of the largest experimental uncertainty.

Considering that we can not expect a calculation of the next-to-next-to-leading order corrections to the inclusive jet and the dijet cross sections to become available at a short time scale, the question arises: “What theoretical progress can be obtained in the near future?”.

At low Q^2 a very large amount of high E_T jet data is available at HERA. In this kinematic region where $E_T^2 \gg Q^2$ terms of $\ln \frac{E_T^2}{Q^2}$ become large and fixed order calculations in NLO are no longer predictive. If theorists would provide resummed calculations (matched to the NLO prediction) these data could be included in QCD analyses giving important additional information on the gluon density.

In the present analysis we have presented the first measurement of the three jet cross section in deep-inelastic scattering (together with A. Heister [96]). The luminosity upgrade of the HERA machine will allow to measure this process in the future at larger transverse jet energies with high statistics. An observable as the ratio of the three-jet cross section and the dijet cross section will be well suited to determine $\alpha_s(M_Z)$ since this ratio is fairly insensitive to the parton densities and experimental (and maybe also parts of the theoretical) uncertainties are expected to cancel to a large extent. This analysis will require the availability of NLO calculations of the three-jet cross section. A NLO calculation of the three-jet cross section in $\bar{p}p$ collisions has recently been published [125]. The basic tools should therefore be available to provide a corresponding calculation for DIS in the near future which will allow a new generation of $\alpha_s(M_Z)$ determinations to be performed.

A

The Boost to the Breit Frame

In section 2.1 we have discussed the reasons why we chose to perform the jet finding on the hadronic final state particles in the Breit frame[1]. The reconstruction of the boost vector to the Breit frame requires the knowledge of the kinematic variables $x_{\rm Bj}$ and Q^2, as well as the direction of $\vec{q}$. The latter is obtained from the azimuthal angle ϕ_e of the scattered positron in the laboratory frame. To determine $x_{\rm Bj}$ and Q^2 we can use any one of the methods introduced in section 4.3. However, a bad reconstruction of the kinematic variables can lead to a bias in the reconstruction of the boost vector and may therefore also bias the measurement. In the following we describe the problem and demonstrate that the bias can be reduced using an appropriate reconstruction method.

A.1 Radiative QED Corrections in the Breit Frame

Measurements of the inclusive DIS cross section are typically performed in bins of $x_{\rm Bj}$ and Q^2. The main criterion for the choice of a specific reconstruction method is that the resolution must be sufficient to allow a fine binning with small migrations between bins. In the analysis of hadronic final states in the Breit frame the kinematic variables also define the boost vector event by event. Here it is not sufficient to only achieve a resolution compatible with the size of the chosen bins. It is also necessary to avoid introducing a bias in the final state properties through a definition of the boost vector which is e.g. disturbed by real photon emissions. The main reason to perform analyses in the Breit frame is the sensitivity to (soft and hard) QCD processes coming in through the detection of transverse energy, relative to the z-axis (given by the proton-photon direction). If this axis is badly reconstructed the energy flow along the true z-axis receives a transverse component relative to the reconstructed z-axis which is misinterpreted as the indication of an underlying QCD process. Especially events in which photons, emitted collinear to the initial state positron, escape undetected through the backward beam pipe, may introduce a systematic effect, depending on the kinematic

---

[1] The Breit frame is defined by $2x_{\rm Bj}\vec{p} + \vec{q} = \vec{0}$, where $x_{\rm Bj}$ is the Bjorken scaling variable and $\vec{p}$ and $\vec{q}$ are the momenta of the incoming proton and the virtual photon. The orientation in the x-y plane of the Breit frame is chosen such that the scattered positron points in the positive x-direction (i.e. $\phi_{e,\,\rm Breit} = 0°$).

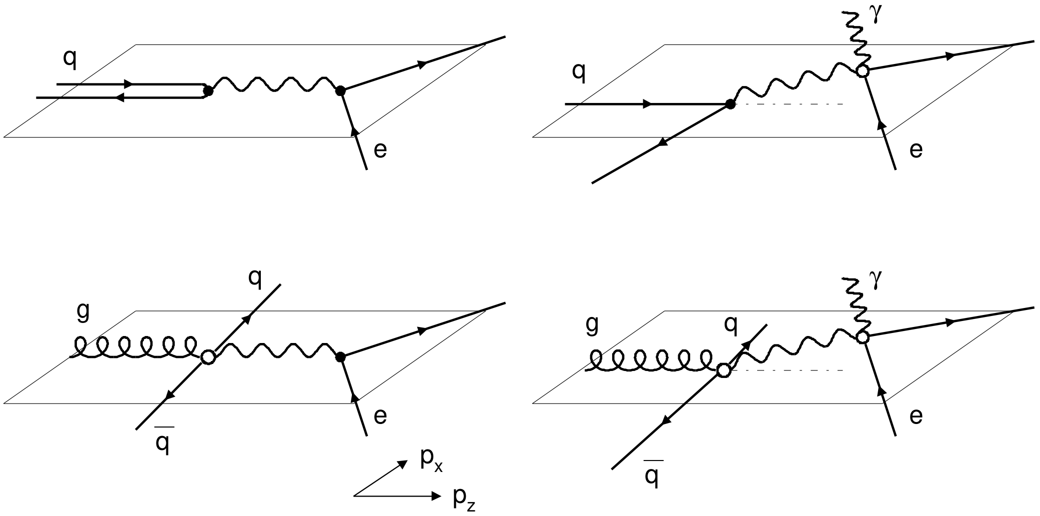

Figure A.1: The processes of $eq \to eq$ (top) and $eg \to eq\bar{q}$ (bottom) in the Breit frame in Born approximation (left) and in the presence of QED corrections from real photon emissions collinear to the initial state positron (right), when the boost vector to the Breit frame is calculated from the scattered positron kinematics.

reconstruction method.

In Fig. A.1 we have displayed the topology of different types of events in the Breit frame in the Born approximation (left) and in the presence of photon radiation collinear to the initial state positron (right). The upper plots show the purely electromagnetic scattering of the positron off a quark via photon exchange. In this process no QCD corrections are involved and in the Born process (left) the quark is backscattered without any transverse momentum component. The lower plots show a gluon induced process of $\mathcal{O}(\alpha_s)$ with an outgoing quark-antiquark pair with finite transverse momenta. In the Born process these are balanced in the x-y plane (left).

QED corrections from photon radiation may lead to a quantitative change of this picture. On the right hand side of Fig. A.1 the same processes as on the left are displayed with an additional photon radiated collinear to the initial state positron (i.e. in the x-z plane). If the boost vector is reconstructed from the scattered positron the virtual photon does not lie on the z-axis, and the final state momenta are no longer balanced in the x-y plane. By definition only the x-component of the final state momenta is affected while the y-component is unchanged[2]. This increases the energy flow along the negative x-direction, leading to a different bias for different observables.

Jets at large transverse energies $E_{T,\text{jet}}$ are typically produced in pairs of similar $E_{T,\text{jet}}$. In genuine dijet events the single $E_{T,\text{jet}}$ may be wrongly reconstructed, but the sum is stable

---

[2] Of course, also the z-momenta may be altered, but since all observables studied in this analysis are invariant under longitudinal boosts along the z-direction we will not discuss this aspect here.

with respect to a common shift along the x-direction. Furthermore we do not have to worry that event topologies as displayed in the upper right plot of Fig. A.1 give contributions to the cross section, since they contain only a single jet. A dijet analysis should therefore be less sensitive to such processes.

This situation is different for inclusive final state analyses as in the measurement of the transverse energy flow or for event shape variables, where (by definition) the observable receives contributions from all events. In such cases special care has to be taken, as we will demonstrate here for the case of the inclusive jet cross section. If the error in the reconstruction of the boost vector is large enough, topologies as in the upper right plot in Fig. A.1 may be mistaken for single high E_T jets, leading to large radiative QED corrections in the inclusive jet cross section.

A.2 Reconstruction of the Boost Vector

We study the dependence of the boost on the kinematic reconstruction by investigating the transverse momentum components of the final state in the Breit frame. When the positron is excluded, the total transverse momentum should be exactly zero. Some mismeasurements (e.g. particle energies in crack regions) and the detector acceptance (e.g. the beam pipes) will lead to fluctuations which should be similar for the x- and the y-component. A wrong reconstruction of the boost vector is, however, likely to have an increased influence on the component corresponding to the scattered positron direction i.e. the x-component (see Fig. A.1).

In Fig. A.2 we show distributions of the reconstructed momentum components $p_{x,\,\mathrm{Breit}}$ (left) and $p_{y,\,\mathrm{Breit}}$ (right) for the inclusive DIS sample (top), the inclusive jet sample (center) and the dijet sample (bottom). The boost vector is reconstructed using either the Electron Method (open circles) or the Electron-Sigma Method (full circles). The $p_{y,\,\mathrm{Breit}}$ distribution is in all cases narrow and symmetric around zero. The width is approximately the same for both reconstruction methods.

The $p_{x,\,\mathrm{Breit}}$ distribution is in all cases broader than the $p_{y,\,\mathrm{Breit}}$ distribution and shows a tail towards negative $p_{x,\,\mathrm{Breit}}$. For the inclusive DIS sample and for the inclusive jet sample this tail is larger for the Electron Method than for the Electron-Sigma Method. In the inclusive jet sample an excess of jets is seen at $p_{x,\,\mathrm{Breit}} < -7\,\mathrm{GeV}$. In this region configurations as the one in the upper right plot in Fig. A.1 are accepted by the inclusive jet selection. Only for the dijet sample both reconstruction methods give similar results. This is consistent with our expectation that the reconstruction of dijet events is less sensitive to photon radiation processes.

To demonstrate that the effects discussed here are truly related to collinear photon radiation, we remove the cut on $\sum(E - p_z)$ introduced in (5.5) and thus include events with high energetic collinear photon radiation. The distributions for the Electron Method with (full circles) and without this cut (open circles) are compared in Fig. A.3. As expected we

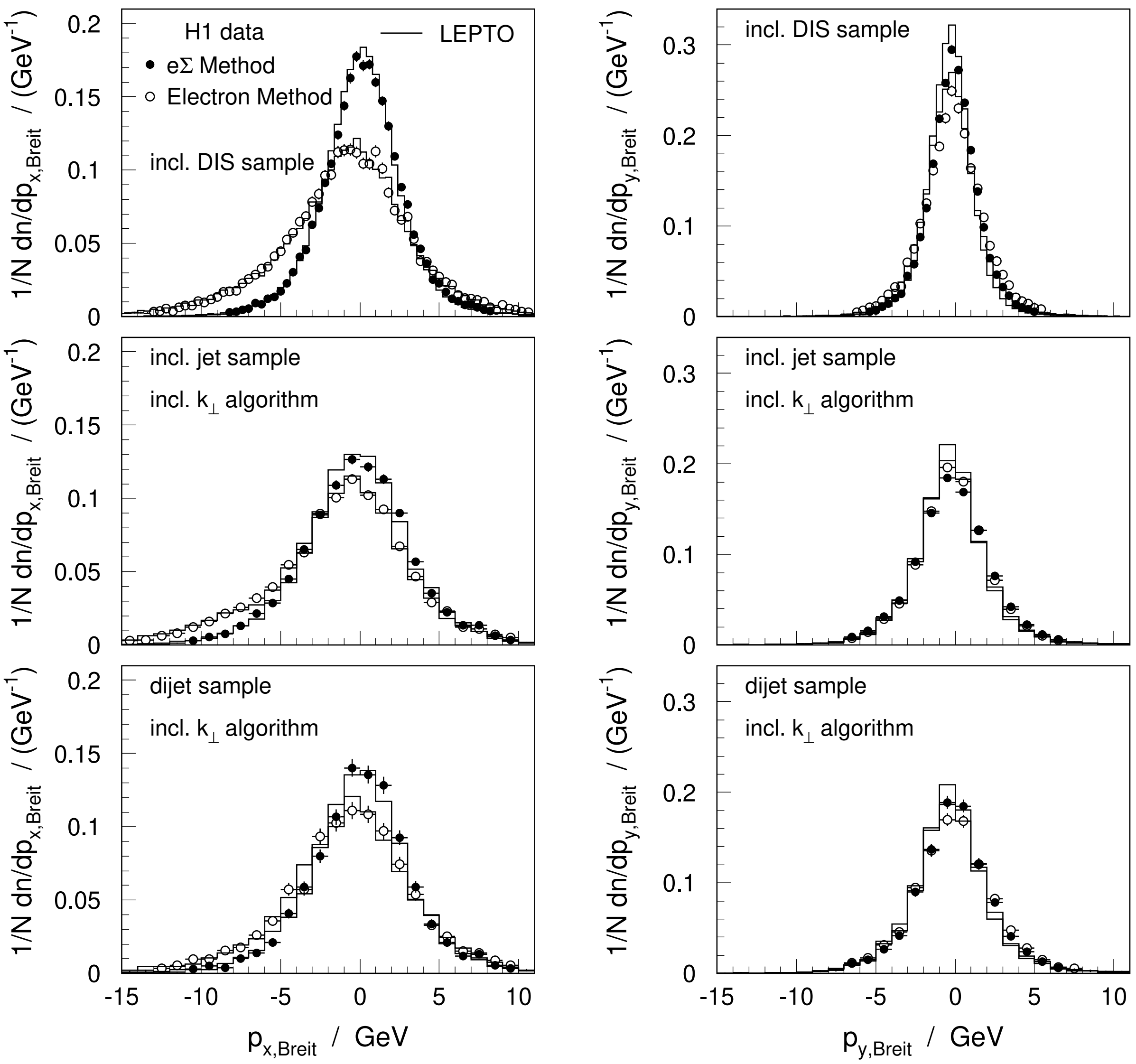

Figure A.2: The distribution of the hadronic final state momentum in the Breit frame. The boost vector is calculated using either the Electron-Sigma Method (full marker) or the Electron Method (open marker). Shown are the components parallel ($p_{x,\,\mathrm{Breit}}$, left) and transverse ($p_{y,\,\mathrm{Breit}}$, right) to the plane spanned by the incoming and the scattered positron. All analysis cuts are applied, including the cut on $\sum(E - p_z)$ (see section 5.1.3).

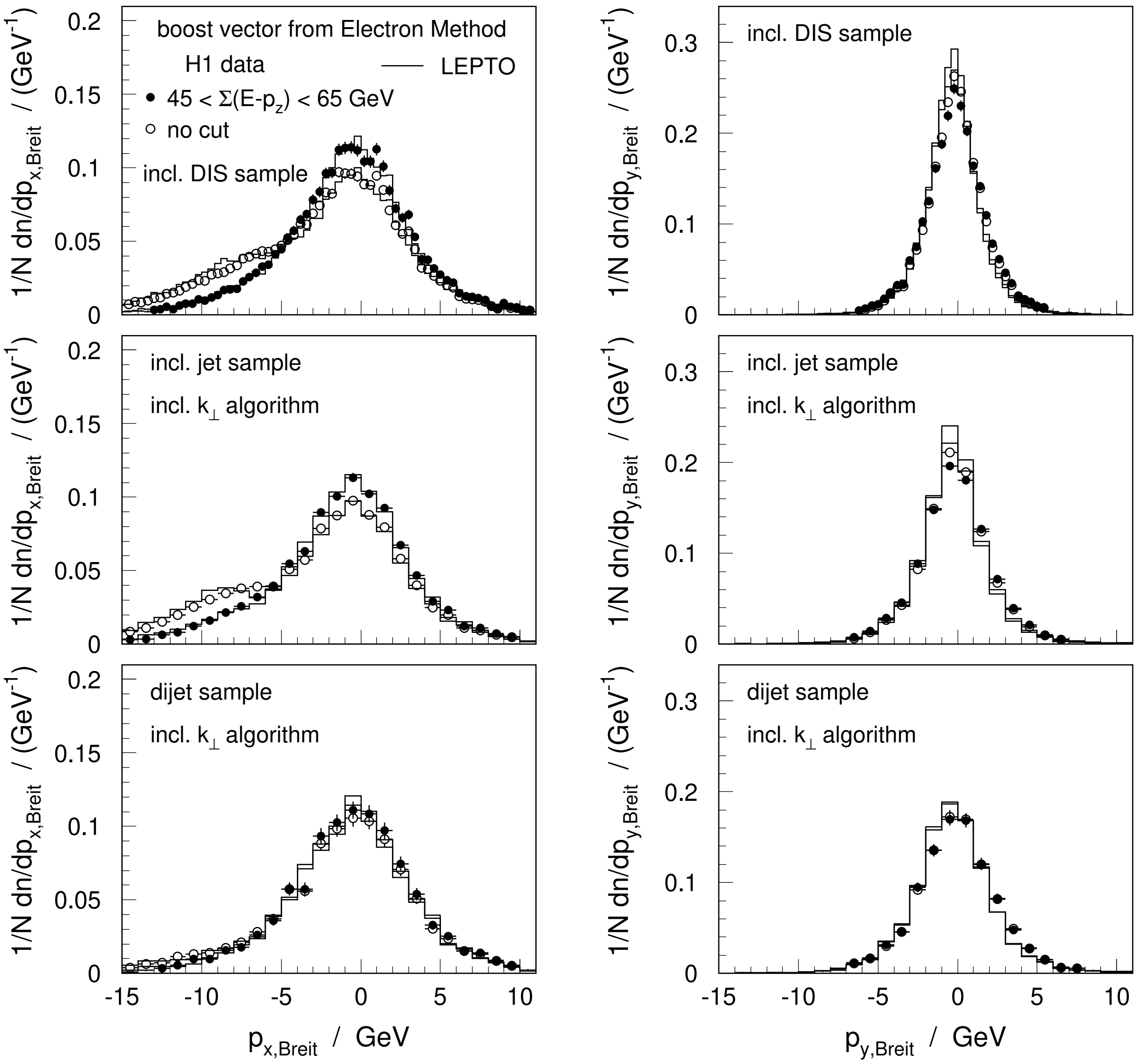

Figure A.3: The distribution of the hadronic final state momentum in the Breit frame. The boost vector is calculated using the Electron Method with (full marker) and without a cut on $\sum(E - p_z)$ (open marker). Shown are the components parallel ($p_{x,\,\mathrm{Breit}}$, left) and transverse ($p_{y,\,\mathrm{Breit}}$, right) to the plane spanned by the incoming and the scattered positron.

observe a further increase of the tail towards negative $p_{x,\,\mathrm{Breit}}$.

It has to be noted that in all distributions shown in Figs. A.2 and A.3 the simulation describes all observed effects well. This gives confidence that the implementation of the QED corrections in HERACLES (interfaced to LEPTO and ARIADNE by DJANGO) is reliable and that the remaining effects are therefore appropriately taken into account in the correction procedure.

A.3 Conclusion

We have demonstrated the importance of controlling the boost in analyses in the Breit frame to avoid biases in the observables. While these biases can be small for high E_T dijet cross sections[3] they can have large effects for inclusive analyses of the final state in the Breit frame. Although for the Electron Method a hard cut on $\sum(E-p_z)$ can reduce this bias, a further improvement is obtained by using the Electron-Sigma Method for the reconstruction of the kinematic variables.

---

[3] This is, of course, only true if the basic dijet selection criterion is not too sensitive to the potential shift in the transverse jet energies, as in the case of a cut on the sum of the transverse jet energies or on the invariant dijet mass.

B

Fitting Techniques

A theory which predicts events in the real world may still depend on parameters not predicted by the theory itself. Such parameters can be determined in a statistical analysis by fitting the theoretical predictions to measured data. Any result obtained in a fitting procedure to a set of data points with different uncertainties will depend on the statistical assumptions made in the fit, as for example on the way the information of the single data points is weighted and how point-to-point correlations between different observables are treated.

In this appendix we will introduce methods which are needed in such fits. The central point is to define a measure of disagreement between data and theory, the so-called χ^2 variable. Two standard methods are shown to give statistically unreasonable results. Two further approaches are discussed which have both satisfying properties. Both allow to consider point-to-point correlations in a consistent way.

B.1 The Probability Model

We start by assuming a theory which is able to describe (parts of) the real world, if some parameters $\vec{p}$ were known. If this is the case, these parameters $\vec{p}$ can be determined as those for which the theoretical predictions $T_i(\vec{p})$ for a set of observables i are in agreement with the true values of these observables M_i in the real world

$$M_i = T_i(\vec{p}) \quad \forall\, i \,. \tag{B.1}$$

Experimental uncertainties

In practice the true values M_i of the observables are not known. Any experimental measurement can only provide an estimate m_i of the true value, together with estimates of the relative uncertainties $\Delta m^{\pm}_{i,k}$ (from different sources k) inherent in the measurement[1]. If the

---

[1] The uncertainty $\Delta m^{\pm}_{i,k}$ from source k is not necessarily distributed symmetrically around the central value. In general the upper uncertainty $\Delta m^{+}_{i,k}$ can be different from the lower uncertainty $\Delta m^{-}_{i,k}$. This is indicated by the "±" signs in $\Delta m^{\pm}_{i,k}$.

uncertainties are assumed to obey a Gaussian distribution the relation between the true value M_i and the estimate m_i is given by

$$M_i \;=\; m_i \left(1 + \sum_{k=1}^{N_{\rm exp}} \delta_{i,k}(\epsilon_k)\right) \;, \tag{B.2}$$

where the sum runs over all sources of experimental uncertainties. The ϵ_k are independent random variables which follow a Gaussian distribution with zero average and unity dispersion

$$\langle\epsilon_k\rangle = 0\,, \qquad \langle\epsilon_k^2\rangle - \langle\epsilon_k\rangle^2 = 1\;. \tag{B.3}$$

The $\delta_{i,k}(\epsilon_k)$ are defined such that they vanish for $\epsilon_k = 0$ and represent the $\Delta m^{\pm}_{i,k}$for $\epsilon_k = \pm 1$

$$\delta_{i,k}(\epsilon_k = 0) \equiv 0\;, \qquad \delta_{i,k}(\epsilon_k = +1) \equiv \Delta m^{+}_{i,k}\;, \qquad \delta_{i,k}(\epsilon_k = -1) \equiv \Delta m^{-}_{i,k}\;. \tag{B.4}$$

In the simplest case of symmetric uncertainties (i.e. $\Delta m_{i,k} \equiv \Delta m^{+}_{i,k} = -\Delta m^{-}_{i,k}$) the functional form is given by

$$\delta_{i,k}(\epsilon_k) \;=\; \epsilon_k\,\Delta m_{i,k}\,. \tag{B.5}$$

For asymmetric uncertainties the functional form can be approximated by a second order polynomial

$$\delta_{i,k}(\epsilon_k) = \epsilon_k\,\frac{\Delta m^{+}_{i,k} - \Delta m^{-}_{i,k}}{2} \;+\; \epsilon_k^2\,\frac{\Delta m^{+}_{i,k} + \Delta m^{-}_{i,k}}{2}\;. \tag{B.6}$$

Theoretical uncertainties

Often also the predictions of the theory $T_i(\vec{p})$ are not exactly known. This is for example the case when perturbative expansions are truncated and only some of the leading orders are calculated or when non-perturbative contributions are approximated by phenomenological models. The approximations $t_i(\vec{p})$ represent the true predictions of the theory only within the relative uncertainties $\Delta t^{\pm}_{i,k}$ (here the index k labels different sources of theoretical uncertainties which represent the deviations from the true value)[2]. These theoretical uncertainties can be modeled in the same way as the experimental ones, with further Gaussian random variables ϵ_k

$$T_i(\vec{p}) \;=\; t_i(\vec{p}) \left(1 - \sum_{k=1}^{N_{\rm theo}} \delta_{i,k}(\epsilon_k)\right) \;, \tag{B.7}$$

---

[2] In general it is, of course, not possible to determine these theoretical uncertainties — if the deviations could be calculated they would have been used to improve the theoretical approximation. However, in chapter 3 we have described some methods to obtain estimates of the possible size of higher order corrections in perturbative QCD calculations as well as uncertainties in the estimates of the hadronization corrections. For simplicity we neglect here that the relative uncertainties Δt_i may also depend on the parameters $\vec{p}$. This approximation is reasonable when the expected dependence is much smaller than the uncertainty in the determination of the Δt_i.

with

$$\delta_{i,k}(\epsilon_k = 0) \equiv 0 \; , \qquad \delta_{i,k}(\epsilon_k = +1) \equiv -\Delta t^+_{i,k} \; , \qquad \delta_{i,k}(\epsilon_k = -1) \equiv -\Delta t^-_{i,k} \; . \tag{B.8}$$

This definition is analogous to the experimental uncertainties in (B.2), except for the sign of the $\delta_{i,k}$ so that the error variables appear with the same sign in the following formulae. Inserting (B.2) and (B.7) in (B.1) we obtain the final formula[3]

$$m_i \;=\; t_i(\vec{p}) \left(1 - \sum_{k=1}^{N_{\text{exp}}+N_{\text{theo}}} \delta_{i,k}(\epsilon_k) \right) \; . \tag{B.9}$$

Remarks

It has been pointed out [126] that the assumption of a Gaussian distribution of the error is not necessarily justified for experimental uncertainties (e.g. the model dependence of a detector correction factor). It is often found that the probability for the actual error to be many standard deviations is small, but much larger than indicated by a Gaussian distribution. The assumption of that theoretical uncertainties follow a Gaussian distribution is even more problematic, especially since these are only very rough estimates anyway. However, when no better knowledge on the distributions of the uncertainties is available, we consider (B.9) as a reasonable model. Furthermore (B.9) demonstrates the necessity to consider correlations of both, experimental and theoretical uncertainties in a statistical data analysis.

B.2 Definitions of χ^2

Starting from (B.9), we define the best estimate for the parameters $\vec{p}$ as the one for which the $t_i(\vec{p})$ show the best agreement with the corresponding m_i considering the presence of the uncertainties $\delta_{i,k}$. Therefore a quantitative measure χ^2 of the disagreement has to be introduced. The parameters $\vec{p}$ are determined such that the χ^2 is minimized. If the uncertainties $\delta_{i,k}$ from all sources k are uncorrelated between the single observables i, χ^2 can be defined by

$$\chi^2(\vec{p}) \;=\; \sum_i \frac{(m_i \;-\; t_i(\vec{p}))^2}{\delta^2_{i,\text{uncorr}}} \; , \tag{B.10}$$

where the sum runs over all measurements i and $\delta_{i,\text{uncorr}}$ is the quadratic sum of all (uncorrelated) experimental and theoretical uncertainties. Unfortunately in most practical cases we have to deal with uncertainties which are correlated between different data points (e.g. overall normalization uncertainties). In such cases the simple formula (B.10) can not be used.

---

[3] For the experimental uncertainties we have replaced $(1 + \sum \delta)$ by $(1 - \sum \delta)^{-1}$ and we neglect terms proportional to $\delta_{i,k} \cdot \delta_{i,l}$. These are valid approximations if the δ are small.

B.2.1 Independent Variation of Systematic Parameters

A standard method to consider the correlation between uncertainties, is to perform a series of independent fits. At the first stage of the statistical analysis the correlated uncertainties are ignored and a fit is performed using (B.10) where only the uncorrelated uncertainties are considered. This yields the central result of $\vec{p}$. To evaluate the uncertainty of $\vec{p}$ the fit is then repeated for the data points shifted by one standard deviation of each correlated uncertainty upwards and downwards. All changes of the parameters $\vec{p}$ with respect to their central result are added in quadrature to obtain the total uncertainty. In this method the asymmetry of uncertainties is naturally taken into account.

Since in each of the single fits only the uncorrelated uncertainties are considered, a data point with small uncorrelated uncertainties (but large correlated ones) has a larger impact in the determination of the central value, compared to a point with larger uncorrelated and smaller correlated uncertainties. As demonstrated in example No.1 in section B.3 this may lead to unreasonable fit results.

B.2.2 Using the Covariance Matrix

A standard approach to fit correlated data includes the covariance matrix C_{ij} in the definition of χ^2. Equation (B.10) is then modified to

$$\chi^2(\vec{p}) = \sum_{ij} \left(m_i - t_i(\vec{p})\right) \left(C^{-1}\right)_{ij} \left(m_j - t_j(\vec{p})\right) \ . \tag{B.11}$$

In this formulation χ^2 also receives contributions from the non-diagonal elements of C_{ij} which carry the information on the point-to-point correlations of the data. However, the definition of the covariance matrix is not unique and different definitions may lead to different results of $\vec{p}$ in the χ^2 minimization procedure. The ambiguity arises from the freedom in the interpretation of the nature of the relative uncertainties $\delta_{i,k}$.

One possibility is their interpretation as relative uncertainties of the measured data. Another way of viewing the problem is that e.g. in a counting experiment there is no uncertainty on the counted number of events. The uncertainty is only present in the expectation, which in this case also involves experimental uncertainties due to the limited knowledge of the measuring device or the uncertainty in the luminosity measurement. Although these approaches sound very similar (and (B.9) is symmetric between theory and data) both may lead to different results. This has been shown to be an artifact of the linearization upon which the error propagation is based [127].

In the following we show that an attempt, based on the symmetry between measurement and expectation as in (B.9) gives satisfying results.

Covariance Matrix from the Data

In the first approach [127] the absolute uncertainties are obtained by multiplying the relative uncertainties $\delta_{i,k}$ ($= \Delta m_{i,k}$, $\Delta t_{i,k}$) by the measured values m_i. As in all definitions of the covariance matrix presented here, it is not possible to consider the asymmetry of uncertainties. The $\delta_{i,k}$ are therefore taken as the average uncertainties

$$\delta_{i,k} = \Delta m_{i,k} = \frac{\Delta m_{i,k}^{+} - \Delta m_{i,k}^{-}}{2} \,, \quad \text{and} \quad \delta_{i,k} = \Delta t_{i,k} = \frac{\Delta t_{i,k}^{+} - \Delta t_{i,k}^{-}}{2} \,. \tag{B.12}$$

The covariance matrix is then given by

$$C_{ij} = \sum_k \delta_{i,k}\, m_i \;\; \delta_{j,k}\, m_j \,. \tag{B.13}$$

The covariance matrix is calculated once, at the beginning of the χ^2 minimization procedure. It has been shown [127] that this definition can lead to a bias of fit results such that the produced results are lower than expected. This is demonstrated in example No.2 in section B.3.

Covariance Matrix from the Predictions

In the second approach [128] the absolute uncertainties are obtained by multiplying the relative uncertainties $\delta_{i,k}$ by the theoretical predictions $t_i(\vec{p})$, leading to

$$C_{ij} = \sum_k \delta_{i,k}\, t_i(\vec{p}) \;\; \delta_{j,k}\, t_j(\vec{p}) \,. \tag{B.14}$$

Because the covariance matrix depends now implicitly on the parameters $\vec{p}$ it has to be recalculated in each iteration of the minimization procedure when the parameters are varied.

It turns out that the bias discussed in [127] for (B.13) is only “mirrored” for this definition. In those cases where definition (B.13) produces too low results, this definition produces results larger than expected (example No.2 in section B.3).

Covariance Matrix from Averages

Based on the symmetry between the measurement and the theoretical expectation in (B.9) we propose to use the average of both to obtain the absolute values of the uncertainties that enter the covariance matrix

$$C_{ij} = \sum_k \delta_{i,k} \frac{(m_i + t_i(\vec{p}))}{2} \;\; \delta_{j,k} \frac{(m_j + t_j(\vec{p}))}{2} \,. \tag{B.15}$$

As in (B.14) the covariance matrix depends implicitly on the parameters $\vec{p}$ and therefore has to be recalculated in each iteration of the minimization procedure. Example No.2 in section

B.3 shows that definition (B.15) is not affected by the problems encountered in (B.13) and (B.14).

Therefore we consider this third approach as a reasonable solution that may be used in statistical data analysis. However, since it does not consider the asymmetry of uncertainties, we will only use it to cross-check the results that we obtain by using the most flexible method, which is presented in the following.

B.2.3 Fitting Systematic Parameters

A further approach to define χ^2 has been proposed in [129, 27]. Based on the formulation in (B.9) the Gaussian random variables ϵ_k are considered as parameters in the fit. The ϵ_k dependence of the $\delta_{i,k}(\epsilon_k)$ is parameterized as in (B.6). Since the ϵ_k are known to obey a Gaussian distribution, their values are added in quadrature to the χ^2. Uncorrelated uncertainties are taken into account as in the simple formulation of χ^2 in (B.10). The χ^2 that is minimized during the fit is defined by

$$\chi^2(\vec{p}, \vec{\epsilon}) = \sum_i \frac{\left(m_i \, - \, t_i(\vec{p}) \, \left[1 - \sum_k \delta_{i,k}(\epsilon_k)\right]\right)^2}{\delta^2_{i,\mathrm{uncorr}}} \; + \; \sum_k \epsilon_k^2 \, , \tag{B.16}$$

where i runs over all measurements and k runs over all sources of uncertainties. The vector $\vec{\epsilon}$ contains all ϵ_k. The ϵ_k are not free parameters in the fit, since they are determined according to the Gaussian law hypothesis, and give contributions to the total χ^2. Correspondingly the ϵ_k do not decrease the degrees of freedom of the fit. The definition of χ^2 of (B.16) allows to consider the asymmetry of uncertainties and is used throughout the statistical data analysis in the present work. The functional form of the $\delta_{i,k}(\epsilon_k)$ is always taken from (B.6).

B.3 Examples

To demonstrate the weak points in some of the methods mentioned above we briefly discuss two examples of making a combined fit of two $\alpha_s(M_Z)$ values. Each $\alpha_s(M_Z)$ has some uncorrelated uncertainty and some uncertainty which is correlated between both values. The two examples are shown in Table B.1 including the results according to the five different fit methods discussed above.

Example 1

In the first example one of the $\alpha_s(M_Z)$ values (a) has a considerably smaller uncorrelated, but a larger correlated uncertainty than the second value. This is a typical situation that appears in the present jet analysis: we have high statistics (i.e. small uncorrelated uncertainties) of events with relatively small E_T for which the theoretical predictions are less safe (i.e. have larger correlated uncertainties).

All methods which consider point-to-point correlations agree in their central values and in the uncertainties of the combined results. The central value is close to the more precise value b. The fact that it is slightly higher is a direct consequence of the presence of a positive correlation in the uncertainties.

Only the method of independent variations of systematic parameters gives a result significantly lower with an uncertainty that is much larger than the results from the other methods. This is a consequence of neglecting the correlated uncertainties in the single fits. Each fit is pulled towards the value a due to its larger impact on the single fits, and the uncertainty of the result only reflects the uncertainty of this value. In this case the uncertainty of the result is even larger than the uncertainty of the more precise single measurement b.

This is in clear contradiction to what we expect from a proper statistical analysis: and increased amount of information must not decrease the total information. This method is therefore unreasonable for a statistical data analysis.

Example 2

The second example is similar to the one discussed in [127]. We have two $\alpha_s(M_Z)$ values with the same uncertainty. Both values are in some disagreement: they are not compatible within their uncorrelated uncertainties, and the correlated uncertainty can not account for the difference. In this case the three methods of "independent variation of systematic parameters", "covariance matrix from averages" and "fitting systematic parameters" give the same results for the central value and for the uncertainty. As expected from the symmetry of the input $\alpha_s(M_Z)$ values the final result is in between both values for these methods.

The two other methods, based on the covariance matrix as determined from the data or from the prediction, show the curious effect of producing a significantly lower or higher result than expected. Their disagreement points to a problem related to limitations in the formalism of the error propagation (see [127] for a detailed discussion).

We conclude that the methods of "fitting systematic parameters" and using "the covariance matrix based on averages" are reasonable for a statistical data analysis. Since

	example No.1	example No.2
a: $\alpha_s(M_Z)$ =	$0.120 \pm 2\%$(uncorr.) $\pm 5\%$ (corr.)	$0.120 \pm 2\%$(uncorr.) $\pm 10\%$ (corr.)
b: $\alpha_s(M_Z)$ =	$0.110 \pm 0.2\%$(uncorr.) $\pm 20\%$ (corr.)	$0.110 \pm 2\%$(uncorr.) $\pm 10\%$ (corr.)
χ^2 definition by:	fitted $\alpha_s(M_Z)$ value:	
independent variations	$0.1101 \pm 0.0022\,^{+0.0273}_{-0.0183}$	$0.1146 \pm 0.0016\,^{+0.0127}_{-0.0104}$
cov. matrix (data)	0.1235 ± 0.0033	0.1047 ± 0.0111
cov. matrix (theory)	0.1231 ± 0.0033	0.1261 ± 0.0133
cov. matrix (average)	0.1233 ± 0.0033	0.1149 ± 0.0119
fitting syst. parameters	0.1231 ± 0.0032	0.1146 ± 0.0116

Table B.1: Two examples of fits to two $\alpha_s(M_Z)$ values whose uncertainties are partially correlated. Shown are the results for all of the fit methods as described in the text.

the former is able to consider asymmetries of uncertainties this is the method of choice in this analysis. The latter method is used to cross-check the result and to demonstrate its independence of the precise formulation of χ^2.

B.4 The χ^2 Minimization

The minimization of the $\chi^2(\vec{p},\vec{\epsilon})$ with respect to the parameters $\vec{p}$ and $\vec{\epsilon}$ is performed by the program MINUIT [130]. The algorithm is based on Newton's minimization method. In the one dimensional case the minimum of the function $\chi^2(p)$ with respect to the parameter p is found in iterations

$$p_{n+1} = p_n + \Delta p \qquad \text{with} \qquad \Delta p = \frac{\frac{\partial \chi^2(p)}{\partial p}}{\frac{\partial^2 \chi^2(p)}{\partial p^2}} \Big|_{p_n} . \tag{B.17}$$

In the multidimensional case the second derivative is replaced by the matrix of second derivatives (Hessian) as e.g. implemented in the MIGRAD and HESSE procedures. The inverse of this matrix is returned as the error matrix by MIGRAD. The errors on the single parameters are the square roots of the diagonal elements of this matrix, which take into account all parameter correlations, but neglect non-linearities. Since these errors are estimated using the curvature at the minimum, assuming a parabolic shape, they are by definition symmetric.

For the determination of the exact (an in general asymmetric) errors on fit parameters (i.e. taking into account non-linearities) the MINOS algorithm is used. MINOS determines the error of a parameter p_n (corresponding to one standard deviation) by varying p_n, each time minimizing χ^2 with respect to all other parameters, to find numerically the two values of p_n where χ^2 is increased by one. Analogously the correlation of the errors between two fit parameters can be visualized by the contour in the two-parameter space where χ^2 (minimized with respect to all other parameters) is increased by one. Both of these options will be used in this work.

B.5 Errors on the Fit Parameters

Errors on the Parton Density Functions and α_s

The free parameters in the QCD fits that we perform in chapter 9 are the parton density functions and the value of the strong coupling constant. The strong coupling constant can directly be inserted as a fit parameter, such that the fit will directly provide its error.

To fit the x-dependence of the parton densities we use one of the functional forms from (8.9). We are, however, not interested in the values and the uncertainties of the fit parameters $(A, b, c, \cdots)$, but directly in the value of e.g. the gluon density $xG(x)$ and its uncertainty at a specific value x_0. We therefore replace the parameter A by the value of the gluon density

$x_0G(x_0)$ by rewriting formulae (8.9). The four parameter formula is then given by

$$xG(x) \;=\; A\,x^b\,(1-x)^c\,(1+d\,x) \quad\Rightarrow\quad xG(x) \;=\; x_0G(x_0)\,\frac{x^b\,(1-x)^c\,(1+d\,x)}{x_0^b\,(1-x_0)^c\,(1+d\,x_0)}\;. \tag{B.18}$$

In this case the MINOS algorithm will directly return the value of $x_0G(x_0)$ as a result, including its error. By repeating the fits at different values of x_0 we are able to produce an error band of the gluon density over the entire x-range.

In another part of the analysis we want to determine the integral I over a specific range $x_1 < x < x_2$ of the gluon density

$$I \equiv \int_{x_1}^{x_2} \mathrm{d}x\; x\,G(x) \;=\; \int_{x_1}^{x_2} \mathrm{d}x\; Ax^b\,(1-x)^c\,(1+d\,x)\,. \tag{B.19}$$

Replacing the parameter A by the value of I we obtain the formula

$$xG(x) \;=\; I\,\frac{x^b\,(1-x)^c\,(1+d\,x)}{\int_{x_1}^{x_2}\mathrm{d}x\; x^b\,(1-x)^c\,(1+d\,x)}\,, \tag{B.20}$$

where I is a fit parameter whose error can be calculated by MINOS.

The Contributions from Single Sources of Uncertainties

Using the χ^2 definition from (B.16) each fit has the knowledge of all sources of uncertainties which are then reflected in the errors of the corresponding fit results. Within this approach it is not directly possible to disentangle the contributions from the different sources of uncertainties.

It is nevertheless interesting to know which sources give the largest contributions to the total error. For this purpose we redo the fits excluding source by source (or groups of sources). On one hand this may lead to different central values of our results, since the single data points enter the χ^2 formula now with a different weight. This new central result has no further meaning. On the other hand we also obtain a different, reduced error of the fit result. We define the uncertainty contribution from the corresponding source to be the square root of the difference of the total and the reduced errors squared.

In some cases the uncertainty contribution assigned in this procedure to a specific source may depend on the order in which the sources are excluded and is therefore not well defined. However, the total uncertainty is always well defined.

To have a unique treatment within the present analysis we always start to exclude the theoretical uncertainties (in the order: factorization scale dependence, renormalization scale dependence, uncertainties of the hadronization corrections). The remaining uncertainty is purely experimental and from the difference to the total uncertainty we calculate the theoretical contribution as discussed above.

The order in which the experimental sources of uncertainties are then excluded can be seen in table D.1 (from bottom to top).

C

Method of a Fast Evaluation of NLO Jet Cross Sections

In the QCD fits the free parameters are determined in an iterative minimization procedure of a suitably defined χ^2 function. This requires the iterative calculation of perturbative cross sections in next-to-leading order (NLO) for varying values of $\alpha_s(M_Z)$ and changing parameterizations of the parton density functions. The number of iterations needed will among other things depend on the number of parameters in the fit and is of the order of several thousands for the fits performed in chapter 9. The standard way of calculating NLO jet cross sections using the existing programs takes computing time of about one day (with still not too high precision) and is therefore not suitable for fast iterative calculations.

In this appendix we introduce a flexible method for a very fast numerical evaluation of arbitrary cross sections in NLO. Similar methods, formulated in Mellin space have been proposed elsewhere [131, 132]. The method proposed here is formulated in momentum space ("x-space") and thus allows an easy access of available parameterizations of parton density functions from global fits. The time-consuming calculation of the NLO matrix elements in a Monte-Carlo integration needs to be done only once (and can therefore be done with very high precision). The calculation of the NLO cross section from the convolution of the matrix elements with parton density functions can then be performed within fractions of a second. This method can therefore be used whenever a fast repeated evaluation of NLO cross sections is needed using available parameterizations of parton density functions, especially in iterative fitting procedures or in cases when cross sections have to be computed for many different parton density functions.

C.1 Introduction

In perturbative QCD the cross section of any process in deep-inelastic lepton-hadron scattering can be written as a convolution of (process specific) perturbative coefficients $c_{a,n}$ with (universal) parton density functions $f_{a/h}$ of the hadron h, summed over all parton flavors a

(see chapter 1)

$$\sigma = \sum_{a,n} \int_0^1 \mathrm{d}x \; \alpha_s^n(\mu_r) \; c_{a,n}\left(\frac{x_{\mathrm{Bj}}}{x}, \mu_r, \mu_f\right) \; f_{a/h}(x, \mu_f) \, . \tag{C.1}$$

The sum runs over all parton flavors a and all orders n considered in the perturbative expansion. The integration is carried out over all fractional parton momenta[1] x. The truncation of the perturbative expansion at a fixed order introduces a dependence of the cross section on the choice of the renormalization scale μ_r and the factorization scale μ_f. These scales are usually identified with large final state momenta (E_T, Q) which are in general integrated over.

Our aim is now to rewrite this equation to obtain a factorizable expression where the convolution of the perturbative coefficients and the parton density functions is reduced to a product. In the following we explain how this can be achieved and which approximations are needed, to reproduce the results obtained in a direct integration according to (C.1) within two per mil.

C.2 Approximation of the x-dependence

For the moment we ignore the dependences on μ_r and μ_f in (C.1), assuming that both have fixed values. The x-dependence of the parton density functions $f_{a/h}(x)$ can be approximated using a linear interpolation within sufficiently small intervals in $\log_{10}(x)$. We therefore introduce a discrete set of x-values labeled x_i ($i = 0, 1, 2, \cdots$) with $x_i < x_{i-1} < x_{i-2} < \cdots < x_0 = 1$. The x_i are equidistant in $\log_{10}(x)$ with distances $\Delta l \equiv (\log_{10}(x_i) - \log_{10}(x_{i+1}))$. We define a set of eigenfunctions $E^{(i)}(x)$ by

$$E^{(i)}(x) \equiv \begin{cases} 1 & x = x_i \\ \frac{\log_{10}(x_{i-1}) - \log_{10}(x)}{\Delta l} & x_{i-1} < x < x_i \\ \frac{\log_{10}(x) - \log_{10}(x_{i+1})}{\Delta l} & x_i < x < x_{i+1} \\ 0 & x < x_{i-1} \, , \quad \text{or} \quad x > x_{i+1} \end{cases} \, . \tag{C.2}$$

The parton distributions $f_{a/h}(x)$ can then be approximated by a linear combination of the $E^{(i)}(x)$ with coefficients given by the values $f_{a/h}(x_i)$ of the parton distributions at the discrete points x_i

$$f_{a/h}(x) \; \simeq \; \sum_i \; f_{a/h}(x_i) \; E^{(i)}(x) \, . \tag{C.3}$$

An example, where a given parameterization of the gluon density is approximated by a linear combination of the $E^{(i)}(x)$ is shown in Fig. C.1 for a choice of 25 divisions per $\log_{10}(x)$ corresponding to $\Delta l = 1/25$. Fig. C.2 shows the ratio of the approximation and the original

---

[1] The parton momentum fraction is here labeled x and must not be confused with the Bjorken scaling variable which is here throughout written with a subscript: x_{Bj}.

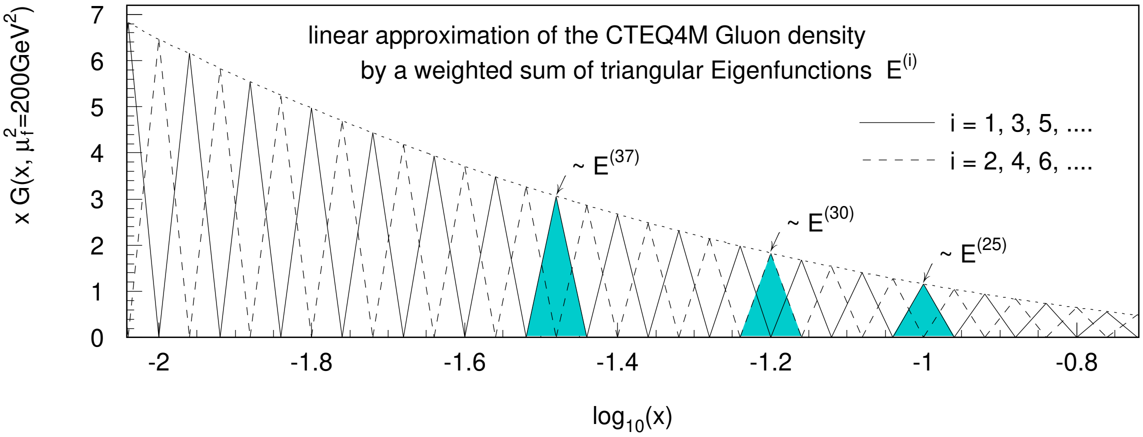

Figure C.1: A graphical representation of a linear combination of eigenfunctions $E^{(i)}(x)$ to approximate the CTEQ4M gluon density at a factorization scale $\mu_f^2 = 200\,\mathrm{GeV}^2$.

distribution for different parton flavors (as defined in section 8.2.2). We see that for $x < 0.3$ we achieve a precision better than two per mil.

Now we can insert the approximation of the parton density functions (C.3) in the perturbative cross section formula (C.1) and obtain

$$\sigma \simeq \sum_{a,n,i} \alpha_s^n \, f_{a/h}(x_i) \int \mathrm{d}x \, c_{a,n}\left(\frac{x_{\mathrm{Bj}}}{x}\right) \, E^{(i)}(x) \,. \tag{C.4}$$

The $f_{a/h}(x_i)$ are no longer functions of x but constants which can be pulled out of the integral, together with α_s. The integral is therefore independent of the parton density functions and the value of α_s. For a short hand notation of the integral we use the following definition

$$\tilde{\sigma}_{a,n}^{(i)} \equiv \int \mathrm{d}x \, c_{a,n}\left(\frac{x_{\mathrm{Bj}}}{x}\right) \, E^{(i)}(x) \,. \tag{C.5}$$

The $\tilde{\sigma}_{a,n}^{(i)}$ can now be computed once for the eigenfunctions of every i in all orders n and for all parton flavors a. Using the $\tilde{\sigma}_{a,n}^{(i)}$ the final cross section can be calculated for arbitrary parameterizations of the parton distributions and for any α_s value as

$$\sigma \simeq \sum_{a,n,i} \alpha_s^n \, \tilde{\sigma}_{a,n}^{(i)} \, f_{a/h}(x_i) \,. \tag{C.6}$$

The time consuming step of the procedure is only the computation of the $\tilde{\sigma}_{a,n}^{(i)}$ in (C.5) which involves the integration over the phase space and the calculation of the (jet-) observable(s). All further calculations to obtain the final cross section can be performed very fast, according to (C.6).

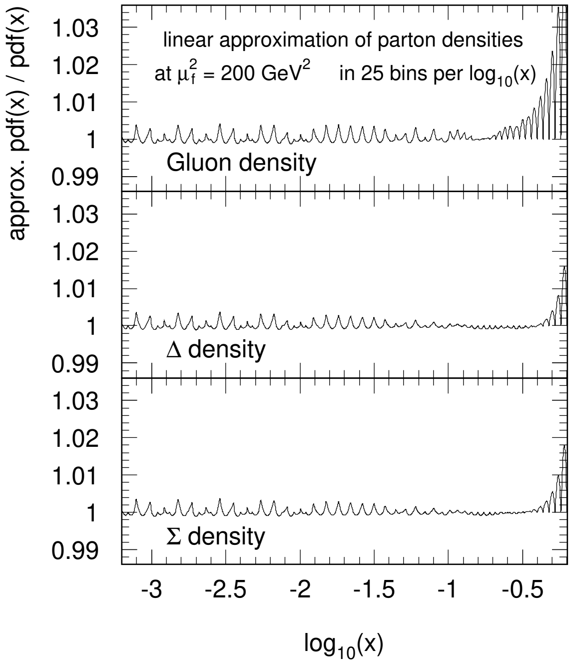

Figure C.2: The ratio of the approximations using a linear interpolation and the original parton distributions (for CTEQ4M partons). The approximations are shown for the gluon density ($xG(x)$), the charge squared weighted sum of the quark densities ($x\Delta(x)$), and the sum of the quark densities ($x\Sigma(x)$).

C.3 Approximations of the Renormalization and the Factorization Scale Dependence

In (C.1) the perturbative coefficients, the parton density functions and the strong coupling constant also depend on the renormalization and/or the factorization scales μ_r and μ_f. In the following we assume that both scales are set to the same value $\mu_r = \mu_f = \mu$ (this can be easily generalized).

The scale dependences can be considered by calculating the total cross section σ as a sum of cross sections σ_j which are calculated within sufficiently small intervals of μ. The contribution from each interval (with some intermediate value $\mu^{(j)}$) is given by (C.6) and the total cross section by

$$\sigma \;\simeq\; \sum_{a,n,i,j} \alpha_s^n(\mu_r^{(j)}) \;\tilde{\sigma}_{a,n,j}^{(i)}(\mu_r^{(j)}, \mu_f^{(j)}) \;\, f_{a/h}(x_i, \mu_f^{(j)}) \;. \tag{C.7}$$

Within the j-th interval approximations for the factorization and the renormalization scale dependences are made.

The Factorization Scale

The factorization scale dependence of the parton distributions is given by the DGLAP evolution equations and involves a mixing of different parton flavors. An exact treatment of this dependence has been proposed in [132]. We follow the approximation made in [131] to divide the range of the factorization scale into sufficiently small bins, using the fixed value $\mu_f^{(j)}$ for the computations within these bins. Since the parton distributions depend only logarithmically on the scale μ_f this is no strong restriction. At NLO a large part of the μ_f dependence is compensated by a corresponding term in the perturbative coefficients $c_{a,n}(\mu_r, \mu_f)$, so that the error is of higher order in α_s. In general the bin width (and the number of bins) can be adjusted to keep the error arbitrarily small.

The Renormalization Scale

As for the factorization scale μ_f, the integration over the renormalization scale μ_r is replaced in (C.7) by a sum over intervals of μ_r. In principle the same arguments as in the discussion for the factorization scale can be applied and the calculations can be performed at fixed values $\mu_r^{(j)}$.

C.4 The Final Formula

Based on the discussions above we have obtained the following formula

$$\sigma = \sum_{a,n,i,j} \alpha_s^n(\mu_r^{(j)})\; \tilde{\sigma}_{a,n,j}^{(i)}(\mu_r^{(j)}, \mu_f^{(j)})\; f_{a/h}(x_i, \mu_f^{(j)}) \; . \tag{C.8}$$

The sum runs over four indices n, a, i, j where n denotes the power of the strong coupling constant, and a the flavor of the parton density functions. The index i refers to a set of discrete x-values (x_i) between which the parton distributions are interpolated. The index j denotes the ranges within which the approximations of the renormalization and the factorization scale dependences are made.

Using expression (C.8), the $\tilde{\sigma}_{a,n,j}^{(i)}(\mu_r^{(j)}, \mu_f^{(j)})$ can be calculated once, with very high precision. The cross section can then be calculated for arbitrary parameterizations of the parton density functions and arbitrary α_s values within fractions of a second.

For the present analysis we have used the DISENT program to calculate the $\tilde{\sigma}_{a,n,j}^{(i)}(\mu_r^{(j)}, \mu_f^{(j)})$ for all cross sections with a statistical precision, corresponding to an integrated luminosity of $\mathcal{L}_{\text{int}} \simeq 8000\,\text{pb}^{-1}$. The difference between the direct integration in DISENT and the fast integration, using the approximations described above, is always below 2 per mil for all bins of all distributions.

D

Tables of the Results

D.1 Jet Cross Sections

In this appendix we list the numerical values of all jet cross sections that were used in the QCD analysis, i.e. the inclusive jet and the dijet cross sections at $Q^2 > 150\,\mathrm{GeV}^2$. Quoted are the values of the cross sections *integrated* over the corresponding bin (in the result plots in chapter 7 the values are divided by the bin-size).

The listing includes all experimental uncertainties (as described in section 6.3) which are here separated into the correlated and the uncorrelated part. Since the interpretation of the results (as e.g. in a QCD analysis) does not require the knowledge of the single contributions to the uncorrelated part of the uncertainties, we only present the total uncorrelated uncertainty while we list the single contributions to the correlated uncertainty in separate columns for all sources. The uncertainty from the hadronic energy scale of the Liquid Argon calorimeter is quoted asymmetric. The left (right) value corresponds to an increase (decrease) of the calibration constants. The uncertainties of the positron energy and the positron polar angle are defined to be symmetric by taking the maximum of the upwards and downwards deviations. The signs are quoted for a positive variation of the corresponding source. Note that only the *correlated* contribution from these sources is listed. As described in section 6.3 some of these sources contribute also to the uncorrelated uncertainty. The latter contribution is already contained in the (quadratic) sum of all uncorrelated uncertainties.

The full phase space definitions of the observables have been given in chapter 7. Please note that all measured jet cross sections are corrected for higher order QED effects (as described in section 4.4) whereas no corrections for non-perturbative effects (hadronization corrections) have been applied to the data. The size of the latter has been estimated according to the procedure as described in chapter 3 and the values are quoted in the last column of the result tables. The values are given in percent and refer to the difference by which the partonic cross sections are larger than the corresponding hadronic cross sections (i.e. *after* hadronization).

We refer to the bins in which the jet cross sections are measured by a number and a letter. The ranges of the variables are quoted in the tables in the corresponding sections.

D.1.1 The Inclusive Jet Cross Section $d^2\sigma_{\mathrm{jet}}/(dE_T\,dQ^2)$

number	corresponding Q^2 range
1	$150 < Q^2 < 200\,\mathrm{GeV}^2$
2	$200 < Q^2 < 300\,\mathrm{GeV}^2$
3	$300 < Q^2 < 600\,\mathrm{GeV}^2$
4	$600 < Q^2 < 5000\,\mathrm{GeV}^2$

letter	corresponding E_T range
a	$7 < E_T < 11\,\mathrm{GeV}$
b	$11 < E_T < 18\,\mathrm{GeV}$
c	$18 < E_T < 30\,\mathrm{GeV}$
d	$30 < E_T < 50\,\mathrm{GeV}$

the inclusive jet cross section $d^2\sigma_{\mathrm{jet}}/(dE_T\,dQ^2)$ — inclusive $k_\perp$ jet algorithm

									single contributions to correlated uncertainty					
bin No.	cross section (in pb)	statistical uncert. (in percent)	total uncertainty (in percent)		uncorrelated uncertainty (in percent)		correlated uncertainty (in percent)		model dep. detector corr. (in percent)	positron energy scale (in percent)	positron polar angle (in percent)	LAr hadr. energy scale (in percent)		hadroniz. correct. (percent)
1 a	62.220	± 2.9	9.6	-9.5	7.6	-7.4	5.9	-5.9	± 4.7	0.8	1.7	2.6	-2.6	8.4
1 b	26.084	± 4.4	16.3	-13.9	13.6	-11.3	9.0	-8.0	± 6.3	0.8	1.6	6.0	-4.4	5.2
1 c	5.819	± 9.2	13.8	-15.6	12.3	-13.8	6.3	-7.2	± 4.3	1.0	1.7	3.9	-5.3	4.7
1 d	0.719	± 27.8	34.0	-35.4	32.4	-33.4	10.4	-11.6	± 3.4	1.9	2.7	9.2	-10.5	4.9
2 a	62.256	± 2.6	7.6	-7.2	6.4	-6.1	4.1	-3.9	± 2.3	0.2	1.0	2.8	-2.5	8.8
2 b	29.802	± 3.7	12.2	-12.7	10.3	-10.8	6.5	-6.7	± 4.0	0.7	0.2	4.9	-5.2	4.7
2 c	6.989	± 7.6	16.8	-14.8	14.3	-12.4	8.9	-8.1	± 6.7	0.3	1.9	5.3	-3.8	4.8
2 d	0.994	± 20.0	28.7	-33.5	26.0	-29.9	12.1	-15.0	± 8.6	2.7	1.9	7.7	-11.8	5.1
3 a	61.577	± 2.7	5.8	-6.1	4.9	-5.3	3.0	-3.1	± 1.2	0.7	0.8	2.0	-2.2	8.8
3 b	35.010	± 3.5	11.9	-9.9	10.1	-8.2	6.3	-5.5	± 3.5	0.5	1.4	4.8	-3.6	4.2
3 c	9.644	± 6.6	15.7	-17.9	13.3	-15.3	8.4	-9.4	± 4.2	1.6	3.7	5.9	-7.2	4.7
3 d	1.362	± 20.0	36.3	-29.7	32.1	-26.4	17.1	-13.7	± 11.4	1.1	1.6	12.5	-7.1	4.9
4 a	46.515	± 3.1	7.4	-6.8	6.3	-5.8	3.8	-3.5	± 0.7	0.0	1.4	3.1	-2.7	9.9
4 b	26.409	± 4.1	8.8	-8.8	7.6	-7.6	4.4	-4.4	± 1.6	0.6	1.5	3.5	-3.5	4.2
4 c	11.288	± 6.0	11.5	-11.6	10.3	-10.3	5.3	-5.4	± 2.4	0.3	0.5	4.4	-4.6	3.4
4 d	1.993	± 15.1	27.2	-23.0	24.6	-21.2	11.5	-8.9	± 1.2	0.9	1.9	11.1	-8.4	3.3

the inclusive jet cross section $d^2\sigma_{\mathrm{jet}}/(dE_T\,dQ^2)$ — Aachen jet algorithm

									single contributions to correlated uncertainty					
bin No.	cross section (in pb)	statistical uncert. (in percent)	total uncertainty (in percent)		uncorrelated uncertainty (in percent)		correlated uncertainty (in percent)		model dep. detector corr. (in percent)	positron energy scale (in percent)	positron polar angle (in percent)	LAr hadr. energy scale (in percent)		hadroniz. correct. (percent)
1 a	59.249	± 2.9	9.9	-9.7	8.0	-7.8	5.9	-5.8	± 4.4	0.8	1.7	3.0	-2.9	12.2
1 b	24.660	± 4.5	15.4	-14.3	12.9	-11.9	8.5	-7.9	± 5.8	0.5	1.5	5.7	-4.9	10.8
1 c	5.266	± 9.7	15.1	-16.3	13.0	-14.0	7.6	-8.2	± 5.8	1.6	2.6	3.6	-4.7	9.5
1 d	0.761	± 27.9	37.1	-33.8	35.0	-32.4	12.3	-9.7	± 1.6	0.0	0.0	12.1	-9.4	8.9
2 a	60.286	± 2.6	7.3	-7.9	6.1	-6.6	4.1	-4.3	± 2.5	0.2	1.1	2.6	-2.9	12.1
2 b	28.446	± 3.7	12.2	-12.1	10.4	-10.4	6.4	-6.2	± 3.5	0.8	0.2	5.1	-4.8	9.8
2 c	6.786	± 7.7	17.7	-16.5	14.8	-13.6	9.8	-9.3	± 7.8	1.2	1.5	5.4	-4.4	9.0
2 d	0.935	± 20.5	28.8	-37.8	26.4	-33.9	11.5	-16.7	± 7.5	1.8	2.0	8.2	-14.5	8.5
3 a	61.343	± 2.7	7.3	-6.3	6.3	-5.2	3.8	-3.5	± 1.6	1.2	1.0	2.6	-2.2	11.4
3 b	33.301	± 3.5	10.3	-9.6	8.6	-8.0	5.6	-5.3	± 3.3	0.3	1.6	3.9	-3.5	8.5
3 c	9.037	± 6.9	17.6	-18.4	15.2	-15.8	9.0	-9.4	± 3.8	1.5	3.2	7.2	-7.7	8.8
3 d	1.197	± 21.4	38.7	-29.9	33.9	-26.4	18.7	-14.2	± 13.0	2.5	1.9	13.0	-4.5	8.0
4 a	45.452	± 3.2	8.0	-6.5	6.8	-5.4	4.1	-3.5	± 1.4	0.5	1.4	3.2	-2.4	11.8
4 b	25.046	± 4.1	8.0	-8.6	6.8	-7.3	4.2	-4.4	± 2.6	0.4	1.1	2.6	-3.0	7.6
4 c	10.873	± 6.2	13.0	-13.5	11.6	-11.9	6.0	-6.3	± 2.0	0.5	0.5	5.4	-5.7	6.7
4 d	1.690	± 16.4	30.0	-23.5	27.1	-21.8	12.9	-8.9	± 0.2	2.4	2.7	12.3	-8.0	6.3

D.1.2 The Dijet Cross Section $d^2\sigma_{\mathrm{dijet}}/dQ^2$

bin No.	corresponding Q^2 range
1	$150 < Q^2 < 175\,\mathrm{GeV}^2$
2	$175 < Q^2 < 200\,\mathrm{GeV}^2$
3	$200 < Q^2 < 235\,\mathrm{GeV}^2$
4	$235 < Q^2 < 280\,\mathrm{GeV}^2$
5	$280 < Q^2 < 350\,\mathrm{GeV}^2$
6	$350 < Q^2 < 450\,\mathrm{GeV}^2$

bin No.	corresponding Q^2 range
7	$450 < Q^2 < 600\,\mathrm{GeV}^2$
8	$600 < Q^2 < 900\,\mathrm{GeV}^2$
9	$900 < Q^2 < 1500\,\mathrm{GeV}^2$
10	$1500 < Q^2 < 3000\,\mathrm{GeV}^2$
11	$3000 < Q^2 < 6000\,\mathrm{GeV}^2$
12	$6000 < Q^2 < 15000\,\mathrm{GeV}^2$

the dijet cross section $d^2\sigma_{\mathrm{dijet}}/dQ^2$

									single contributions to correlated uncertainty				
bin No.	cross section (in pb)	statistical uncert. (in percent)	total uncertainty (in percent)		uncorrelated uncertainty (in percent)		correlated uncertainty (in percent)		model dep. detector corr. (in percent)	positron energy scale (in percent)	positron polar angle (in percent)	LAr hadr. energy scale (in percent)		hadroniz. correct. (percent)
	inclusive $k_\perp$ jet algorithm													
1	14.136	± 6.5	15.6	-17.0	12.5	-13.9	9.3	-9.8	± 8.0	2.7	0.9	3.5	-4.6	6.4
2	12.459	± 6.4	12.6	-12.6	10.6	-10.6	6.8	-6.8	± 3.1	2.2	3.9	3.9	-3.9	5.7
3	11.934	± 6.1	11.0	-12.8	9.6	-11.2	5.4	-6.2	± 2.0	2.1	2.2	3.7	-4.8	6.2
4	13.583	± 5.8	12.1	-13.6	10.0	-11.3	6.9	-7.5	± 4.7	1.8	2.9	3.5	-4.6	5.8
5	13.607	± 5.8	9.4	-10.1	8.5	-9.2	3.9	-4.3	± 1.3	0.5	0.5	3.2	-3.8	5.4
6	12.372	± 6.2	10.1	-10.8	8.8	-9.5	4.9	-5.1	± 0.8	1.3	2.7	3.4	-3.7	5.9
7	11.761	± 6.6	12.0	-10.3	10.9	-9.4	5.0	-4.0	± 1.0	0.6	0.6	4.6	-3.5	6.0
8	12.263	± 6.5	13.1	-11.7	11.6	-10.3	6.1	-5.5	± 2.9	0.6	0.9	5.1	-4.3	5.7
9	8.777	± 7.4	11.8	-9.3	10.6	-8.6	5.0	-3.6	± 1.9	1.1	1.1	4.1	-2.1	5.8
10	6.487	± 9.2	11.2	-11.3	10.5	-10.6	3.7	-3.9	± 0.7	1.6	1.3	2.6	-2.8	6.3
11	2.341	± 14.1	17.0	-17.3	15.7	-16.0	6.5	-6.6	± 5.8	0.7	1.1	2.2	-2.5	5.9
12	0.468	± 27.3	31.1	-31.5	29.1	-29.4	11.0	-11.3	± 2.7	7.9	6.3	3.2	-4.0	9.5
	Aachen jet algorithm													
1	13.837	± 6.6	15.7	-16.0	12.6	-13.0	9.3	-9.3	± 7.8	2.7	0.9	3.8	-4.0	11.0
2	12.243	± 6.5	11.6	-11.3	9.8	-9.6	6.1	-5.9	± 2.5	1.4	3.5	3.8	-3.5	10.0
3	11.280	± 6.2	10.9	-12.7	9.1	-10.8	6.0	-6.6	± 2.6	3.1	2.8	3.0	-4.2	10.6
4	13.229	± 5.9	12.7	-13.0	10.6	-10.9	7.0	-7.2	± 3.5	2.4	3.5	4.1	-4.5	9.8
5	13.178	± 5.9	11.4	-10.0	10.1	-8.9	5.2	-4.6	± 2.6	1.3	0.7	4.0	-3.1	9.6
6	11.895	± 6.4	10.2	-10.7	9.0	-9.4	4.8	-5.0	± 0.7	0.8	2.8	3.4	-3.7	9.7
7	11.427	± 6.8	11.8	-10.2	10.7	-9.4	4.9	-3.9	± 0.0	0.4	0.7	4.6	-3.5	9.6
8	11.848	± 6.6	11.6	-12.1	10.3	-10.7	5.4	-5.6	± 2.9	0.7	1.1	4.1	-4.4	8.9
9	8.327	± 7.6	10.9	-9.9	10.0	-9.2	4.3	-3.7	± 1.7	1.0	0.8	3.5	-2.6	8.8
10	5.834	± 9.6	11.1	-11.8	10.5	-11.1	3.5	-4.1	± 0.2	2.1	1.3	2.1	-2.9	8.8
11	2.239	± 14.3	17.1	-18.2	15.8	-16.7	6.6	-7.3	± 5.3	1.9	2.3	2.0	-3.6	8.7
12	0.519	± 26.6	31.3	-32.0	28.8	-29.4	12.3	-12.8	± 3.9	9.3	6.6	2.5	-4.1	10.9
	exclusive $k_\perp$ jet algorithm													
1	10.392	± 7.8	18.7	-17.9	15.4	-14.6	10.6	-10.4	± 7.3	3.7	3.1	5.8	-5.3	21.8
2	9.920	± 7.2	13.0	-15.0	11.0	-12.9	6.9	-7.6	± 0.8	3.0	4.1	4.4	-5.4	19.6
3	9.717	± 6.8	12.4	-11.3	11.2	-10.2	5.4	-4.8	± 1.6	1.0	1.8	4.5	-3.8	19.6
4	11.686	± 6.3	12.6	-13.3	10.7	-11.3	6.7	-7.0	± 4.2	2.5	2.2	3.7	-4.3	17.2
5	13.288	± 5.9	14.5	-10.4	13.0	-9.3	6.5	-4.7	± 1.4	1.0	1.2	6.0	-3.9	14.4
6	13.546	± 6.1	11.7	-10.7	10.5	-9.5	5.2	-4.9	± 0.1	1.7	2.1	4.2	-3.8	11.6
7	15.129	± 6.1	11.7	-11.2	10.1	-9.5	6.0	-5.8	± 3.8	1.7	1.7	3.7	-3.4	7.7
8	14.456	± 6.1	10.8	-9.3	9.6	-8.4	4.9	-4.1	± 1.8	0.8	1.4	4.0	-2.9	6.3
9	11.209	± 6.6	9.6	-9.4	8.8	-8.6	3.9	-3.9	± 0.4	1.2	1.5	3.0	-3.0	5.3
10	8.943	± 7.6	10.1	-10.4	9.3	-9.6	3.9	-4.1	± 0.1	2.1	1.2	2.7	-3.0	6.3
11	3.205	± 11.6	14.3	-14.6	13.2	-13.5	5.4	-5.6	± 4.1	1.5	0.8	2.7	-3.0	6.9
12	1.044	± 18.5	25.3	-24.4	22.3	-21.6	11.8	-11.3	± 9.1	6.2	2.2	3.3	-0.5	9.7
	Cambridge jet algorithm													
1	7.013	± 9.7	23.5	-23.4	18.8	-18.7	14.1	-14.1	± 12.5	3.1	2.0	5.1	-5.3	25.0
2	7.721	± 8.8	15.5	-14.1	13.4	-12.1	7.8	-7.3	± 1.6	2.7	4.7	5.2	-4.4	23.6
3	7.383	± 8.0	14.3	-13.9	12.7	-12.3	6.7	-6.4	± 3.0	0.6	2.8	5.0	-4.7	23.2
4	8.952	± 7.5	16.2	-15.6	13.4	-12.8	9.2	-9.0	± 6.5	3.4	3.1	4.3	-3.9	21.5
5	10.829	± 6.8	11.6	-12.4	10.4	-11.1	5.0	-5.6	± 2.8	0.4	0.5	3.9	-4.5	17.8
6	11.593	± 6.8	13.8	-13.1	12.0	-11.4	6.8	-6.3	± 1.4	3.0	2.9	4.9	-4.3	13.8
7	13.083	± 6.7	10.6	-11.5	9.4	-10.2	4.8	-5.4	± 3.3	1.4	0.9	2.8	-3.6	9.4
8	13.737	± 6.4	10.5	-9.5	9.5	-8.7	4.4	-3.9	± 1.4	0.4	0.8	3.8	-3.2	7.1
9	9.645	± 7.2	10.6	-9.4	9.8	-8.8	4.2	-3.6	± 0.2	1.0	1.2	3.6	-2.8	6.7
10	8.084	± 8.1	10.2	-10.4	9.5	-9.6	3.5	-3.9	± 0.6	1.8	1.3	2.2	-2.7	7.2
11	2.800	± 12.5	16.9	-17.1	14.9	-15.1	7.8	-7.9	± 7.2	1.5	1.3	1.9	-2.3	8.5
12	0.769	± 21.2	29.6	-29.1	25.8	-25.5	14.4	-14.2	± 12.2	5.8	3.5	3.5	-2.3	12.2

D.1.3 The Dijet Cross Section $d^2\sigma_{\rm dijet}/(d\overline{E}_T\,dQ^2)$

bin number	corresponding Q^2 range
1	$150 < Q^2 < 200\,{\rm GeV}^2$
2	$200 < Q^2 < 300\,{\rm GeV}^2$
3	$300 < Q^2 < 600\,{\rm GeV}^2$
4	$600 < Q^2 < 5000\,{\rm GeV}^2$

letter	corresponding $\overline{E}_T$ range
a	$8.5 < \overline{E}_T < 11.5\,{\rm GeV}$
b	$11.5 < \overline{E}_T < 15\,{\rm GeV}$
c	$15 < \overline{E}_T < 20\,{\rm GeV}$
d	$20 < \overline{E}_T < 35\,{\rm GeV}$

the dijet cross section $d^2\sigma_{\rm dijet}/(d\overline{E}_T\,dQ^2)$

									single contributions to correlated uncertainty					
bin No.	cross section (in pb)	statistical uncert. (in percent)	total uncertainty (in percent)		uncorrelated uncertainty (in percent)		correlated uncertainty (in percent)		model dep. detector corr. (in percent)	positron energy scale (in percent)	positron polar angle (in percent)	LAr hadr. energy scale (in percent)		hadroniz. correct. (percent)
	inclusive $k_\perp$ jet algorithm													
1 a	14.270	± 6.3	11.2	-13.0	9.5	-11.2	5.9	-6.6	± 4.7	0.6	1.7	2.8	-4.0	7.3
1 b	6.662	± 9.0	16.5	-15.7	14.1	-13.4	8.5	-8.2	± 7.0	0.7	1.7	4.0	-3.4	4.2
1 c	4.141	± 12.0	19.1	-21.3	16.2	-18.2	10.2	-11.1	± 8.7	1.4	3.4	3.6	-5.7	5.9
1 d	1.576	± 18.2	26.5	-22.1	24.6	-21.0	9.9	-6.8	± 0.8	2.4	2.3	9.1	-5.7	4.4
2 a	15.824	± 5.5	8.6	-11.0	7.8	-9.9	3.6	-4.9	± 0.9	1.2	0.9	2.8	-4.3	7.3
2 b	7.356	± 7.6	9.6	-11.2	9.0	-10.3	3.4	-4.4	± 0.9	0.3	1.3	2.6	-3.8	3.8
2 c	4.694	± 10.1	23.5	-21.1	19.4	-17.3	13.2	-12.1	± 10.8	1.4	1.4	7.2	-5.0	5.5
2 d	1.829	± 14.5	22.1	-21.8	19.6	-19.2	10.2	-10.2	± 8.2	0.4	2.3	5.4	-5.4	4.4
3 a	14.545	± 5.8	8.8	-9.3	8.0	-8.5	3.7	-3.8	± 0.6	0.8	1.4	2.9	-3.0	7.6
3 b	10.282	± 6.9	10.4	-11.2	9.5	-10.2	4.2	-4.8	± 1.9	1.0	1.3	3.0	-3.8	4.5
3 c	4.882	± 9.7	13.7	-15.6	12.4	-14.1	5.8	-6.7	± 2.4	2.0	2.3	4.0	-5.3	3.0
3 d	3.378	± 12.1	24.2	-17.4	21.5	-15.5	11.1	-7.9	± 0.4	2.8	4.9	9.4	-5.2	4.4
4 a	13.029	± 6.4	10.2	-7.7	9.3	-7.1	4.2	-2.8	± 1.6	0.8	0.6	3.5	-1.4	8.5
4 b	7.833	± 8.1	12.5	-10.9	11.0	-9.7	5.8	-5.0	± 3.5	2.6	0.9	3.4	-1.5	5.0
4 c	4.324	± 10.6	13.7	-14.9	12.7	-13.7	5.1	-5.8	± 1.9	1.6	2.1	3.6	-4.6	2.7
4 d	4.008	± 11.0	15.9	-18.9	14.7	-17.2	6.0	-7.8	± 0.5	1.4	1.2	5.5	-7.3	3.6

the dijet cross section $d^2\sigma_{\mathrm{dijet}}/(d\overline{E}_T\,dQ^2)$

									single contributions to correlated uncertainty					
bin No.	cross section (in pb)	statistical uncert. (in percent)	total uncertainty (in percent)		uncorrelated uncertainty (in percent)		correlated uncertainty (in percent)		model dep. detector corr. (in percent)	positron energy scale (in percent)	positron polar angle (in percent)	LAr hadr. energy scale (in percent)		hadroniz. correct. (percent)
	Aachen jet algorithm													
1 a	14.503	± 6.2	10.3	-10.4	8.8	-9.0	5.3	-5.2	± 3.9	1.4	1.6	2.6	-2.3	11.1
1 b	6.104	± 9.3	16.5	-16.9	14.4	-14.8	8.0	-8.2	± 5.3	1.3	1.9	5.3	-5.6	9.5
1 c	3.968	± 12.3	26.6	-27.4	21.0	-21.6	16.3	-16.8	± 15.2	2.9	4.2	2.7	-4.8	11.3
1 d	1.578	± 18.6	25.5	-22.8	23.7	-21.5	9.5	-7.5	± 4.7	0.9	1.2	8.0	-5.4	8.4
2 a	14.993	± 5.6	7.6	-9.0	7.0	-8.3	2.9	-3.6	± 0.2	0.5	1.0	2.2	-3.1	11.1
2 b	7.606	± 7.6	12.8	-12.6	11.7	-11.5	5.3	-5.1	± 1.1	0.5	0.8	4.9	-4.6	8.4
2 c	4.106	± 10.5	21.3	-20.2	17.5	-16.4	12.2	-11.8	± 10.8	0.7	2.3	4.9	-3.6	9.8
2 d	1.808	± 14.7	24.8	-27.0	21.3	-23.2	12.7	-13.8	± 10.9	0.5	1.6	6.1	-8.2	9.3
3 a	14.627	± 5.9	9.7	-7.9	8.8	-7.3	4.1	-2.9	± 0.9	0.8	1.1	3.4	-1.9	11.1
3 b	9.319	± 7.2	10.4	-12.5	9.6	-11.3	4.1	-5.3	± 0.8	0.1	1.5	3.4	-4.8	8.5
3 c	5.140	± 9.6	14.8	-17.1	13.4	-15.3	6.3	-7.7	± 2.8	1.8	2.4	4.5	-6.3	7.6
3 d	2.839	± 13.0	20.4	-17.0	18.4	-15.5	8.9	-7.0	± 0.2	2.4	4.4	7.2	-4.6	8.5
4 a	11.853	± 6.7	7.3	-9.1	6.9	-8.4	2.5	-3.5	± 0.8	1.0	1.4	0.5	-2.5	10.9
4 b	8.138	± 8.1	13.6	-10.2	12.1	-9.4	6.1	-4.2	± 2.4	2.0	1.3	4.8	-2.0	8.4
4 c	3.602	± 11.4	14.5	-16.2	13.5	-14.9	5.3	-6.5	± 3.5	0.8	1.4	3.4	-5.0	5.7
4 d	4.049	± 11.1	17.6	-16.4	16.2	-15.2	7.0	-6.2	± 0.3	1.0	0.9	6.7	-5.9	7.1
	exclusive $k_\perp$ jet algorithm													
1 a	7.028	± 9.7	16.5	-13.6	14.9	-12.3	7.2	-5.6	± 3.2	2.0	1.3	5.8	-3.6	24.6
1 b	7.337	± 8.5	15.9	-15.6	13.9	-13.6	7.8	-7.6	± 5.3	0.6	1.2	5.3	-5.1	13.0
1 c	3.870	± 12.2	14.6	-17.3	13.4	-15.8	5.6	-7.2	± 4.3	0.8	2.6	1.8	-4.9	17.5
1 d	1.762	± 17.6	21.6	-23.2	20.3	-21.6	7.5	-8.7	± 5.7	0.8	1.1	4.5	-6.2	15.9
2 a	8.020	± 7.9	11.2	-12.0	10.2	-10.8	4.6	-5.2	± 1.8	2.6	1.3	2.6	-3.6	18.6
2 b	8.250	± 7.4	11.9	-11.3	10.8	-10.5	4.9	-4.2	± 1.8	1.1	1.0	4.1	-3.1	8.9
2 c	4.901	± 9.7	21.1	-15.2	18.7	-13.6	9.8	-6.9	± 4.2	1.0	2.0	8.4	-4.8	11.9
2 d	2.021	± 14.4	24.7	-26.5	20.6	-22.3	13.6	-14.4	± 12.8	0.4	0.9	4.0	-6.3	13.6
3 a	11.571	± 6.9	14.1	-11.0	12.3	-9.4	6.9	-5.8	± 4.1	2.8	1.6	4.3	-2.1	10.2
3 b	10.706	± 6.8	12.1	-11.5	11.0	-10.4	5.1	-4.9	± 2.0	0.8	1.0	4.3	-4.1	3.5
3 c	6.214	± 8.8	14.8	-12.6	13.3	-11.4	6.4	-5.3	± 2.0	1.6	2.2	5.3	-3.8	8.3
3 d	3.145	± 12.3	18.0	-18.6	16.4	-16.8	7.4	-7.9	± 0.2	2.1	4.1	5.6	-6.3	10.6
4 a	10.341	± 7.2	11.6	-11.9	10.2	-10.5	5.5	-5.7	± 3.6	1.9	1.1	3.2	-3.5	7.8
4 b	8.327	± 7.7	11.7	-11.2	10.2	-9.7	5.8	-5.5	± 4.8	1.0	1.1	2.4	-1.8	2.3
4 c	5.659	± 9.5	11.1	-13.3	10.6	-12.3	3.5	-5.0	± 1.3	1.1	1.3	2.4	-4.3	0.7
4 d	4.594	± 10.3	19.1	-13.4	17.2	-12.6	8.1	-4.6	± 1.7	0.2	0.5	7.8	-3.9	3.4
	Cambridge jet algorithm													
1 a	4.645	± 12.3	19.8	-16.1	17.9	-14.5	8.4	-7.1	± 6.2	1.2	1.8	5.1	-2.3	34.0
1 b	5.012	± 11.0	22.4	-24.1	18.4	-20.0	12.7	-13.5	± 11.4	1.4	1.3	5.3	-6.8	13.8
1 c	3.320	± 13.5	19.6	-19.6	16.5	-16.4	10.6	-10.7	± 6.9	3.6	6.8	2.0	-2.5	16.8
1 d	1.486	± 20.1	24.8	-26.5	23.6	-25.0	7.6	-8.9	± 1.8	1.0	1.4	7.0	-8.4	13.9
2 a	6.121	± 9.4	10.5	-14.3	9.8	-13.0	3.6	-5.8	± 0.5	2.4	2.2	0.1	-4.5	25.2
2 b	6.120	± 8.9	17.2	-12.6	15.3	-11.2	7.8	-5.7	± 4.5	0.6	1.9	5.9	-2.5	10.8
2 c	3.721	± 11.3	19.2	-18.6	16.8	-16.2	9.4	-9.1	± 6.3	0.2	3.2	6.0	-5.6	12.5
2 d	1.691	± 15.9	33.5	-33.6	27.0	-27.2	19.8	-19.8	± 18.7	0.8	0.9	6.3	-6.4	13.7
3 a	9.311	± 8.0	13.7	-12.9	11.8	-11.1	6.9	-6.5	± 5.2	1.3	2.0	3.5	-2.7	15.0
3 b	8.491	± 7.9	12.9	-11.3	11.8	-10.5	5.1	-4.3	± 0.2	0.4	1.0	4.8	-3.9	5.7
3 c	5.519	± 9.7	13.2	-17.7	11.7	-15.6	6.2	-8.3	± 3.5	2.7	3.1	2.7	-6.2	7.8
3 d	2.736	± 13.8	22.9	-19.4	20.7	-17.8	9.7	-7.8	± 0.7	2.1	4.2	8.4	-6.0	9.2
4 a	9.681	± 7.6	11.5	-9.8	10.4	-8.9	5.0	-4.2	± 3.1	1.7	0.5	3.1	-1.5	9.8
4 b	7.204	± 8.4	12.2	-12.6	10.7	-11.1	5.8	-6.1	± 5.1	0.4	1.2	1.9	-2.7	2.6
4 c	5.066	± 10.1	14.8	-14.4	13.7	-13.2	5.8	-5.6	± 2.4	1.2	0.7	4.9	-4.6	1.2
4 d	4.247	± 10.9	15.7	-14.4	14.5	-13.4	6.0	-5.1	± 1.1	1.6	0.8	5.3	-4.3	3.4

D.1.4 The Dijet Cross Section $d^2\sigma_{\mathrm{dijet}}/(dM_{jj}\,dQ^2)$

bin number	corresponding Q^2 range
1	$150 < Q^2 < 200\,\mathrm{GeV}^2$
2	$200 < Q^2 < 300\,\mathrm{GeV}^2$
3	$300 < Q^2 < 600\,\mathrm{GeV}^2$
4	$600 < Q^2 < 5000\,\mathrm{GeV}^2$

letter	corresponding M_{jj} range
a	$15 < M_{jj} < 22\,\mathrm{GeV}$
b	$22 < M_{jj} < 31\,\mathrm{GeV}$
c	$31 < M_{jj} < 45\,\mathrm{GeV}$
d	$45 < M_{jj} < 85\,\mathrm{GeV}$

the dijet cross section $d^2\sigma_{\mathrm{dijet}}/(dM_{jj}\,dQ^2)$													
								single contributions to correlated uncertainty					
bin No.	cross section (in pb)	statistical uncert. (in percent)	total uncertainty (in percent)		uncorrelated uncertainty (in percent)		correlated uncertainty (in percent)		model dep. detector corr. (in percent)	positron energy scale (in percent)	positron polar angle (in percent)	LAr hadr. energy scale (in percent)		hadroniz. correct. (percent)
	inclusive $k_\perp$ jet algorithm													
1 a	6.559	± 8.9	15.7	-19.3	13.1	-16.6	8.5	-9.9	± 7.4	1.5	1.7	3.1	-5.9	7.4
1 b	10.621	± 7.3	12.8	-12.6	10.7	-10.5	7.1	-6.9	± 5.2	0.5	3.6	2.9	-2.5	5.6
1 c	7.306	± 9.2	16.3	-13.1	14.4	-11.6	7.6	-6.2	± 3.8	1.7	3.0	5.5	-3.0	5.0
1 d	2.356	± 14.9	19.9	-21.1	18.5	-19.4	7.4	-8.2	± 4.4	0.6	0.0	5.8	-6.7	6.0
2 a	8.248	± 7.4	12.2	-14.9	10.3	-12.9	6.5	-7.4	± 5.9	0.6	0.9	2.0	-4.1	6.8
2 b	10.829	± 6.4	10.5	-11.0	9.5	-9.9	4.4	-4.9	± 2.2	0.7	0.7	3.4	-4.0	5.1
2 c	7.283	± 7.9	13.7	-12.6	12.2	-11.2	6.3	-5.7	± 3.7	0.7	0.6	4.8	-4.0	5.5
2 d	3.107	± 12.4	24.7	-26.5	20.4	-22.1	14.0	-14.7	± 12.4	1.1	2.2	5.8	-7.4	6.6
3 a	6.723	± 8.2	11.9	-15.2	10.8	-13.9	4.9	-6.3	± 3.1	0.4	0.2	3.5	-5.2	7.1
3 b	12.550	± 6.3	9.3	-8.7	8.4	-7.8	4.0	-3.9	± 1.6	0.1	2.2	2.4	-2.2	5.1
3 c	9.626	± 7.4	13.6	-12.2	12.1	-10.8	6.2	-5.6	± 2.1	1.5	2.1	5.0	-4.2	5.1
3 d	4.070	± 10.9	17.4	-16.6	15.3	-14.7	8.1	-7.7	± 4.7	1.3	3.1	5.5	-4.8	6.1
4 a	5.876	± 9.4	14.7	-11.1	13.3	-10.3	6.3	-4.1	± 3.1	1.8	1.1	4.8	-0.6	9.6
4 b	9.509	± 7.4	10.8	-10.2	10.0	-9.5	4.1	-3.7	± 0.7	0.9	0.8	3.6	-3.1	5.8
4 c	8.503	± 7.8	9.4	-10.3	8.9	-9.6	3.1	-3.7	± 1.0	0.2	0.9	2.4	-3.1	4.1
4 d	5.216	± 10.1	14.4	-16.9	13.3	-15.3	5.4	-7.0	± 1.5	0.8	0.6	4.9	-6.6	5.1

the dijet cross section $d^2\sigma_{\mathrm{dijet}}/(dM_{jj}\,dQ^2)$

bin No.	cross section (in pb)	statistical uncert. (in percent)	total uncertainty (in percent)		uncorrelated uncertainty (in percent)		correlated uncertainty (in percent)		single contributions to correlated uncertainty					hadroniz. correct. (percent)
									model dep. detector corr. (in percent)	positron energy scale (in percent)	positron polar angle (in percent)	LAr hadr. energy scale (in percent)		
	Aachen jet algorithm													
1 a	6.914	± 8.8	14.2	-12.5	12.7	-11.4	6.4	-5.2	± 2.5	1.2	2.7	4.9	-3.1	11.4
1 b	9.824	± 7.5	12.8	-14.4	10.1	-11.7	7.8	-8.4	± 6.4	0.8	4.0	1.0	-3.2	10.0
1 c	7.301	± 9.3	20.2	-13.6	17.6	-11.7	9.8	-6.8	± 3.6	3.1	3.5	7.7	-3.1	9.6
1 d	2.080	± 15.8	23.9	-27.6	20.7	-24.0	12.0	-13.7	± 11.0	0.6	0.9	4.3	-8.0	11.7
2 a	8.056	± 7.5	10.4	-11.7	9.5	-10.9	4.2	-4.3	± 2.0	0.7	1.3	3.0	-3.1	9.8
2 b	10.208	± 6.5	9.6	-10.6	8.9	-9.6	3.6	-4.4	± 0.8	0.4	0.5	3.1	-4.0	9.3
2 c	7.223	± 8.0	14.6	-13.7	12.5	-11.7	7.5	-7.0	± 5.9	0.4	0.8	4.3	-3.3	10.8
2 d	2.931	± 12.5	26.1	-27.3	22.1	-23.0	14.0	-14.6	± 11.2	1.1	1.6	7.9	-9.0	11.1
3 a	6.532	± 8.3	11.2	-11.3	10.3	-10.4	4.5	-4.6	± 3.1	1.3	0.1	2.6	-2.8	10.5
3 b	12.076	± 6.4	11.5	-10.1	10.2	-9.2	5.2	-4.4	± 0.9	0.8	2.5	4.1	-3.1	8.3
3 c	9.460	± 7.4	13.2	-13.1	11.7	-11.5	6.2	-6.3	± 3.6	1.1	1.8	4.4	-4.5	9.9
3 d	3.953	± 11.3	16.7	-17.7	15.0	-15.9	7.5	-7.9	± 4.2	1.5	3.2	4.8	-5.4	10.9
4 a	5.566	± 9.6	13.4	-11.7	12.1	-10.7	5.7	-4.7	± 1.1	2.4	2.9	3.9	-2.2	11.9
4 b	9.491	± 7.4	9.2	-9.5	8.6	-8.9	3.3	-3.4	± 0.8	1.3	1.2	2.2	-2.4	8.1
4 c	7.672	± 8.1	9.7	-10.7	9.2	-10.0	3.1	-3.8	± 1.2	0.3	0.4	2.4	-3.2	7.2
4 d	4.918	± 10.4	16.4	-17.4	15.0	-15.9	6.5	-7.2	± 1.6	0.8	0.6	6.0	-6.8	9.1
	exclusive $k_\perp$ jet algorithm													
1 a	2.064	± 17.1	20.8	-21.8	19.9	-20.8	6.0	-6.7	± 1.9	2.2	2.3	4.6	-5.4	67.4
1 b	7.107	± 9.3	15.9	-17.9	13.3	-15.2	8.7	-9.5	± 7.7	0.9	2.1	2.9	-4.9	20.2
1 c	7.450	± 8.8	17.4	-14.3	15.3	-12.6	8.4	-6.8	± 3.8	2.3	2.2	6.6	-4.4	10.7
1 d	3.746	± 11.3	18.6	-18.5	16.8	-16.7	7.9	-7.9	± 4.3	0.0	0.6	6.4	-6.4	7.6
2 a	4.260	± 11.2	15.9	-17.9	14.3	-16.0	7.0	-8.1	± 3.9	3.9	1.9	3.5	-5.5	38.8
2 b	7.042	± 7.9	11.6	-11.3	10.6	-10.2	4.6	-4.7	± 1.6	1.6	1.9	3.2	-3.3	16.3
2 c	8.471	± 7.3	13.2	-11.2	12.0	-10.5	5.5	-4.0	± 1.2	0.3	0.2	5.1	-3.5	8.8
2 d	5.014	± 9.4	17.6	-17.7	15.2	-15.2	8.8	-9.1	± 6.7	0.4	1.3	5.2	-5.7	5.9
3 a	6.973	± 8.7	14.5	-14.0	12.8	-12.3	6.7	-6.7	± 4.0	2.6	2.3	3.8	-3.9	13.0
3 b	11.833	± 6.6	11.1	-8.9	10.2	-8.2	4.5	-3.4	± 1.3	1.5	1.5	3.4	-1.7	8.6
3 c	10.566	± 6.9	14.7	-9.9	13.3	-9.0	6.3	-4.0	± 0.1	1.0	1.7	5.8	-3.2	7.0
3 d	5.959	± 9.1	18.5	-17.6	16.4	-15.5	8.5	-8.2	± 2.8	1.5	2.5	7.4	-7.0	7.4
4 a	9.827	± 7.4	9.6	-9.7	9.2	-9.1	2.9	-3.5	± 0.1	0.7	1.1	2.1	-2.8	4.5
4 b	9.866	± 7.2	9.4	-9.0	8.7	-8.3	3.7	-3.5	± 1.4	1.9	0.9	2.2	-1.8	1.6
4 c	8.618	± 7.5	10.9	-10.3	10.0	-9.6	4.2	-3.6	± 1.1	0.3	0.8	3.7	-3.0	3.3
4 d	6.885	± 8.7	16.4	-16.9	14.7	-15.1	7.2	-7.5	± 2.3	0.2	0.4	6.7	-7.0	3.9
	Cambridge jet algorithm													
1 a	1.456	± 20.3	25.6	-21.7	24.1	-21.0	8.7	-5.7	± 1.4	1.3	4.4	7.1	-2.6	70.9
1 b	5.692	± 10.6	19.2	-21.1	15.7	-17.4	11.1	-11.9	± 10.6	0.3	1.9	2.1	-4.8	20.3
1 c	5.753	± 10.7	20.8	-16.7	18.1	-14.2	10.3	-8.7	± 6.6	2.2	3.8	6.4	-3.4	13.4
1 d	1.981	± 16.8	26.2	-28.8	23.0	-25.2	12.6	-13.9	± 10.7	0.0	0.0	6.4	-8.7	11.2
2 a	3.539	± 12.3	13.9	-14.3	13.3	-13.6	3.9	-4.3	± 0.1	2.4	2.2	1.6	-2.3	41.0
2 b	6.443	± 8.5	12.2	-12.4	11.4	-11.5	4.3	-4.8	± 0.2	1.0	1.8	3.5	-4.1	16.9
2 c	6.129	± 9.0	17.5	-16.7	14.8	-13.9	9.4	-9.1	± 7.8	1.2	1.5	4.6	-4.0	12.3
2 d	3.145	± 12.8	27.5	-28.9	22.6	-24.0	15.6	-16.1	± 13.8	0.7	0.8	7.1	-8.1	11.6
3 a	6.023	± 9.4	17.3	-14.2	15.5	-12.8	7.8	-6.2	± 4.8	1.4	1.8	5.5	-2.8	13.7
3 b	10.717	± 7.3	11.8	-12.4	10.5	-10.9	5.5	-5.8	± 3.1	1.6	1.9	3.6	-4.0	11.5
3 c	8.433	± 8.0	12.7	-15.3	11.4	-13.5	5.8	-7.3	± 2.3	1.7	2.9	3.8	-5.9	9.6
3 d	3.708	± 12.2	20.0	-14.4	18.3	-13.7	8.1	-4.6	± 1.9	1.7	1.7	7.4	-3.1	10.7
4 a	9.302	± 7.7	10.2	-11.3	9.2	-10.2	4.3	-5.1	± 3.3	1.5	1.1	1.6	-3.0	5.3
4 b	9.209	± 7.5	10.4	-8.9	9.6	-8.3	4.1	-3.2	± 1.6	1.6	0.5	3.1	-1.6	2.5
4 c	7.673	± 8.3	12.1	-11.1	10.9	-10.0	5.2	-4.8	± 3.7	0.1	1.4	3.0	-2.3	4.2
4 d	5.257	± 10.2	17.4	-19.2	15.9	-17.4	7.1	-8.2	± 0.5	0.9	0.5	6.9	-8.0	5.2

D.1.5 The Dijet Cross Section $d^2\sigma_{\rm dijet}/(d\xi\, dQ^2)$

bin number	corresponding Q^2 range	ξ range
1 a	$150 < Q^2 < 200\,\mathrm{GeV}^2$	$0.009 < \xi < 0.017$
1 b		$0.017 < \xi < 0.025$
1 c		$0.025 < \xi < 0.035$
1 d		$0.035 < \xi < 0.05$
1 e		$0.05 < \xi < 0.12$
2 a	$200 < Q^2 < 300\,\mathrm{GeV}^2$	$0.01 < \xi < 0.02$
2 b		$0.02 < \xi < 0.03$
2 c		$0.03 < \xi < 0.04$
2 d		$0.04 < \xi < 0.06$
2 e		$0.06 < \xi < 0.15$
3 a	$300 < Q^2 < 600\,\mathrm{GeV}^2$	$0.015 < \xi < 0.025$
3 b		$0.025 < \xi < 0.035$
3 c		$0.035 < \xi < 0.045$
3 d		$0.045 < \xi < 0.065$
3 e		$0.065 < \xi < 0.18$
4 a	$600 < Q^2 < 5000\,\mathrm{GeV}^2$	$0.025 < \xi < 0.045$
4 b		$0.045 < \xi < 0.065$
4 c		$0.065 < \xi < 0.1$
4 d		$0.1 < \xi < 0.3$

the dijet cross section $d^2\sigma_{\rm dijet}/(d\xi\, dQ^2)$

									single contributions to correlated uncertainty					
bin No.	cross section (in pb)	statistical uncert. (in percent)	total uncertainty (in percent)		uncorrelated uncertainty (in percent)		correlated uncertainty (in percent)		model dep. detector corr. (in percent)	positron energy scale (in percent)	positron polar angle (in percent)	LAr hadr. energy scale (in percent)		hadroniz. correct. (percent)
	inclusive $k_\perp$ jet algorithm													
1 a	4.147	± 11.0	24.7	-27.7	19.9	-22.9	14.7	-15.6	± 13.7	1.9	1.8	4.3	-6.9	6.4
1 b	6.272	± 9.1	14.9	-13.8	13.2	-12.2	6.9	-6.4	± 3.4	2.1	2.8	4.7	-3.8	5.6
1 c	6.544	± 9.8	12.3	-13.2	11.2	-12.0	5.1	-5.6	± 3.1	3.0	1.2	1.8	-3.0	6.0
1 d	5.059	± 10.9	14.3	-15.3	13.2	-14.1	5.3	-5.9	± 1.9	2.3	2.2	3.5	-4.4	5.7
1 e	4.800	± 11.3	18.4	-17.8	15.1	-14.5	10.6	-10.3	± 7.9	3.3	5.3	2.9	-1.7	6.7
2 a	6.324	± 8.8	13.7	-18.1	12.0	-16.0	6.5	-8.6	± 3.8	3.6	1.2	3.4	-6.5	6.5
2 b	7.309	± 7.8	10.9	-12.5	10.0	-11.3	4.4	-5.3	± 2.6	0.3	1.0	3.1	-4.3	5.1
2 c	6.023	± 8.6	11.7	-11.8	10.5	-10.5	5.2	-5.5	± 1.1	1.5	3.7	2.8	-3.2	5.3
2 d	5.512	± 8.9	14.9	-11.9	13.4	-11.0	6.6	-4.6	± 2.6	1.6	1.9	5.3	-2.4	5.1
2 e	4.186	± 10.3	17.8	-19.3	14.7	-16.1	10.1	-10.8	± 8.3	3.1	3.6	3.0	-4.8	8.2
3 a	5.997	± 9.3	12.7	-15.4	11.9	-14.4	4.5	-5.6	± 1.5	0.9	1.0	3.8	-5.1	5.7
3 b	7.006	± 8.3	11.3	-12.4	10.1	-11.1	5.0	-5.6	± 3.5	0.4	2.1	2.4	-3.4	5.0
3 c	6.104	± 9.0	16.0	-11.9	14.5	-11.1	6.9	-4.5	± 1.2	2.2	1.0	6.1	-3.3	4.7
3 d	7.249	± 8.1	10.1	-10.4	9.0	-9.2	4.7	-4.9	± 1.9	0.6	3.8	1.2	-1.9	6.6
3 e	6.082	± 8.8	14.7	-14.3	13.1	-12.7	6.7	-6.5	± 3.0	1.2	2.4	5.1	-4.9	6.2
4 a	6.077	± 9.4	15.0	-12.6	13.6	-11.6	6.3	-5.0	± 2.3	0.6	2.0	5.2	-3.5	6.6
4 b	6.759	± 8.5	13.3	-11.9	11.7	-10.5	6.3	-5.6	± 3.8	2.3	1.9	3.8	-2.4	5.9
4 c	8.305	± 8.0	11.0	-10.2	10.2	-9.5	4.1	-3.5	± 0.6	0.9	1.0	3.6	-2.8	5.0
4 d	7.520	± 8.2	10.2	-11.2	9.6	-10.4	3.3	-4.1	± 0.4	1.3	0.3	2.7	-3.5	6.1

the dijet cross section $d^2\sigma_{\mathrm{dijet}}/(d\xi\, dQ^2)$

bin No.	cross section (in pb)	statistical uncert. (in percent)	total uncertainty (in percent)		uncorrelated uncertainty (in percent)		correlated uncertainty (in percent)		single contributions to correlated uncertainty: model dep. detector corr. (in percent)	positron energy scale (in percent)	positron polar angle (in percent)	LAr hadr. energy scale (in percent)		hadroniz. correct. (percent)
	Aachen jet algorithm													
1 a	3.973	± 10.9	17.4	-17.4	15.4	-15.5	8.2	-8.0	± 5.4	1.6	2.7	5.1	-4.7	9.5
1 b	6.214	± 9.4	14.2	-13.7	12.5	-12.1	6.7	-6.3	± 4.8	0.5	2.4	3.6	-2.9	9.3
1 c	6.473	± 9.7	14.1	-15.9	12.7	-14.2	6.0	-7.2	± 4.5	1.1	1.3	3.2	-5.1	11.5
1 d	4.537	± 11.4	13.9	-14.6	13.0	-13.6	4.8	-5.2	± 1.1	3.1	1.1	3.0	-3.6	10.2
1 e	4.819	± 11.3	19.8	-18.8	15.7	-14.7	12.0	-11.6	± 8.5	3.5	6.9	3.1	-0.6	12.2
2 a	6.020	± 9.0	14.1	-15.9	12.9	-14.6	5.7	-6.2	± 0.2	2.3	1.2	4.8	-5.4	9.4
2 b	7.100	± 7.9	11.7	-11.2	10.8	-10.3	4.5	-4.3	± 2.5	0.4	0.6	3.4	-3.1	8.9
2 c	5.656	± 8.8	11.5	-12.5	10.5	-11.2	4.9	-5.5	± 1.0	1.7	3.1	2.8	-3.8	10.1
2 d	5.484	± 8.9	12.7	-12.8	11.3	-11.3	5.9	-6.0	± 3.5	2.1	2.7	2.9	-3.1	10.1
2 e	3.990	± 10.6	17.3	-18.6	14.5	-15.7	9.4	-10.0	± 8.1	2.3	2.8	2.8	-4.3	13.2
3 a	5.725	± 9.7	12.9	-12.7	11.9	-11.8	4.9	-4.7	± 1.7	1.0	1.8	3.7	-3.5	7.9
3 b	6.695	± 8.5	11.9	-13.8	10.7	-12.4	5.3	-6.1	± 4.4	0.6	0.4	2.6	-3.9	8.8
3 c	6.209	± 9.1	16.0	-11.8	14.4	-10.7	7.1	-5.0	± 2.6	2.5	2.0	5.5	-2.4	8.6
3 d	6.817	± 8.2	10.8	-13.3	9.8	-11.8	4.6	-6.0	± 3.4	1.3	2.1	1.0	-4.0	10.5
3 e	5.925	± 9.0	18.8	-12.5	16.4	-10.9	9.1	-6.1	± 1.9	2.8	3.7	7.5	-3.0	11.7
4 a	5.903	± 9.6	13.6	-14.1	12.3	-12.8	5.7	-6.0	± 3.4	1.1	2.1	3.7	-4.1	9.2
4 b	6.241	± 8.8	12.0	-11.9	10.9	-10.8	5.1	-4.9	± 3.3	1.2	1.4	3.0	-2.6	8.2
4 c	7.877	± 8.1	11.1	-10.5	10.2	-9.7	4.4	-4.1	± 2.1	1.0	1.3	3.2	-2.7	8.6
4 d	7.121	± 8.5	10.7	-11.6	10.1	-10.8	3.7	-4.3	± 0.5	1.1	0.6	3.1	-3.8	9.4
	exclusive $k_\perp$ jet algorithm													
1 a	1.224	± 20.2	23.0	-31.2	21.9	-28.6	7.1	-12.6	± 4.0	2.7	3.8	3.3	-10.9	55.7
1 b	3.033	± 14.0	24.1	-21.3	21.4	-18.8	11.1	-10.0	± 7.9	2.8	2.8	6.5	-4.4	32.5
1 c	5.397	± 11.0	17.3	-18.6	15.2	-16.4	8.3	-8.7	± 6.3	1.6	2.2	4.5	-5.2	21.5
1 d	4.248	± 11.8	17.3	-17.8	16.0	-16.4	6.7	-7.0	± 2.1	1.8	1.1	5.8	-6.2	13.0
1 e	5.920	± 9.5	14.9	-14.4	12.9	-12.5	7.5	-7.3	± 4.4	3.1	3.3	3.7	-3.2	9.8
2 a	3.843	± 12.2	22.8	-22.7	20.0	-19.8	11.0	-11.0	± 2.8	6.2	4.4	7.4	-7.3	40.0
2 b	4.146	± 10.7	15.2	-16.4	13.4	-14.5	7.2	-7.8	± 6.2	1.9	0.5	2.7	-3.9	22.6
2 c	5.003	± 9.7	16.6	-13.7	14.9	-12.0	7.5	-6.6	± 4.8	3.2	2.0	4.2	-2.1	14.6
2 d	5.384	± 8.9	11.9	-13.2	10.9	-11.9	4.8	-5.5	± 0.3	1.6	2.9	3.2	-4.2	8.9
2 e	6.483	± 8.2	14.5	-11.9	12.9	-10.7	6.6	-5.3	± 3.6	1.1	1.3	5.1	-3.1	8.8
3 a	5.897	± 10.4	14.5	-14.7	13.8	-13.8	4.7	-4.9	± 0.5	2.4	0.4	3.8	-4.0	16.6
3 b	7.227	± 8.5	11.6	-12.1	10.5	-10.9	4.8	-5.2	± 1.4	2.2	2.2	3.1	-3.7	11.4
3 c	6.841	± 8.8	17.9	-13.3	15.8	-11.7	8.5	-6.4	± 4.9	1.0	2.1	6.4	-3.1	7.6
3 d	8.262	± 7.6	11.8	-10.5	10.8	-9.7	4.6	-3.9	± 0.3	1.7	1.1	3.8	-2.9	7.4
3 e	8.173	± 7.4	14.0	-13.2	12.2	-11.4	6.8	-6.6	± 3.7	1.2	2.5	4.7	-4.5	7.4
4 a	8.185	± 8.3	12.6	-10.5	11.3	-9.6	5.4	-4.4	± 0.3	1.8	2.8	4.0	-2.4	8.0
4 b	8.340	± 7.8	9.2	-9.2	8.7	-8.8	2.8	-2.9	± 0.7	0.9	0.8	2.0	-2.0	5.0
4 c	9.484	± 7.2	9.5	-10.8	8.8	-9.9	3.5	-4.4	± 1.4	1.0	0.5	2.6	-3.7	4.8
4 d	10.207	± 6.9	10.3	-9.6	9.5	-8.9	4.1	-3.7	± 0.0	0.7	1.0	3.6	-3.1	5.3
	Cambridge jet algorithm													
1 a	0.861	± 24.8	31.4	-31.9	28.8	-29.1	12.5	-13.0	± 11.7	1.7	2.2	2.8	-4.6	56.3
1 b	2.743	± 14.5	21.3	-23.7	18.7	-20.8	10.3	-11.4	± 7.9	2.1	4.2	4.5	-6.5	33.1
1 c	3.815	± 13.7	23.9	-18.9	21.8	-17.0	10.0	-8.3	± 5.1	3.3	3.2	7.1	-4.5	24.5
1 d	3.141	± 13.9	18.0	-18.0	16.6	-16.7	7.0	-6.8	± 2.2	4.8	1.6	4.0	-3.7	14.7
1 e	4.088	± 12.6	22.2	-20.6	18.3	-16.8	12.5	-11.8	± 8.3	3.1	6.7	5.5	-3.7	13.2
2 a	3.359	± 13.0	23.2	-17.6	20.9	-16.0	10.2	-7.2	± 3.7	2.9	3.4	8.2	-4.0	40.8
2 b	4.131	± 11.1	14.3	-13.4	13.3	-12.5	5.3	-4.7	± 2.6	2.2	1.6	3.5	-2.5	25.2
2 c	3.626	± 11.4	15.4	-18.1	14.0	-16.1	6.4	-8.1	± 4.2	2.7	2.4	2.9	-5.8	16.7
2 d	4.303	± 10.3	16.5	-18.4	14.0	-15.8	8.7	-9.5	± 5.3	4.5	3.6	3.6	-5.2	12.9
2 e	3.850	± 11.4	20.0	-18.6	17.0	-15.7	10.6	-10.0	± 9.4	1.1	0.6	4.4	-2.8	13.4
3 a	5.998	± 10.4	13.3	-16.0	12.2	-14.6	5.4	-6.5	± 3.3	3.4	1.2	1.7	-4.0	17.3
3 b	6.663	± 9.0	13.1	-13.1	11.9	-12.0	5.4	-5.2	± 1.0	3.0	1.2	4.0	-3.8	12.1
3 c	5.769	± 9.9	15.9	-14.6	13.9	-12.6	7.8	-7.3	± 3.9	2.6	4.3	4.2	-3.3	9.9
3 d	6.216	± 9.0	12.6	-13.0	11.5	-11.8	5.1	-5.4	± 0.1	2.7	1.8	3.7	-4.1	11.0
3 e	5.784	± 9.3	15.2	-15.3	13.5	-13.5	7.1	-7.3	± 4.2	1.8	2.5	4.6	-4.9	10.3
4 a	7.846	± 8.6	12.2	-12.3	11.2	-11.3	4.8	-4.9	± 1.9	0.3	1.7	3.8	-4.0	8.7
4 b	7.866	± 8.2	10.4	-9.3	9.9	-8.9	3.2	-2.7	± 0.3	1.1	0.8	2.5	-1.7	6.3
4 c	8.867	± 7.8	10.2	-9.7	9.6	-9.1	3.6	-3.3	± 0.8	0.9	0.2	3.0	-2.6	6.7
4 d	8.229	± 7.7	9.7	-10.0	9.2	-9.3	3.3	-3.5	± 0.8	0.6	0.3	2.7	-2.9	6.0

D.1.6 The Dijet Cross Section $d^2\sigma_{\mathrm{dijet}}/(dx_p\,dQ^2)$

bin number	corresponding Q^2 range	x_p range
1 a	$150 < Q^2 < 200\,\mathrm{GeV}^2$	$0.05 < x_p < 0.13$
1 b		$0.13 < x_p < 0.20$
1 c		$0.20 < x_p < 0.30$
1 d		$0.30 < x_p < 0.45$
2 a	$200 < Q^2 < 300\,\mathrm{GeV}^2$	$0.07 < x_p < 0.15$
2 b		$0.15 < x_p < 0.25$
2 c		$0.25 < x_p < 0.35$
2 d		$0.35 < x_p < 0.6$
3 a	$300 < Q^2 < 600\,\mathrm{GeV}^2$	$0.08 < x_p < 0.20$
3 b		$0.20 < x_p < 0.35$
3 c		$0.35 < x_p < 0.50$
3 d		$0.50 < x_p < 0.80$
4 a	$600 < Q^2 < 5000\,\mathrm{GeV}^2$	$0.18 < x_p < 0.35$
4 b		$0.35 < x_p < 0.55$
4 c		$0.55 < x_p < 0.70$
4 d		$0.70 < x_p < 0.95$

the dijet cross section $d^2\sigma_{\mathrm{dijet}}/(dx_p\,dQ^2)$

									single contributions to correlated uncertainty				
bin No.	cross section (in pb)	statistical uncert. (in percent)	total uncertainty (in percent)		uncorrelated uncertainty (in percent)		correlated uncertainty (in percent)		model dep. detector corr. (in percent)	positron energy scale (in percent)	positron polar angle (in percent)	LAr hadr. energy scale (in percent)		hadroniz. correct. (percent)
	inclusive $k_\perp$ jet algorithm													
1 a	6.522	± 9.5	13.6	-14.0	12.4	-12.8	5.6	-5.8	± 0.6	3.3	0.8	4.2	-4.4	6.0
1 b	6.139	± 9.3	13.9	-14.7	11.8	-12.6	7.2	-7.6	± 5.8	2.1	2.9	1.9	-3.0	4.8
1 c	9.628	± 7.8	19.1	-19.3	15.1	-15.3	11.7	-11.7	± 10.1	1.6	3.4	4.2	-4.2	5.5
1 d	3.579	± 12.3	19.0	-20.0	17.2	-18.0	8.2	-8.8	± 4.8	3.4	2.8	4.7	-5.7	8.8
2 a	5.070	± 9.3	17.3	-16.3	14.5	-13.5	9.6	-9.1	± 8.1	1.4	1.8	4.3	-3.1	7.0
2 b	8.692	± 7.3	11.2	-9.6	10.2	-8.9	4.4	-3.5	± 2.2	0.3	0.6	3.5	-2.3	4.2
2 c	8.209	± 7.4	10.1	-12.9	9.0	-11.4	4.6	-6.0	± 2.8	2.2	1.4	2.0	-4.4	6.4
2 d	6.717	± 8.3	14.9	-18.5	13.1	-16.2	7.2	-8.9	± 4.4	3.2	0.7	4.5	-6.8	6.5
3 a	5.508	± 9.3	16.0	-17.4	13.0	-14.2	9.4	-10.0	± 7.2	1.0	4.8	3.1	-4.6	6.1
3 b	11.638	± 6.5	9.1	-12.1	8.4	-11.0	3.4	-5.1	± 1.3	1.3	0.8	2.3	-4.4	4.2
3 c	11.141	± 6.7	9.8	-9.0	9.1	-8.5	3.8	-3.1	± 0.6	0.4	0.7	3.3	-2.5	5.8
3 d	4.388	± 10.3	19.5	-16.5	17.3	-14.6	9.1	-7.5	± 3.7	3.1	3.0	6.9	-4.7	8.7
4 a	5.268	± 10.2	12.6	-15.2	12.0	-14.0	4.1	-5.9	± 0.8	0.9	0.8	3.5	-5.5	4.3
4 b	10.025	± 7.1	12.6	-12.5	10.7	-10.6	6.6	-6.6	± 5.4	1.1	0.9	3.1	-3.1	4.6
4 c	7.368	± 8.2	13.5	-11.1	12.0	-9.9	6.2	-4.9	± 3.5	1.4	1.7	4.5	-2.3	5.5
4 d	6.633	± 8.9	14.8	-11.2	13.6	-10.5	5.8	-4.0	± 1.3	2.6	0.7	4.7	-2.0	10.2

the dijet cross section $d^2\sigma_{\rm dijet}/(dx_p\, dQ^2)$

bin No.	cross section (in pb)	statistical uncert. (in percent)	total uncertainty (in percent)		uncorrelated uncertainty (in percent)		correlated uncertainty (in percent)		single contributions to correlated uncertainty					hadroniz. correct. (percent)
									model dep. detector corr. (in percent)	positron energy scale (in percent)	positron polar angle (in percent)	LAr hadr. energy scale (in percent)		
	Aachen jet algorithm													
1 a	6.259	± 9.7	13.7	-13.8	12.2	-12.3	6.1	-6.1	± 1.8	3.1	2.8	3.7	-3.8	11.4
1 b	6.415	± 9.2	16.6	-17.2	13.9	-14.4	9.2	-9.3	± 7.6	2.3	2.9	3.3	-3.6	9.4
1 c	8.555	± 8.1	17.5	-16.3	13.7	-12.5	10.9	-10.5	± 8.6	1.8	5.2	3.7	-1.9	9.3
1 d	4.299	± 11.5	15.8	-18.4	14.4	-16.9	6.4	-7.4	± 0.2	4.2	2.1	4.1	-5.5	12.9
2 a	4.654	± 9.6	15.3	-14.7	13.2	-12.7	7.9	-7.6	± 6.7	0.8	1.6	3.3	-2.6	12.1
2 b	8.488	± 7.3	12.3	-10.5	11.2	-9.6	5.1	-4.3	± 1.8	1.6	0.8	4.2	-3.1	9.0
2 c	8.394	± 7.4	8.8	-11.7	8.1	-10.6	3.4	-5.0	± 1.5	1.8	1.4	1.2	-3.9	10.3
2 d	6.044	± 8.6	16.4	-15.7	14.8	-14.4	7.1	-6.1	± 1.9	1.9	0.8	6.4	-5.3	9.6
3 a	5.638	± 9.4	14.7	-15.0	12.8	-13.0	7.1	-7.4	± 4.2	1.7	3.6	3.9	-4.4	11.1
3 b	11.426	± 6.6	10.5	-12.6	9.5	-11.3	4.5	-5.6	± 2.3	1.3	1.0	3.2	-4.6	8.6
3 c	10.341	± 6.9	11.6	-8.9	10.4	-8.2	5.0	-3.4	± 0.6	1.5	1.7	4.1	-2.1	8.7
3 d	4.324	± 10.4	15.6	-15.8	14.1	-14.3	6.8	-6.8	± 3.4	3.1	1.6	4.5	-4.5	12.1
4 a	5.098	± 10.5	14.0	-15.0	13.0	-13.8	5.3	-5.9	± 3.1	0.4	0.4	3.9	-4.7	8.3
4 b	8.925	± 7.6	12.9	-12.1	11.0	-10.3	6.7	-6.3	± 5.4	0.7	1.5	3.3	-2.5	7.8
4 c	7.371	± 8.2	12.3	-11.1	11.3	-10.3	4.9	-4.0	± 0.0	1.6	1.5	4.1	-3.0	7.8
4 d	6.341	± 9.2	12.4	-14.5	10.9	-12.8	5.8	-6.9	± 3.3	3.8	1.7	1.6	-4.1	11.8
	exclusive $k_\perp$ jet algorithm													
1 a	7.100	± 8.6	18.5	-13.5	15.9	-11.5	9.4	-7.2	± 4.7	2.7	3.4	6.7	-2.9	9.8
1 b	5.829	± 9.9	17.3	-19.9	14.3	-16.8	9.6	-10.7	± 8.6	0.7	2.5	3.1	-5.7	14.8
1 c	5.464	± 11.7	22.0	-20.6	18.7	-17.2	11.7	-11.3	± 8.6	3.0	4.3	5.8	-4.9	28.4
1 d	0.712	± 25.7	31.3	-37.8	29.9	-35.4	9.2	-13.2	± 0.4	6.6	5.3	3.3	-10.0	96.3
2 a	7.495	± 7.7	12.1	-11.5	11.1	-10.5	4.7	-4.7	± 2.7	0.2	0.7	3.4	-3.5	7.4
2 b	7.192	± 7.8	12.8	-11.4	11.6	-10.6	5.4	-4.3	± 0.1	1.5	1.3	4.8	-3.5	10.7
2 c	5.189	± 9.8	13.1	-13.5	12.3	-12.7	4.5	-4.8	± 1.3	2.1	1.4	3.1	-3.6	21.0
2 d	3.467	± 12.1	20.6	-19.9	18.3	-17.5	9.5	-9.5	± 4.9	4.8	1.7	6.2	-6.1	43.5
3 a	8.098	± 7.8	14.0	-12.8	12.5	-11.5	6.2	-5.7	± 1.3	1.0	2.1	5.4	-4.8	7.0
3 b	11.820	± 6.3	11.2	-10.7	10.4	-9.7	4.1	-4.4	± 0.0	0.6	1.5	3.4	-3.8	7.6
3 c	9.126	± 7.5	13.2	-9.3	11.8	-8.6	5.8	-3.5	± 0.6	1.5	2.0	5.0	-2.0	10.0
3 d	7.847	± 8.7	15.1	-14.8	13.4	-13.0	7.0	-7.2	± 2.1	5.1	1.3	3.9	-4.2	17.5
4 a	5.682	± 9.4	13.6	-15.7	12.5	-14.3	5.3	-6.5	± 0.8	1.4	1.0	4.7	-6.0	3.6
4 b	9.294	± 7.3	11.6	-11.3	10.2	-10.0	5.4	-5.4	± 4.0	0.8	1.2	3.0	-2.9	3.8
4 c	8.702	± 7.7	12.6	-9.5	11.3	-8.7	5.7	-3.9	± 1.9	1.9	1.7	4.4	-1.6	3.2
4 d	12.454	± 6.5	8.7	-8.9	8.0	-8.2	3.4	-3.7	± 1.3	1.7	0.4	2.1	-2.5	10.8
	Cambridge jet algorithm													
1 a	5.002	± 11.1	19.3	-17.2	16.5	-14.5	10.2	-9.3	± 8.0	3.3	2.6	4.4	-1.9	13.4
1 b	4.459	± 11.8	16.8	-19.7	15.2	-17.9	7.2	-8.2	± 3.7	1.9	3.0	4.9	-6.2	15.0
1 c	3.722	± 13.8	26.7	-25.1	22.1	-20.4	14.9	-14.5	± 12.6	3.2	4.6	5.4	-4.3	28.2
1 d	0.740	± 26.6	32.2	-33.9	30.1	-31.2	11.5	-13.2	± 8.3	7.6	0.1	2.3	-6.8	104.2
2 a	4.490	± 10.4	20.1	-21.3	16.0	-17.2	12.0	-12.6	± 11.3	1.1	3.0	2.2	-4.3	12.5
2 b	6.488	± 8.6	12.7	-12.7	11.7	-11.7	4.9	-5.0	± 1.2	0.2	1.7	4.2	-4.3	13.3
2 c	4.057	± 11.2	15.6	-15.1	14.6	-14.2	5.6	-5.3	± 3.0	1.4	0.3	4.3	-3.8	21.0
2 d	3.357	± 12.5	21.0	-16.5	19.1	-15.3	8.7	-6.4	± 1.2	4.0	2.9	6.9	-3.6	45.8
3 a	5.275	± 10.0	16.1	-14.6	13.7	-12.3	8.5	-7.9	± 4.5	2.5	5.1	4.2	-2.8	9.8
3 b	9.851	± 7.3	9.2	-14.7	8.6	-13.2	3.3	-6.4	± 1.4	1.1	1.2	2.0	-5.9	10.7
3 c	8.100	± 8.3	15.5	-11.1	13.7	-9.8	7.3	-5.3	± 1.7	2.0	3.5	5.7	-2.5	13.0
3 d	8.145	± 8.5	13.7	-15.3	12.2	-13.7	6.1	-6.7	± 1.2	4.6	0.7	3.5	-4.5	16.5
4 a	4.605	± 10.9	14.4	-16.6	13.3	-15.2	5.5	-6.8	± 2.6	2.2	0.4	4.0	-5.6	5.3
4 b	8.820	± 7.7	13.7	-11.6	12.2	-10.2	6.3	-5.5	± 4.4	0.4	0.5	4.1	-2.8	4.7
4 c	7.421	± 8.3	11.1	-10.2	10.2	-9.5	4.5	-3.9	± 1.8	1.8	1.6	2.9	-2.0	4.1
4 d	11.991	± 6.7	10.9	-10.8	9.4	-9.3	5.5	-5.5	± 4.4	1.7	0.2	2.5	-2.4	11.7

D.1.7 The Dijet Cross Section $d^2\sigma_{\rm dijet}/(dx_{\rm Bj}\,dQ^2)$

bin number	corresponding Q^2 range	$x_{\rm Bj}$ range
1 a	$150 < Q^2 < 200\,{\rm GeV}^2$	$0.003 < x_{\rm Bj} < 0.004$
1 b		$0.004 < x_{\rm Bj} < 0.0055$
1 c		$0.0055 < x_{\rm Bj} < 0.007$
1 d		$0.007 < x_{\rm Bj} < 0.01$
2 a	$200 < Q^2 < 300\,{\rm GeV}^2$	$0.004 < x_{\rm Bj} < 0.0055$
2 b		$0.0055 < x_{\rm Bj} < 0.0075$
2 c		$0.0075 < x_{\rm Bj} < 0.01$
2 d		$0.01 < x_{\rm Bj} < 0.015$
3 a	$300 < Q^2 < 600\,{\rm GeV}^2$	$0.006 < x_{\rm Bj} < 0.009$
3 b		$0.009 < x_{\rm Bj} < 0.012$
3 c		$0.012 < x_{\rm Bj} < 0.017$
3 d		$0.017 < x_{\rm Bj} < 0.03$
4 a	$600 < Q^2 < 5000\,{\rm GeV}^2$	$0.012 < x_{\rm Bj} < 0.023$
4 b		$0.023 < x_{\rm Bj} < 0.035$
4 c		$0.035 < x_{\rm Bj} < 0.06$
4 d		$0.06 < x_{\rm Bj} < 0.2$

the dijet cross section $d^2\sigma_{\rm dijet}/(dx_{\rm Bj}\,dQ^2)$

									single contributions to correlated uncertainty					
bin No.	cross section (in pb)	statistical uncert. (in percent)	total uncertainty (in percent)		uncorrelated uncertainty (in percent)		correlated uncertainty (in percent)		model dep. detector corr. (in percent)	positron energy scale (in percent)	positron polar angle (in percent)	LAr hadr. energy scale (in percent)		hadroniz. correct. (percent)
	inclusive $k_\perp$ jet algorithm													
1 a	6.462	± 8.7	19.5	-20.9	15.7	-17.1	11.5	-11.9	± 10.1	3.3	1.3	3.9	-5.1	4.2
1 b	8.505	± 7.7	15.7	-14.6	13.5	-12.4	8.2	-7.6	± 5.8	2.2	1.5	4.9	-3.8	5.9
1 c	5.500	± 10.5	15.2	-17.1	12.7	-14.5	8.3	-9.1	± 3.5	3.5	5.8	2.9	-4.7	6.9
1 d	5.876	± 11.1	15.2	-15.0	12.9	-12.6	8.1	-8.2	± 0.5	2.4	7.1	2.5	-2.8	7.6
2 a	5.934	± 8.8	12.6	-13.9	11.1	-12.4	5.8	-6.3	± 3.0	1.0	3.2	3.4	-4.1	4.2
2 b	8.896	± 7.1	10.6	-11.7	9.6	-10.5	4.4	-5.2	± 2.2	1.6	0.9	3.0	-4.0	5.9
2 c	8.057	± 7.5	13.4	-13.6	11.9	-12.0	6.2	-6.3	± 2.3	3.2	1.2	4.4	-4.6	6.2
2 d	6.328	± 8.2	12.6	-15.1	11.2	-13.3	5.9	-7.1	± 4.0	0.9	1.7	3.6	-5.3	7.3
3 a	6.346	± 8.9	11.6	-13.0	10.8	-12.1	4.2	-4.9	± 2.3	0.6	0.1	3.1	-4.0	4.5
3 b	9.304	± 7.4	10.8	-13.1	9.5	-11.5	5.2	-6.3	± 0.2	1.8	3.7	2.9	-4.5	4.5
3 c	10.764	± 6.8	11.1	-10.5	10.1	-9.6	4.6	-4.2	± 0.1	1.0	0.7	4.1	-3.7	6.3
3 d	6.747	± 8.1	13.3	-11.4	12.1	-10.4	5.6	-4.6	± 1.8	1.1	2.2	4.4	-3.2	7.7
4 a	7.989	± 8.2	14.9	-11.3	13.4	-10.3	6.5	-4.6	± 1.3	2.7	0.5	5.5	-3.1	4.6
4 b	7.345	± 8.2	12.8	-11.6	11.6	-10.7	5.3	-4.6	± 1.2	1.0	1.3	4.7	-3.8	6.2
4 c	8.333	± 7.9	11.5	-11.7	10.3	-10.4	5.0	-5.2	± 3.4	1.3	1.0	3.0	-3.3	6.0
4 d	5.891	± 9.4	12.6	-11.6	11.5	-10.7	5.3	-4.6	± 3.4	2.2	0.6	2.9	-1.5	7.1

the dijet cross section $d^2\sigma_{\mathrm{dijet}}/(dx_{\mathrm{Bj}}\,dQ^2)$

									single contributions to correlated uncertainty					
bin No.	cross section (in pb)	statistical uncert. (in percent)	total uncertainty (in percent)		uncorrelated uncertainty (in percent)		correlated uncertainty (in percent)		model dep. detector corr. (in percent)	positron energy scale (in percent)	positron polar angle (in percent)	LAr hadr. energy scale (in percent)		hadroniz. correct. (percent)
	Aachen jet algorithm													
1 a	6.586	± 8.7	18.1	-20.2	14.7	-16.7	10.6	-11.3	± 9.3	2.6	1.7	3.7	-5.4	8.3
1 b	7.997	± 7.9	15.7	-15.0	13.2	-12.7	8.4	-8.1	± 6.3	2.3	1.8	4.6	-3.9	9.9
1 c	5.325	± 10.7	16.0	-14.8	13.5	-12.5	8.5	-7.9	± 0.5	3.3	6.4	4.2	-2.8	11.3
1 d	6.035	± 11.2	14.7	-14.0	12.7	-11.9	7.5	-7.4	± 0.9	2.7	6.5	1.9	-1.5	12.9
2 a	5.803	± 8.9	13.6	-14.4	11.9	-12.6	6.7	-6.8	± 4.5	0.5	3.0	3.7	-3.8	8.2
2 b	8.832	± 7.2	10.9	-11.1	9.9	-10.0	4.6	-4.8	± 1.0	1.9	1.5	3.5	-3.7	9.7
2 c	7.626	± 7.7	14.1	-12.2	12.6	-11.0	6.4	-5.3	± 1.8	2.8	1.0	5.1	-3.8	10.4
2 d	5.861	± 8.5	12.4	-15.8	10.8	-13.9	5.9	-7.6	± 4.9	0.8	1.3	2.5	-5.4	12.1
3 a	6.351	± 9.0	13.6	-12.0	12.3	-11.1	5.6	-4.7	± 3.1	0.4	0.7	4.4	-3.1	8.4
3 b	8.870	± 7.7	11.2	-13.2	9.9	-11.6	5.4	-6.1	± 1.1	1.4	3.8	3.1	-4.2	8.2
3 c	10.339	± 6.9	10.8	-10.0	9.9	-9.2	4.4	-3.8	± 0.2	0.4	1.0	4.0	-3.3	10.0
3 d	6.463	± 8.3	13.6	-12.4	12.4	-11.2	5.6	-5.3	± 2.3	0.5	2.0	4.5	-4.0	12.0
4 a	7.640	± 8.3	12.2	-12.0	11.1	-11.0	5.0	-4.9	± 1.4	2.4	1.2	3.7	-3.6	7.8
4 b	7.022	± 8.4	12.5	-11.7	11.4	-10.8	5.1	-4.5	± 1.6	0.9	1.4	4.3	-3.6	9.4
4 c	7.522	± 8.3	11.2	-11.9	10.2	-10.8	4.5	-5.0	± 2.8	1.3	1.0	2.8	-3.5	8.5
4 d	5.736	± 9.5	11.3	-11.8	10.5	-11.0	4.0	-4.3	± 2.0	1.9	1.3	2.1	-2.7	9.7
	exclusive $k_\perp$ jet algorithm													
1 a	5.008	± 10.1	19.0	-21.6	16.1	-18.4	10.1	-11.3	± 8.1	1.9	1.8	5.2	-7.3	16.7
1 b	6.633	± 8.9	14.8	-16.4	13.1	-14.5	6.9	-7.8	± 4.6	2.4	0.4	4.3	-5.5	18.7
1 c	3.970	± 12.3	17.8	-16.9	16.2	-15.5	7.4	-6.8	± 0.7	1.9	3.7	5.9	-5.1	22.8
1 d	4.509	± 13.1	20.9	-19.1	17.2	-15.7	11.8	-10.9	± 1.4	5.4	9.0	5.0	-2.2	25.9
2 a	5.208	± 9.7	18.6	-14.1	16.3	-12.3	8.9	-6.9	± 1.8	3.9	3.9	6.6	-3.4	14.9
2 b	7.835	± 7.8	14.0	-14.7	12.3	-12.9	6.6	-7.0	± 3.7	2.9	1.1	4.3	-4.9	16.3
2 c	6.509	± 8.4	12.9	-13.5	11.6	-12.0	5.7	-6.2	± 1.6	4.0	1.0	3.3	-4.1	20.0
2 d	5.279	± 8.9	12.7	-13.5	11.5	-12.1	5.5	-5.9	± 0.7	3.1	2.3	3.5	-4.2	19.7
3 a	6.122	± 9.3	14.0	-12.4	13.1	-11.7	4.8	-4.2	± 1.5	0.2	1.1	4.2	-3.4	11.7
3 b	9.548	± 7.7	17.2	-14.6	14.7	-12.3	8.9	-7.9	± 4.6	3.4	3.0	5.9	-4.3	10.6
3 c	12.862	± 6.3	12.5	-11.3	11.1	-10.0	5.7	-5.2	± 1.9	1.5	1.3	4.8	-4.1	10.9
3 d	9.118	± 7.1	11.3	-10.2	10.1	-9.1	4.9	-4.7	± 0.6	1.8	2.8	3.2	-2.9	10.2
4 a	9.179	± 7.7	11.9	-11.5	10.8	-10.5	5.0	-4.7	± 0.9	1.5	1.9	4.1	-3.7	5.6
4 b	8.962	± 7.4	11.3	-9.7	10.3	-8.8	4.8	-4.1	± 1.7	2.2	1.2	3.5	-2.3	5.8
4 c	10.703	± 7.0	9.0	-11.0	8.4	-10.0	3.1	-4.5	± 0.2	1.0	0.7	2.4	-4.0	5.7
4 d	8.335	± 7.6	11.3	-9.9	10.2	-9.0	4.8	-4.0	± 2.6	1.6	0.4	3.4	-2.1	7.1
	Cambridge jet algorithm													
1 a	3.795	± 12.2	24.3	-26.5	19.6	-21.5	14.5	-15.4	± 13.6	2.1	2.3	3.5	-6.4	21.4
1 b	4.807	± 10.9	18.5	-19.8	15.8	-16.9	9.7	-10.4	± 7.6	1.6	3.3	4.5	-5.8	22.3
1 c	2.543	± 16.0	26.8	-20.0	23.0	-16.8	13.8	-10.9	± 1.5	4.7	9.5	8.5	-0.7	26.5
1 d	3.500	± 15.5	20.2	-20.5	18.0	-18.3	9.0	-9.3	± 2.3	2.4	6.9	4.6	-5.1	28.2
2 a	3.883	± 11.4	19.3	-18.6	16.7	-16.2	9.5	-9.2	± 4.9	2.9	4.6	5.9	-5.4	19.2
2 b	6.338	± 9.1	16.2	-14.9	14.2	-13.0	7.9	-7.3	± 2.7	4.6	2.2	5.1	-4.2	21.1
2 c	4.908	± 9.8	16.2	-14.1	14.5	-12.5	7.3	-6.6	± 3.1	4.4	1.6	4.4	-3.1	22.3
2 d	4.193	± 10.4	15.4	-17.7	13.2	-15.3	7.9	-8.9	± 6.2	2.2	3.1	2.7	-4.9	23.5
3 a	4.729	± 10.8	14.4	-14.5	13.6	-13.7	4.9	-4.8	± 1.5	0.7	0.9	4.2	-4.1	14.7
3 b	8.110	± 8.5	14.4	-16.0	12.1	-13.6	7.7	-8.6	± 1.7	3.4	5.2	3.9	-5.4	13.9
3 c	10.917	± 7.2	13.6	-13.8	12.0	-12.2	6.4	-6.3	± 3.8	1.1	1.1	4.7	-4.6	13.0
3 d	8.043	± 7.9	11.2	-11.2	10.2	-10.0	4.7	-4.8	± 0.7	2.5	2.4	2.8	-2.9	11.1
4 a	7.739	± 8.6	12.6	-11.1	11.7	-10.4	4.8	-3.9	± 0.3	1.4	0.5	4.3	-3.2	6.5
4 b	8.848	± 7.7	11.9	-10.7	10.7	-9.7	5.1	-4.4	± 2.2	1.6	1.1	3.9	-2.9	6.8
4 c	9.481	± 7.5	10.0	-10.2	9.4	-9.5	3.4	-3.8	± 1.1	0.4	0.8	2.7	-3.2	6.9
4 d	7.443	± 8.2	10.4	-10.2	9.5	-9.4	4.1	-4.0	± 2.7	1.7	0.2	2.1	-1.8	8.2

D.1.8 The Dijet Cross Section $d^2\sigma_{\rm dijet}/(dy\,dQ^2)$

bin number	corresponding Q^2 range
1	$150 < Q^2 < 200\,{\rm GeV}^2$
2	$200 < Q^2 < 300\,{\rm GeV}^2$
3	$300 < Q^2 < 600\,{\rm GeV}^2$
4	$600 < Q^2 < 5000\,{\rm GeV}^2$

letter	corresponding y range
a	$0.2 < y < 0.3$
b	$0.3 < y < 0.4$
c	$0.4 < y < 0.5$
d	$0.5 < y < 0.6$

the dijet cross section $d^2\sigma_{\rm dijet}/(dy\,dQ^2)$														
									single contributions to correlated uncertainty					
bin No.	cross section (in pb)	statistical uncert. (in percent)	total uncertainty (in percent)		uncorrelated uncertainty (in percent)		correlated uncertainty (in percent)		model dep. detector corr. (in percent)	positron energy scale (in percent)	positron polar angle (in percent)	LAr hadr. energy scale (in percent)		hadroniz. correct. (percent)
	inclusive $k_\perp$ jet algorithm													
1 a	8.403	± 9.5	14.4	-13.1	12.2	-11.0	7.7	-7.1	± 4.5	2.9	4.4	2.9	-0.8	7.6
1 b	7.183	± 8.5	12.5	-18.2	11.4	-16.2	5.2	-8.2	± 2.3	1.8	1.7	3.6	-7.3	6.6
1 c	5.646	± 9.1	16.6	-16.3	14.2	-14.0	8.5	-8.3	± 6.8	0.9	1.6	4.6	-4.1	5.1
1 d	5.470	± 9.5	17.9	-18.6	14.8	-15.6	10.1	-10.2	± 8.7	1.0	3.1	3.7	-4.0	4.0
2 a	9.299	± 6.9	11.8	-12.9	10.3	-11.3	5.8	-6.4	± 3.8	1.6	1.6	3.6	-4.4	7.4
2 b	8.245	± 7.4	11.7	-13.5	10.7	-12.2	4.5	-5.7	± 1.4	1.1	0.2	3.8	-5.2	6.0
2 c	6.272	± 8.4	12.5	-11.9	11.3	-10.8	5.3	-5.0	± 2.8	0.8	1.3	3.9	-3.5	5.3
2 d	6.046	± 8.9	12.1	-14.3	11.0	-13.0	4.9	-6.1	± 3.6	1.0	0.0	2.9	-4.6	4.0
3 a	10.099	± 6.6	10.8	-9.0	9.9	-8.3	4.4	-3.6	± 0.8	0.9	1.6	3.7	-2.6	7.4
3 b	8.959	± 7.5	12.3	-12.7	11.0	-11.4	5.4	-5.5	± 0.3	0.5	2.4	4.5	-4.6	6.0
3 c	8.512	± 7.7	11.1	-13.6	10.2	-12.3	4.4	-5.7	± 0.9	1.4	1.6	3.5	-5.1	4.5
3 d	5.805	± 9.5	12.6	-13.5	11.6	-12.4	5.0	-5.3	± 2.3	2.5	1.7	3.0	-3.4	4.2
4 a	9.624	± 7.4	11.7	-11.7	10.6	-10.6	4.9	-5.0	± 0.9	1.6	1.2	4.2	-4.2	7.4
4 b	7.384	± 8.2	11.5	-9.6	10.7	-9.2	4.2	-3.0	± 1.2	0.6	0.9	3.6	-2.1	5.7
4 c	6.266	± 8.9	13.4	-11.9	12.2	-11.0	5.4	-4.4	± 2.1	1.2	0.7	4.5	-3.3	5.2
4 d	6.359	± 9.3	13.0	-12.0	11.7	-10.8	5.7	-5.2	± 2.9	1.0	2.9	3.6	-2.6	4.5

the dijet cross section $d^2\sigma_{\mathrm{dijet}}/(dy\,dQ^2)$															
									single contributions to correlated uncertainty						
bin No.	cross section (in pb)	statistical uncert. (in percent)	total uncertainty (in percent)		uncorrelated uncertainty (in percent)		correlated uncertainty (in percent)		model dep. detector corr. (in percent)	positron energy scale (in percent)	positron polar angle (in percent)	LAr hadr. energy scale (in percent)		hadroniz. correct. (percent)
	Aachen jet algorithm													
1 a	8.473	± 9.5	14.7	-13.1	12.6	-11.0	7.7	-7.0	± 4.4	3.1	4.3	3.2	0.2	13.0
1 b	6.978	± 8.7	12.8	-14.6	11.6	-13.1	5.4	-6.5	± 1.6	1.6	2.4	4.1	-5.4	10.8
1 c	5.324	± 9.4	16.1	-16.0	13.8	-13.8	8.3	-8.1	± 6.8	0.4	1.4	4.2	-3.9	8.9
1 d	5.507	± 9.5	17.0	-19.7	14.2	-16.7	9.4	-10.3	± 8.2	1.0	2.3	3.6	-5.6	8.0
2 a	8.453	± 7.1	11.5	-13.0	10.1	-11.3	5.6	-6.3	± 3.8	1.7	1.5	3.0	-4.2	12.2
2 b	8.064	± 7.5	11.7	-12.0	10.7	-11.0	4.7	-4.8	± 0.7	1.3	1.1	4.1	-4.2	10.2
2 c	6.414	± 8.3	12.3	-11.8	11.1	-10.7	5.2	-4.9	± 2.8	0.7	1.5	3.8	-3.3	9.2
2 d	5.820	± 9.1	13.9	-14.3	12.4	-12.9	6.2	-6.3	± 4.3	1.0	0.5	4.0	-4.2	7.6
3 a	9.770	± 6.7	11.4	-9.4	10.3	-8.6	4.7	-3.8	± 1.3	1.0	1.3	3.9	-2.8	11.7
3 b	8.231	± 7.8	11.3	-13.2	10.3	-11.9	4.7	-5.7	± 0.1	0.5	2.5	3.7	-4.9	9.8
3 c	8.476	± 7.8	12.6	-12.2	11.5	-11.2	5.1	-5.0	± 0.5	1.1	1.7	4.4	-4.2	7.9
3 d	5.761	± 9.7	13.7	-12.7	12.5	-11.8	5.5	-4.7	± 2.7	1.9	1.3	4.0	-2.7	8.1
4 a	9.320	± 7.5	11.0	-12.3	10.1	-11.2	4.4	-5.1	± 0.6	1.1	1.3	3.7	-4.6	10.5
4 b	7.024	± 8.4	11.1	-9.6	10.4	-9.1	4.1	-3.0	± 1.9	0.9	0.8	3.1	-1.4	8.7
4 c	5.681	± 9.3	12.7	-13.5	11.7	-12.4	4.9	-5.3	± 2.1	1.4	1.3	3.7	-4.2	8.1
4 d	5.972	± 9.5	11.5	-12.5	10.6	-11.4	4.4	-5.0	± 2.0	0.7	2.6	2.4	-3.4	7.2
	exclusive $k_\perp$ jet algorithm													
1 a	6.387	± 11.1	18.1	-15.2	15.6	-13.1	9.2	-7.6	± 3.6	3.9	5.0	5.5	-1.6	25.5
1 b	4.991	± 10.3	15.0	-17.1	13.8	-15.5	5.8	-7.2	± 0.8	0.5	2.5	4.9	-6.5	21.4
1 c	4.590	± 10.3	16.9	-19.1	14.6	-16.5	8.5	-9.6	± 6.4	1.9	2.6	4.3	-6.2	18.0
1 d	4.422	± 10.8	17.8	-19.1	15.8	-17.0	8.2	-8.8	± 5.4	1.1	1.1	5.7	-6.6	15.5
2 a	7.715	± 7.6	13.0	-11.1	11.4	-9.8	6.1	-5.2	± 1.0	3.6	1.9	4.2	-2.7	20.8
2 b	6.798	± 8.0	12.8	-15.4	11.7	-13.8	5.3	-6.8	± 3.1	0.6	0.5	3.9	-5.8	18.6
2 c	5.521	± 9.1	12.1	-12.8	11.1	-11.8	4.7	-5.0	± 2.0	0.9	2.3	3.1	-3.5	16.0
2 d	5.446	± 9.8	19.4	-14.6	17.7	-13.4	7.9	-5.8	± 1.8	0.8	1.5	7.4	-5.0	13.4
3 a	12.822	± 6.0	12.4	-9.7	11.0	-8.5	5.6	-4.6	± 1.0	2.6	1.6	4.3	-2.9	12.3
3 b	9.903	± 7.3	14.0	-14.1	12.1	-12.1	7.2	-7.2	± 5.0	1.0	1.7	4.5	-4.5	10.5
3 c	9.239	± 7.8	14.3	-12.1	12.8	-10.8	6.3	-5.4	± 3.0	1.4	1.4	5.0	-3.8	9.8
3 d	5.959	± 9.8	13.7	-13.7	12.7	-12.7	5.2	-5.1	± 1.4	1.7	2.5	3.7	-3.6	9.5
4 a	12.784	± 6.2	10.7	-9.1	9.7	-8.3	4.5	-3.6	± 0.7	0.8	0.8	4.1	-3.0	7.1
4 b	9.431	± 7.3	9.5	-8.3	8.8	-7.8	3.4	-2.7	± 1.3	1.4	0.3	2.4	-1.2	5.9
4 c	7.670	± 8.3	11.0	-12.5	10.2	-11.5	4.1	-4.9	± 0.6	1.7	0.8	3.2	-4.2	5.4
4 d	7.201	± 8.6	11.0	-12.5	10.3	-11.4	4.0	-5.0	± 0.3	0.8	2.0	3.0	-4.3	4.9
	Cambridge jet algorithm													
1 a	4.598	± 13.6	19.8	-17.1	17.4	-15.0	9.5	-8.1	± 4.6	2.7	5.7	5.3	-1.9	27.9
1 b	3.396	± 12.8	21.0	-19.5	18.9	-17.3	9.2	-8.8	± 6.0	0.5	2.7	6.2	-5.7	25.2
1 c	3.384	± 12.8	22.5	-23.5	18.9	-19.8	12.3	-12.7	± 11.0	1.1	2.2	4.7	-5.8	21.3
1 d	3.380	± 13.0	18.8	-20.1	16.8	-17.9	8.5	-9.3	± 6.7	1.5	2.0	4.3	-5.8	20.9
2 a	5.746	± 9.0	15.1	-14.4	13.0	-12.3	7.8	-7.5	± 4.9	3.4	3.0	3.8	-3.0	24.0
2 b	5.453	± 9.4	14.3	-15.7	13.0	-14.1	6.1	-7.0	± 2.8	2.3	1.9	4.2	-5.4	22.2
2 c	4.675	± 10.4	15.3	-14.2	13.8	-12.9	6.5	-5.9	± 3.1	1.0	2.8	4.7	-3.7	19.9
2 d	3.965	± 11.7	20.5	-18.5	18.3	-16.4	9.4	-8.7	± 6.1	2.7	1.8	6.2	-5.1	18.6
3 a	11.075	± 6.7	12.0	-11.6	10.6	-10.2	5.7	-5.6	± 0.5	3.8	1.4	3.6	-3.5	13.6
3 b	8.306	± 8.1	14.2	-14.7	12.7	-13.2	6.4	-6.5	± 1.7	1.4	2.8	5.1	-5.3	13.0
3 c	7.734	± 8.9	13.3	-12.3	11.8	-10.9	6.0	-5.6	± 4.3	1.8	1.3	3.2	-2.4	12.5
3 d	4.897	± 11.0	13.9	-18.8	13.0	-17.3	4.8	-7.3	± 2.3	0.4	2.3	3.0	-6.3	12.4
4 a	12.312	± 6.5	9.4	-8.7	8.7	-8.1	3.6	-3.3	± 0.8	0.8	0.5	3.1	-2.6	7.9
4 b	8.330	± 7.9	10.3	-9.3	9.6	-8.7	3.8	-3.1	± 0.5	1.9	0.5	2.7	-1.8	7.4
4 c	6.724	± 8.9	11.9	-12.2	11.2	-11.3	4.1	-4.5	± 1.2	1.2	0.6	3.3	-3.8	6.5
4 d	6.084	± 9.6	13.2	-13.0	12.2	-12.0	5.0	-5.0	± 1.6	0.6	2.1	3.9	-3.9	5.7

D.1.9 The Dijet Cross Section $d^2\sigma_{\mathrm{dijet}}/(d\eta'\, d\overline{E}_T)$

bin number	corresponding $\overline{E}_T$ range
1	$8.5 < \overline{E}_T < 12\,\mathrm{GeV}$
2	$12 < \overline{E}_T < 17\,\mathrm{GeV}$
3	$17 < \overline{E}_T < 35\,\mathrm{GeV}$

letter	corresponding η' range
a	$0.0 < \eta' < 0.2$
b	$0.2 < \eta' < 0.45$
c	$0.45 < \eta' < 0.8$
d	$0.8 < \eta' < 1.5$

the dijet cross section $d^2\sigma_{\mathrm{dijet}}/(d\eta'\, d\overline{E}_T)$														
									single contributions to correlated uncertainty					
bin No.	cross section (in pb)	statistical uncert. (in percent)	total uncertainty (in percent)		uncorrelated uncertainty (in percent)		correlated uncertainty (in percent)		model dep. detector corr. (in percent)	positron energy scale (in percent)	positron polar angle (in percent)	LAr hadr. energy scale (in percent)		hadroniz. correct. (percent)
	inclusive $k_\perp$ jet algorithm													
1 a	11.854	± 6.5	8.8	-9.4	8.1	-8.6	3.5	-3.8	± 1.5	1.3	1.1	2.2	-2.6	6.6
1 b	15.894	± 5.7	12.4	-12.8	10.1	-10.5	7.2	-7.4	± 6.4	0.5	1.6	2.6	-3.1	6.9
1 c	17.329	± 5.4	9.8	-8.4	8.7	-7.5	4.6	-3.7	± 1.5	1.8	0.9	3.5	-2.2	6.4
1 d	18.605	± 5.4	9.3	-11.3	8.2	-9.9	4.4	-5.4	± 1.4	2.0	0.9	3.2	-4.5	8.3
2 a	8.399	± 7.8	14.4	-11.5	13.0	-10.5	6.3	-4.6	± 0.6	1.3	1.7	5.7	-3.8	5.4
2 b	9.423	± 7.1	9.8	-10.3	9.1	-9.4	3.7	-4.1	± 0.9	0.1	1.3	3.0	-3.4	4.6
2 c	9.421	± 7.0	15.3	-18.9	12.1	-15.5	9.4	-10.8	± 8.9	1.6	1.4	1.8	-5.5	2.6
2 d	7.632	± 8.6	16.8	-15.9	15.0	-14.1	7.6	-7.2	± 2.9	2.6	0.3	6.3	-5.9	4.3
3 a	5.166	± 9.4	16.8	-17.6	14.3	-15.0	8.8	-9.1	± 7.3	1.2	0.3	4.5	-5.1	4.2
3 b	5.534	± 9.2	16.0	-15.0	14.5	-13.6	6.8	-6.4	± 2.0	0.7	1.7	6.1	-5.6	3.4
3 c	6.390	± 8.8	16.0	-12.4	14.2	-11.0	7.4	-5.6	± 4.4	1.4	0.7	5.5	-2.7	4.2
3 d	2.779	± 14.4	24.3	-23.9	21.8	-21.5	10.6	-10.5	± 5.5	0.6	1.4	8.8	-8.6	5.1

the dijet cross section $d^2\sigma_{\rm dijet}/(d\eta'\, d\overline{E}_T)$

									single contributions to correlated uncertainty					
bin No.	cross section (in pb)	statistical uncert. (in percent)	total uncertainty (in percent)		uncorrelated uncertainty (in percent)		correlated uncertainty (in percent)		model dep. detector corr. (in percent)	positron energy scale (in percent)	positron polar angle (in percent)	LAr hadr. energy scale (in percent)		hadroniz. correct. (percent)
Aachen jet algorithm														
1 a	11.678	± 6.6	9.1	-9.2	8.2	-8.4	3.8	-3.8	± 2.5	1.1	1.1	1.9	-1.9	9.7
1 b	15.227	± 5.8	8.4	-12.3	7.1	-10.6	4.5	-6.1	± 3.3	2.0	1.6	0.8	-4.2	9.8
1 c	16.716	± 5.5	10.0	-8.3	8.9	-7.5	4.5	-3.6	± 0.1	1.6	1.6	3.6	-2.4	9.7
1 d	17.958	± 5.5	9.8	-9.8	8.7	-8.8	4.5	-4.3	± 1.3	1.2	1.0	3.7	-3.5	12.8
2 a	7.741	± 8.0	13.7	-12.5	12.2	-11.3	6.2	-5.3	± 2.3	1.8	1.4	5.0	-3.9	8.8
2 b	8.986	± 7.2	12.9	-10.3	11.8	-9.4	5.2	-4.0	± 0.5	1.1	1.2	4.7	-3.3	8.8
2 c	9.391	± 7.1	14.4	-16.6	11.5	-13.6	8.6	-9.4	± 7.9	0.7	1.4	2.5	-4.7	7.1
2 d	6.814	± 9.2	15.1	-12.2	13.6	-11.2	6.6	-4.9	± 3.5	1.3	0.2	5.3	-2.9	10.0
3 a	5.085	± 9.6	17.9	-17.5	15.5	-15.1	9.0	-8.9	± 6.9	1.0	0.6	5.4	-5.2	7.8
3 b	5.309	± 9.4	15.6	-14.1	14.0	-12.7	7.0	-6.1	± 3.4	0.4	2.0	5.6	-4.4	7.0
3 c	6.290	± 9.0	16.8	-15.2	14.8	-13.5	7.8	-7.1	± 5.1	0.9	0.4	5.7	-4.7	7.5
3 d	2.491	± 14.9	21.9	-26.0	20.0	-23.4	8.9	-11.4	± 4.8	2.0	1.4	7.0	-9.9	10.6
exclusive $k_\perp$ jet algorithm														
1 a	9.032	± 8.2	13.3	-10.8	12.2	-10.0	5.3	-4.2	± 3.0	0.2	1.2	3.9	-2.3	10.9
1 b	10.995	± 7.3	12.5	-12.2	10.5	-10.3	6.7	-6.7	± 5.8	1.4	1.5	2.4	-2.2	12.5
1 c	11.991	± 6.8	15.1	-11.9	12.7	-9.8	8.1	-6.7	± 6.1	1.3	1.5	4.7	-1.2	12.7
1 d	10.190	± 6.9	13.5	-14.5	11.7	-12.5	6.7	-7.3	± 4.5	2.7	0.5	3.9	-4.8	15.9
2 a	9.223	± 7.6	14.7	-11.8	13.0	-10.7	6.8	-5.1	± 2.9	0.9	1.0	5.8	-3.6	8.2
2 b	9.834	± 6.8	9.8	-10.9	8.8	-9.6	4.4	-5.2	± 3.8	1.1	1.2	0.8	-2.9	6.9
2 c	10.784	± 6.7	14.4	-16.1	11.8	-13.4	8.2	-8.9	± 7.4	0.7	0.7	3.2	-4.6	5.6
2 d	9.153	± 7.5	13.3	-13.1	11.9	-11.6	5.9	-5.9	± 2.6	1.8	0.8	4.7	-4.7	7.7
3 a	5.941	± 9.0	15.4	-17.6	13.4	-15.2	7.7	-8.8	± 6.3	0.1	0.2	4.1	-5.9	8.2
3 b	5.768	± 9.1	17.6	-13.6	15.7	-12.4	7.9	-5.6	± 2.4	0.5	2.1	7.1	-4.3	8.7
3 c	6.769	± 8.7	17.0	-14.0	14.9	-12.3	8.1	-6.6	± 4.5	1.5	1.1	6.2	-4.1	7.5
3 d	3.224	± 12.9	24.7	-20.7	22.3	-18.9	10.7	-8.4	± 2.9	1.1	0.7	10.2	-7.7	11.4
Cambridge jet algorithm														
1 a	7.686	± 8.8	12.6	-11.9	11.4	-10.7	5.5	-5.2	± 4.0	1.1	1.2	3.0	-2.4	10.7
1 b	9.601	± 8.0	11.7	-10.9	10.2	-9.4	5.7	-5.4	± 3.6	3.0	1.9	1.9	-0.8	13.3
1 c	9.748	± 7.7	16.2	-12.6	14.0	-10.7	8.2	-6.7	± 6.0	0.4	1.2	5.3	-2.3	18.3
1 d	7.618	± 8.8	12.7	-12.6	11.7	-11.5	4.9	-5.2	± 2.4	2.4	1.1	3.1	-3.5	30.7
2 a	7.522	± 8.3	16.1	-11.3	14.4	-10.4	7.3	-4.6	± 1.8	1.7	1.6	6.5	-3.1	6.8
2 b	8.744	± 7.4	9.6	-16.9	8.5	-14.9	4.3	-7.9	± 3.9	0.8	1.1	-0.1	-6.6	7.1
2 c	9.269	± 7.6	19.3	-20.0	15.0	-15.6	12.2	-12.5	± 11.9	1.3	0.7	2.0	-3.2	6.4
2 d	6.078	± 9.9	18.4	-14.1	16.6	-12.9	8.1	-5.6	± 1.7	2.0	1.5	7.3	-4.5	10.1
3 a	4.990	± 10.1	18.1	-16.5	15.7	-14.3	8.9	-8.2	± 6.8	1.3	0.7	5.4	-4.1	8.1
3 b	5.346	± 9.6	18.2	-14.1	16.2	-12.6	8.4	-6.2	± 2.9	0.9	3.0	7.1	-4.4	6.9
3 c	5.517	± 9.6	17.8	-19.4	15.6	-17.1	8.5	-9.3	± 5.4	1.0	0.9	6.3	-7.3	7.1
3 d	2.408	± 15.7	21.1	-23.0	19.4	-21.1	8.2	-9.1	± 3.5	4.0	1.6	5.8	-7.0	11.0

D.1.10 The Dijet Cross Section $d^2\sigma_{\mathrm{dijet}}/(d\eta'\,dQ^2)$

bin number	corresponding Q^2 range
1	$150 < Q^2 < 200\,\mathrm{GeV}^2$
2	$200 < Q^2 < 300\,\mathrm{GeV}^2$
3	$300 < Q^2 < 600\,\mathrm{GeV}^2$
4	$600 < Q^2 < 5000\,\mathrm{GeV}^2$

letter	corresponding range
a	$0.0 < \eta' < 0.2$
b	$0.2 < \eta' < 0.4$
b	$0.4 < \eta' < 0.6$
c	$0.6 < \eta' < 0.9$
d	$0.9 < \eta' < 1.5$

the dijet cross section $d^2\sigma_{\mathrm{dijet}}/(d\eta'\,dQ^2)$

									single contributions to correlated uncertainty				
bin No.	cross section (in pb)	statistical uncert. (in percent)	total uncertainty (in percent)		uncorrelated uncertainty (in percent)		correlated uncertainty (in percent)		model dep. detector corr. (in percent)	positron energy scale (in percent)	positron polar angle (in percent)	LAr hadr. energy scale (in percent)		hadroniz. correct. (percent)
	inclusive $k_\perp$ jet algorithm													
1 a	4.831	± 10.4	16.2	-14.7	14.3	-12.9	7.7	-6.9	± 5.2	1.3	3.1	4.3	-2.7	7.8
1 b	7.096	± 9.2	13.3	-15.6	11.6	-13.7	6.6	-7.4	± 3.6	0.7	4.4	2.9	-4.6	5.8
1 c	4.398	± 11.1	28.9	-30.4	22.0	-23.6	18.7	-19.3	± 18.3	1.3	2.5	2.6	-5.3	5.0
1 d	6.264	± 9.5	13.9	-15.5	12.8	-14.3	5.2	-6.0	± 1.2	0.4	1.6	4.6	-5.4	3.4
1 e	4.049	± 11.8	15.9	-14.2	14.6	-13.2	6.2	-5.2	± 3.1	1.9	2.5	4.2	-2.4	7.9
2 a	7.344	± 7.8	11.9	-12.4	10.6	-11.0	5.5	-5.7	± 3.7	1.8	0.9	3.1	-3.5	5.3
2 b	6.374	± 8.4	14.3	-14.3	12.7	-12.7	6.7	-6.5	± 4.2	1.2	1.5	4.6	-4.4	5.7
2 c	4.554	± 9.5	14.6	-16.7	12.5	-14.4	7.6	-8.5	± 6.6	2.4	1.4	2.0	-4.3	5.3
2 d	6.444	± 8.4	12.1	-12.5	11.2	-11.5	4.7	-5.0	± 1.2	1.1	0.9	4.1	-4.4	4.9
2 e	5.388	± 10.2	16.3	-18.5	14.8	-16.6	7.0	-8.2	± 3.1	0.9	1.5	5.8	-7.3	8.1
3 a	7.342	± 8.2	11.2	-13.1	10.3	-12.0	4.3	-5.3	± 0.1	0.4	2.2	3.4	-4.5	4.4
3 b	6.953	± 8.3	12.0	-10.3	10.9	-9.5	4.9	-4.1	± 0.4	1.9	2.3	3.6	-2.3	5.1
3 c	5.992	± 8.8	12.7	-14.3	11.5	-13.1	5.4	-5.8	± 0.5	1.2	3.1	3.9	-4.4	5.5
3 d	6.890	± 8.3	13.3	-11.4	12.1	-10.5	5.4	-4.3	± 1.1	0.4	1.9	4.7	-3.3	5.0
3 e	5.967	± 9.4	13.2	-16.0	11.8	-14.1	6.1	-7.5	± 5.3	0.8	1.0	2.3	-5.0	8.3
4 a	6.051	± 9.3	14.3	-11.9	13.0	-11.1	5.9	-4.5	± 0.9	2.7	0.9	4.9	-3.0	5.4
4 b	5.756	± 9.0	12.7	-12.6	11.6	-11.4	5.3	-5.3	± 3.8	0.4	1.5	3.0	-3.1	6.0
4 c	4.886	± 10.0	12.7	-12.4	11.8	-11.6	4.5	-4.4	± 2.7	0.9	1.3	2.9	-2.8	5.4
4 d	6.859	± 9.0	14.7	-14.7	12.7	-12.7	7.5	-7.4	± 6.0	2.2	1.0	3.5	-3.4	3.9
4 e	5.955	± 9.9	16.7	-13.6	14.9	-12.4	7.5	-5.7	± 2.9	2.0	1.9	6.1	-3.7	7.6

the dijet cross section $d^2\sigma_{\rm dijet}/(d\eta'\,dQ^2)$

									single contributions to correlated uncertainty					
bin No.	cross section (in pb)	statistical uncert. (in percent)	total uncertainty (in percent)		uncorrelated uncertainty (in percent)		correlated uncertainty (in percent)		model dep. detector corr. (in percent)	positron energy scale (in percent)	positron polar angle (in percent)	LAr hadr. energy scale (in percent)		hadroniz. correct. (percent)
	Aachen jet algorithm													
1 a	4.908	± 10.4	13.3	-13.6	12.1	-12.4	5.4	-5.5	± 3.9	0.4	2.3	2.6	-2.7	11.8
1 b	6.798	± 9.4	12.2	-13.6	11.4	-12.5	4.5	-5.4	± 0.7	1.0	2.7	3.0	-4.2	10.5
1 c	4.488	± 11.1	26.7	-26.1	20.9	-20.4	16.5	-16.3	± 15.4	0.7	3.1	4.8	-3.9	8.9
1 d	5.780	± 9.8	14.2	-14.6	13.0	-13.5	5.5	-5.6	± 0.4	0.9	2.1	4.8	-4.8	7.3
1 e	4.063	± 11.9	19.9	-18.2	16.7	-15.2	10.7	-10.0	± 8.7	2.5	3.5	4.3	-1.7	13.8
2 a	6.983	± 8.0	14.0	-12.2	12.3	-10.7	6.7	-5.8	± 4.8	1.5	0.5	4.1	-2.4	8.9
2 b	5.874	± 8.7	12.2	-14.6	10.9	-13.0	5.5	-6.5	± 2.7	2.2	2.5	3.1	-4.7	8.8
2 c	4.717	± 9.4	14.0	-15.2	12.3	-13.4	6.7	-7.2	± 3.6	3.5	2.4	3.5	-4.3	8.7
2 d	5.978	± 8.8	10.6	-13.6	10.0	-12.4	3.4	-5.5	± 0.0	1.8	0.9	2.4	-4.9	10.6
2 e	5.341	± 10.1	18.1	-12.6	16.4	-11.8	7.7	-4.5	± 0.1	0.6	2.3	7.2	-3.5	13.4
3 a	6.925	± 8.3	13.2	-12.6	11.9	-11.4	5.7	-5.5	± 1.6	1.9	2.2	4.3	-4.1	7.3
3 b	6.946	± 8.4	9.9	-11.5	9.2	-10.6	3.5	-4.5	± 1.1	0.4	2.1	2.0	-3.5	8.8
3 c	5.630	± 9.0	13.9	-12.3	12.7	-11.3	5.7	-4.9	± 1.8	0.6	2.7	4.4	-3.3	8.9
3 d	6.767	± 8.6	13.8	-11.6	12.7	-10.9	5.4	-4.0	± 0.4	0.7	0.9	5.0	-3.4	8.6
3 e	5.569	± 9.8	14.5	-14.7	13.1	-13.4	6.1	-6.0	± 4.0	1.1	1.0	4.1	-4.0	14.4
4 a	5.882	± 9.4	12.3	-12.6	11.3	-11.7	4.7	-4.7	± 1.7	1.5	2.0	3.3	-3.3	7.9
4 b	5.201	± 9.6	12.3	-11.7	11.5	-10.9	4.4	-4.1	± 2.0	0.5	1.6	3.1	-2.7	8.6
4 c	4.860	± 10.0	14.9	-15.3	13.0	-13.3	7.2	-7.4	± 6.0	1.7	0.7	3.1	-3.5	7.6
4 d	6.486	± 9.2	15.2	-16.0	13.0	-13.7	8.0	-8.3	± 6.1	2.3	2.6	3.5	-4.2	7.6
4 e	5.657	± 10.1	13.9	-14.4	12.5	-12.9	6.1	-6.3	± 3.3	3.7	0.6	3.0	-3.4	11.2
	exclusive $k_\perp$ jet algorithm													
1 a	4.185	± 12.3	22.4	-19.1	19.5	-16.5	11.1	-9.7	± 8.1	2.2	2.6	6.6	-4.0	24.5
1 b	4.153	± 12.0	14.0	-15.1	13.2	-14.1	4.7	-5.4	± 2.9	0.7	3.0	1.7	-3.1	22.2
1 c	3.866	± 12.1	21.0	-25.0	17.3	-21.1	11.9	-13.5	± 9.4	3.6	4.6	4.2	-7.6	19.3
1 d	4.758	± 11.1	20.7	-21.7	17.5	-18.4	11.2	-11.5	± 9.0	2.3	2.3	5.6	-6.1	15.6
1 e	3.087	± 12.6	20.7	-19.9	18.5	-17.8	9.3	-8.8	± 4.7	4.1	1.3	6.6	-5.9	19.0
2 a	6.998	± 8.5	15.0	-15.9	12.7	-13.5	8.0	-8.3	± 6.4	2.1	2.2	3.6	-4.2	18.3
2 b	4.704	± 9.8	15.0	-13.6	13.9	-12.6	5.8	-5.2	± 1.1	2.4	1.2	4.8	-4.1	18.7
2 c	4.018	± 10.4	13.5	-14.5	12.4	-13.3	5.3	-5.9	± 3.9	1.7	1.4	2.5	-3.6	16.2
2 d	4.694	± 9.8	16.3	-13.3	15.0	-12.4	6.4	-4.8	± 1.9	2.0	0.6	5.5	-3.6	16.3
2 e	4.708	± 9.9	15.4	-16.1	13.9	-14.5	6.5	-7.1	± 2.1	3.0	1.5	5.0	-5.7	17.3
3 a	8.798	± 7.9	13.3	-12.0	11.9	-10.7	5.9	-5.3	± 2.4	1.9	2.1	4.3	-3.6	8.6
3 b	8.655	± 8.0	10.6	-11.0	9.6	-9.9	4.4	-4.7	± 0.3	1.6	2.7	2.7	-3.2	9.9
3 c	6.604	± 8.6	14.0	-12.2	12.7	-11.0	6.1	-5.2	± 3.5	1.6	1.6	4.2	-2.7	9.2
3 d	6.895	± 8.4	12.0	-13.7	11.2	-12.5	4.2	-5.6	± 1.6	1.5	1.4	2.9	-4.7	10.6
3 e	6.238	± 8.7	20.2	-12.1	18.1	-10.9	9.0	-5.2	± 2.1	3.1	1.7	7.8	-2.6	15.8
4 a	9.185	± 7.7	10.1	-10.7	9.1	-9.7	4.3	-4.6	± 1.6	1.1	2.4	2.6	-3.1	5.4
4 b	8.205	± 7.8	11.2	-10.0	10.2	-9.0	4.8	-4.4	± 3.0	2.2	1.2	2.2	-1.2	4.8
4 c	6.175	± 9.0	13.1	-11.2	12.0	-10.5	5.2	-3.9	± 2.6	1.4	0.6	4.0	-2.0	4.6
4 d	7.598	± 8.3	16.6	-14.2	14.7	-12.3	7.9	-7.2	± 5.8	1.4	0.9	4.9	-3.7	5.7
4 e	5.452	± 9.6	11.5	-16.2	10.9	-14.8	3.8	-6.6	± 1.8	2.3	0.7	1.9	-5.7	7.5
	Cambridge jet algorithm													
1 a	3.054	± 14.5	26.5	-25.0	22.5	-20.9	14.1	-13.6	± 11.8	3.7	2.5	6.2	-4.9	24.5
1 b	3.506	± 13.4	17.0	-17.7	14.8	-15.4	8.3	-8.6	± 4.4	2.3	6.4	1.0	-2.5	24.2
1 c	2.436	± 15.7	33.3	-33.3	26.6	-26.6	20.0	-20.0	± 18.9	2.7	2.2	5.4	-5.5	20.5
1 d	3.585	± 13.6	28.5	-27.4	23.8	-22.4	15.7	-15.6	± 13.3	4.2	3.2	6.4	-6.2	20.9
1 e	2.262	± 16.7	27.2	-21.1	24.5	-19.5	11.8	-8.2	± 2.1	1.4	5.4	10.1	-5.4	31.7
2 a	5.166	± 9.8	14.7	-14.4	13.1	-12.7	6.8	-6.7	± 5.3	1.5	1.2	3.5	-3.3	19.0
2 b	4.561	± 10.4	16.1	-14.9	14.8	-13.8	6.3	-5.6	± 2.5	0.2	0.8	5.6	-4.8	19.4
2 c	2.948	± 12.3	15.4	-16.7	14.1	-15.3	6.2	-6.8	± 5.5	0.5	1.3	1.9	-3.5	19.7
2 d	3.737	± 11.3	18.1	-16.7	16.5	-15.2	7.6	-6.8	± 4.0	0.9	1.5	6.0	-5.0	21.4
2 e	3.144	± 13.7	24.3	-19.5	22.1	-17.9	10.1	-7.8	± 0.0	4.8	0.3	8.8	-5.9	30.2
3 a	8.038	± 8.4	14.6	-12.5	12.9	-11.1	6.9	-5.8	± 2.2	2.8	2.7	5.0	-3.4	7.7
3 b	8.147	± 8.5	12.1	-12.9	10.9	-11.6	5.2	-5.7	± 2.4	2.7	2.2	2.7	-3.5	9.8
3 c	5.721	± 9.5	15.6	-16.1	14.2	-14.8	6.3	-6.3	± 2.1	1.8	2.1	5.1	-5.0	12.3
3 d	5.697	± 9.6	11.3	-13.3	10.7	-12.3	3.6	-5.0	± 0.5	2.3	1.3	2.0	-3.9	15.4
3 e	3.912	± 11.3	14.8	-18.3	14.0	-16.7	4.8	-7.3	± 0.5	2.1	0.6	4.0	-6.7	26.4
4 a	8.451	± 8.0	10.9	-9.7	10.1	-9.1	4.1	-3.3	± 1.7	0.6	1.1	3.2	-2.1	4.8
4 b	8.310	± 7.8	9.8	-9.9	9.1	-9.2	3.6	-3.9	± 2.1	1.9	0.8	1.6	-2.1	4.8
4 c	5.741	± 9.4	12.8	-11.8	11.6	-10.8	5.3	-4.7	± 3.7	0.5	1.5	3.2	-2.0	5.0
4 d	6.469	± 9.2	15.1	-14.8	13.4	-13.1	6.9	-6.9	± 5.2	0.5	0.7	4.3	-4.3	7.7
4 e	4.402	± 11.4	13.7	-15.3	13.0	-14.3	4.3	-5.5	± 1.9	0.9	1.3	3.2	-4.7	12.9

D.1.11 The Dijet Cross Section $d^2\sigma_{\rm dijet}/(d\eta_{\rm forwd,lab}\, dQ^2)$

bin number	corresponding Q^2 range
1	$150 < Q^2 < 200\,{\rm GeV}^2$
2	$200 < Q^2 < 300\,{\rm GeV}^2$
3	$300 < Q^2 < 600\,{\rm GeV}^2$
4	$600 < Q^2 < 5000\,{\rm GeV}^2$

letter	corresponding $\eta_{\rm forwd,lab}$ range
a	$-1.0 < \eta_{\rm forwd,lab} < 0.0$
b	$0.0 < \eta_{\rm forwd,lab} < 1.0$
c	$1.0 < \eta_{\rm forwd,lab} < 1.5$
d	$1.5 < \eta_{\rm forwd,lab} < 2.0$
e	$2.0 < \eta_{\rm forwd,lab} < 2.5$

the dijet cross section $d^2\sigma_{\rm dijet}/(d\eta_{\rm forwd,lab}\, dQ^2)$

									single contributions to correlated uncertainty					
bin No.	cross section (in pb)	statistical uncert. (in percent)	total uncertainty (in percent)		uncorrelated uncertainty (in percent)		correlated uncertainty (in percent)		model dep. detector corr. (in percent)	positron energy scale (in percent)	positron polar angle (in percent)	LAr hadr. energy scale (in percent)		hadroniz. correct. (percent)
	inclusive $k_\perp$ jet algorithm													
1 a	0.127	± 51.5	62.3	-62.9	60.7	-61.2	13.9	-14.6	± 10.2	5.1	2.4	7.5	-8.7	84.5
1 b	9.963	± 7.5	18.0	-18.8	14.4	-15.2	10.7	-11.0	± 9.6	0.6	2.0	4.1	-4.7	12.0
1 c	8.073	± 8.2	13.3	-15.2	11.1	-13.0	7.2	-8.0	± 5.8	2.3	2.6	2.2	-4.0	-0.4
1 d	4.999	± 10.7	13.6	-13.2	12.4	-12.1	5.6	-5.4	± 0.6	1.8	3.9	3.3	-2.8	-0.8
1 e	3.842	± 12.7	18.7	-15.1	17.4	-14.3	6.9	-4.6	± 0.1	2.0	1.7	6.2	-3.5	-0.6
2 a	0.409	± 32.1	37.0	-48.2	34.9	-44.5	12.3	-18.5	± 8.1	7.4	3.0	4.5	-14.6	76.3
2 b	10.299	± 6.9	12.6	-13.8	11.1	-12.1	6.0	-6.7	± 4.2	1.1	0.3	3.8	-4.8	12.1
2 c	8.276	± 7.0	11.3	-11.5	10.1	-10.2	5.1	-5.3	± 3.3	0.7	0.5	3.5	-3.7	-0.2
2 d	6.311	± 8.3	10.0	-11.8	9.3	-10.8	3.8	-4.7	± 1.4	1.7	1.8	2.0	-3.4	-0.3
2 e	4.345	± 10.5	16.8	-15.6	15.1	-14.0	7.5	-6.8	± 2.7	2.9	2.1	5.8	-4.9	0.9
3 a	0.120	± 60.3	75.7	-75.6	73.4	-73.4	18.4	-18.3	± 17.1	3.6	5.1	2.6	-1.8	81.5
3 b	11.046	± 7.2	10.7	-11.9	9.7	-10.9	4.5	-4.8	± 0.9	1.4	1.4	3.6	-4.1	11.6
3 c	10.301	± 6.7	11.8	-11.4	10.6	-10.2	5.2	-5.1	± 0.6	0.9	2.4	4.1	-4.1	2.0
3 d	6.833	± 7.9	13.3	-14.2	11.4	-12.2	6.9	-7.3	± 5.8	1.2	0.5	3.0	-4.0	0.7
3 e	4.835	± 9.8	13.8	-11.6	12.6	-10.8	5.7	-4.3	± 2.1	1.0	2.6	4.2	-2.0	2.0
4 b	7.627	± 8.9	14.7	-11.5	13.2	-10.5	6.3	-4.7	± 2.6	2.6	0.9	4.8	-2.3	13.0
4 c	8.136	± 7.7	11.1	-10.9	10.0	-9.7	4.9	-4.8	± 3.5	1.3	0.4	2.8	-2.7	5.0
4 d	8.532	± 7.6	11.5	-9.2	10.5	-8.7	4.5	-3.1	± 0.5	0.3	1.4	3.9	-2.3	3.1
4 e	5.342	± 9.8	14.9	-16.9	13.6	-15.2	6.2	-7.2	± 0.9	1.8	2.2	5.3	-6.4	0.2

the dijet cross section $d^2\sigma_{\mathrm{dijet}}/(d\eta_{\mathrm{forwd,lab}}\,dQ^2)$

									single contributions to correlated uncertainty					
bin No.	cross section (in pb)	statistical uncert. (in percent)	total uncertainty (in percent)		uncorrelated uncertainty (in percent)		correlated uncertainty (in percent)		model dep. detector corr. (in percent)	positron energy scale (in percent)	positron polar angle (in percent)	LAr hadr. energy scale (in percent)		hadroniz. correct. (percent)
	Aachen jet algorithm													
1 a	0.158	± 46.6	51.4	-56.9	49.3	-54.0	14.4	-18.2	± 12.0	3.6	5.1	4.9	-12.1	94.8
1 b	9.610	± 7.7	14.6	-13.4	12.6	-11.5	7.5	-6.9	± 5.3	1.0	1.8	4.6	-3.5	16.9
1 c	7.860	± 8.4	14.1	-15.4	11.7	-12.9	8.0	-8.5	± 6.7	2.4	2.6	2.0	-3.4	3.3
1 d	4.888	± 10.6	14.6	-13.6	13.1	-12.2	6.6	-6.0	± 1.3	2.8	4.0	4.0	-2.9	3.5
1 e	3.868	± 12.9	22.8	-22.1	19.2	-18.6	12.3	-11.9	± 10.8	2.5	0.9	5.0	-4.1	3.2
2 a	0.342	± 34.8	39.9	-41.6	38.3	-40.1	11.0	-11.3	± 1.8	5.3	3.3	8.7	-9.1	91.6
2 b	9.862	± 7.0	13.6	-13.0	12.1	-11.5	6.3	-6.0	± 3.6	1.0	0.3	4.8	-4.4	16.4
2 c	8.009	± 7.1	10.0	-11.8	9.0	-10.7	4.2	-5.1	± 2.6	0.5	0.9	2.7	-4.0	3.6
2 d	6.086	± 8.5	11.2	-11.2	10.2	-10.1	4.7	-4.7	± 3.3	1.5	1.3	2.3	-2.3	3.6
2 e	4.279	± 10.6	13.6	-14.6	12.6	-13.4	5.2	-5.9	± 2.7	2.5	1.5	3.1	-4.0	5.3
3 a	0.125	± 60.4	63.8	-63.8	62.2	-62.2	14.2	-14.2	± 12.1	3.4	4.8	4.3	-4.3	92.7
3 b	10.507	± 7.3	10.4	-11.3	9.5	-10.4	4.1	-4.6	± 1.1	1.0	1.3	3.3	-3.8	15.7
3 c	9.944	± 6.9	11.4	-11.2	10.3	-10.1	4.9	-4.8	± 1.0	1.1	2.1	3.9	-3.8	5.2
3 d	6.652	± 8.1	13.9	-11.4	12.4	-10.2	6.2	-4.9	± 3.2	1.4	1.5	4.6	-2.7	4.4
3 e	4.791	± 10.1	15.1	-14.1	13.7	-12.8	6.4	-6.0	± 3.2	1.0	2.5	4.6	-4.0	6.4
4 b	7.160	± 9.1	11.7	-12.4	10.9	-11.5	4.2	-4.6	± 0.7	2.0	0.6	3.2	-3.7	16.3
4 c	7.858	± 7.8	11.8	-11.7	10.5	-10.4	5.4	-5.3	± 3.8	1.2	0.7	3.2	-3.1	7.8
4 d	8.308	± 7.7	11.6	-11.0	10.5	-9.9	5.0	-4.7	± 3.0	0.4	1.1	3.4	-3.1	5.7
4 e	4.678	± 10.4	13.5	-14.4	12.4	-13.2	5.4	-6.0	± 2.5	2.0	2.6	3.2	-4.1	3.5
	exclusive $k_\perp$ jet algorithm													
1 a	0.282	± 35.8	42.9	-43.4	41.1	-41.4	12.1	-13.0	± 1.0	5.0	7.1	8.3	-9.5	116.4
1 b	7.926	± 9.1	19.4	-20.5	16.1	-17.0	10.9	-11.4	± 9.4	1.0	1.1	5.0	-6.0	37.1
1 c	6.284	± 9.6	17.7	-17.4	14.8	-14.6	9.7	-9.5	± 8.1	1.0	2.3	4.4	-3.9	11.4
1 d	3.513	± 12.5	17.5	-18.2	15.8	-16.5	7.5	-7.7	± 3.6	1.7	3.7	4.9	-5.3	6.3
1 e	2.700	± 13.7	19.1	-18.4	17.6	-17.0	7.4	-7.2	± 3.1	1.6	3.1	5.5	-5.2	0.9
2 a	0.524	± 28.7	39.1	-41.0	36.2	-37.8	14.9	-15.8	± 2.9	8.0	5.7	10.7	-11.9	83.1
2 b	9.566	± 7.4	13.3	-13.1	11.8	-11.6	6.1	-6.2	± 3.8	2.0	0.6	4.0	-4.2	30.4
2 c	6.532	± 8.1	11.5	-11.3	10.5	-10.3	4.7	-4.5	± 2.2	0.9	1.4	3.5	-3.3	8.9
2 d	4.954	± 9.3	12.5	-13.9	11.5	-12.6	5.1	-5.8	± 2.5	2.0	1.5	3.3	-4.3	4.7
2 e	3.764	± 10.7	21.4	-13.0	19.4	-12.2	8.9	-4.3	± 2.2	1.9	0.5	8.3	-2.7	0.2
3 a	1.416	± 22.4	36.5	-35.0	31.0	-29.8	19.3	-18.5	± 13.6	9.3	7.2	6.8	-3.6	39.4
3 b	14.610	± 6.4	11.2	-11.8	9.8	-10.3	5.5	-5.7	± 2.9	2.5	1.1	3.4	-3.8	17.5
3 c	10.573	± 6.7	11.6	-9.6	10.4	-8.5	5.1	-4.3	± 0.6	1.4	2.5	3.8	-2.8	4.4
3 d	6.698	± 8.1	15.6	-13.0	14.0	-11.7	6.9	-5.8	± 2.9	2.6	1.1	5.4	-3.9	3.0
3 e	4.273	± 10.0	19.5	-14.9	17.5	-13.5	8.5	-6.2	± 1.1	2.9	1.8	7.6	-4.8	2.5
4 a	0.378	± 38.1	48.5	-52.6	43.6	-47.1	21.2	-23.5	± 21.0	2.9	0.3	0.3	-10.0	24.8
4 b	13.425	± 6.7	9.9	-9.0	9.0	-8.3	4.1	-3.6	± 0.0	2.2	0.9	3.0	-2.3	12.7
4 c	10.562	± 6.8	10.1	-9.9	9.0	-8.8	4.6	-4.5	± 3.4	1.0	0.5	2.5	-2.3	3.8
4 d	7.993	± 7.7	12.1	-10.4	10.9	-9.5	5.2	-4.3	± 2.6	1.0	1.0	4.0	-2.8	0.3
4 e	5.024	± 9.7	16.4	-18.9	14.3	-16.4	8.2	-9.3	± 3.6	4.0	3.1	5.2	-6.8	0.8
	Cambridge jet algorithm													
1 a	0.193	± 52.4	62.1	-60.0	58.5	-56.7	20.9	-19.6	± 15.9	6.8	6.4	9.6	-6.4	127.3
1 b	5.846	± 10.5	20.0	-20.1	16.7	-16.8	10.9	-11.1	± 9.7	0.8	0.7	4.5	-5.0	37.3
1 c	4.219	± 12.0	20.8	-19.8	17.8	-16.8	10.7	-10.4	± 9.0	1.8	2.2	4.7	-4.0	12.6
1 d	2.775	± 14.9	21.8	-20.5	18.8	-17.8	11.0	-10.3	± 3.7	2.8	7.9	5.9	-4.4	9.8
1 e	1.924	± 19.0	28.4	-28.4	24.8	-24.8	13.7	-13.7	± 11.4	1.3	3.7	6.4	-6.4	11.0
2 a	0.419	± 31.1	44.5	-42.6	41.6	-40.1	15.8	-14.4	± 5.4	3.5	5.5	13.3	-11.6	91.1
2 b	8.276	± 8.1	14.9	-12.2	13.3	-10.9	6.7	-5.4	± 1.5	3.5	0.7	5.3	-3.5	31.7
2 c	5.156	± 9.2	13.7	-14.6	12.0	-12.8	6.5	-7.0	± 5.4	0.3	1.7	2.8	-3.8	10.7
2 d	3.744	± 11.0	16.5	-18.1	14.5	-15.9	7.9	-8.6	± 5.3	2.6	3.2	3.7	-5.1	7.9
2 e	2.228	± 15.8	24.1	-23.6	20.9	-20.4	12.0	-11.7	± 11.0	0.9	1.3	4.4	-3.6	10.6
3 a	1.256	± 22.6	39.4	-36.8	33.4	-31.1	20.8	-19.6	± 16.7	6.9	5.6	8.6	-4.9	42.6
3 b	13.216	± 6.8	11.5	-12.7	10.0	-11.1	5.6	-6.1	± 3.1	3.0	1.1	3.0	-3.9	17.1
3 c	9.033	± 7.5	11.3	-11.4	10.1	-10.3	4.9	-4.9	± 0.5	1.2	2.7	3.6	-3.5	6.0
3 d	5.518	± 9.3	14.5	-15.4	13.2	-13.9	6.0	-6.7	± 2.7	1.6	1.4	4.7	-5.5	6.7
3 e	2.770	± 13.7	19.0	-18.2	17.8	-16.9	6.6	-6.7	± 1.9	1.1	2.7	5.4	-5.5	10.3
4 a	0.319	± 38.2	50.8	-54.5	46.0	-49.2	21.5	-23.4	± 21.0	2.7	0.3	-3.6	-9.9	22.7
4 b	12.335	± 7.0	11.3	-9.5	10.2	-8.6	4.8	-3.9	± 1.7	2.1	0.4	3.6	-2.4	12.4
4 c	10.500	± 6.9	9.9	-9.8	8.9	-8.8	4.2	-4.2	± 2.7	1.0	0.6	2.6	-2.6	4.5
4 d	6.895	± 8.3	11.7	-11.0	10.7	-10.0	4.7	-4.4	± 2.8	0.7	1.0	3.3	-2.8	2.2
4 e	3.665	± 12.2	18.9	-19.2	16.4	-16.7	9.4	-9.5	± 6.4	4.0	2.9	4.5	-4.8	4.0

D.1.12 The Dijet Cross Section $d^2\sigma_{\rm dijet}/(d\eta_{\rm backwd,lab}\, dQ^2)$

bin number	corresponding Q^2 range
1	$150 < Q^2 < 200\,{\rm GeV}^2$
2	$200 < Q^2 < 300\,{\rm GeV}^2$
3	$300 < Q^2 < 600\,{\rm GeV}^2$
4	$600 < Q^2 < 5000\,{\rm GeV}^2$

letter	corresponding $\eta_{\rm backwd,lab}$ range
a	$-1.0 < \eta_{\rm backwd,lab} < -0.5$
b	$-0.5 < \eta_{\rm backwd,lab} < 0.0$
c	$0.0 < \eta_{\rm backwd,lab} < 0.5$
d	$0.5 < \eta_{\rm backwd,lab} < 1.0$
e	$1.0 < \eta_{\rm backwd,lab} < 1.5$
f	$1.5 < \eta_{\rm backwd,lab} < 2.5$

the dijet cross section $d^2\sigma_{\rm dijet}/(d\eta_{\rm backwd,lab}\, dQ^2)$

									single contributions to correlated uncertainty					
bin No.	cross section (in pb)	statistical uncert. (in percent)	total uncertainty (in percent)		uncorrelated uncertainty (in percent)		correlated uncertainty (in percent)		model dep. detector corr. (in percent)	positron energy scale (in percent)	positron polar angle (in percent)	LAr hadr. energy scale (in percent)		hadroniz. correct. (percent)
	inclusive $k_\perp$ jet algorithm													
1 a	3.283	± 13.2	23.9	-27.6	19.5	-23.2	13.8	-14.9	± 13.4	1.4	1.3	2.6	-6.2	21.3
1 b	6.501	± 8.8	18.3	-16.9	15.3	-14.1	9.9	-9.4	± 8.0	1.4	2.5	4.9	-3.9	11.1
1 c	8.901	± 8.1	11.4	-12.8	10.2	-11.5	4.9	-5.5	± 3.3	0.5	1.5	2.9	-3.8	2.0
1 d	6.429	± 9.8	14.9	-15.5	12.9	-13.5	7.4	-7.7	± 2.2	3.4	4.4	4.0	-4.6	-5.1
1 e	1.496	± 18.1	27.4	-27.9	23.7	-24.1	13.7	-14.2	± 12.6	2.4	3.4	2.9	-4.6	-1.6
1 f	0.216	± 43.1	49.6	-48.0	47.1	-45.8	15.7	-14.4	± 11.2	8.8	0.0	6.2	0.0	9.0
2 a	3.766	± 11.7	17.7	-19.6	15.7	-17.4	8.2	-9.2	± 4.0	4.5	3.0	4.4	-6.0	17.6
2 b	7.312	± 8.0	11.7	-12.6	10.9	-11.6	4.3	-5.0	± 0.6	0.8	0.7	3.8	-4.6	11.8
2 c	9.606	± 7.1	9.3	-10.5	8.7	-9.8	3.3	-4.0	± 0.3	0.7	0.5	2.7	-3.5	2.4
2 d	6.251	± 8.1	13.9	-15.8	11.9	-13.6	7.2	-8.0	± 4.6	3.1	2.2	3.8	-5.2	-3.1
2 e	1.766	± 13.5	18.6	-16.2	17.1	-15.2	7.1	-5.6	± 3.9	1.8	1.9	5.1	-2.6	-1.2
2 f	0.918	± 20.1	31.4	-35.3	26.3	-29.9	17.2	-18.6	± 15.8	5.2	3.7	1.8	-7.3	3.9
3 a	4.021	± 11.2	14.2	-15.8	13.4	-14.8	4.9	-5.7	± 3.3	1.1	0.6	3.1	-4.3	15.7
3 b	6.756	± 8.9	12.9	-13.4	11.6	-12.1	5.6	-5.8	± 3.3	1.8	1.2	3.6	-3.9	10.9
3 c	11.914	± 6.7	11.4	-11.1	10.2	-9.8	5.1	-5.1	± 1.5	1.1	2.4	3.8	-3.8	3.9
3 d	7.407	± 7.9	11.3	-10.8	10.4	-10.0	4.4	-4.1	± 0.9	0.7	1.8	3.5	-3.2	-0.5
3 e	2.623	± 11.5	15.6	-17.4	14.1	-15.7	6.7	-7.6	± 3.9	3.3	2.1	3.5	-5.0	-2.6
3 f	0.624	± 24.9	36.0	-30.8	32.4	-28.1	15.7	-12.6	± 10.2	7.1	0.0	9.5	-1.4	9.6
4 a	1.944	± 14.9	21.6	-21.3	19.0	-18.7	10.5	-10.3	± 9.2	2.6	1.4	3.7	-3.3	9.4
4 b	3.741	± 11.6	13.7	-13.4	12.9	-12.7	4.5	-4.2	± 2.1	2.6	0.2	2.6	-2.1	10.1
4 c	9.303	± 8.1	13.7	-12.3	11.9	-10.6	6.8	-6.1	± 4.7	2.3	1.1	3.8	-2.5	6.3
4 d	9.213	± 7.6	11.3	-10.3	10.5	-9.7	4.1	-3.6	± 0.5	0.4	0.7	3.7	-3.1	3.7
4 e	4.754	± 9.7	15.8	-13.5	14.2	-12.3	7.0	-5.7	± 1.6	2.5	2.3	5.7	-3.9	1.8
4 f	0.755	± 22.2	28.4	-30.6	25.9	-27.7	11.7	-13.0	± 7.2	6.0	4.5	5.3	-7.7	2.0

the dijet cross section $d^2\sigma_{\rm dijet}/(d\eta_{\rm backwd,lab}\,dQ^2)$

									single contributions to correlated uncertainty				
bin No.	cross section (in pb)	statistical uncert. (in percent)	total uncertainty (in percent)		uncorrelated uncertainty (in percent)		correlated uncertainty (in percent)		model dep. detector corr. (in percent)	positron energy scale (in percent)	positron polar angle (in percent)	LAr hadr. energy scale (in percent)		hadroniz. correct. (percent)
	Aachen jet algorithm													
1 a	3.153	± 13.4	22.1	-28.3	18.5	-24.3	12.2	-14.6	± 10.8	3.0	3.5	3.1	-8.6	26.4
1 b	6.378	± 9.0	16.8	-15.2	14.1	-12.7	9.1	-8.3	± 7.3	0.9	2.3	4.5	-2.8	16.1
1 c	8.421	± 8.3	11.9	-11.1	10.8	-10.2	4.9	-4.3	± 2.4	0.9	1.7	3.5	-2.6	6.0
1 d	6.067	± 9.9	15.3	-15.3	13.2	-13.2	7.7	-7.8	± 2.7	3.9	4.4	3.8	-4.0	-1.7
1 e	1.765	± 17.2	21.1	-22.3	19.3	-20.2	8.5	-9.3	± 6.8	0.9	4.0	2.6	-4.6	2.9
1 f	0.356	± 36.3	45.3	-43.0	42.0	-40.1	17.1	-15.5	± 9.2	10.1	7.1	7.1	0.0	16.9
2 a	3.525	± 12.0	19.7	-18.7	17.2	-16.4	9.6	-9.0	± 4.0	5.0	4.0	5.7	-4.6	22.9
2 b	7.087	± 8.1	12.6	-12.3	11.6	-11.3	5.0	-4.9	± 1.3	1.3	1.0	4.3	-4.1	16.5
2 c	9.487	± 7.2	10.0	-10.3	9.3	-9.6	3.6	-3.6	± 0.0	0.4	0.5	3.2	-3.2	6.5
2 d	5.915	± 8.3	13.6	-14.9	11.8	-12.9	6.6	-7.3	± 3.9	2.9	2.3	3.7	-4.8	-0.1
2 e	1.752	± 13.6	15.8	-16.4	14.9	-15.4	5.2	-5.7	± 3.8	1.8	2.0	2.0	-2.9	1.7
2 f	0.807	± 22.0	35.8	-39.9	29.7	-33.7	20.0	-21.5	± 17.6	8.4	4.0	0.0	-7.9	8.1
3 a	3.747	± 11.7	17.7	-15.3	16.4	-14.5	6.7	-5.0	± 1.9	2.0	0.8	5.9	-3.9	21.6
3 b	6.762	± 8.9	13.2	-12.9	11.8	-11.4	6.0	-5.8	± 4.7	1.0	1.0	3.1	-2.8	15.5
3 c	11.638	± 6.8	11.6	-11.3	10.2	-9.9	5.5	-5.5	± 2.9	0.8	2.4	3.7	-3.6	7.2
3 d	6.935	± 8.1	11.9	-11.2	10.8	-10.2	5.0	-4.6	± 0.6	1.5	2.4	3.9	-3.3	2.6
3 e	2.765	± 11.5	15.0	-17.8	13.9	-16.2	5.7	-7.3	± 1.4	3.4	1.9	3.7	-5.8	0.7
3 f	0.411	± 29.6	38.1	-32.7	36.1	-31.9	12.0	-7.2	± 6.2	1.8	0.6	10.0	-2.8	13.3
4 a	1.737	± 15.6	21.5	-21.6	19.2	-19.3	9.8	-9.8	± 8.6	2.0	1.4	3.6	-3.7	11.5
4 b	3.591	± 11.9	14.1	-14.4	13.2	-13.4	4.9	-5.1	± 3.2	2.7	0.4	2.1	-2.5	14.5
4 c	8.616	± 8.3	13.4	-12.9	11.6	-11.2	6.6	-6.4	± 4.2	2.8	1.9	3.5	-3.1	9.1
4 d	8.926	± 7.8	10.1	-10.5	9.5	-9.8	3.4	-3.6	± 0.0	0.9	0.6	2.9	-3.1	6.9
4 e	4.669	± 9.9	14.5	-14.4	13.2	-13.1	6.1	-6.1	± 2.3	2.4	2.0	4.5	-4.4	3.5
4 f	0.571	± 24.3	29.5	-31.9	27.0	-28.9	12.1	-13.5	± 7.2	6.9	5.8	3.3	-6.8	4.1
	exclusive $k_\perp$ jet algorithm													
1 a	2.826	± 13.3	33.6	-30.8	28.3	-25.8	18.1	-16.8	± 12.5	2.1	4.5	12.0	-9.9	46.5
1 b	4.896	± 10.3	17.7	-18.3	15.2	-15.7	9.1	-9.4	± 7.0	1.6	2.6	4.7	-5.2	31.3
1 c	7.286	± 9.5	14.0	-13.5	12.9	-12.5	5.6	-5.2	± 3.0	0.8	0.8	4.2	-3.7	17.1
1 d	4.313	± 12.0	15.3	-17.7	13.6	-15.7	6.9	-8.1	± 1.1	3.3	5.2	2.6	-5.0	1.0
1 e	1.121	± 22.0	23.9	-25.9	22.9	-24.6	6.8	-8.2	± 2.2	1.0	5.7	2.2	-5.1	-8.9
1 f	0.174	± 48.2	62.7	-55.7	57.9	-51.6	24.1	-21.1	± 10.4	6.0	16.7	12.5	-4.2	-8.9
2 a	3.564	± 11.2	21.9	-17.9	19.8	-16.2	9.2	-7.6	± 1.8	3.5	2.3	7.8	-5.9	39.3
2 b	6.546	± 8.6	15.6	-13.7	14.0	-12.3	6.9	-5.9	± 0.8	2.9	1.5	5.8	-4.6	29.4
2 c	8.084	± 7.8	9.2	-11.9	8.7	-10.9	3.1	-4.6	± 1.5	1.2	0.9	1.7	-3.8	13.0
2 d	5.040	± 9.4	14.8	-11.8	13.5	-10.9	6.2	-4.7	± 1.0	1.6	2.7	5.0	-3.0	-0.8
2 e	1.559	± 15.0	18.7	-19.2	17.3	-17.8	7.0	-7.2	± 3.2	4.2	2.6	3.4	-3.8	-8.8
2 f	0.480	± 26.0	33.9	-35.2	30.6	-32.0	14.6	-14.8	± 14.2	3.4	0.0	0.0	-2.4	-0.7
3 a	5.547	± 9.7	16.6	-15.9	15.1	-14.5	6.9	-6.4	± 2.4	2.0	1.6	5.8	-5.2	28.9
3 b	8.851	± 7.9	11.6	-12.5	10.7	-11.4	4.5	-5.0	± 0.3	2.3	0.4	3.5	-4.1	20.2
3 c	12.463	± 6.5	14.3	-10.7	12.5	-9.2	7.0	-5.5	± 3.2	1.7	2.3	5.3	-3.0	7.8
3 d	7.541	± 8.0	13.4	-11.4	12.1	-10.2	5.7	-5.0	± 2.3	2.2	2.2	4.0	-2.8	-4.1
3 e	3.062	± 11.9	14.8	-15.5	13.8	-14.2	5.5	-6.1	± 2.4	2.6	3.1	2.4	-3.6	-11.0
3 f	0.286	± 35.6	42.7	-38.7	41.6	-38.3	9.4	-5.8	± 1.2	2.9	0.0	8.7	-4.6	4.2
4 a	2.324	± 13.5	16.8	-15.7	15.9	-15.1	5.4	-4.5	± 0.7	1.8	1.5	4.6	-3.5	25.5
4 b	5.434	± 9.5	14.4	-14.3	12.6	-12.5	6.9	-6.9	± 5.9	1.0	0.9	3.1	-3.1	19.7
4 c	11.170	± 7.1	10.6	-10.5	9.4	-9.3	4.8	-4.8	± 2.5	2.3	1.1	2.8	-2.8	8.7
4 d	11.592	± 6.8	9.0	-9.1	8.3	-8.5	3.4	-3.3	± 1.2	1.3	0.6	2.4	-2.4	-1.9
4 e	5.858	± 8.9	14.3	-11.1	13.1	-10.4	5.8	-3.7	± 0.3	1.4	0.5	5.3	-3.0	-10.3
4 f	0.845	± 21.0	28.4	-33.0	24.9	-28.9	13.6	-15.8	± 7.5	9.2	5.9	2.6	-8.4	-9.7
	Cambridge jet algorithm													
1 a	1.948	± 17.3	36.0	-31.2	31.4	-26.6	17.7	-16.3	± 12.6	0.9	5.3	11.1	-8.7	57.8
1 b	3.530	± 12.7	24.5	-25.9	20.1	-21.4	14.0	-14.6	± 12.7	1.1	2.5	4.9	-6.5	36.0
1 c	4.813	± 11.7	14.3	-14.7	13.4	-13.7	5.1	-5.5	± 3.3	1.1	2.0	2.8	-3.5	19.9
1 d	3.618	± 13.8	22.1	-17.8	19.7	-16.0	9.9	-7.9	± 2.4	3.7	5.2	7.1	-3.7	1.8
1 e	0.916	± 25.3	27.5	-27.5	26.2	-26.3	8.2	-8.2	± 5.3	0.0	5.7	1.9	-1.9	-7.1
2 a	2.982	± 13.0	25.3	-21.0	22.3	-18.3	12.0	-10.2	± 7.2	4.7	0.9	8.2	-5.1	48.6
2 b	4.731	± 10.4	15.8	-17.1	14.5	-15.6	6.4	-7.0	± 0.2	3.0	1.4	5.3	-6.0	34.6
2 c	6.768	± 8.8	12.1	-12.7	10.9	-11.4	5.2	-5.6	± 3.5	1.0	2.0	2.8	-3.4	15.9
2 d	3.897	± 11.0	17.3	-14.3	15.5	-12.9	7.6	-6.2	± 5.2	0.3	1.5	5.1	-2.4	0.5
2 e	1.154	± 18.0	21.8	-22.8	20.0	-20.8	8.5	-9.2	± 6.0	3.0	4.3	2.7	-4.3	-4.8
2 f	0.263	± 36.8	49.5	-54.4	44.3	-48.5	22.1	-24.6	± 19.6	10.1	0.0	0.0	-10.7	1.3
3 a	5.000	± 10.4	17.3	-18.7	15.2	-16.5	8.3	-8.7	± 5.4	3.6	1.4	4.8	-5.3	33.0
3 b	7.634	± 8.7	12.0	-12.6	11.0	-11.5	4.7	-5.1	± 0.4	2.8	1.9	2.9	-3.6	23.2
3 c	10.210	± 7.5	13.0	-13.8	11.6	-12.2	5.9	-6.4	± 2.4	1.9	2.5	4.1	-4.8	9.3
3 d	6.679	± 8.9	12.4	-12.6	11.4	-11.5	4.9	-5.0	± 2.4	1.6	1.8	3.3	-3.4	-2.6
3 e	2.244	± 14.2	22.8	-20.1	20.0	-17.4	10.9	-9.9	± 6.4	5.5	3.9	5.4	-2.9	-10.1
3 f	0.203	± 43.3	45.2	-47.6	44.7	-46.6	6.4	-9.8	± 1.2	3.5	0.0	5.0	-9.0	4.5
4 a	2.384	± 13.4	17.2	-16.1	16.3	-15.3	5.8	-4.8	± 0.8	2.0	1.2	5.0	-3.9	27.3
4 b	4.425	± 10.6	13.7	-13.5	12.6	-12.4	5.4	-5.4	± 3.9	1.5	0.5	2.9	-2.9	21.4
4 c	10.212	± 7.6	11.1	-11.0	10.0	-9.8	4.8	-4.9	± 3.2	1.5	0.7	2.7	-2.9	10.1
4 d	10.833	± 7.3	10.3	-9.4	9.5	-8.8	3.8	-3.4	± 0.8	1.5	0.8	3.0	-2.5	-1.1
4 e	5.178	± 9.6	12.0	-10.5	11.3	-10.2	3.9	-2.7	± 1.2	0.6	0.3	3.3	-1.7	-10.2
4 f	0.709	± 23.8	31.7	-35.1	28.6	-31.4	13.7	-15.6	± 5.1	10.8	4.5	4.8	-8.8	-12.2

D.2 Results of the QCD Fits

the main $\alpha_s(M_Z)$ results from the inclusive jet cross section using the inclusive $k_\perp$ algorithm			
		$\mu_r = E_T$	$\mu_r = Q$
$\alpha_s(M_Z) =$		0.1181	0.1221
total uncertainty		$^{+0.0061}_{-0.0058}$	$^{+0.0074}_{-0.0070}$
experimental	statistical uncertainty	$^{+0.0007}_{-0.0007}$	$^{+0.0008}_{-0.0008}$
	luminosity uncertainty	$^{+0.0010}_{-0.0010}$	$^{+0.0011}_{-0.0011}$
	positron energy	$^{+0.0004}_{-0.0004}$	$^{+0.0004}_{-0.0004}$
	LAr calo hadronic energy	$^{+0.0021}_{-0.0021}$	$^{+0.0023}_{-0.0023}$
	other exp. uncertainties	$^{+0.0017}_{-0.0017}$	$^{+0.0019}_{-0.0019}$
theoretical	hadronization corrections unc.	$^{+0.0028}_{-0.0030}$	$^{+0.0030}_{-0.0032}$
	μ_r dependence	$^{+0.0026}_{-0.0034}$	$^{+0.0044}_{-0.0049}$
	μ_f dependence	$^{+0.0007}_{-0.0005}$	$^{+0.0010}_{-0.0012}$
parton density functions		$^{+0.0036}_{-0.0017}$	$^{+0.0037}_{-0.0016}$
$\chi^2/\mathrm{N.d.f.}$ of fit		3.81 / 15	4.17 / 15

Table D.1: The main results of the α_s fits in sections 9.1.2 and 9.1.3 for two different choices of the renormalization scale. Shown is a detailed overview of all experimental and theoretical contributions to the uncertainties of the fit results.

E_T dependence of $\alpha_s(E_T)$ ($\mu_r = E_T$) inclusive jet cross section — inclusive $k_\perp$ algorithm				
average E_T of data point:	$\sqrt{70}\,\mathrm{GeV}$	$\sqrt{200}\,\mathrm{GeV}$	$\sqrt{500}\,\mathrm{GeV}$	$\sqrt{1500}\,\mathrm{GeV}$
$\alpha_s(E_T) =$	0.1929	0.1619	0.1551	0.1458
total uncertainty	$^{+0.0164}_{-0.0133}$	$^{+0.0152}_{-0.0131}$	$^{+0.0161}_{-0.0152}$	$^{+0.0296}_{-0.0266}$
exp.	$^{+0.0082}_{-0.0081}$	$^{+0.0105}_{-0.0102}$	$^{+0.0122}_{-0.0121}$	$^{+0.0255}_{-0.0235}$
theor.	$^{+0.0105}_{-0.0097}$	$^{+0.0082}_{-0.0076}$	$^{+0.0092}_{-0.0082}$	$^{+0.0095}_{-0.0104}$
pdf	$^{+0.0096}_{-0.0042}$	$^{+0.0074}_{-0.0031}$	$^{+0.0051}_{-0.0042}$	$^{+0.0116}_{-0.0069}$
$\alpha_s(M_Z) =$	0.1206	0.1165	0.1210	0.1256
total uncertainty	$^{+0.0059}_{-0.0055}$	$^{+0.0075}_{-0.0070}$	$^{+0.0094}_{-0.0095}$	$^{+0.0215}_{-0.0196}$
exp.	$^{+0.0031}_{-0.0031}$	$^{+0.0052}_{-0.0052}$	$^{+0.0072}_{-0.0074}$	$^{+0.0183}_{-0.0172}$
theor.	$^{+0.0036}_{-0.0041}$	$^{+0.0038}_{-0.0043}$	$^{+0.0053}_{-0.0054}$	$^{+0.0077}_{-0.0066}$
pdf	$^{+0.0036}_{-0.0016}$	$^{+0.0037}_{-0.0016}$	$^{+0.0031}_{-0.0025}$	$^{+0.0084}_{-0.0051}$

Table D.2: The α_s results from the fits presented in section 9.1.2. Displayed are the fit results of $\alpha_s(E_T)$ at different E_T (top) and the values extrapolated to $\mu_r = M_Z$ (bottom).

$\alpha_s(M_Z)$ from different jet definitions ($\mu_r = E_T$)

fit to $\mathrm{d}^2\sigma_{\mathrm{jet}}/\mathrm{d}E_T\mathrm{d}Q^2$ measured from	$\alpha_s(M_Z)$	exp.	theor.	PDF	$\chi^2/\mathrm{N.d.f.}$
incl. jet cross section – incl. $k_\perp$ algo	$0.1181\,^{+0.0061}_{-0.0058}$	± 0.0030	$^{+0.0039}_{-0.0046}$	$^{+0.0036}_{-0.0017}$	3.81 / 15
incl. jet cross section – Aachen algo	$0.1172\,^{+0.0068}_{-0.0063}$	± 0.0032	$^{+0.0046}_{-0.0052}$	$^{+0.0037}_{-0.0016}$	5.45 / 15
dijet cross section – incl. $k_\perp$ algo	$0.1189\,^{+0.0062}_{-0.0058}$	$^{+0.0034}_{-0.0035}$	$^{+0.0036}_{-0.0041}$	$^{+0.0037}_{-0.0019}$	11.75 / 15
dijet cross section – Aachen algo	$0.1174\,^{+0.0068}_{-0.0065}$	$^{+0.0031}_{-0.0033}$	$^{+0.0046}_{-0.0052}$	$^{+0.0037}_{-0.0018}$	13.45 / 15
dijet cross section – excl. $k_\perp$ algo	$0.1180\,^{+0.0067}_{-0.0060}$	± 0.0040	$^{+0.0038}_{-0.0042}$	$^{+0.0038}_{-0.0015}$	4.20 / 15
dijet cross section – Cambridge algo	$0.1136\,^{+0.0067}_{-0.0057}$	± 0.0045	$^{+0.0030}_{-0.0030}$	$^{+0.0039}_{-0.0016}$	6.41 / 15

Table D.3: The α_s results from the fits presented in sections 9.1.5 and 9.1.5.

$\alpha_s(M_Z)$ from different dijet variables using the inclusive $k_\perp$ algorithm

$\mu_r = E_T$	$\alpha_s(M_Z)$	exp.	theor.	pdf	$\chi^2/\mathrm{N.d.f.}$
$\mathrm{d}^2\sigma_{\mathrm{dijet}}/\mathrm{d}\overline{E}_T\mathrm{d}Q^2$	$0.1189\,^{+0.0062}_{-0.0058}$	$^{+0.0034}_{-0.0035}$	$^{+0.0036}_{-0.0041}$	$^{+0.0037}_{-0.0019}$	11.75 / 15
$\mathrm{d}^2\sigma_{\mathrm{dijet}}/\mathrm{d}M_{jj}\mathrm{d}Q^2$	$0.1190\,^{+0.0062}_{-0.0058}$	± 0.0036	$^{+0.0034}_{-0.0040}$	$^{+0.0038}_{-0.0019}$	7.14 / 15
$\mathrm{d}^2\sigma_{\mathrm{dijet}}/\mathrm{d}\xi\mathrm{d}Q^2$	$0.1199\,^{+0.0063}_{-0.0061}$	$^{+0.0038}_{-0.0040}$	$^{+0.0037}_{-0.0042}$	$^{+0.0034}_{-0.0017}$	6.75 / 18
$\mathrm{d}^2\sigma_{\mathrm{dijet}}/\mathrm{d}x_p\mathrm{d}Q^2$	$0.1218\,^{+0.0063}_{-0.0058}$	$^{+0.0039}_{-0.0040}$	$^{+0.0031}_{-0.0035}$	$^{+0.0038}_{-0.0022}$	5.89 / 15
$\mathrm{d}^2\sigma_{\mathrm{dijet}}/\mathrm{d}x_{\mathrm{Bj}}\mathrm{d}Q^2$	$0.1188\,^{+0.0063}_{-0.0061}$	$^{+0.0042}_{-0.0044}$	$^{+0.0036}_{-0.0040}$	$^{+0.0029}_{-0.0013}$	4.37 / 15
$\mathrm{d}^2\sigma_{\mathrm{dijet}}/\mathrm{d}y\mathrm{d}Q^2$	$0.1173\,^{+0.0071}_{-0.0064}$	$^{+0.0049}_{-0.0047}$	$^{+0.0035}_{-0.0041}$	$^{+0.0038}_{-0.0015}$	5.65 / 15
$\mathrm{d}^2\sigma_{\mathrm{dijet}}/\mathrm{d}\eta'\mathrm{d}Q^2$	$0.1193\,^{+0.0057}_{-0.0062}$	$^{+0.0045}_{-0.0043}$	$^{+0.0037}_{-0.0042}$	$^{+0.0034}_{-0.0013}$	10.96 / 19
$\mathrm{d}^2\sigma_{\mathrm{dijet}}/\mathrm{d}\eta'\mathrm{d}\overline{E}_T$	$0.1203\,^{+0.0065}_{-0.0063}$	± 0.0037	$^{+0.0040}_{-0.0047}$	$^{+0.0035}_{-0.0019}$	3.59 / 11

Table D.4: The α_s results from the fits presented in section 9.1.5 to different dijet distributions measured using the inclusive $k_\perp$ algorithm.

The Gluon Density in the Proton at $\mu_f = \sqrt{200}\,\mathrm{GeV}$
parameterized by $xG(x) = Ax^b\,(1-x)^c\,(1+dx)$ in $0.01 < x < 0.1$
central result: A=0.4963 ; b = –0.593 ; c = 4.71 ; d = –0.553

$\log_{10}(x)$	$xG(x) =$	exp.	theor.	from $\Delta\alpha_s(M_Z)$
-2.0	$7.23\,^{+1.40}_{-1.28}$	$^{+0.93}_{-0.94}$	$^{+0.77}_{-0.71}$	$^{+0.70}_{-0.51}$
-1.9	$6.22\,^{+1.10}_{-1.01}$	$^{+0.64}_{-0.65}$	$^{+0.65}_{-0.63}$	$^{+0.61}_{-0.45}$
-1.8	$5.34\,^{+0.87}_{-0.81}$	$^{+0.45}_{-0.45}$	$^{+0.51}_{-0.54}$	$^{+0.52}_{-0.41}$
-1.7	$4.55\,^{+0.70}_{-0.65}$	$^{+0.32}_{-0.32}$	$^{+0.44}_{-0.46}$	$^{+0.44}_{-0.33}$
-1.6	$3.86\,^{+0.58}_{-0.54}$	$^{+0.26}_{-0.25}$	$^{+0.36}_{-0.38}$	$^{+0.38}_{-0.29}$
-1.5	$3.25\,^{+0.48}_{-0.45}$	$^{+0.23}_{-0.21}$	$^{+0.28}_{-0.31}$	$^{+0.31}_{-0.25}$
-1.4	$2.71\,^{+0.41}_{-0.38}$	$^{+0.21}_{-0.20}$	$^{+0.22}_{-0.25}$	$^{+0.27}_{-0.21}$
-1.3	$2.24\,^{+0.34}_{-0.31}$	$^{+0.19}_{-0.18}$	$^{+0.18}_{-0.19}$	$^{+0.22}_{-0.17}$
-1.2	$1.82\,^{+0.28}_{-0.26}$	$^{+0.17}_{-0.16}$	$^{+0.13}_{-0.14}$	$^{+0.18}_{-0.15}$
-1.1	$1.44\,^{+0.23}_{-0.22}$	$^{+0.15}_{-0.14}$	$^{+0.12}_{-0.11}$	$^{+0.14}_{-0.13}$
-1.0	$1.12\,^{+0.20}_{-0.18}$	$^{+0.13}_{-0.13}$	$^{+0.08}_{-0.10}$	$^{+0.12}_{-0.09}$

Table D.5: The gluon density in the proton from the fit in section 9.2.1. Displayed are the results and the uncertainties of the gluon density $xG(x)$ at eleven values of x in the interval $0.01 < x < 0.1$. Also displayed are the parameters A, b, c, d of the central result.

The Δ Quark Density in the Proton at $\mu_f = \sqrt{200}\,\mathrm{GeV}$

$x\,\Delta = x\sum_i e_i^2(q_i + \overline{q}_i)$

parameterized by $x\Delta(x) \;=\; Ax^b\,(1-x)^c\,(1+dx)$ in $0.01 < x < 0.1$

central result: A=0.1587 ; b = –0.382 ; c = 3.58 ; d = 5.85

$\log_{10}(x)$	$x\Delta(x) =$
-2.0	$0.942\,^{+0.023}_{-0.023}$
-1.9	$0.868\,^{+0.019}_{-0.019}$
-1.8	$0.799\,^{+0.016}_{-0.016}$
-1.7	$0.737\,^{+0.014}_{-0.014}$
-1.6	$0.680\,^{+0.013}_{-0.013}$
-1.5	$0.628\,^{+0.012}_{-0.012}$
-1.4	$0.580\,^{+0.011}_{-0.011}$
-1.3	$0.536\,^{+0.010}_{-0.010}$
-1.2	$0.495\,^{+0.010}_{-0.010}$
-1.1	$0.455\,^{+0.0088}_{-0.0087}$
-1.0	$0.416\,^{+0.0084}_{-0.0083}$

Table D.6: The Δ quark density in the proton from the fit in section 9.2.1. Displayed are the results and the uncertainties of the quark density $x\Delta(x)$ at eleven values of x in the interval $0.01 < x < 0.1$. Also displayed are the parameters A, b, c, d of the central result.

		No. of standard deviations by which the parameter is varied in the Fit		
	source of correlated uncertainties	Fit of $\alpha_s(M_Z)$	Fit of $xG(x)$ and $x\Delta(x)$	Fit of $\alpha_s(M_Z)$, $xG(x)$, $x\Delta(x)$
experimental	luminosity	+0.025	–0.019	–0.021
	model dependence of detector correction	-0.323	+0.227	+0.216
	positron energy	+0.001	–0.172	–0.186
	positron polar angle	-0.030	+0.052	+0.063
	LAr cluster energy	-0.117	–0.399	–0.379
	LAr noise	—	+0.714	+0.704
	photoproduction background	—	–0.105	–0.118
theoretical	renormalization scale (inclusive DIS)	—	–0.698	–0.754
	renormalization scale (jets)	+0.291	+0.253	+0.297
	factorization scale (jets)	+0.032	+0.274	+0.308
	hadronization corrections	–0.147	+0.120	+0.213
external	$\alpha_s(M_Z) = 0.1190 \pm 0.0040$	(free)	+0.0003	(free)
$\chi^2/\mathrm{N.d.f.}$ of fit		3.81 / 15	61.16 / 105	61.10 / 104

Table D.7: The values of the systematic parameters in the fits in sections 9.1.2, 9.2.1 and 9.3.1 in which the main results are obtained.

List of Figures

Bibliography

[1] R.E. Taylor, H.W. Kendall and J.I. Friedman, lectures on the occasion of the presentation of the 1990 Nobel Prize in Physics, Rev. Mod. Phys. 63 (1991) 573.

[2] E665 Collaboration, M.R. Adams et al., Phys. Rev. Lett. 69 (1992) 1026.

[3] H1 Collaboration, C. Adloff et al., Eur. Phys. J. C6 (1999) 575.

[4] H1 Collaboration, C. Adloff et al., Eur. Phys. J. C5 (1998) 625.

[5] ZEUS Collaboration, M. Derrick et al., Phys. Lett. B363 (1995) 201.

[6] F. Halzen and A.D. Martin, Quarks and Leptons, J. Wiley, New York (1984).

[7] V. Barger and R. Phillips, Collider physics, Addison-Wesley (1987).

[8] R.G. Roberts, The structure of the proton: deep inelastic scattering, Cambridge university press, Cambridge (1990).

[9] Yu.L. Dokshitzer, V.A. Kohze, A.H. Mueller and S.I. Trojan, Basics of perturbative QCD, Editions Frontiere, France (1991).

[10] R.K. Ellis, W.J. Stirling and B.R. Webber, QCD and collider physics, Cambridge university press, Cambridge (1996).

[11] D.E. Soper, proceedings of the 24th Annual SLAC Summer Institute on Particle Physics (SSI 96), Stanford, CA, 19-30 Aug. (1996) hep-ph/9702203.

[12] D.E. Soper, Talk at Lattice 96 Conference, St. Lois, June 1996, hep-lat/9609018.

[13] G. 't Hooft and M. Veltman, Nucl. Phys. B (1972) 189.

[14] W.A. Bardeen, A.J. Buras, D.W. Duke and T.A. Muta, Phys. Rev. D 18 (1978) 3998.

[15] H.D. Politzer, Phys. Rev. Lett. 30 (1973) 1346;
D.J. Gross and F. Wilczek, Phys. Rev. Lett. 30 (1973) 1343.

[16] W.A. Caswell, Phys. Rev. Lett. 33 (1974) 244.

[17] O.V. Tarasov, A.A. Vladirmirov and A.Yu. Zharkov, Phys. Lett. B 93 (1980) 429; S.A. Larin and J.A.M. Vermaseren, Phys. Lett. B 303 (1993) 334.

[18] T. van Ritbergen, J.A.M. Vermaseren and S.A. Larin, Phys. Lett. B 400 (1997) 379.

[19] K.G. Chetyrkin, B. A. Kniehl and M. Steinhauser, Phys. Rev. Lett. 79 (1997) 2184.

[20] W.J. Stirling, in: Les Houches 1997, New non-perturbative methods and quantization on the light cone (1997) 225 , hep-ph/9709429.

[21] C. Caso et al., Eur. Phys. J. C 3 (1998) 1 and 1999 off-year partial update for the 2000 edition available on the PDG WWW pages (URL: http://pdg.lbl.gov/).

[22] S. Bethke, in proceedings of: 4th International Symposium on Radiative Corrections (RADCOR 98), Catalonia, Spain, (1998) hep-ex/9812026.

[23] S. Catani, proceeding of 18th International Symposium on Lepton-Photon Interactions (LP 97), Hamburg, Germany (1997) 149.

[24] V.N. Gribov and L.N. Lipatov, Sov. J. Nucl. Phys. 15 (1972) 438 and 675; Yu.L. Dokshitzer, Sov. Phys. JETP 46 (1977) 641.

[25] G. Altarelli and G. Parisi, Nucl. Phys. B 126 (1977) 298.

[26] W. Furmanski and R. Petronzio, Phys. Lett. B 97 (1980) 437.

[27] V. Barone, C. Pascaud and F. Zomer, A new global analysis of deep inelastic scattering data, Eur. Phys. J. C12 (2000) 243.

[28] M. Glück, E. Reya and A. Vogt, Z. Phys. C 48 (1990) 471.

[29] H.L. Lai et al., Global QCD analysis of parton structure of the nucleon: CTEQ5 parton distributions, Eur. Phys. J. C12 (2000) 375.

[30] A.D. Martin, R.G. Roberts, W.J. Stirling and R.S. Thorne, Eur. Phys. J. C14 (2000) 133.

[31] M. Glück, E. Reya and A. Vogt, Eur. Phys. J. C 5 (1998) 461.

[32] H1 Collaboration, C. Adloff et al., Eur. Phys. J. C13 (2000) 609.

[33] H1 Collaboration, preliminary result presented by M. Klein at the XIX International Symposium on Lepton and Photon Interactions at High Energies, Stanford, August 1999.

[34] S. Catani, Yu.L. Dokshitzer, M.H. Seymour and B.R. Webber, Nucl. Phys. B406 (1993) 187.

[35] B.R. Webber, J. Phys. G19 (1993) 1567.

[36] M. Dasgupta and B.R. Webber, Eur. Phys. J. C1 (1998) 539.

[37] H1 Collaboration, C. Adloff et al., Phys. Lett. B 406 (1997) 256.

[38] K. Rabbertz, PhD Thesis, RWTH Aachen, Germany (1998) PITHA 98/44.

[39] S. Moretti, L. Lönnblad and T. Sjöstrand, JHEP 08 (1998) 001.

[40] L. Lönnblad, Z. Phys. C 58 (1993) 471.

[41] G. Sterman and S. Weinberg, Phys. Rev. Lett. 39 (1977) 1436.

[42] J. Huth et al., proceedings of the Summer Study on High Energy Physics, Snowmass, Colorado (1990) 134.

[43] M. Fleischer, G. Ingelman, G. Knies, K. Meier, A. Wegner and C. Pichler, proceedings of the Workshop Physics at HERA, vol. 1, DESY, Hamburg, Germany (1991) 303.

[44] M.H. Seymour, in: Les Rencontres de la Valée d'Aoste, La Thuile, France (1997) and Nucl. Phys. B 513 (1998) 269.

[45] D.E. Soper, in: Rencontres de Moriond, Les Arc, France (1997) hep-ph/9706320.

[46] JADE Collaboration, W. Bartel et al., Z. Phys. C 33 (1986) 23;
JADE Collaboration, S. Bethke et al., Phys. Lett. B 213 (1988) 235.

[47] D. Graudenz and N. Magnussen, proceedings of the Workshop Physics at HERA, vol. 1, DESY, Hamburg, Germany (1991) 261, and references therein.

[48] S. Catani, in: Rencontres de Moriond, Les Arcs, France (1993) CERN-TH.6895/93.

[49] N. Brown and W.J. Stirling, Z. Phys. C 53 629 (1992) 629.

[50] S. Catani, Yu.L. Dokshitzer and B.R. Webber, Phys. Lett. B 285 (1992) 291.

[51] Yu.L. Dokshitzer, G.D. Leder, S. Moretti and B.R. Webber, JHEP 08 (1997) 001.

[52] Z. Kunszt, P. Nason, G. Marchesini and B.R. Webber, in: LEP Physics Workshop, vol.1 (1989) 373.

[53] M. Wobisch and T. Wengler, proceedings of the HERA Monte Carlo Workshop, eds. G. Grindhammer, G. Ingelman, H. Jung, T. Doyle, (1999), PITHA 99/16, hep-ph/9907280.

[54] S.D. Ellis and D.E. Soper, Phys. Rev. D 48 (1993) 3160.

[55] J.G. Körner, E. Mirkes and G.A. Schuler, Int. J. Mod. Phys. A 4 (1989) 1781.

[56] W.T. Giele and E.W.N. Glover , Phys. Rev. D 46 (1992) 1980.

[57] E. Mirkes and D. Zeppenfeld, Phys. Lett. B 380 (1996) 205.

[58] G.Kramer and B. Pötter, Phys. Lett. B 453 (1999) 295.

[59] Z. Kunszt and D.E. Soper, Phys. Rev. D 46 (1992) 192.

[60] S. Catani and M.H. Seymour, Nucl. Phys. B 485 (1997) 291, Erratum-ibid. B 510 (1997) 503.

[61] D. Graudenz, DISASTER++: version 1.0 program manual (1997) hep-ph/9710244.

[62] C. Duprel, N. Kauer, T. Hadig and M. Wobisch, proceedings of the HERA Monte Carlo Workshop, ed. G. Grindhammer, G. Ingelman, H. Jung, T. Doyle, (1999), PITHA 99/30, hep-ph/9910448.

[63] T. Sjöstrand, Phys. Lett. B 157 (1985) 321.

[64] G. Marchesini et al., Comp. Phys. Comm. 67 (1992) 465.

[65] G. Ingelman, A. Edin and J. Rathsman, Comp. Phys. Comm. 101 (1997) 108.

[66] G. Gustafson and U. Petterson, Nucl. Phys. B 306 (1988);
G. Gustafson, Phys. Lett. B 175 (1986) 453;
B. Andersson, G. Gustafson, L. Lönnblad and U. Petterson, Z. Phys. C 43 (1989) 625.

[67] L. Lönnblad, Comp. Phys. Comm. 71 (1992) 15.

[68] L. Lönnblad, Z. Phys. C 65 (1995) 285.

[69] B.R. Webber, Nucl. Phys. B 238 (1984) 492.

[70] B. Andersson et al., Phys. Rep. 97 (1983) 31.

[71] T. Sjöstrand, Comp. Phys. Comm. 39 (1986) 347;
T. Sjöstrand and M. Bengtsson, ibid. 43 (1987) 367.

[72] K. Charchula, G. Schuler and H. Spiesberger, Comp. Phys. Comm. 81 (1994) 381.

[73] A. Kwiatkowski, H. Spiesberger and H.-J. Möhring, Comp. Phys. Comm. 69 (1992) 155.

[74] S. Catani and B.R. Webber, JHEP 10 (1997) 005.

[75] St. Frixione and G. Ridolfi, Nucl. Phys. B 507 (1997) 315.

[76] M. Wobisch, proceedings of the 6th International Workshop on Deep Inelastic Scattering and QCD (DIS98), Brussels (1998).

[77] CTEQ Collaboration, H.L. Lai et al., Phys. Rev. D 55 (1997) 1280.

[78] E.B. Zijlstra and W.L. van Neerven , Nucl. Phys. B 383 (1992) 525.

[79] H1 Collaboration, I. Abt et al., Nucl. Instr. Meth. A 386 (1997) 310 and 348.

[80] H1 Calorimeter Group, B. Andrieu et al., Nucl. Instr. Meth. A 336 (1993) 460.

[81] B. Heinemann, PhD Thesis, University Hamburg, Germany (1999).

[82] H1 Spacal Group, R.D. Appuhn et al., Nucl. Instr. Meth. A 386 (1997) 397.

[83] S. Bentvelsen, J. Engelen and P. Kooijman, proceedings of the Workshop Physics at HERA, vol. 1, DESY, Hamburg, Germany (1991) 23.

[84] F. Jacquet and A. Blondel, proceedings of the study of an *ep* facility for Europe 97/48, ed. U. Amaldi, DESY, Hamburg (1979) 391.

[85] U. Bassler and G. Bernardi, Nucl. Instr. Meth. A 361 (1995) 197.

[86] U. Bassler and G. Bernardi, Nucl. Instr. Meth. A 426 (1998) 583.

[87] G. Cowan, Statistical Data Analysis, Clarendon Press, Oxford (1998).

[88] V. Blobel, proceedings of CERN School of Computing, Aiguablava, Spain, CERN 85-09, (1984) 88.

[89] G. D'Agostini, Nucl. Instr. Meth. A362 (1995) 487.

[90] M. Wobisch, Diploma Thesis, RWTH Aachen, Germany (1995) PITHA 95/38.

[91] CERN, GEANT, detector description an simulation tool, CERN Program Library Long Writeup W 5013 (1994).

[92] A.D. Martin, W.J. Stirling and R.G. Roberts, proceeding of the Workshop on Quantum Field Theoretical Aspects of High Energy Physics, Eds. B. Geyer and E. M. Ilgenfritz, Leipzig (1993) 11.

[93] T. Sjöstrand and M. Bengtsson, Comp. Phys. Comm. 43 (1987) 74.

[94] P. Bruel, Ph.D. Thesis, Orsay (1998).

[95] E. Mirkes and S. Willfahrt, Phys. Lett. B 414 (1997) 205.

[96] A. Heister, Diploma Thesis, RWTH Aachen, Germany (1999).

[97] L. Sonnenschein, Diploma Thesis, RWTH Aachen, Germany (1998) PITHA 98/4.

[98] M. Wobisch, internal H1 note H1-05/98-543 (1998).

[99] H1 Collaboration, Measurement of Dijet Cross Sections in Deep-Inelastic Scattering at HERA and a Direct Determination of the Gluon Density in the Proton, Contributed paper 520 to the 29th International Conference on High-Energy Physics (ICHEP 98), Vancouver, Canada, 23-29 July (1998).

[100] H1 Collaboration, First Measurement of Three Jet Cross Sections in DIS at HERA, Contributed paper 157 to the International Europhysics Conference on High Energy Physics (EPS-HEP 99), Tampere, Finland, 15-21 July (1999).

[101] H1 Collaboration, C. Adloff et al., Nucl. Phys. B 545 (1999) 3.

[102] OPAL Collaboration, G. Abbiendi et al. , Eur. Phys. J. C 10 (1999) 547.

[103] P.-O. Meyer, proceedings of the 7th International Workshop on Deep Inelastic Scattering and QCD (DIS99), Nucl. Phys. B (Proc. Suppl) 79 (1999) 472.

[104] H1 Collaboration, C. Adloff et al., DESY-98-076 Hamburg, Germany (1998), submitted to Eur. Phys. J. C.

[105] H1 Collaboration, C. Adloff et al., Eur. Phys. J. C13 (2000) 397.

[106] A.D. Martin, W.J. Stirling and R.G. Roberts, Phys. Lett. B 356 (1995) 89.

[107] H1 Collaboration, Study of Differential Dijet Event Distributions and Determination of α_s in Deeply Inelastic Scattering at Large Q^2, Contributed paper 157 to the International Europhysics Conference on High Energy Physics (EPS-HEP 99), Tampere, Finland, 15-21 July (1999).

[108] E. Tassi, proceedings of the 7th International Workshop on Deep Inelastic Scattering and QCD (DIS99), Nucl. Phys. B (Proc. Suppl) 79 (1999).

[109] ZEUS Collaboration, Measurement of Differential Cross Sections for Dijet Production in Neutral Current DIS at High Q^2 and Determination of α_s, Contributed paper 543 to the International Europhysics Conference on High Energy Physics (EPS-HEP 99), Tampere, Finland, 15-21 July (1999).

[110] A. Akopian, proceedings of the 7th International Workshop on Deep Inelastic Scattering and QCD (DIS99), Nucl. Phys. B (Proc. Suppl) 79 (1999).

[111] J. Huston et al., Phys. Rev. D 58 (1998) 114034.

[112] P. Pfeifenschneider, PhD Thesis, RWTH Aachen, Germany (1999) PITHA 99/14.

[113] H1 Collaboration, S. Aid et al., Nucl. Phys. B 449 (1995) 3.

[114] J. Stier, PhD Thesis, Hamburg (1996).

[115] M. Hampel, PhD Thesis, RWTH Aachen, Germany (1997) PITHA 97/13.

[116] G. Lobo, PhD Thesis, Orsay (1997) LAL-97-21.

[117] A.D. Martin, R.G. Roberts and W.J. Stirling, Phys. Lett. B 387 (1996) 419.

[118] S. Forte, talk given at 4th International Symposium on Radiative Corrections (RADCOR 98), Barcelona, Catalonia, Spain (1998) hep-ph/982382.

[119] CCFR Collaboration, W.G. Seligman et al., Phys. Rev. Lett. 79 (1997) 1213.

[120] CCFR Collaboration, J.H. Kim et al., Phys. Rev. Lett. 81 (1998) 3595.

[121] JADE and OPAL Collaborations, P. Pfeifenschneider et al., hep-ex/0001055, to appear in Eur. Phys. J. C.

[122] OPAL Collaboration, K. Ackerstaff et al., Eur. Phys. J C7 (1999) 571.

[123] ALEPH Collaboration, R. Barate et al., Eur. Phys. J C4 (1998) 409.

[124] H1 Collaboration, C. Adloff et al., Nucl. Phys. B 545 (1999) 21.

[125] W.B. Kilgore and W.T. Giele, Hadronic three jet production at next-to-leading order (1999) hep-ph/9903361.

[126] D.E. Soper and J.C.Collins, CTEQ 94/01 (1994) hep-ph/9411214.

[127] G. D'Agostini, Nucl. Instr. Meth. A 346 (1994) 306.

[128] S. Alekhin, Eur.Phys.J.C 10 (1996) 395.

[129] G. Lobo, C. Pascaud and F. Zomer, internal H1 note, H1-01/98-536 (1998).

[130] F. James and M. Roos, Comp. Phys. Comm. 10 (1975) 343.

[131] D. Graudenz, M. Hampel, A. Vogt and C. Berger, Z. Phys. C 70 (1996) 77.

[132] D.A. Kosower, Nucl. Phys. B 520 (1998) 263.

Acknowledgments

First I wish to thank Hermann Küster who initiated this analysis by setting the goal of a direct determination of the gluon density from jet cross sections. In many discussions I profited very much from his extensive knowledge and intuition on this subject.

The theoretical foundation of the QCD analysis was developed in many valuable discussions with Erwin Mirkes, Dieter Zeppenfeld, Mike Seymour and Björn Pötter who helped me to understand the basics of perturbative QCD.

I wish to thank Fabian Zomer for helpful exchanges on the consistency of the QCD analysis and on the proper use of statistical methods which had a big impact on the methods and the results of this work.

I want to thank Beate Heinemann for her excellent work on the measurement of the inclusive DIS cross section and for her help to make this knowledge available for my measurement.

My room mates in 1d33 and my colleagues from the H1 group of our institute made these years one the greatest pleasures of my life. Thank you very much Herbert Gräßler, Peer-Oliver Meyer, Heiko Itterbeck, Carlo Duprel, Thomas Kluge and Martin Wessels. Lars Sonnenschein and Arno Heister were not only nice room mates but also great collaborators whose hard work allowed us to set the present studies on this broad basis.

Very special thanks to Peter Pfeifenschneider and Thorsten Wengler for many important discussions on the consistency of methods during the whole analysis and especially for the proofreading of the final thesis.

Lebenslauf von Markus Wobisch

28.7.1965	geboren in Düsseldorf, als Sohn von Walter Wobisch und Christel Wobisch, geb. Volmer
1971–1975	Besuch der katholischen Grundschule an der Essener Straße in Düsseldorf
1975–1984	Besuch des Leibniz Gymnasiums in Düsseldorf
Mai 1984	Abitur
Oktober 1984 – Mai 1986	Zivildienst in Düsseldorf, NRW
Oktober 1986	Beginn des Maschinenbaustudiums an der RWTH Aachen
Oktober 1987	Wechsel des Studienfaches Beginn des Physikstudiums an der RWTH Aachen
April 1991	Vordiplom in Physik an der RWTH Aachen
Frühjahr 1994	Beginn der Diplomarbeit am III. Physikalischen Institut B der RWTH Aachen bei Prof. Dr. G. Flügge im Rahmen der H1-Kollaboration, DESY, Hamburg
Dezember 1995	Diplom in Physik an der RWTH Aachen
seit Januar 1996	Anfertigung der Dissertation als wissenschaftlicher Mitarbeiter des III. Physikalischen Instituts am Lehrstuhl von Prof. Dr. G. Flügge